NTNU
Norwegian University of
Science and Technology

Investigation of Moonpool Resonance as Vessel Damping Device

Lars M. Utnes Reiersen

Marine Technology
Submission date: June 2016
Supervisor: Trygve Kristiansen, IMT

Norwegian University of Science and Technology
Department of Marine Technology

NTNU Trondheim
Norwegian University of Science and Technology
Department of Marine Technology

M.Sc. thesis

Spring 2016

Lars Mikkel U. Reiersen

Investigation of Moonpool Resonance as Vessel Damping Device

The Norwegian Public Roads Administration has set an aim on a "ferry free E39" coastal highway. Due to large widths and depths of the seven remaining fjord crossings, new technological developments are needed. An occurring issue for these fjords is excitation of bridge eigenmodes for specific ocean swells, which gives rise to large motions on the bridge deck.

In that regard, Multiconsult has proposed a suspension bridge supported on elliptical floaters equipped with two moonpools. The purpose of the moonpools is to cancel pitch motions at the most important natural period of the bridge. To check the feasibility of this design, a suggestion has been to investigate two-dimensional aspects regarding the hydrodynamics of such floaters, with a special concern related to the pitch response of the construction.

The purpose of the present project is, therefore, to study the feasibility of the moonpools as a vessel damping device.

The work may be carried out in steps as follows:

1. The literature study should concentrate on basic theory for potential and viscous flow field around a 2D moonpool section. Part of this review has already been carried out during the project thesis.
2. Describe the structural dynamics of a 2D system free to move in three degrees of freedom. This study should lead to the 3x3 coupled equation of motion and its corresponding undamped homogeneous solution utilized to calculate the eigenvalue problem of a moonpool geometry with two moonpools.
3. Construct and perform forced motion experiments in heave and pitch on a two-dimensional double moonpool section to inspect the radiation problem, which can be utilized to evaluate the piston mode of motion inside the moonpools.
4. Perform a similar numerical study of the radiation problem to verify and validate the physical experiments. The simulations ought to be carried out in PVC3D, and a part of the survey should include an explanation of CFD problems
5. To capture a more realistic case, conduct a two-dimensional freely-floating experiment to measure the rigid-body motions and the flow field inside the moonpools.

6. A parameter study for five different moonpool inlets should be carried out for all numerical studies and experiments. The hope is to capture beneficial rigid-body motions and flow characteristics for some of the different configurations.
7. Output the radiation force from the numerical simulation and evaluate the eigenvalue problem for the freely-floating geometry. Utilize the mass, inertia and restoring parameters from the freely floating experiment to solve the eigenvalue problem.

The candidate should in his/her report give a personal contribution to the solution of the problem formulated in this text. All assumptions and conclusions should be supported by mathematical models and/or references to physical effects in a logical manner. The candidate should apply all available sources to find relevant literature and information on the actual problem.

The report should be well organized and give a clear presentation of the work and all conclusions. It is important that the text is well written and that tables and figures are used to support the verbal presentation. The report should be complete, but still as short and concise as possible.

The final report must contain this text, acknowledgment, summary, main body, conclusion, suggestions for future work, nomenclature, references, and appendices. All figures and tables in the main body must be identified with numbers and included in the contents. References should be given by author name and year in the text, and presented alphabetically by name in the reference list.

In the report, it should be possible to identify the work carried out by the candidate and what has been found in the available literature or new studies given to the candidate from other authors. It is important to clearly display the references to the original source for theories and experimental results.

The report must be signed by the candidate.

The thesis is to be submitted in DAIM.

Supervisor: Professor Trygve Kristiansen
Start: 10.01.2016
Deadline: 10.06.2016

Preface

This thesis is the final part of my Master of Science degree with a specialization in Marine Hydrodynamics at the Department of Marine Technology(IMT), Norwegian University of Science and Technology(NTNU). The work has been carried out during the spring semester of 2016, and the workload corresponds to 30 ECTS.

The idea behind the work was provided by Arnt Fredriksen at Multiconsult, and the present work builds upon the project thesis completed in the fall of 2015, with the same title "Investigation of Moonpool Resonance as Vessel Damping Device."

We intend to publish key parts of the work in a journal article.

Even though fundamental concepts of this work are explained in detail, the readers of this report should be familiar with the basic theory of hydrodynamics.

Lars M. R

Trondheim, June 10, 2016, Lars Mikkel Utnes Reiersen

Acknowledgment

This work has been carried out under supervision of Professor Trygve Kristiansen at the Department of Marine Technology, Norwegian University of Science and Technology. His support, understanding for hydrodynamics and divine guidance are most appreciated.

I would also like to thank Arnt Fredriksen for initiating the objectives of this thesis and his willingness to share numerical results employed in this work.

The following persons are acknowledged for their contributions to this work: Babak Ommani at MARINTEK for helping me with obstacles regarding computational fluid dynamics and OpenFOAM, and the boys at the NTNU lab: Ole Erik Vinje, Torgeir Wahl and Trond Innset, for helping me build a model and constructing satisfactory test setups.

A Special attention and all my gratitude goes to my girlfriend for always supporting me.

O.N.

(LMUR)

Abstract

The starting point of this thesis is to introduce the potential and the viscous flow formulations of a two-dimensional moonpool geometry, and the viscous approach demonstrates compliance with physical experiments. The dynamics of a three degrees of freedom system are explained through the 3x3 coupled equation of motion, and the undamped homogeneous solution is later employed to solve the systems eigenvalue problem.

Both a numerical simulation and a physical experiment of the radiation problem in heave and pitch are carried out for the model scale of a bridge pontoon. The CFD problem is conducted in an OpenFOAM extension, PVC3D, while the model test is performed in a wave flume at Marine Technology Centre. The tests investigate the piston mode of motion and involve a parameter study of five moonpool inlets, two drafts, and three forced amplitudes. The following inlets are employed: rounded, squared and three different vertical appendages.

In general, there is a satisfactory result between the numerical study and the experiments. The parameter analysis displays that the rounded inlet corners give rise to large water elevations inside the gaps, while the designs with geometrical singularities introduce vortex shedding and non-linear damping contributions resulting in smaller water responses. The effective draft changes with the inlet configurations and introduces a shift in the natural periods. The draft parameter study supports this finding, and a smaller draft triggers resonance for lower periods.

The second experiment is the spring-moored freely-floating moonpool geometry subjected to incoming regular waves, free to move in surge, heave, and pitch. The corresponding numerical results are obtained from Arnt Fredriksen's fully nonlinear hybrid scheme. A first observation is that the solution of the eigenvalue problem corresponds to the resonance peaks in heave and pitch. No resonant water motion occurs around the piston-mode resonance frequencies of the moonpools. Further, a cancellation in the heave and the pitch RAOs are experienced for particular incoming wave periods, especially for round and square inlets. This is connected to the pressure- and flow field of the moonpools, and the effects are most prominent when the moonpool wave elevations and rigid-body motions are 90 degrees out of phase with each other. Hence, the installation can be thought of as an integrated anti-pitch tank, and the bridge floaters will exert advantageous hydrodynamic properties in a given range of the incoming ocean swells.

Sammendrag

Oppgaven tar utgangspunkt i en todimensjonal struktur. Første del av studiet er rettet mot å presentere potesial- og viskøs fluidteori, og det er tydelig at en viskøs tilnæming til brønnproblemet gir mest realistiske responser. Videre fokuserer prosjektet på å utlede den koblede bevegelsesligningen for et fartøy fri til å bevege seg i tre frihetsgrader. Den udempede homogenløsningen kan dessuten benyttes til å løse egenverdiproblemet til strukturen.

Tvungne hiv-og stampebevegelser er kartlagt gjennom et numerisk studie og fysiske eksperimenter. Simuleringene ble utført i OpenFOAM-utvidelsen, PVC3D, og samsvarende eksperimenter er foretatt i en bølgetank på Marinteknisk senter. Studiet undersøker bølgehevingen i brønnene, og deler av resultatene er et parameterstudie hvor geometrien er testet for fem forskjellige inngangshjørner, to dypganger og tre forskjellige oscillasjonsamplituder i både hiv og stamp. De forskjellige hjørnene er avrunede, firkantete og tre appendiksstrukturer.

Resultatene mellom numeriske studier og eksperimenter er tilfredsstillende. Videre gir parameteranalysen følgende resultater: avrundede inngangshjørner gir høyere vannheving inni brønnene enn for de resterende designene hvor geometriske singulariteter introduserer virvelavløsninger og ikke-lineære dempningsbidrag. Hjørnepartiene resulterer også i forskjellig effektive dypganger som igjen har innvirkning på resonansperioden for strukturen. Resultatene samsvarer med dypgangstudiet, hvor mindre dypgang gir resonans for lavere perioder.

En frittflytende struktur er det andre forsøket. Geometrien er forankret og utsatt for innkomne regulære bølger, noe som gjør det mulig å måle strukturbevegelsene i jag, hiv og stamp. Resultatene fra disse forsøkene har blitt sammenlignet med numeriske resultater fra Arnt Fredriskens ikkelineære hybridmetode. Sammenligningen mellom løsningen av egenverdiproblemet og eksperimentelle resonanstopper i hiv og stamp sammenfaller. Videre ser man at resonansperiodene fra de tvungne bevegelsene ikke dukker opp i eksperimentene. Fra transferfunksjonene er det observert kanselleringsperioder i hiv og stamp. Dette har sammenheng med forandringer i trykk- og strømningsfeltet som oppstår i brønnene. Når strukturbeveglesen og vannbevegelsen inni brønnene er 90 grader ut av fase vil kanselleringsfenomenet oppstå. Effektene er tydeligst for avrundede og firkantete hjørner, og det antas at installasjonen virker som en integrert antistampetank som gir fordelaktige hydrodynamiske egenskaper for pontongene til flytebroen.

Contents

List of Tables

List of Figures

Nomenclature

Acronyms

ADI	Alternating Direction Implicit
CFD	Computation Fluid Dynamics
CFL	Courant-Fredrichs-Levi number
CPU	Central Processing Unit
DAF	Dynamic Amplification Factor
DoF	Degrees of Freedom
Fn	Froude number
KC	Keulegan-Carpenter number
NS	Navier-Stokes
NUPS	Node Update Per Second
OpenFOAM	Open source Field Operation And Manipulation
PVC3D	Potential Viscous Code 3D
RAO	Response Amplitude Operator
Re	Reynolds number

Greek Letters

α	Phase angle between geometry motion and moonpool motion
β	Phase angle between rigid body motion and moonpool motion
η_j	Body motion in j-direction
η_{3a}	Forced heave amplitude
η_{5a}	Forced pitch amplitude
λ	Wavelength
λ_s	Scaling factor

μ	Dynamic viscosity
ν	Kinematic viscosity
Ω	Fluid domain
ω	Angular frequency
ϕ	Spatial velocity potential
ρ	Liquid density
ε	Artificial damping coefficient
ζ	Free surface
ζ_a	Wave amplitude

Coordinates

(x, z)	Earth-fixed coordinate system
x_B, z_B	Center of buoyancy from calm free surface
x_G, z_G	Center of gravity

Roman Letters

a_0	Distance between center of gravity and mooring mounting
A_{kj}	Added mass in j-direction due to the force in k-direction
A_{WP}	Water plane area
B	Width of boxes
b	Moonpool gap
b'	Distance from geometry center to center of moonpool
B_{kj}	Potential damping in j-direction due to the force in k-direction
C	Phase velocity
C_g	Group velocity
CoG	Center of gravity
d	Hull draft
d^*	Non-dimensional draft
F_{ja}^{ex}	Excitation force in j-direction
g	Gravity
h	Water depth
H_j	Transfer function in j-direction

I	Mass moment of inertia
k	Stiffness coefficient
k	Wave number
$L1$	Length of fore- and aft body
$L2$	Length of center body
M	Body mass
n	Unit vector pointing into the fluid
p	Pressure
r_{yy}	Radii of gyration
t	Tangential vector
T^*	Non-dimensional period
u	Particle velocity

Chapter 1

Introduction

The E39 highway in the western part of Norway stretches approximately 1100km from Kristiansand in the south to Trondheim in the north, crossing many fjords along the way. By commissioning the Coastal Highway E39 project, the Norwegian Public Roads Administration has set an aim on a "ferry free E39." The intention of the project is to investigate technological challenges and society benefits of replacing the seven remaining ferry fjord crossings with bridges. As a direct benefit, the traveling time between Kristiansand and Trondheim will be reduced by 7-9 hours.

Due to large widths and depths of some of these fjords, bridge crossings will depend on concept innovations and technological development. For one of the crossings, Sulafjorden, Multiconsult has proposed a suspension bridge supported on floaters in the water, designed to cross the 4km long fjord.

Preliminary studies revealed excitation of eigenmode of motion for relevant bridge eigenperiods, especially for long crested ocean swells. As an attempt to counteract these eigenmodes, Multiconsult has proposed several possible bridge foundation concepts.

As of today, they are left with three different floater design for further investigation, including a spar buoy, TLP design and lastly, an elliptical bridge pontoon equipped with two moonpools. The last concept is the basis for investigating moonpools as vessel damping device, and the present work will focus on cancellation of pitch resonance.

A definition of a moonpool is a bottomless vertical well connecting the deck of a vessel with an interior free surface. The opening is traditionally applied for marine operations that require better shelter and protection from the sea environment. The present application is different, and the concept can be seen in Figure 1.1.

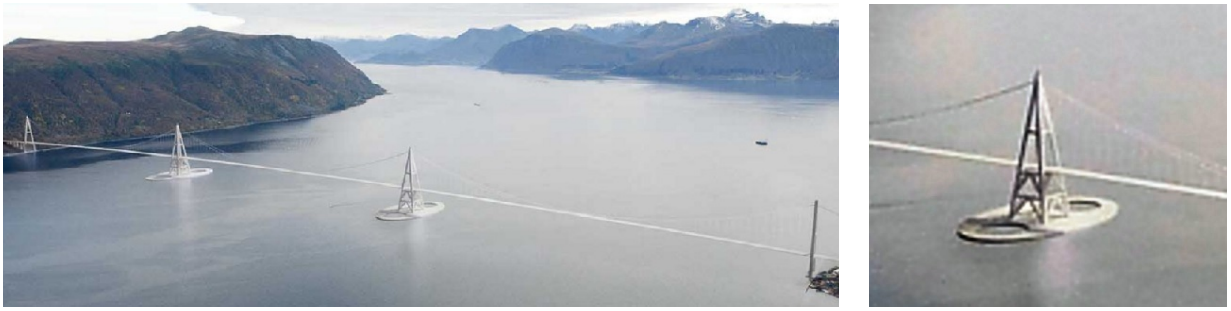

a_i b_i

Figure 1.1: Figure a) A a suspension bridge supported by elliptical moonpool pontoons. Figure b) zoomed picture of the floater. (Mul, a)

Literature Survey

Many authors have studied the two-dimensional hydrodynamic moonpool problem exposed to waves.

One of the first well-known papers on the subject was written by Aalbers (1984), which related the vertical moonpool motion to a mass-spring system. The same approach was proposed by Faltinsen (1990) who found the natural frequencies by neglecting the effects from the flow field outside the moonpool and calculated the fluid motion as a rigid block moving vertically up and down.

Later, Molin (2001) introduced an approximate linearized potential flow theory to describe the natural frequencies and the associated free surface motions inside the moonpool.

In general, the potential flow theory tends to overpredict the water motion inside the elevation. Thus, Fornier et al. (2006) proposed "the damping lid method," which restricts the water flow by introducing an artificial damping constant in the linearized free surface condition.

Other theories approach the problem by usage of viscous flow theory and Navier-Stokes equations. An example is a paper written by Kristiansen and Faltinsen (2008) which investigates the impacts that limit the vertical fluid motions inside a gap.

Previous papers have looked into moonpool configurations and how they affect the flow field and resonance for the geometry. Based on a CFD study, Moradi et al. (2015) identified different flow properties by changing draft, inlet geometry and moonpool gap size of the section.

One paper has looked at two narrow gaps in between three identical structures. The paper describes the piston mode resonance phenomena for this arrangement (Lu et al., 2010).

Another moonpool study is presented in the doctoral thesis of Fredriksen (2015), who carried out a numerical and experimental study on a two-dimensional moonpool in waves and current. The experiments were conducted for both the radiation and the incoming wave problem. An observation was cancellation of heave exaction force for particular incoming wave frequencies.

Fredriksen (2015) study was conducted for a single moonpool case with the effect of heave cancellation periods. In our work we focus on pitch cancellation which is possible due to that we have two moonpools present.

1.1 Objectives

The overall goal of this thesis is to investigate a double moonpool section to broaden the knowledge whether this concept is feasible as a vessel damping device. As an attempt to answer this question, the thesis aims to inspect following objectives:

1. Present basic theory for a potential and viscous flow field around a moonpool section
2. Describe the dynamics of a three degree of freedom system exposed to an external load
3. Construct and perform forced motion experiments in heave and pitch on a double moonpool section to inspect the radiation problem, which can be utilized to evaluate the piston mode of motion and the radiated outgoing waves
4. Create a similar numerical study of the radiation problem and compare with the physical experiments. A part of the survey should include an explanation of CFD problems
5. Inspect five different moonpool inlets to quantify the difference in flow field
6. Conduct a freely-floating experiment to measure the rigid body motions and the flow field inside the moonpool.

7. Output the radiation force from the numerical simulation and evaluate the eigenvalue problem for a floating geometry free to move in three degrees of freedom. Utilize the mass, inertia and restoring parameters, found from the previous paragraph, to solve the eigenvalue problem

1.2 Limitations

The thesis is limited to a 2D consideration of the moonpool geometry.

The present work is restricted to only account for one moonpool gap width-to-barge ratio.

1.3 Approach

A solid theoretical foundation of the fluid domain around a moonpool section is needed to fulfill the two first objectives. Thus, a literature survey is performed. Parts of the flow investigation are already covered in Reiersen (2015).

The third objective was to construct a forced motion experiment on the moonpool section. Trond Innset, Ole Erik Vinje and Torgeir Wahl built the model and prepared the lab ready to investigate the piston mode resonance problem of the moonpool section. The experiments were done in both heave and pitch, with two different moonpool draft, three different motion amplitudes, and five different moonpool inlets.

This led to the fourth objective, namely the numerical study of the same moonpool section with same geometrical and physical properties. The meshing procedure was done in an indoor software, MEGA, while the actual simulations ran on the OpenFOAM application, Potential Viscous Code 3D(PVC3D). Results obtained from the numerical experiment could be utilized to validate and verify the forced motion model tests.

From these procedures, it was possible to perform the fifth problem, namely the investigation of the effects of moonpool inlet properties.

Also for the sixth objective, the freely-floating study, five moonpool inlets were tested. Here the goal was to identify the rigid-body motions, in surge, heave and pitch, with a special focus on the pitch movements.

The last objective was to solve the eigenvalue problem, obtained through results from both the numerical radiation problem and moonpool properties utilized in the freely-floating experiments.

1.4 Structure of the Report

Chapter 2 introduces the basic concepts behind the fluid flow formulation and the dynamics of a structure. The section begins by defining the governing equations for a fluid domain. Here, both the potential and viscous flow problems are explained. Examples of different potential theories to obtain natural frequencies are given, and the radiation and diffraction problem are further explained through a practical example from the literature. Next, concepts around linear wave theory, Keulegan-Carpenter and Reynolds number are presented. Lastly, a section regarding the structural dynamics for both one and three degrees of freedom are discussed.

Chapter 3 presents the numerical study performed in this thesis. The first part describes the theory behind computational fluid dynamics. This yields important aspects of the discretization process, numerical schemes, and the CFD solver, etc. The second part enlighten the process of running the numerical simulations, including meshing procedures, boundary condition, convergence studies and choice of domain size.

Chapter 4 is a thorough explanation of the experimental setups, both the forced oscillations and the freely-floating structure. It also describes the potential sources to the error of the model tests and the post-processing procedure, where the measured raw data are converted to results.

Chapter 5 includes observations and findings from the model tests and the numerical study. The first part display the results from the forced piston mode of motion experiments, obtained both from the numerical simulations and model tests. Here, much effort is made to compare these tests and display key findings of a parameter study of the moonpool section. The eigenvalue problem is also solved from the forces carried out in the numerical study. The second part of the chapter visualize the results and discussion regarding the freely-floating experiments.

Chapter 6 is the conclusive summary and recommendations for future work.

Chapter 2

Theory

The aim of this chapter is to give a mathematical description of a two-dimensional a moonpool geometry with emphasis on moonpool wave amplitude, its resonance, and the dynamic response.

The first part will introduce the governing equations regarding potential flow theory and the viscous formulation. It should be noted that the flow field in the proximity of the moonpool problem is best described by the viscous approach. Though, one of the following subsections will discuss a method to reduce the discrepancy in response between potential flow and the physical problem. Next, linear potential hydrodynamic coefficients and forced motions are described through a practical example of a freely-floating structure and its moonpool motions. Further, a paragraph of the viscous problem is going to be discussed, including a hybrid scheme combining both potential and viscous fluid domain. A section regarding linear wave theory is carried out because of its importance for the two-dimensional wave tank problem displayed in figure 2.1.

Lastly, as an attempt to explain the rigid motions of the two-dimensional freely-floating section, the second part of this chapter is dedicated to describe the structural dynamics of a geometry.

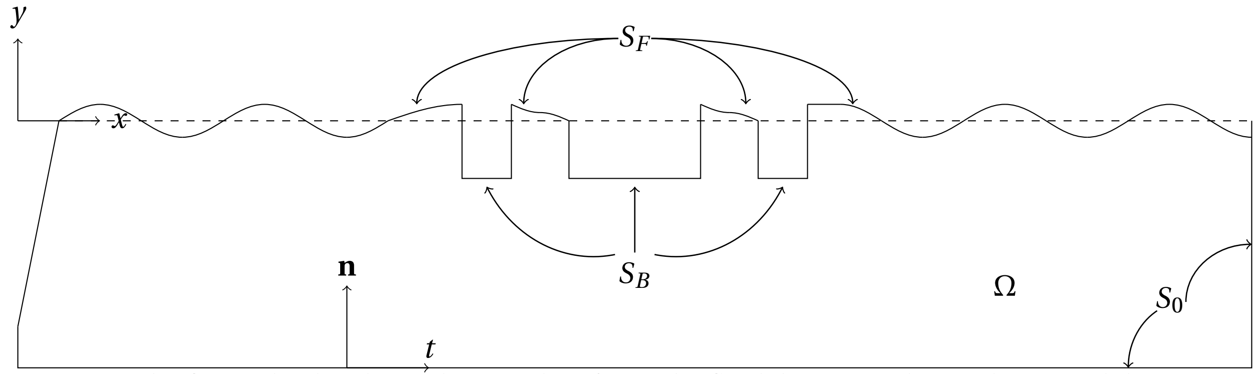

Figure 2.1: The figure display the tank control surface. The fluid domain is denoted as Ω and the boundary $S = S_0 + S_B + S_F$. The coordinate system(x,y) is defined with $x = 0$ at the wavemaker neutral position and $y = 0$ at still water level. The normal vector, n, is defined as positive into the fluid domain and t is the tangential vector pointing in the positive direction in the figure.

2.1 Governing Equations

The hydrodynamics inside a moonpool is usually described by potential or viscous flow theory. For the potential flow domain, the fluid is assumed to be incompressible, inviscid and irrotational.

From these assumptions, it's possible to evaluate the fluid with the Laplace's equation, which implies that there exists a velocity potential in the fluid domain that satisfies following equation,

$$\nabla^2\phi = 0 \tag{2.1}$$

where ∇ is the nabla operator and the absolute liquid velocity is defined as $u = \nabla\phi$. The goal is to solve the unknown, ϕ, over the domain Ω. Conditions at the boundaries are known and utilized as tools to calculate the velocity potential. The dynamic and kinematic free-surface conditions are defined along $\mathrm{S_F}$, while the impermeability condition applies for $\mathrm{S_0}$ and $\mathrm{S_B}$ in Figure 2.1.

The necessary equation on the free surface is the dynamic free-surface boundary condition that evolves from Bernoulli's equation. This formula relates the pressure, p, to the fluid velocity and the gravitational force per fluid volume at any point in the fluid

$$p + \rho\frac{\partial\phi}{\partial t} + \rho\frac{1}{2}(\frac{\partial\phi}{\partial x})^2 + \rho\frac{1}{2}(\frac{\partial\phi}{\partial y})^2 + \rho g y = C, \tag{2.2}$$

where g is the gravity, ρ is the fluid density, p is the pressure in the fluid relative to the atmospheric pressure, and y is the vertical coordinate defined as zero at the still water level and positive direction pointing upward. Gravity is assumed to be the only external force field. C is an arbitrary function, and by including the time dependence of C in the velocity potential, it's possible to denote C as a constant. For the case of zero flow in the fluid domain, it follows from equation 2.2 that $p + \rho g y = C$, and C is equal to the ambient pressure at $y = 0$. Thus, the water pressure can be assumed equal to the constant atmospheric pressure on the free surface the dynamic condition on S_F,

$$g\zeta + \frac{\partial\phi}{\partial t} + \frac{1}{2}((\frac{\partial\phi}{\partial x})^2 + (\frac{\partial\phi}{\partial y})^2) = 0 \qquad on \;\; S_F \tag{2.3}$$

The free surface of a wave is governed by the kinematic free-surface condition such that S_F is tracked by following the velocity of the free surface itself. This means that $F(x, y, t) = y - \zeta(x, t) = 0$ describes the water elevation, and consequently, the kinematic boundary condition can be written as follows:

$$\frac{\partial\zeta}{\partial t} + \frac{\partial\phi}{\partial x}\frac{\partial\zeta}{\partial x} - \frac{\partial\phi}{\partial y} = 0 \qquad on \;\; y = \zeta \tag{2.4}$$

On the solid boundaries, S_0 and S_B, it's possible to write the generalized impermeability condition as

$$\frac{\partial\phi}{\partial n} = U \cdot n \qquad on \;\; S_0, S_B \tag{2.5}$$

where U is the velocity of the boundary S_0 and S_B relative to the defined Earth-fixed coordinate system.

If the linearized problem is explored, the boundary itself does not evolve in time. The boundary condition is therefore imposed on the initial position and equation 2.3 and 2.4 reduces to

$$\begin{aligned} \frac{\partial\phi}{\partial t} &= -g\zeta \qquad on \;\; y = 0 \\ \frac{\partial\zeta}{\partial t} &= \frac{\partial\phi}{\partial y} \qquad on \;\; y = 0 \end{aligned} \tag{2.6}$$

Note that $\partial/\partial y = -\partial/\partial n$ since the normal vector is pointing into the water.

The free surface elevation can be found when the velocity potential is known. If the potential is oscillating harmonically in time with circular frequency ω, one can combine the equations given in 2.6, and the combined free surface condition is given as

$$-\omega^2\phi + g\frac{\partial \phi}{\partial y} = 0 \qquad on \;\; S_F \tag{2.7}$$

It will later be discovered that the potential flow description of the fluid will not give desired results in some parts of the domain, for instance around moonpool corners in figure 2.1. The explanation is found from the assumptions for potential flow. Incompressibility is often a good assumption in water, while the requirements of irrotational and inviscid flow are at best a gross simplification.

Instead, if the core assumptions yield conservation of mass, energy and momentum it is possible to establish the governing equations for fluid flows: Continuity equation, momentum equation, and the energy equation. By applying the Newton's second law of motion to the fluid motion under the assumption that the stress in the fluid arises due to velocity gradient and a pressure term, one can derive the Navier-Stokes equations.

A thorough derivation of the formulas is found in Çengel and Cimbala (2010) and the deduction for incompressible fluids result in the following governing equations,

$$\nabla \cdot u = 0 \tag{2.8}$$

$$\frac{\partial u}{\partial t} + u \cdot \nabla u = -\frac{1}{\rho}\nabla p - g\hat{j} + \nu \nabla^2 u \tag{2.9}$$

where equation 2.8 is known as the continuity equation for liquid mass. Equation 2.9 is the Navier-Stokes equation, where $u = (u, v)$ is the two-dimensional fluid velocity in xy-plane, $\hat{y}$ is the unit vector in the positive y-direction and ν is the kinematic viscosity.

There are hardly any analytic solutions for this expression, except a few very simple problems. Nowadays approximate solutions of Navier-Stokes problems are computed numerically through discretization of the fluid domain and solved with a set of algebraic equations for each element. Chapter 3 propose a solution scheme for these problems.

2.2 Potential Flow Formulation of Natural Frequency

Again, the attention is turned towards the potential flow problem for a single moonpool case. There are several known theories that can be used to describe the problem. One of the studies neglect the effect from the flow field outside the moonpool, and the fluid motions and natural frequencies are calculated assuming only one-dimensional vertical potential flow inside the gap, known as the piston mode. Other natural modes also exist and are described as standing waves called sloshing modes, Figure 2.2.

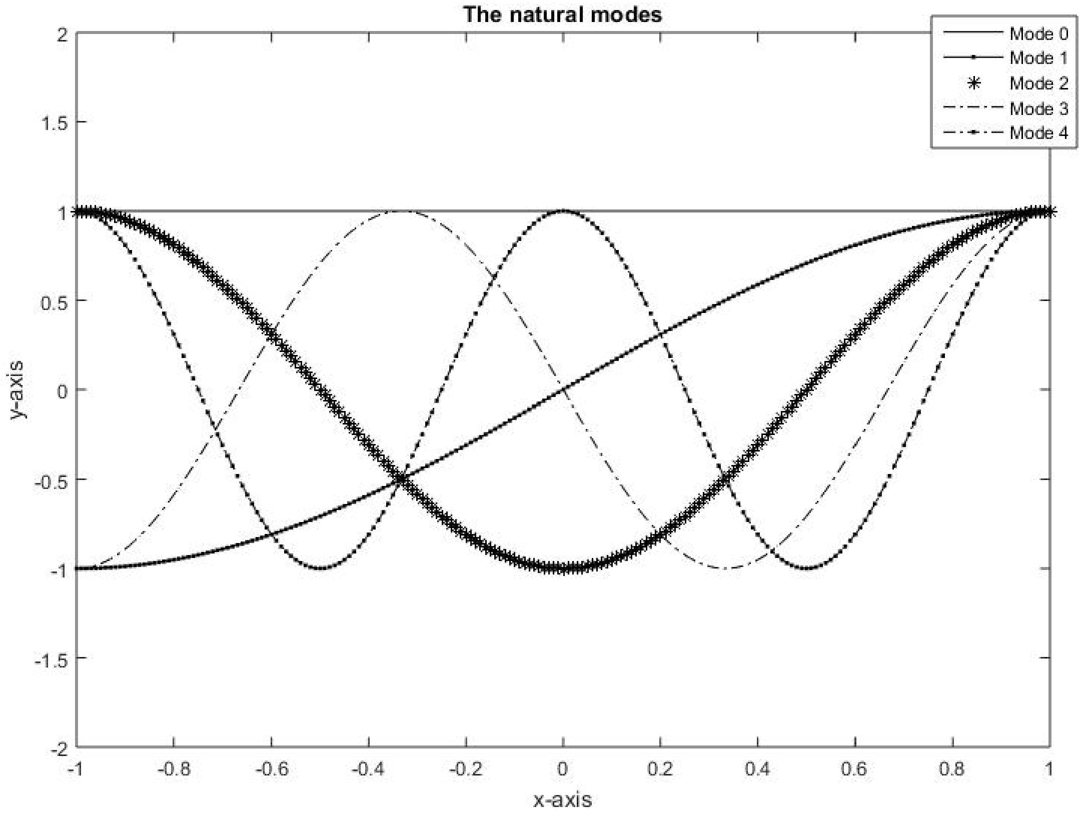

Figure 2.2: Visualization of the natural modes, piston (0-mode) and sloshing modes (1- up to 4-mode).

Faltinsen (1990) proposed a theory based on the fluid-momentum equation given by Euler's formula.

$$\rho\frac{d^2\zeta}{dt^2} = -\frac{\partial p}{\partial z} - \rho g \tag{2.10}$$

The deduction relates the fluid motions to a mass-spring system. By assuming steady state harmonic wave excitation the natural frequency can be derived to:

$$\frac{d^2\zeta}{dt^2} + \frac{g}{d}\zeta = 0 \tag{2.11}$$

$$\omega_n = \sqrt{\frac{g}{d}} \tag{2.12}$$

The same approach can be applied to find the natural period for a U-tube tank, which has some similarities to pitch motion piston mode resonance for a geometry equipped with two moonpools.

$$\omega_n = \sqrt{\frac{2g}{l}} \tag{2.13}$$

where l is the length of the tank.

Another theory describes the fluid motion with the possibility of a non-zero mass flux through the moonpool base. This phenomenon often occurs in the piston mode. Paper, written by Molin (2001) accounts for outside effects for the moonpool motion, and the determination of the natural modes and free surface elevation inside the moonpool domain are done under the assumptions of infinite water depth and an infinitely long barge. In a two-dimensional case, the barge is thought of as two motionless rigid blocks with a gap in between.

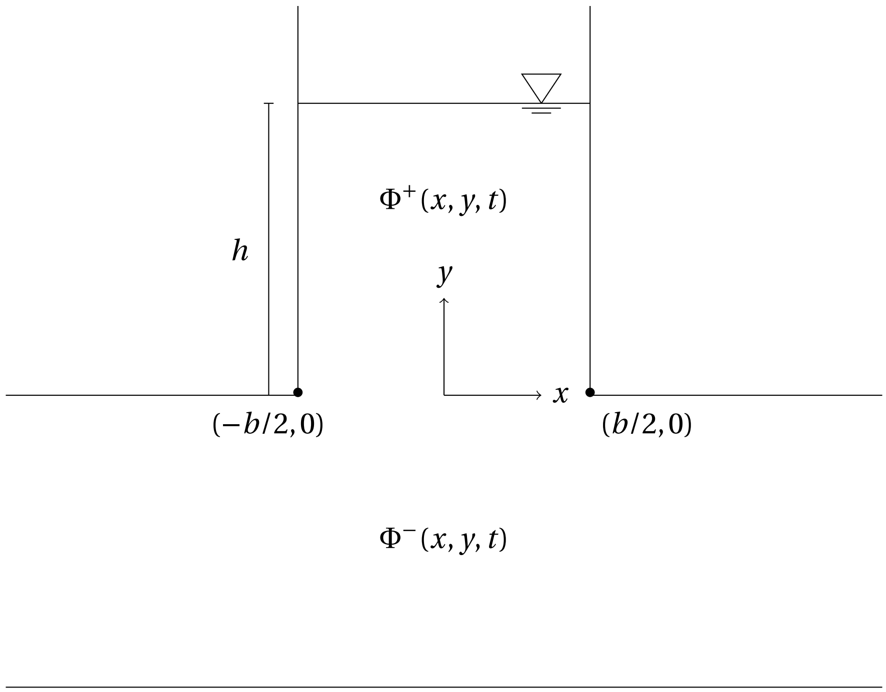

Figure 2.3: Conceptual drawing of the moonpool and its potential flow domains. The area under the moonpool configuration is the lower half plane, and the field "trapped" inside is the moonpool domain. The barge width will extend towards infinity, and the seabed is infinitely deep (Molin, 2001).

The velocity potential of the lower half plane, $\Phi^-(x,y,t)$, is described through complex variables, where z=x+iy. The result of the lower half plane is as follows

$$f^-(z,t) = -\frac{1}{\pi}\int_{-b/2}^{b/2} \Phi_y^-(\zeta,0,t)\, ln(z-\zeta)\, d\zeta \tag{2.14}$$

To create a non-zero mass flux through the moonpool base, the velocity potential at this location has to represent source components. An occurring issue is that the potential becomes singular when x goes to $\pm\infty$, which gives no physical meaning.

Consequently, to capture the physical flow, Molin placed one sink on both sides of the barge with a distance of $\pm\lambda B/2 = H/2$ from the moonpool center (B is the barge beam and λ is a coefficient greater than 1). The sinks were placed in keel height to avoid mass flux through the far field free surface, and turns out to represent a fluid that flows around the keel and up to the surface and radiate waves away from the hull. The potential in the lower plane is now written as:

$$f^-(z,t) = -\frac{1}{\pi}\int_{-b/2}^{b/2} \Phi_y^-(\zeta,0,t)\left[ln(z-\zeta) - \frac{1}{2}ln(z-H/2) - \frac{1}{2}ln(z+H/2)\right] d\zeta \tag{2.15}$$

By introducing an error of (b^2/H^2) and changing away from complex notation, one can simplify the expression through series expansion.

$$\Phi^-(x,0,t) = -\frac{1}{\pi}\int_{-b/2}^{b/2} \Phi_y^-(\zeta,0,t)\ln\frac{|x-\zeta|}{H/2}d\zeta \tag{2.16}$$

The matching principle at the boundary can be used to derive the velocity potential inside the moonpool, namely $\Phi^-(x,0,t) = \Phi^+(x,0,t)$ and $\Phi_y^-(x,0,t) = \Phi_y^+(x,0,t)$. Hence,

$$\Phi^+(x,0,t) = -\frac{1}{\pi}\int_{-b/2}^{b/2} \Phi_y^+(\zeta,0,t)\ln\frac{|x-\zeta|}{H/2}d\zeta \tag{2.17}$$

Combining Laplace's equation, impermeability condition at the moonpool walls and the seabed, and the combined free surface condition(equation 2.1, 2.5 and 2.7) together with the velocity potential inside the moonpool(equation 2.17)it's possible to deduce the piston mode natural frequency to

$$\omega_o \cong \sqrt{\frac{g}{h + (\frac{b}{\pi})(\frac{3}{2} + \ln\frac{H}{2b})}} \tag{2.18}$$

where b is the moonpool gap, h is the draft.

The position of the two sinks, $\pm H$ is optimized by numerical analysis and experiments, and in Molin's case found to be equal to 1.5B. Here, the beam of the structure was three times the moonpool width, and $H/b = 4.5$ gave matching results. The piston mode natural frequency is now written as,

$$\omega_0 = \sqrt{\frac{g}{h + 0.736b}} \tag{2.19}$$

The natural frequency obtained by theory presented by Molin is found to be accurate within 1 percent of experimental results.

However, Molin's method does not consider the wave elevation inside the moonpool. Many studies, like Kristiansen and Faltinsen (2011), revealed an overestimation of resonance wave motion occurring in potential flow theory. This clearly shows that there are other significant damping effects present in the moonpool, not covered by the energy loss from radiated waves.

2.2.1 Potential Theory Using Lid Damping

As stated, linear damping effects obtained by potential theory do not capture all the damping contributions in a moonpool flow. Several different methods are conducted as an attempt to reduce the discrepancy between potential theory and observed results. A method called the "epsilon" damping lid method, first reported by Chen and presented by Fornier et al. (2006), introduced an artificial damping coefficient in the free surface conditions.

The combined free surface condition is now written as Bunnik et al. (2009).

$$g\phi_y - (1 - i\varepsilon)\omega^2\phi = 0 \qquad y = 0 \tag{2.20}$$

where i is the complex number, y is the vertical axis with $y = 0$ is located at the mean water surface.

The ε-lid damping theory limits overestimation of resonant wave elevation in gaps. However, since the method is not related to any physical phenomena, it's necessary to tune the ε-value for each specific case. This can, for instance, be done through model tests. Therefore, the method is somewhat cumbersome and fails to broaden the understanding of the flow field inside the moonpool.

2.3 Results from Fredriksen's Experiments

Another way of inspecting the hydrodynamics around a single moonpool structure is through investigation of the hydrodynamic forces and coefficients for a geometry exposed to forced oscillations, or a freely-floating structure subjected to incoming waves. To broaden the understanding of these problems, a practical example from a doctoral thesis, Fredriksen (2015), will be included. Here, the inspected moonpool geometry consider one gap, instead of two openings evaluated for the present case.

2.3.1 Hydrodynamic Coefficients and Coupling Effects

In linear potential flow theory, the velocity potential can be described by the following equation:

$$\phi = \phi_i + \phi_d + \sum_{j=1}^{6} \phi_j \tag{2.21}$$

where ϕ_i is the incident wave potential, ϕ_d is the diffraction contribution related to the wave generation due to the presence of the body in the incoming waves, and can be found through the body-boundary condition $\partial\phi_i/\partial n = -\partial\phi_d/\partial n$. The ϕ_j are the radiation potentials, obtained from the forced oscillations of the structure in direction *j*.

The forced motions, described by the radiation problem, determines the hydrodynamic added mass and potential flow damping coefficients as a function of the frequency. This is given as,

$$F_{kj}(t) = -A_{kj}(\omega)\ddot{\eta}_j(t) - B_{kj}(\omega)\dot{\eta}_j(t) \tag{2.22}$$

here, $F_{kj}(t)$ is the hydrodynamic force in k-direction due to motions in j-direction. Linear theory is assumed, and changes in the instantaneous wetted surface are not accounted for. Nor are the forces and moments due to hydrostatic pressure.

The added mass term, A_{kj}, accounts for the fact that when the body moves in a fluid, some amount of the fluid must move around it. When the geometry accelerates, so must the fluid in proximity of it as well. Thus, an additional force is required to accelerate the fluid around, namely the added mass term. This term is 180^o out of phase with the acceleration of the body.

In the same manner, as the added mass term relates to the acceleration of the body, it's convenient to apply a component proportional to the velocity. This is the linear potential damping coefficient,B_{kj}, which is 180^o out of phase compared to the body velocity. This term accounts for the amount of energy leaving the structure through radiated waves.

The general expression for potential flow added mass and damping can be written as,

$$A_{kj}(\omega) = \rho \int_{Sb} Re(\phi_k n_j) ds \qquad k = 1,2,...6; j = 1,2,..,6 \tag{2.23}$$

$$B_{kj}(\omega) = \rho\omega \int_{Sb} Im(\phi_k n_j) ds \qquad k = 1,2,...6; j = 1,2,..,6 \tag{2.24}$$

Sb is the body surface, Re() and Im() are respectively real and imaginary part of the expression.

A practical example of the radiation problem was performed by Fredriksen (2015). A numerical and physical experiment on a moonpool section with coupling between sway, heave and roll motion were carried out, and it was conducted four different experiments. In order to determine the hydrodynamic coefficients, three tests were done for the radiation problem. To find the excitation forces, it was also performed a freely floating model test. Examples of output RAOs are visualized in figure 2.4 and 2.5.

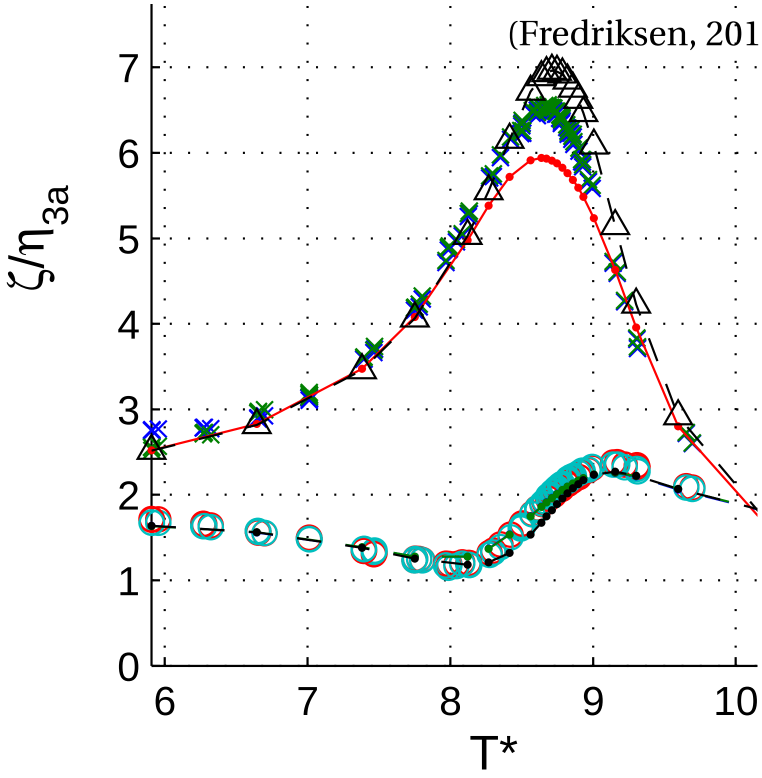

Figure 2.4: The wave amplitude inside the moonpool for forced oscillations. ζ is the moonpool elevation and η_{3a} is the forced oscillation amplitude. The highest lines represent moonpool amplitudes(the x are results from the experiment), while the lower lines represent wave amplitudes outside the moonpool geometry(turquoise circles are experiments). The x-axis is non-dimensional period, $T^* = T\sqrt{\frac{g}{b}}$. (Fredriksen, 2015)

(Fredriksen, 2015)

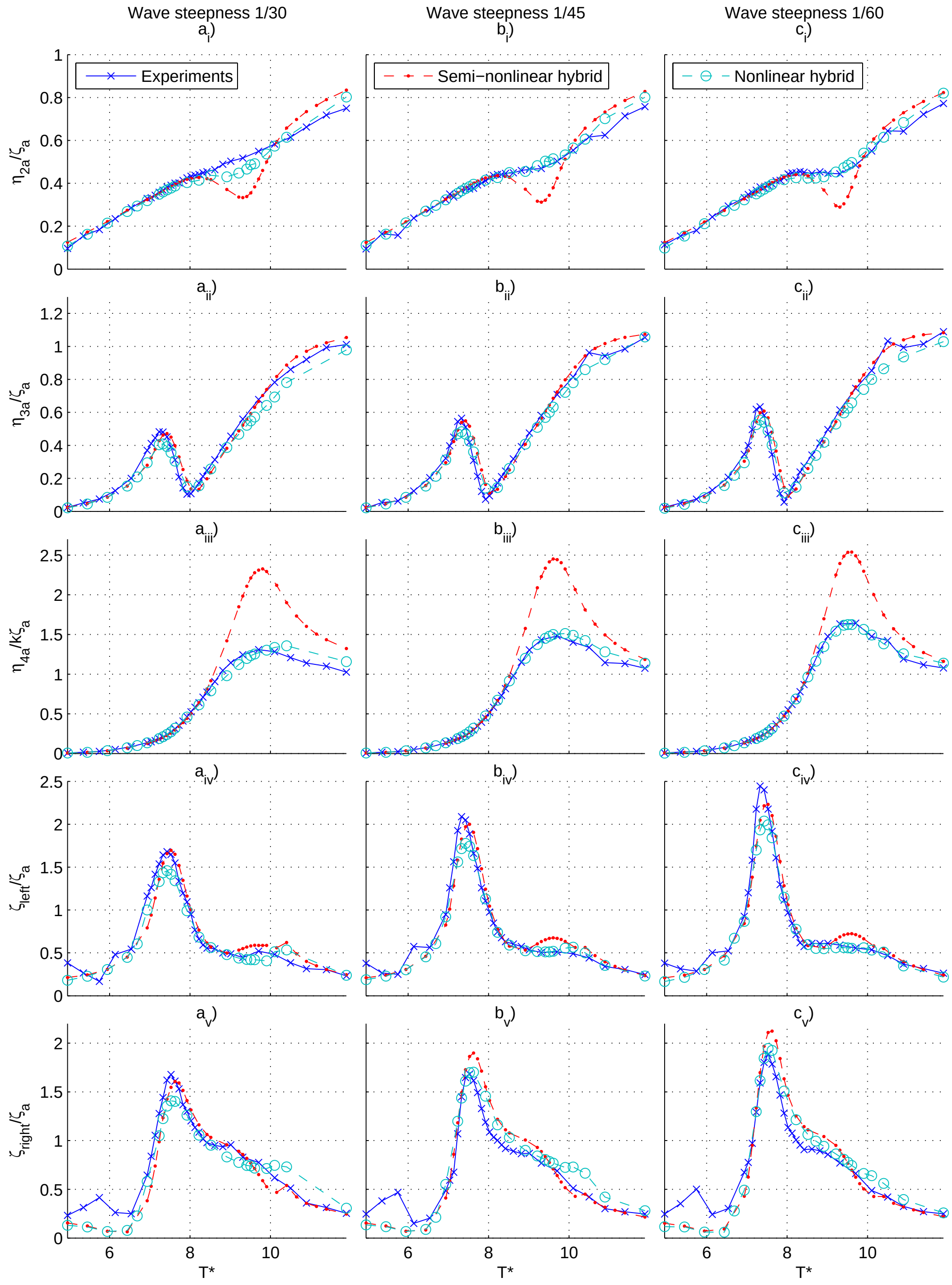

Figure 2.5: Comparison of experimental and numerical rigid body motion amplitudes in η_{2a},η_{3a},η_{4a} and the free surface amplitudes, ζ_{right}, ζ_{left} for single moonpool section with different wave steepness. $T^* = T\sqrt{\frac{g}{b}}$. (Fredriksen, 2015).

2.3.2 Freely-floating Body in Incoming Regular Waves

The preceding section evaluates response due to wave radiation. Another problem occurs on the freely-floating structure exposed for incoming waves. The discrepancies in flow characteristics between these problems are documented by Fredriksen (2015), and it's noticeable that the forced motion resonance behavior from figure 2.4 at $T^* = 8.7$ do not show up in the freely floating experiments in figure 2.5.

Similar observation was done by McIver (2005); around piston mode natural period for freely floating geometries, the linear potential flow theory, equation 2.21, have two main contributions from the radiation and diffraction potentials which are 180^o out of phase. In other words, near piston mode natural period it's observed that the contributions from the diffraction potential, ϕ_d, and the radiation potential, ϕ_3, cancel each other out. This phenomenon is observed in Figure 2.4 and 2.5, where the resonance from the radiation problem is not apparent in for the freely-floating case.

Further, Fredriksen (2015) carried out analysis for a freely-floating body in incoming regular wave. Supported by figure figure 2.5 and 2.6 it is seen that after the first resonance peak in heave, $T^* = 7.4$, the phase angle between the moonpool wave elevation and the heave response becomes in phase. Here, the phase angle, α, is defined as the phase between the heave acceleration in CoG and the moonpool wave motion.

A direct effect is that the moonpool wave motions decrease the heave motion of the vessel. This is illustrated in figure 2.5 a_{iii}, where it's clearly seen that the heave RAO falls after a build up for lower periods. This effect is apparent in both potential and viscous flows. The consequence is

"*This is not only related to the viscous simulations, but also the potential flow calculations capture this effect. It means that the moonpool works as a heave minimization device.*" (Fredriksen, 2015).

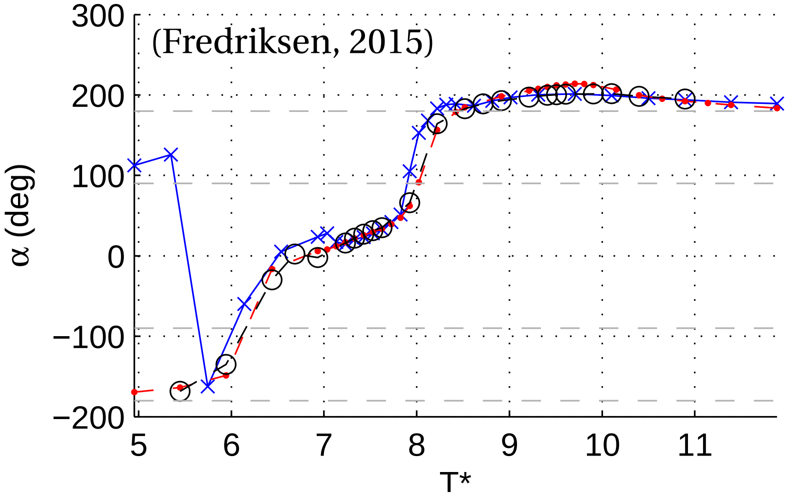

Figure 2.6: The phase angle α between heave acceleration in CoG and moonpool wave motion. The crossed line is experimental values,and filled circle line is Semi-non-linear hybrid code, and the circle line is non-linear hybrid method line. $T^* = T\sqrt{\frac{g}{b}}$. (Fredriksen, 2015).

2.3.3 Comparison with Single Hull

A part of Fredriksen (2015) study was a comparison between the rigid motion of the single moonpool hull and a mono-hull through a semi-nonlinear hybrid method. The dimensions of the two hulls were equal except that the mono-hull had a closed moonpool gap. Accordingly, the mass increased, but the radii of gyration were held constant by increasing the inertia.

Three differences can be observed from Figure 2.7. First, the additional heave resonance introduced by the moonpool, second an increased roll amplitude for the mono-hull, and last, a cancellation effect in heave in the moonpool case.

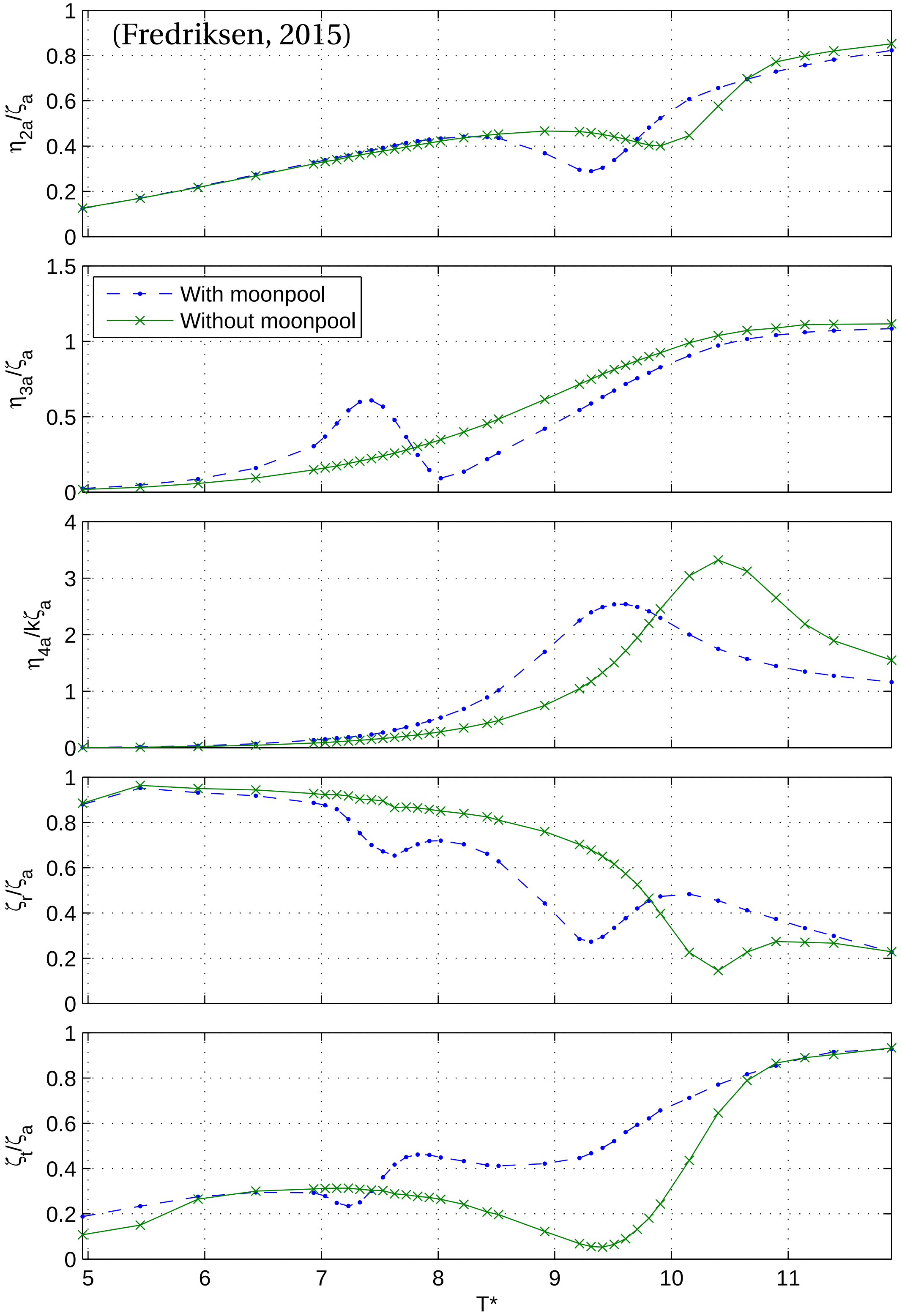

Figure 2.7: Comparison of the rigid-body motion response amplitudes (ζ_t) between a hull with and without a moonpool subjected to waves with steepness 1/60 using a semi-nonlinear hybrid method, $T^* = T\sqrt{\frac{g}{b}}$. (Fredriksen, 2015)

2.4 Present Moonpool Configuration

Different from theories mentioned above is that the present case considers a double moonpool structure, and the comparison must be understood accordingly. A simplification of the two moonpool structure is given in figure 2.8 and is the foundation behind the analysis with single moonpool geometries performed in later sections. Here, it's assumed that the flow fields are similar around the symmetry line, and the simplification is done by considering one-half of the geometry.

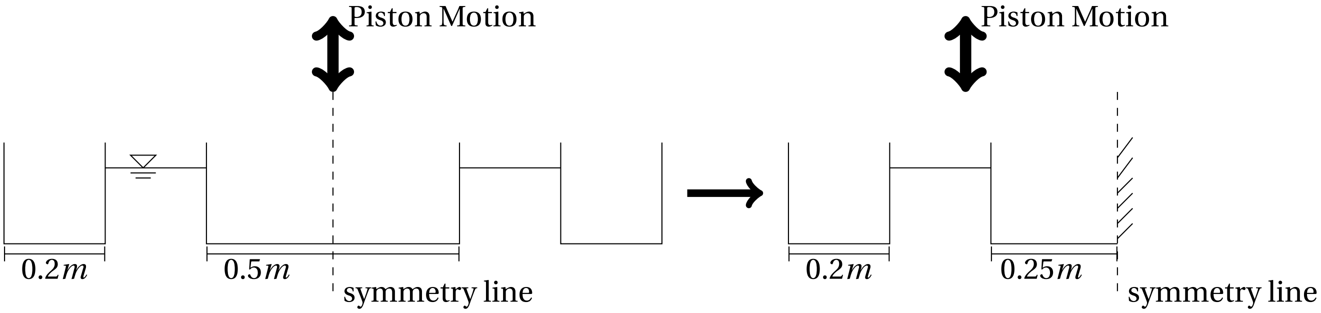

Figure 2.8: The figure display a simplification of the piston mode motion for geometry in heave. It's assumed that the flow is similar around the symmetry line, and the two moonpool problem is simplified to a one moonpool case. This is the basis for the comparisons in Table 5.1

2.5 Viscous Flow

The preceding discussions barely mention that the moonpool problem have viscous effects near the moonpool base, and potential flow theory is not valid in these regions.

In gap resonance problems where it is a well-defined separation point, there will be flow separation. Kristiansen and Faltinsen (2008) performed an investigation of the effect of viscosity and the non-linear effects associated with the free surface conditions. Kristiansen pointed out that the damping effect of in- and outflow of the boundary layer is negligible and that the contribution associated with the non-linear free surface conditions were of minor importance. Further, he concluded that the effects from flow separation, and the change in the pressure field due to that, explains the significant discrepancy between linear theory and model tests.

He also conducted a study on the effects of horizontal appendages in the moonpool inlet. This introduces two major contributions, namely a reduction of the inlet opening and an increases in strength of the shed vorticity, i.e. bigger damping.

Lastly, separation is found to be of great importance when the gap becomes small relative to the dimensions of the structure. The damping will have a significant impact, and possibly of the same order of magnitude or bigger than damping from radiated waves. It's clear that viscous effects are a major contributor, and the fluid domain will, at least partly, be viscous.

2.6 Kristiansen's Hybrid Scheme

A combination between potential and viscous flow was proposed by Kristiansen and Faltinsen (2011). Here, the free-surface and the fluid far away from the body is one domain governed by potential flow theory, while Navier-Stokes equations describe the rest of the fluid, illustrated in figure 2.9.

The reason for coupling these theories is that potential flow theory captures the propagating waves at the free surface most accurate, while the viscous flow, will describe the flow separation around sharp edges, for instance, a moonpool inlet relevant for this case.

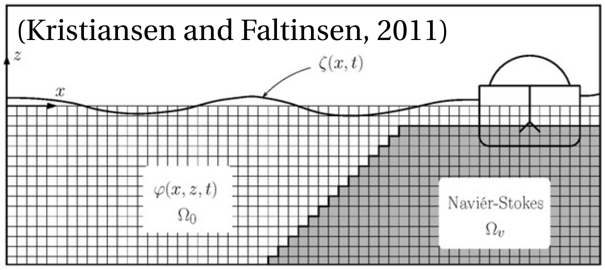
(Kristiansen and Faltinsen, 2011)

Figure 2.9: Domain decomposition. White: Inviscid domain, Shaded: Viscous domain (Kristiansen and Faltinsen, 2011).

2.7 Keulegan-Carpenter-and Reynolds Number

Flow separation is evident around a structure with geometric singularities. That is not necessary the case around cylindrical shapes, and special considerations are needed to determine the appearance and position of the separation point.

The flow around circular geometries will, in general, depend on the radius, period of oscillations and fluid velocity. Both the Keulegan-Carpenter and Reynolds number are employed to determine the flow separation around the geometry.

The Keulegan-Carpenter number is given as:

$$KC = \frac{U_M T}{D} \tag{2.25}$$

where U_M is the maximum velocity of a period, T is the period and D is the characteristic length. For an oscillatory flow the velocity can be written as $U_M = 2\pi A/T$ and the modified equation becomes,

$$KC = \frac{2\pi A}{D} \tag{2.26}$$

here A is related to the water motion amplitude.

A schematically picture of the flow field with different KC numbers are given by Pettersen (2007).

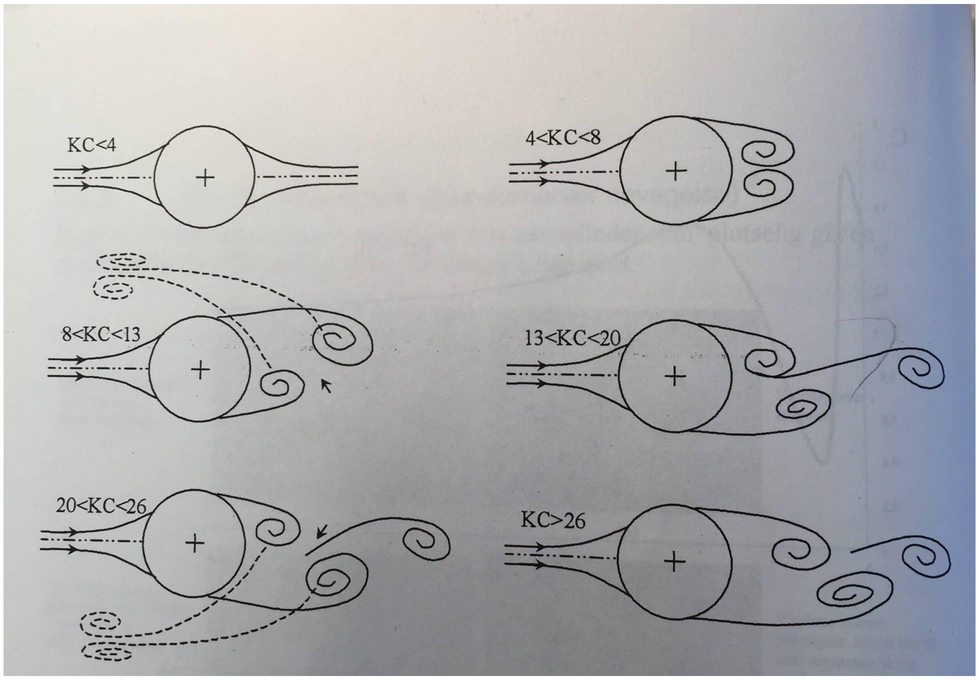

Figure 2.10: Flow regimes around cylinder for different KC-numbers. Pettersen (2007)

The Reynolds number is important to decide upon the flow regime apparent for the model test. For low Reynolds number, there is a laminar boundary layer and separation will occur more upstream on a body compared to turbulent flow. The Reynolds number is given as,

$$Re = \frac{UD}{\nu} \tag{2.27}$$

2.8 Linear Wave Theory

Before the focus moves to the dynamics of structures, some formulations regarding linear waves are going to be presented.

Regular waves are given with period T, the wavelength λ and the wave height H. Further, the circular frequency is given as $\omega = 2\pi/T$ and the wave number is $k = 2\pi/\lambda$. Another property is the wave steepness which is the ratio between H/λ.

It is assumed a constant water depth h for a fluid extending infinitely in the horizontal direction. A steady-state harmonic solution can be found, giving the linear dispersion relation relating the wave frequency ω, wave number k and gravity g,

$$\omega^2 = gk \tanh kh \tag{2.28}$$

By energy consideration of a two-dimensional wave train, it is possible to recover the propagation velocity of the energy associated with the wave, denoted the group velocity $C_g = d\omega/dk$, which is

$$C_g = \frac{C}{2}\left(1 + \frac{2kh}{\sinh 2kh}\right) \tag{2.29}$$

where $C = \omega/k$ is the phase velocity.

If the deep water assumption is valid, the wavelength becomes negligible compared to the water depth, or kh -> 0, C_g is now written as $C_g = C$. This is the foundation for the experiments elaborated in chapter 4.

2.9 Dynamic System

The second aim of this chapter was to investigate the dynamics of a moonpool structure, which can be seen as a dynamic system with three degrees of freedom(DoF). In order explain the basics behind these motions, it's convenient to look at a simple single degree of freedom case, namely the mass-spring system exposed for a harmonic oscillating force.

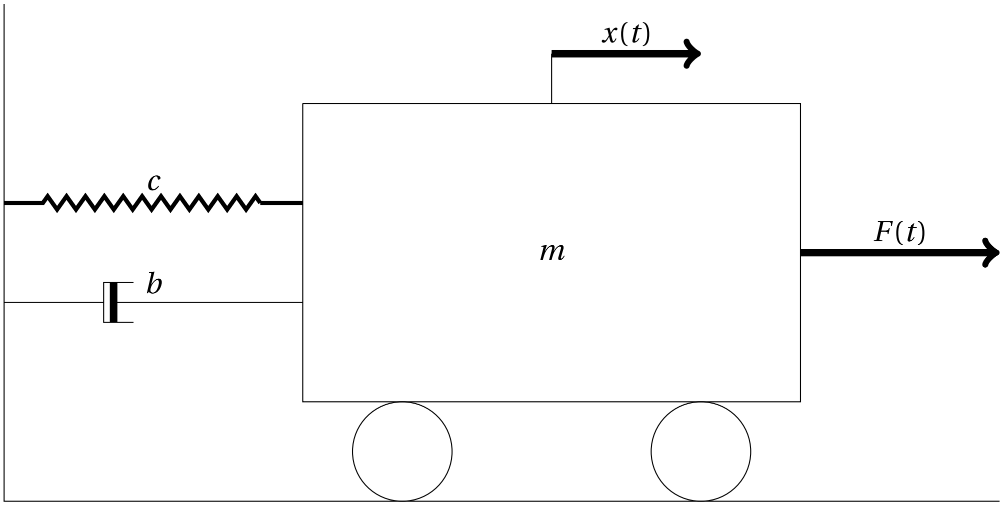

Figure 2.11: Picture displays a 1 DoF mass-spring system where m represents the mass of the system, b is the damping component and c is the stiffness. $x(t)$ is the time dependent displacement and $F(t)$ is the harmonic oscillating force. Figure based on Larsen (2014).

2.9.1 System with One Degree of Freedom

The motions of a 1 DoF dynamic system can be described as;

$$m\ddot{x}(t) + c\dot{x}(t) + kx(t) = F(t) \tag{2.30}$$

where m is the mass of the system, b is the damping coefficient, c is the stiffness of the system, and F(t) is the external load given as $F(t) = F_0 cos(\omega t)$. $\ddot{x}(t)$, $\dot{x}(t)$ and $x(t)$ are respectively the acceleration, velocity and the displacement of the system at a given time.

This is a second order differential equation with the displacement calculated as the superposition of the forced and the free response. The short description is given below, while a more thoroughly explanation is found in Larsen (2014). The displacement can be given as

$$x(t) = x_H(t) + x_P(t) \tag{2.31}$$

x_H is the homogeneous solution obtained from F(t)= 0, and solved for the system's initial conditions. This part of the equation will die out after a short period, and is therefore called the transient solution.

$$x_H(t) = A\sin\omega_0 t + B\cos\omega_0 t \tag{2.32}$$

A and B are calculated at t= 0, i.e. $x(0) = x_0$ and $\dot{x}(0) = \dot{x_0}$.

$$x(t) = \frac{\dot{x_0}}{\omega_0} \sin \omega_0 t + x_0 \cos \omega_0 t \tag{2.33}$$

The other part of the solution for a harmonic system exposed for an external load can be expressed as

$$x_P = C_1 \sin \omega t + C_2 \cos \omega t \tag{2.34}$$

This is the particular part known as the steady-state solution of the equation. By applying x_P into equation 2.30 it possible to write:

$$x_P = \frac{F_0}{\sqrt{(-\omega^2 m + k)^2 - \omega^2 c^2}} sin(\omega t - \beta) \tag{2.35}$$

The total solution of the system is found by superposition of the homogeneous and particular solution.

Next, the response amplitude operator later referred as the RAO, is found by dividing the response amplitude by the amplitude of the forced term.

$$\left| \frac{x_P}{F_0} \right| = \frac{1}{\sqrt{(-\omega^2 m + k)^2 - \omega^2 c^2}} \tag{2.36}$$

Again, consider the equation of motion (2.30), and assume that the system does not experience an external load, F(t). If the system now is set to motion, it will oscillate at a distinct frequency known as the natural or resonance frequency of the system. Since the natural frequencies, in general, are insensitive to small damping of the system, it's possible the find the eigenfrequency by inspecting the undamped equation of motion

$$m\ddot{x} + kx = 0 \tag{2.37}$$

If the system experiences harmonic oscillations, the response can be given as the complex harmonic function. By substitution, the undamped natural frequency can be written as:

$$\begin{gathered} -\omega_{0n}^2 m + c = 0 \\ \omega_{0n} = \sqrt{\frac{c}{m}} \end{gathered} \tag{2.38}$$

In reality, all dynamic systems are exposed for damping contributions, and it's practical to give this measurement as a factor related to the mass and stiffness of the system. This yields:

$$b = b_{cr} = 2m\omega_0 = 2\sqrt{mk} \tag{2.39}$$

where m is the mass of the system and k is the restoring contribution to the system. This equation is referred to as the critical damping and is used to decide the actual damping as a factor of the equation 2.39.

$$\xi = \frac{b}{b_{cr}} = \frac{b}{2\sqrt{mk}} \tag{2.40}$$

Another important identity is the frequency ratio between the natural frequency, ω_0 and the inflicted frequency, ω. This rate is given by:

$$\beta = \frac{\omega}{\omega_0} \tag{2.41}$$

Introducing these factors into the RAO for the particular solution, equation 2.36, it's possible to obtain the dynamic amplification factor(DAF).

$$DAF = \frac{1}{\sqrt{(1-\beta^2)^2 + (2\xi\beta)^2}} \tag{2.42}$$

Further, the phase angle between the force and response can be found from

$$\theta = \arctan(\frac{2\xi\beta}{1-\beta^2}) \tag{2.43}$$

Graphically this can be seen as the following:

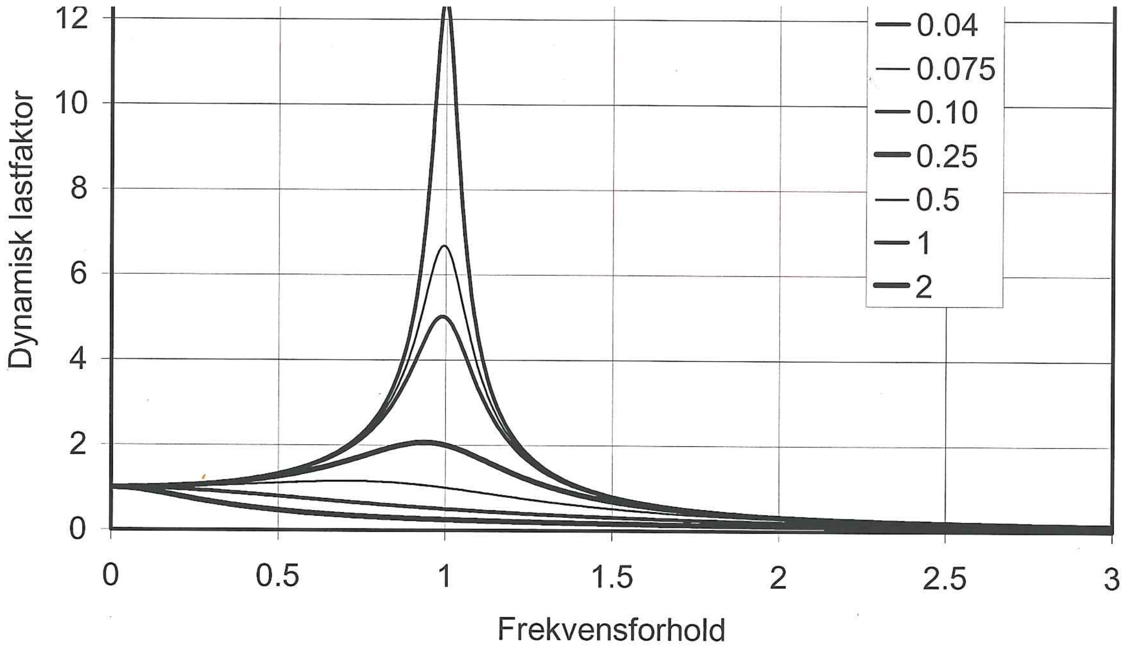

Figur 2.7 **Dynamisk lastfaktor som funksjon av frekvensforholdet for gitte verdier av dempingsforholdet.**

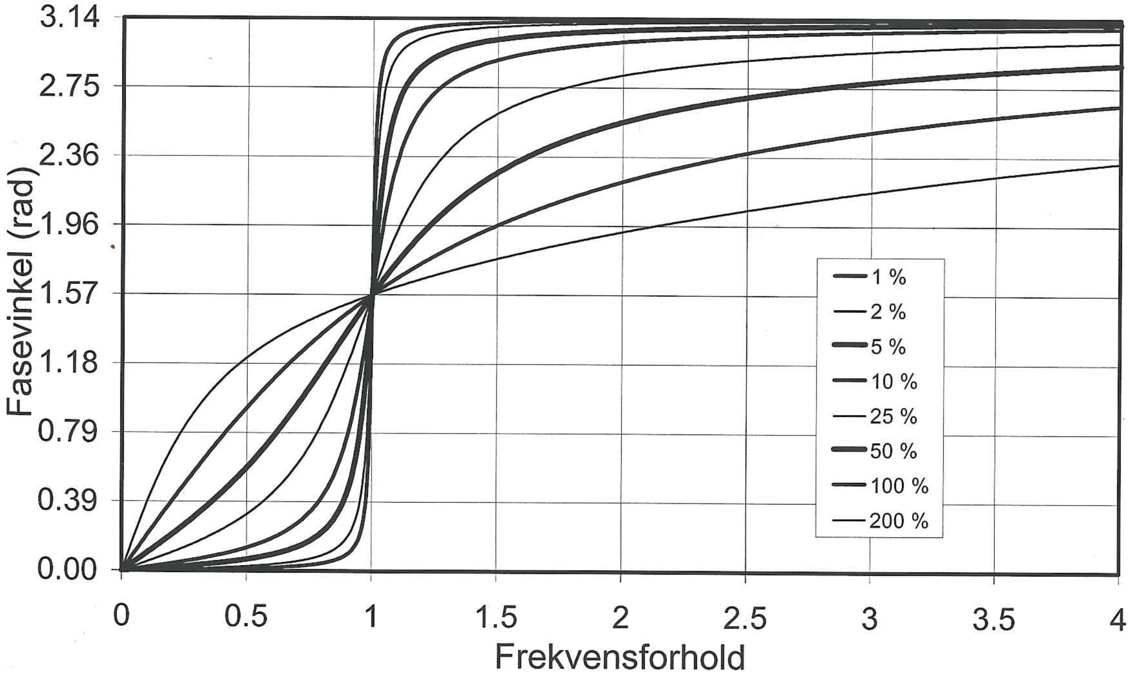

Figure 2.12: Dynamic amplification factor (Larsen, 2014).

2.9.2 System with Three Degrees of Freedom

If the analysis is extended to a two-dimensional dynamic system oscillating in water, it's necessary to evaluate a three degrees of freedom system. For the scope of this project, the equation of motion will depend on a coupled surge, heave and pitch system. The equation of motion is evaluated by a 3 × 3 complex matrix, where the response is written in complex notation, i.e. $\eta_j = \eta_{ja} e^{i\omega t}$ and the external force in k-direction is noted as $F_k^{ex'} = F_j^{ex} e^{i\omega t}$.

$$(-\omega^2[M + A(\omega)] + i\omega B(\omega) + C) \begin{bmatrix} \tilde{\eta_1}_a \\ \tilde{\eta_3}_a \\ \tilde{\eta_5}_a \end{bmatrix} = \begin{bmatrix} F_{1a}^{\tilde{ex}} \\ F_{3a}^{\tilde{ex}} \\ F_{5a}^{\tilde{ex}} \end{bmatrix} \tag{2.44}$$

here, the frequency dependent added mass term $A(\omega)$ is included since it moves in water, and $\tilde{\eta_1}_a = \eta_{1a}/\zeta_a$, $\tilde{\eta_3}_a = \eta_{3a}/\zeta_a$ and $\tilde{\eta_5}_a = \eta_{5a}/k\zeta_a$. And $F_{1a}^{\tilde{ex}} = F_{1a}^{ex}/\zeta_a$, $F_{3a}^{\tilde{ex}} = F_{3a}^{ex}/\zeta_a$ and $F_{5a}^{\tilde{ex}} = F_{5a}^{ex}/k\zeta_a$.

k introduced in the dimensional analysis is the wave number, and conveniently $k\zeta_a$ becomes the wave steepness.

Further The coupled added mass, damping and restoring terms are given as;

$$M + A(\omega) = \begin{bmatrix} M + A_{11}(\omega) & 0 & (Mz_G + A_{15}(\omega))k \\ 0 & M + A_{33}(\omega) & (-Mx_G - A_{35}(\omega))k \\ (Mz_G + A_{51}(\omega))/k & (-Mx_G - A_{53}(\omega))/k & I_5 + A_{55}(\omega) \end{bmatrix} \tag{2.45}$$

$$B(\omega) = \begin{bmatrix} B_{11}(\omega) & 0 & B_{15}(\omega)k \\ 0 & B_{33}(\omega) & -B_{35}(\omega)k \\ B_{51}(\omega)/k & -B_{53}/k & B_{55}(\omega) \end{bmatrix} \tag{2.46}$$

$$C = \begin{bmatrix} K_{11} & 0 & K_{15}k \\ 0 & C_{33} & C_{35}k \\ K_{51}/k & C_{53}/k & C_{55} + K_{55} \end{bmatrix} \tag{2.47}$$

Both added mass and potential damping matrix are determined by theory covered in chapter 2.3.1. x_G and z_G is the coordinate for the center of gravity of the structure, and I_5 is the mass moment of inertia which is found by evaluating mass integral with respect on the distance from the y-axis.

$$I_5 = \int r^2 dm \tag{2.48}$$

where dm is the mass of an infinitesimally small part of the body. The stiffness matrix consists of both mooring stiffness and the restoring terms, C's. This is derived as

$$\begin{aligned} C_{33} &= \rho g A_{WP} \\ C_{35} = C_{53} &= -\rho g \iint_{A_{WP}} x ds \\ C_{55} &= \rho g V(z_B - z_G) + \rho g \iint_{A_{WP}} x^2 ds = \rho g V G\bar{M}_L \end{aligned} \tag{2.49}$$

The mooring stiffness calculation can be found based on the following drawing.

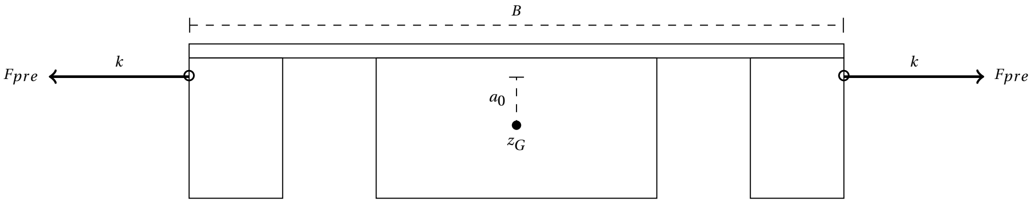

Figure 2.13: Conceptual drawing of mooring stiffness for a moonpool structure

The constants are now determined by evaluating the coupled equation of motion and can be derived to

$$\begin{aligned} K_{11} &= 2k \\ K_{15} = K_{51} &= 2ka_0 \\ K_{55} &= BF_{pre} \end{aligned} \tag{2.50}$$

where a_0 is the vertical distance from thecenter of gravity to the mounting of the mooring system.

With respect to symmetry relations, the coupling term between heave and pitch in added mass, damping, and stiffness matrix is canceled out reducing the number of terms.

For later discussions, it's convenient to transform the added mass and potential damping terms into dimensionless measures.

$$\begin{aligned} A^*_{11} &= \frac{A_{11}}{m} A^*_{13} = \frac{A_{13}}{m} \quad A^*_{15} = \frac{A_{15}}{dm} \\ A^*_{31} &= \frac{A_{31}}{m} A^*_{33} = \frac{A_{33}}{m} \quad A^*_{35} = \frac{A_{35}}{dm} \\ A^*_{51} &= \frac{A_{51}}{dm} A^*_{53} = \frac{A_{53}}{dm} \quad A^*_{55} = \frac{A_{55}}{I_5} \end{aligned} \tag{2.51}$$

$$\begin{aligned} B^*_{11} &= \frac{B_{11}}{m\sqrt{g/(2b'+b)}} B^*_{13} = \frac{A_{13}}{m\sqrt{g/(2b'+b)}} \quad B^*_{15} = \frac{B_{15}}{dm\sqrt{g/(2b'+b)}} \\ B^*_{31} &= \frac{B_{31}}{m\sqrt{g/(2b'+b)}} B^*_{33} = \frac{B_{33}}{m\sqrt{g/(2b'+b)}} \quad B^*_{35} = \frac{B_{35}}{dm\sqrt{g/(2b'+b)}} \\ B^*_{51} &= \frac{B_{51}}{dm\sqrt{g/(2b'+b)}} B^*_{53} = \frac{B_{53}}{dm\sqrt{g/(2b'+b)}} \quad B^*_{55} = \frac{B_{55}}{I_5 m\sqrt{g/(2b'+b)}} \end{aligned} \tag{2.52}$$

where m is the structural mass, d is the draft, I_5 is the mass moment of inertia in pitch, b is the moonpool gap and b' is the distance between geometry center and moonpool gap center.

Again, by inspecting the homogeneous solution of the undamped 3DoF equation of motion, it's possible to derive the eigenvalue problem in matrix form,

$$[-\omega^2(M + A(\omega)) + C] \begin{bmatrix} \eta_{1a} \\ \eta_{3a} \\ \eta_{5a} \end{bmatrix} = 0 \tag{2.53}$$

This is the frequency dependent eigenvalue problem, and the natural periods of the system can be evaluated from the non-trivial solutions of the problem, i.e. if the matrix is singular and if and only if the determinant is equal to zero, it will exist a solution.

$$\det([M + A(\omega)]^{-1} C - \omega^2 [I]) = 0 \tag{2.54}$$

here $[I]$ is the 3×3 identity matrix.

Because the coefficients of the matrix are frequency dependent, it is possible to have several artificial natural modes, ω_i, for each frequency dependent added mass coefficient.

In order to find the real natural frequencies, the artificial ones have to coincide with the frequencies used for the frequency dependent added mass coefficients. This is easiest done graphically by observing when the solutions of $\det([M + A(\omega)]^{-1} C - \omega^2 [I]) = 0$ intersects with the ω-curve. A practical example will be presented in the result section 5.1.5.

Chapter 3

Practical Issues of the CFD Simulation

One of the objectives of the thesis was to validate and verify a numerical scheme, Potential Viscous Code 3D(PVC3D). A successfully performed numerical study that coincides with the physical experiments would also provide additional credibility to the model tests.

A second feature was to measure the radiation forces on the structure. Since these forces were not recorded in the experiments, the results from the CFD program could be utilized to obtain the added mass, potential damping, and eigenperiods mentioned in the previous chapter.

In order for the reader to understand the process around the numerical study and its attributes, the first part is dedicated to describe theory regarding CFD, the PVC3D software and the input parameters in brief. The last part of the chapter aims to enlighten the creation process of the numerical simulations.

For the curious reader, a more thoroughly explanation of the CFD application, OpenFOAM, is found in Appendix C.

3.1 Computational Fluid Dynamics

Fluid flows can be described mathematically by partial differential equations, represented by Navier-Stokes equations, which cannot be solved analytically except in special cases.

In marine applications, the main issue is the hydrodynamic problem where the primary goal is to obtain the global pressure and shear force on the hull to predict the flow field and resistance on the vessel. It's also of interest to determine the global fluid velocity components and thereby calculate the wave pattern around the structure. The problem that arises for marine applications is the presence of a free-surface and the free-surface waves.

Nowadays CFD is becoming an increasingly important tool in the design process of marine structures. Among other it's applied in the design process to rapidly explore how changes in geometry affect the forces and motion characteristics of a vessel. Though, experimental fluid dynamics is still an important tool and is often applied in combination with CFD to verify the final design.

The benefits of CFD are conditional on being able to solve the Navier-Stokes equations accurately, which is extremely difficult for most flows of engineering interest. For those who plan to apply CFD one have to bear in mind that numerical results are always approximate and must be considered when interpreting the outcomes.

3.1.1 Numerical Solution

To obtain satisfactory results to continuity and Navier-Stokes equations explained in chapter 2.1, it's necessary to have knowledge about several disciplines: Fluid mechanics, mathematics, computer science, geometric modeling and meshing (Ferziger and Perić, 2002).

The starting point in CFD is to turn the physical problem into a mathematical model with a set of partial differential equations and corresponding boundary conditions. Here, one can decide whether to approach the problem by for instance considering the fluid as incompressible, inviscid, laminar, two-dimensional, or all properties together.

After selecting the mathematical model, it is necessary to choose a suitable discretization method. This is the process of approximating the differential equations by a system of algebraic equations for the variables at some set of discrete locations in space and time. These locations are where variables are to be calculated, called the numerical grid. This is the discrete representation of the geometric domain. The grid is a division of the fluid field into a finite number of smaller subproblems. There are many options to this process, but the most common are the finite difference, finite volume, and finite element methods.

Based on the chosen grid, one has to select a corresponding approximation to be used in the discretization process. For instance, in the finite difference method, estimates of the derivatives at the grid points have to be determined. For the finite volume method, it's necessary to select methods of approximating the surface and the volume integral. The choice of approximation will, among other, influence the accuracy, the complexity, memory requirements and the speed of the code.

In combination with initial conditions and boundary conditions, it's possible to solve large systems of non-linear algebraic equations obtained from the discretization process. A solution can be achieved by either direct of iterative methods. An efficient iterative approach is the ADI-algorithm, while the most basic direct method is Gaussian elimination, where the algorithm derives from the systematic reduction of the system of equations. An example is shown below

$$Ax = b \tag{3.1}$$

where b is a known column vector, u is the unknowns and A is the coefficient matrix given by:

$$A_{m,n} = \begin{pmatrix} a_{1,1} & a_{1,2} & \cdots & a_{1,n} \\ a_{2,1} & a_{2,2} & \cdots & a_{2,n} \\ \vdots & \vdots & \ddots & \vdots \\ a_{m,1} & a_{m,2} & \cdots & a_{m,n} \end{pmatrix} \tag{3.2}$$

The idea of the Gauss algorithm is to eliminate all A-coefficients but the diagonal. This is obtained through forward elimination and backward substitution and then invert the A matrix to get a solution for x. The example is a computer costly method and are seldom used. Nowadays it's more common to apply iterative methods that iterate to an approximate solution based on a convergence criterion.

A schematically presentation of the CFD procedure is displayed in figure 3.1, (Tu et al., 2013)

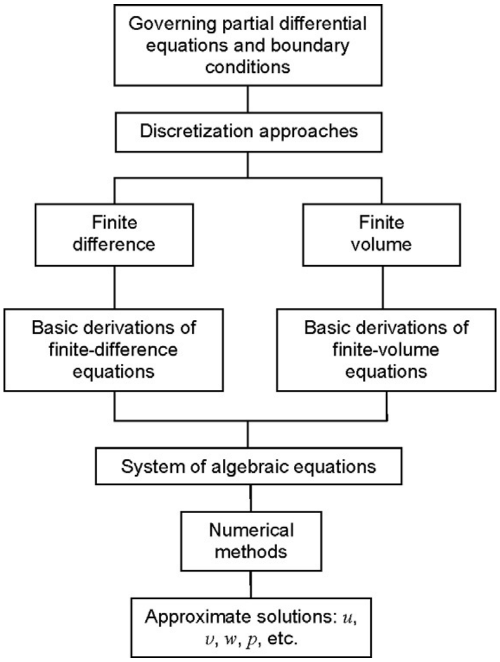

Figure 3.1: A step-wise approach to solve CFD problems (Tu et al., 2013).

3.2 Properties of Numerical Solution Methods

The solution method should have certain properties in order to obtain approximate results of a physical problem. Typically this relies on several aspects but the most important are consistency, stability, convergence, conservation, and accuracy.

3.2.1 Consistency

The numerical scheme is consistent if the approximate solution converges to the exact solution when the discretization approaches zero. I.e. when Δt->0 and Δx, Δy, Δz -> 0, the difference between the exact and approximated solution will then decrease.

3.2.2 Stability

A numerical solution method is said to be stable if it does not magnify the errors that appear due to the discretization. For an unstable solution, the error tends to grow boundlessly and make the solution diverge. A useful parameter to control if the method is stable or not is the

Courant-Fredrichs-Levi number (CFL). In 1D, this condition can be written as

$$CFL = u\frac{\Delta t}{\Delta x} \tag{3.3}$$

Δx is the smallest cell length in the flow direction, u is the velocity and Δt is the time step. This number express how much fluid moves over a cell per time step. Usually, the CFL-number is required to be less than 1, meaning that the fluid moves less than one cell per time step. This is because the solution and differentiation rely on the result of adjacent cell solved previously. Correspondingly, for a 2nd order scheme, this number must not exceed 0.5.

3.2.3 Convergence

The method is converging if the solution of the discretized equations goes to the exact solution of the differential equation as the grid spacing tends to zero. For linear initial value problems, the solution is said to be converging if it satisfies the consistency condition and stability is obtained. Stability is the necessary and sufficient condition.

For non-linear problems, which are strongly influenced by boundary conditions, the stability and convergence of a method are difficult to demonstrate. A typical procedure is instead to perform convergence through a series of numerical experiments with successively refined grids.

3.2.4 Conservation

Since one of the assumptions for the Navier-Stokes equations is the conservation laws, the numerical scheme should on both local and global basis respect these laws. In other words, if the evaluated fluid is assumed to be steady state and no source components are apparent, the amount of a conserved quantity leaving the closed volume is equal the amount entering.

3.2.5 Accuracy

As mentioned in the introduction of this chapter, numerical solutions of fluid flow are only approximate solutions. According to Ferziger and Perić (2002) three additional errors might appear during the implementation of the boundary conditions and the solution algorithm into programming. Those systematic errors are (Ferziger and Perić, 2002):

- Modeling errors, that is the difference between actual flow and the exact solution of the mathematical model.
- Discretization errors, defined as the difference between the exact solution of the conservation equations and the exact solution of the algebraic system of equations obtain by discretizing these equations, and
- Iteration errors, defined as the difference between the iterative and exact solutions of the algebraic equations system

3.3 Finite Volume Method

The numerical approach in the software utilized in this thesis is the finite volume method. The starting point is the Navier-Stokes equation on a conservative integral form. The solution is further subdivided into a finite number of control volumes, and the conservation equations are applied on each control volume(CV). The conservation laws for a control volume relates the rate of change of the amount of that property in a given control mass to externally determined effects. For mass, which is neither created nor destroyed in the flows of interest. The assumptions for Navier-Stokes equations, mentioned in chapter 2 follows:

Mass conservation:

$$\frac{d}{dt}\int_V \rho dV + \int_S \rho(v - v_b) n dS = 0 \tag{3.4}$$

Momentum conservation:

$$\frac{d}{dt}\int_V \rho v dV + \int_S \rho v(v - v_b) n dS = \int_S (T - pI) n dS + \int_V \rho b dv \tag{3.5}$$

Generic transport equation for scalar quantities:

$$\frac{d}{dt}\int_V \rho\phi dV + \int_S \rho\phi(v - v_b) n dS = \int_S \Gamma\nabla\phi n dS + \int_V \rho q_\phi dV \tag{3.6}$$

Application of the Gauss' divergence theorem transform the preceding surface integrals into volume integrals.

$$\frac{d}{dt}\int_V dV - \int_S v_b n dS = 0 \tag{3.7}$$

The notation of the equations have following meaning: ρ is the density, v_b is the velocity of control volume, v is the fluid velocity, n is the unit normal vector of the control surface pointing into the volume integral, T is the stress tensor, p is the pressure, I is the unit tensor, ϕ represents the conserved property, Γ is the diffusivity coefficient of the scalar ϕ, b is the body force and q_ϕ is the sources and sinks of ϕ.

The interpretation of the terms in the transportation equation are as follows: The first term on the left-hand side represents the rate of change of the fluid property ϕ in the control volume. Second term it the net rate transport of ϕ out of the volume due to convection. The first term on the right-hand side is the net transport of ϕ into the control volume due to diffusion, while the last term is the net rate of increase of ϕ due to sources/sinks inside the control volume.

In order to apply these equations to each subdomain in the CFD problem, a discretization of the different terms is needed, as briefly explained in chapter 3.1.1.

3.3.1 The PVC3D Solver

potenitalFreeSurfaceFoam is the solver applied in the present work. According to OpenFOAM the solver can be described as:

> *"a singel phase, incompressible, Navier-Stokes solver that approximates waves through a wave height field that evolves in time. The solver can reliably predict the behavior of a free surface where the effects of the low density phase, e.g. air, can be neglected and where waves do not break. Its computational cost is significantly lower than the interface-capturing solvers.* (OFw).

The waves are actually not mapping the different fluid characteristics to the physical domain, but rather simulated through boundary conditions. The problem is solved with a static grid, and the free surface profile is only known through the values of the vectorfield, zeta, at the free-surface patch.

3.3.2 Post-processing

The primary post-processing tool applied for OpenFOAM is the paraView visualization software. The paraView application has a broad range of capabilities utilized to investigate the flow regime for a given numerical simulation.

The visualization utilities applied in present work were velocity and pressure distribution as well as its vector components.

Another OpenFOAM extension was the SampleDict dictionary which enables the user to plot the surface elevation along a given 2D surface for a set of times during a simulation.

Next, the PVC3D computation was done through the Virtual Box tool on a computer equipped with Intel i7-5500U CPU with four cores and 8GB of RAM.

From the simulations, it was possible to obtain the number of nodes, the amount of iteration and the time it took to finish a simulation. Both execution time, which depends on the CPU performance and the clock time, which is the simulation time observed by the user could be determined.

With these parameters, it was possible to measure the performance of the numerical scheme using the formula for node updates per second(NUPS).

$$NUPS = \frac{n_x \cdot n_y \cdot n_{iter}}{T} \tag{3.8}$$

3.4 Numerical Study

The purpose of this section is to describe the procedure of turning a physical fluid flow domain into a mathematical formulation outlined in the preceding sections. The starting point of the problem was to define the physical input properties of the numerical simulation. For instance, the physical model was going to be evaluated in a two-dimensional fashion, and hence, it was possible to reduce PVC3D to only consider the domain in 2D. Next, inputs regarding the dynamic viscosity, gravity, initial conditions and boundary conditions of the fluid were given, and the discretization process could start.

The meshing procedure was performed in an in-house software, MEGA, developed by the Department of Marine Technology.

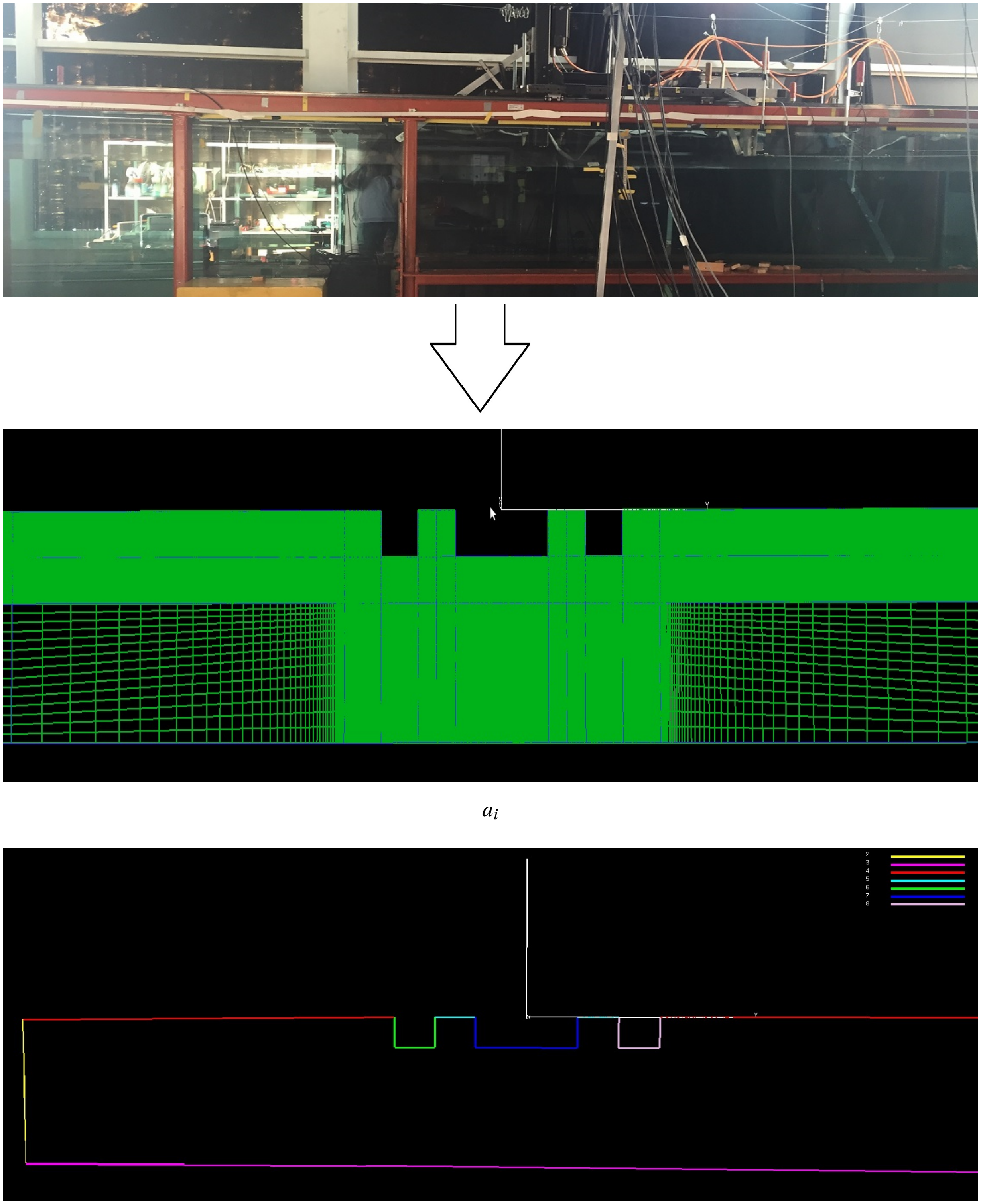

a_i

a_{ii}

Figure 3.2: Figure a_i visualize the change from physical to mathematical fluid domain, while figure a_{ii} display the boundary names of the domain. 1 - frontAndBack, 2 -inletAndOutlet, 3 - bottom, 4 - freeSurface, 5 - intFreeSurface, 6,7,8 - Hull(1,2,3).

3.4.1 Boundary Conditions

The applied boundary conditions were based on the physical boundary conditions displayed in figure 2.1. In OpenFOAM, it was necessary to address boundary conditions for the pressure, free surface elevation, and velocity fields. These conditions are summarized in Table 3.1. Here the numbers in column two refer to the numbering in of the boundaries in figure 5.1 a_{ii}.

Table 3.1: Boundary conditions

Boundary	**Boundaries**	**Mesh**	**Pressure, p**	**Surface elevation,p_gh**	**Velocity, U**
inletAndOutlet	2	patch	calculated	zeroGradient	fixedValue, 0
Bottom	3	patch	calculated	zeroGradient	fixedValue, 0
Hull(1,2,3)	6,7,8	wall	calculated	zeroGradient	fixedNormalInletOutletVelocity, fixTangentialInflow= false
freeSurface	4	patch	calculated	waveSurfacePressure	pressureInletOutletParSlipVelocity
intFreeSurface	5	patch	calculated	waveSurfacePressure	pressureInletOutletParSlipVelocity
frontAndBack	1	empty	empty	empty	empty

3.4.2 Domain Size

The first thing to decide was the domain size of the fluid, where the starting point was to determine how many oscillations of the moonpool geometry that was needed to reach steady state solution. After consultation with an experienced CFD user, Babak Ommani at MARINTEK, a total of 25 oscillations for each forced motion period was chosen.

Now, it was possible to calculate the length of the numerical tank, so that water reflections on the structure were avoided. The highest oscillation period was 1.54s, which was utilized to calculate the time it took for the wave train to go back and forth the model. The group velocity is given by equation 2.29, and the time spent is found from:

$$t_{tr} = \frac{2l}{c_g} = \frac{2l}{\frac{1}{2}\lambda/T} = \frac{4l}{1.56T} \tag{3.9}$$

Here, it's assumed deep water condition, so $C_g = \omega/k = \lambda/T$ and $\lambda = \frac{g}{2\pi}T^2 \cong 1.56T^2$. Hence, the number of oscillation is calculated as

$$n_r = \frac{t_{tr}}{T} = \frac{4l}{1.56T^2} \tag{3.10}$$

The minimum half length of the tank, l, was determined to 23m. The depth of the numerical tank was further set equal to the physical depth, namely 1m.

3.4.3 Grid Refinement Study

Once the geometrical properties of the numerical tank were calculated, one could decide the cell size. It was desirable to minimize the cell number in order to reduce the computational time. Although the mesh should not be too coarse so that the accuracy of the numerical scheme becomes insufficient.

Even though the length of the numerical tank was determined to be 46m, it didn't imply that the solution for the whole tank was of interest. The area of interest was the locations of the wave probes and the geometry, which spanned approximately ±1.7m from the center of the wave flume. To capture the solution of the pressure and velocity field in the proximity of the model, the grid in this area had to be sufficiently small. The rest of the tank were of minor interest, and the grid size away from the geometry was created as large as possible without numerically ruin the results near the structure. Limiting factors of the outer domain were the following,

- The grid size ratio between to adjacent cells should not exceed 2 (Zikanov, 2010, p. 268)
- Based on empirical observations during the numerical experiments, the cell size should not exceed the half of the wavelength. For higher grid sizes sawtooth effects and standing waves may occur. The cells will work as a wall, resulting in reflections before the fluid flow hit the inlet/outlet of the tank.

Accordingly, it was decided to increase the mesh progressively over the half length of the tank. Further, the largest cell was determined to be half of the shortest experienced wavelength, $\lambda/2$. The shortest waves occurred for the lowest oscillation period, namely $T = 0.7$s, which gives a cell length of $\Delta x_{max} = 0.23$m.

The next procedure was to determine the grid size near the geometry. In order reduce the possibility of numerical errors, it was decided to focus on a uniform grid in the moonpools and the surroundings up to 0.2m to the left, right and below the geometry. It was possible to conduct a grid refinement study to choose the most favorable mesh size.

The sensitivity analysis was done for the case study of the geometry with rounded inlets exposed for forced pitch motions. The amplitude of the forcing term was $\eta_{5a} = 0.45^o$. Graph 3.3 display the convergence of both a moonpool wave probe and a wave probe located outside the geometry for six different wave periods near resonance.

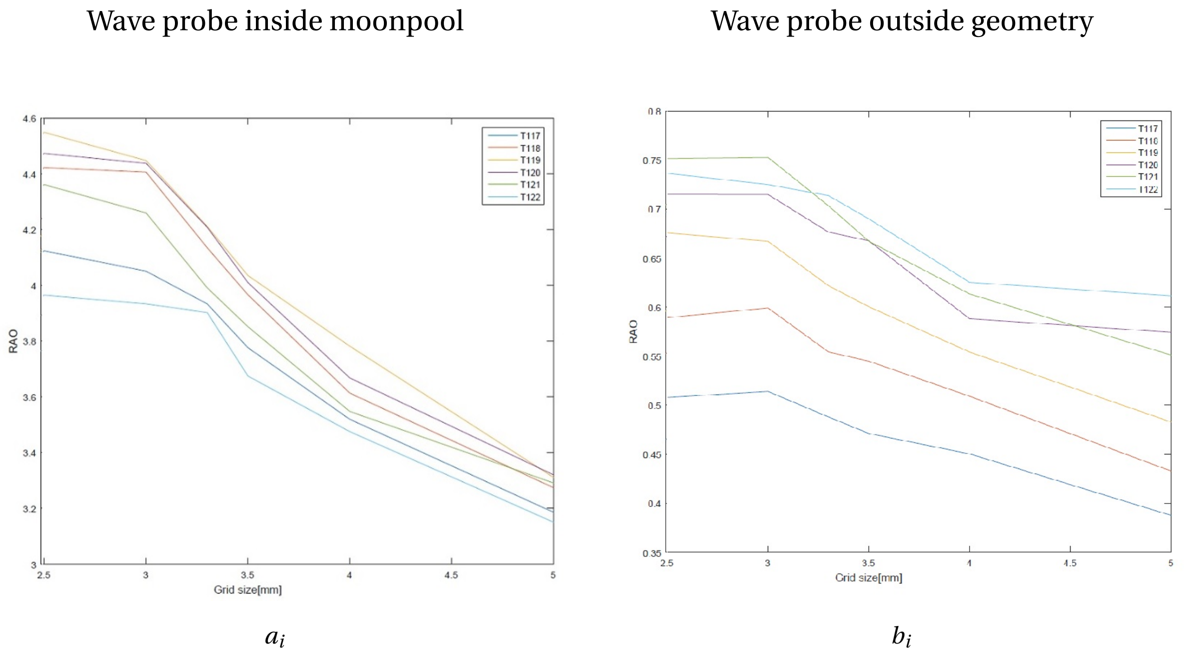

a_i b_i

Figure 3.3: Convergence study of piston mode amplitude with respect on the grid size in the proximity of the geometry. The aspect ratio of grid size is kept constant during the convergence study, $\Delta x/\Delta z = 1$. Figure a_i shows the wave probe convergence of wave height inside the moonpool geometry, while figure b_i shows convergence of the wave elevation outside the moonpool.

The final grid size was chosen based on common engineering practice, < 5% difference between two adjacent results. The difference between grid size of 3mm and 2.5mm was 2.3%, and the CFD-simulations were performed with a uniform grid size of 3mm throughout the analysis.

3.4.4 Time-step Size

Since the numerical scheme operated with an adjustable time-step solver, only a minor effort was made to optimize the time-step. Initially, it was set $\Delta t = T/100$, and the solver automatically modified the time-step to correspond to a CFL-number just below 1. The upper time-step limit was set to $\Delta t = T/25$, but the analyses were always below T/50. No further inspection or optimization of the time step was included in this project.

3.4.5 Numerical Schemes

The last decision regarding the simulations was the choice of the numerical schemes. This was done in collaboration with Babak Ommani, and the result is outlined in Table C.1.

Table 3.2: The numerical solutions schemes

Property	**Numerical Schemes**
Time scheme	Euler, Backward Euler
Gradient	Gauss linear
Divergence	Gauls linear, Gauss upwind
Laplacian scheme	Gauss linear
Interpolation scheme	linear

The numerical schemes for time differentiation are by default an implicit forward Euler method. Though, as stated in chapter 3.3.1 is the fluid domain divided into a potential domain and an internal domain. For the potential domain, covering the free-surface waves, the second order implicit backward Euler schemes was utilized instead.

Since the solution schemes are of an implicit type, the sparse matrix solvers are iterative. In other words, the residual of the solution is evaluated by substituting the current solution into the equation and taking the magnitude of the difference between the left- and the right-hand side and compare the answer against the tolerance determined to be 10^{-7}. The iteration stop if:

- the residual falls below the solver tolerance
- the ratio to initial residuals falls below the solver relative tolerance
- the number of iterations exceeds a maximum number of iterations

Chapter 4

Model Tests

In total, two different experiments were conducted during the master's thesis. The first set of tests were performed in December 2015 and continued in January and February 2016, while another series of experiments were completed in April 2016. In all cases, a two-dimensional section with two moonpools was considered.

The aim for the first set-up was to investigate the radiation problem of the moonpool structure. The results could also figure as verification and validation data for a numerical scheme, explained in Chapter 3. The model was exposed for forced oscillations either in heave or pitch, which easily could be mimicked in PVC3D. Altogether a series of 60 tests with 30 different wave periods each was completed.

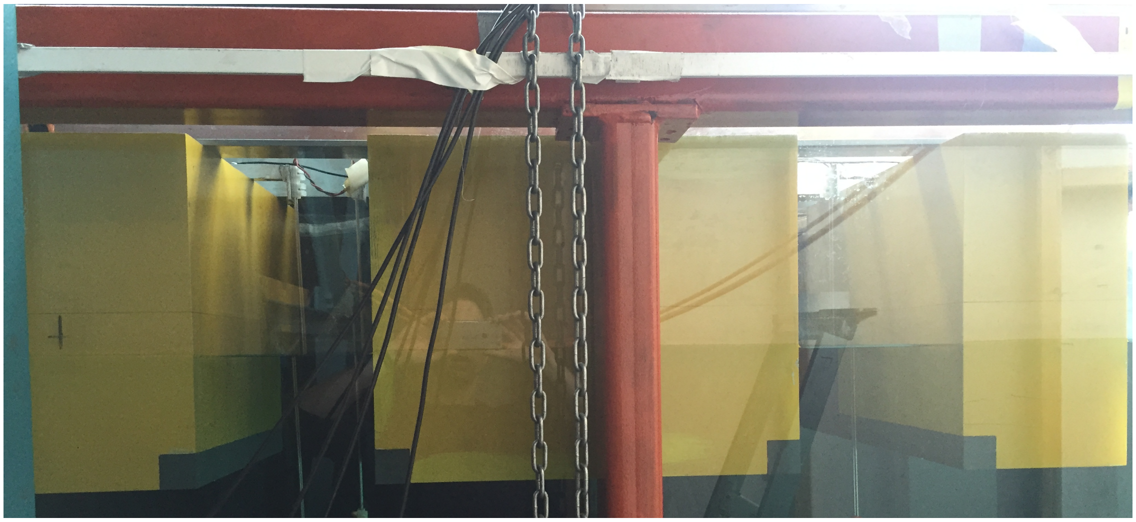

Figure 4.1: The figure display an example of a tested moonpool geometry in a wave flume.

Secondly, the geometry was moored by horizontal, linear springs and consequently free to move in three degrees of freedom. The motivation for these tests was to investigate the flow pattern and resonant behavior inside the moonpool closer to a realistic situation. Also, it was desired to examine the effects of moonpools on the geometry motions and look if the coupling effects between the moonpool water motion and geometry motion gave any favorable results. A last feature of the freely-floating experiments were video recordings of one test condition, which was included as one of the evaluation sources.

For all subproblems, it was desirable to test for different moonpool inlet geometries, and consequently, five different inlet corners could be tested, Figure 4.2.

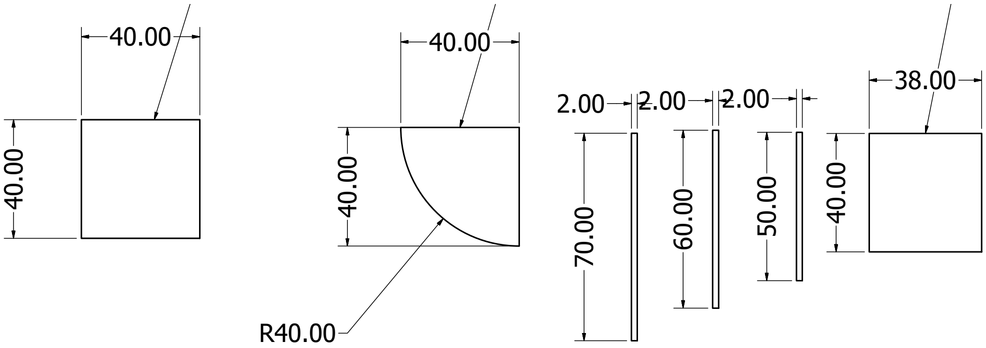

Figure 4.2: The different inlet geometries.

Following chapter aims to describe the experimental setups and the procedure of converting the raw data from the model test into visual results. This process was done in MATLAB version R2015a, and the layout of the programming scripts are explained in depth in Appendix B.

4.1 Forced Oscillation Experiments

The experiments took place in Ladertanken, a wave flume located at Marine Technology Centre at NTNU. The tank has following properties; 13.0m long, 0.6 m wide, and a water depth of 1.0m. Further, it was equipped with two parabolic beaches located at the ends of the tank, and the upper position was approximately 1mm below still water level. The beaches were installed to absorb outgoing waves, preventing them from interfering with the water motion in close proximity of the geometry.

The model was placed under a carriage in the middle of the tank, and an oscillator, performing forced motions, was mounted to the carriage. The degree of freedom to be tested was predetermined, and the oscillator either performed forced heave or pitch motions.

Table 4.1: Dimensions of model geometry for forced oscillation experiments. The properties are visualized in figure 4.3a.

Quantity	**Term**	**Model scale**
Fore-& aft box length[m]	L1	0.200
Center box length[m]	L2	0.500
Height of boxes[m]	H	0.400
Beam of boxes[m]	B	0.592
Moonpool gap[m]	b	0.2
Draft[m]	D	0.15,0.2
Water depth[m]	h	1.0
Center model - center moonpool[m]	b’	0.35
Scale of model	λ_s	1:256

Following four parameters were possible to vary during the experiments; model draft, oscillation period, oscillation amplitude and inlet geometry. In total, this accounted for over 1800 runs, and it was of interest to create an automated test set-up. A MATLAB script developed by prof. Trygve Kristiansen generated a signal file which varied the oscillator period 30 different times between 0.7s to 1.54s. The program also allowed amplitude variations, which was convenient since the model was tested for forced amplitudes of 2.5mm, 5.0mm, and 7.5mm.

The input file made it possible to run the tests without anyone present. Though, the oscillator control system had a memory limitation on approximately 9000kb, which restricted the run time to maximum three hours. Hence, the only automated property was the oscillation periods, and the forced amplitude had to be changed manually every three hours.

The input file was designed with a ramp up period that linearly increased the oscillation amplitude from zero to the desired amplitude. It took 5 periods to reach desired amplitude. Further, it was kept oscillating for 50 periods before the oscillator linearly decelerated the motion to zero. The model was then held at rest for 200 seconds before it accelerated a new period.

The waiting time of 200 seconds was empirically chosen based on when the wave elevation in the tank had dissipated.

To measure the wave height six wave probes were installed in proximity of the model. One was placed 1.0m in front of the model, while another was placed 1.0m behind. These gauges were mounted to the tank wall, and the recorded motions were evaluated with an Earth-fixed coordinate system. In both moonpool gaps, there were two probes in a distance of 6.0cm from each side of the moonpool hull. The wave gauges were placed on the geometry and consequently evaluated in a body-fixed coordinate system. A schematically layout of the probes are displayed in Figure 4.3b. Lastly, an Earth-fixed displacement sensor was mounted to the carriage and measured the actual geometry motions. This value was later employed to verify the control system displacement.

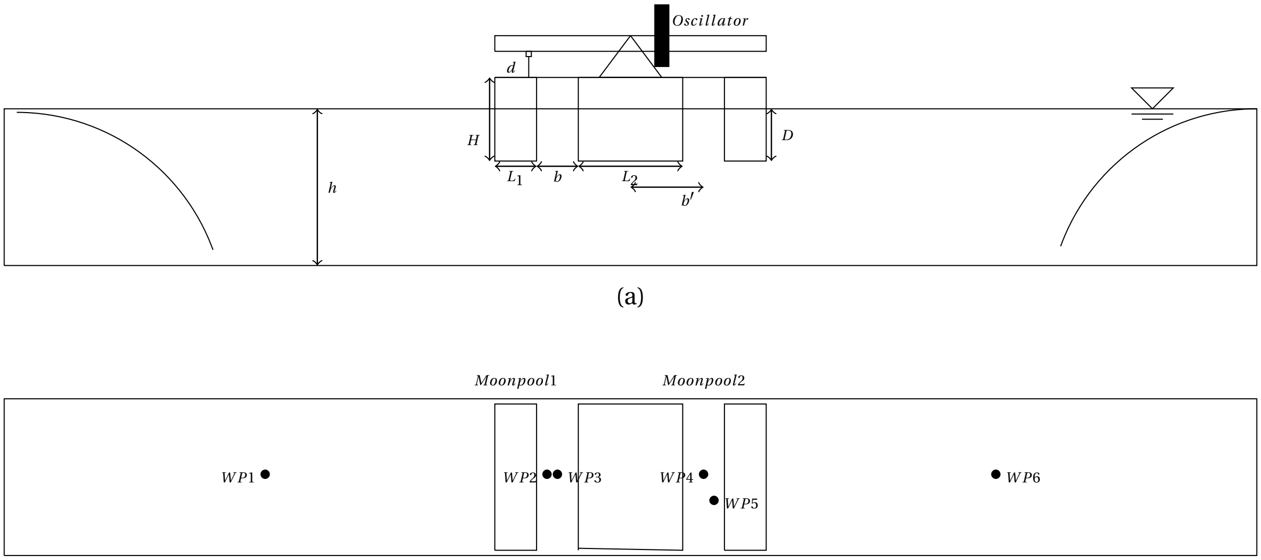

(a)

(b)

Figure 4.3: The figures visualize the experimental set-up for forced oscillations. Subfigure a) display the tank, rig and the model in xz-plane with properties described in Table 4.1 and the displacement sensor marked as d. Subfigure b) shows the location of the different wave probes. Wave probe 5 has an offset from the center because the oscillator takes up that space.

4.1.1 Short Discussion on Error Sources

Although, the belief is that the experimental results were of fairly high quality, a careful analysis of possible error sources with attempts to provide estimates of these is crucial.

There are two kinds of measures: precision and bias errors. The random errors were found through repetition tests, seen in Chapter 5, and the bias errors were continuously tried to be identified such that they could be quantified. Next, a short discussion regarding the bias errors of the forced oscillation experiments is presented.

3D Effects: Firstly, since it's known that the tank wall width slightly deviates from 0.6m it was decided to construct the model with a width of 0.592m. These gaps introduced 3D flow effects in the experiments. No vortex shedding was observed during these tests, but since it is hard to quantify the effect they cannot be neglected as a source of error.

The Leakage phenomenon was observed for the first experiments after a tank refill. At worst, a 3mm decrease in water level was measured over a two hours test. Thus, the model draft was changed by 1.5%. A comparison through Molin's equation, 2.18, showed that the eigenperiod of the piston mode resonance would deviate 2% with this change in draft.

The Parabolic Beaches would also be affected by the water leakage, and consequently, a water penetration would increase the amount of water reflections during the experiments. Even without leakage, some water reflection will occur. This is because the beaches, that trigger wave breaking as a method to remove the wave energy, will not be able to absorb all the wave energy. This is especially apparent for shallow water waves, i.e for T>1.5s. Thus, the oscillations period was for most kept below 1.5s. The wave reflection was not quantified during the experiments but are a typical example of bias error.

Transverse sloshing could interfere with the results. This corresponds to a transverse standing wave of the first eigenmode. With a tank width of 0.6m, the sloshing period is calculated to T=0.87s. The effects from sloshing mode were qualitatively inspected during the experiments and thought to be of minor importance. Also, to reduce potential sloshing effects, the wave gauges were placed with equal spacing from the tank walls such that the probes are located where the transverse standing wave is zero.

A Signal Fault between the computer and the heave actuator was observed at the end of the forced motion experiments. When the computer entered hibernation mode, the signal shut down for a small period and stopped the actuator motion for a second.

Fortunately, the oscillations were kept for 60 periods and the water elevation managed to reach steady-state before the oscillations were done. The hikking is displayed in figure 4.4, where figure a) visualize the stop in the actuator motion and figure b) shows the original evaluation interval in red. The interval was later moved to oscillation periods later in the time series.

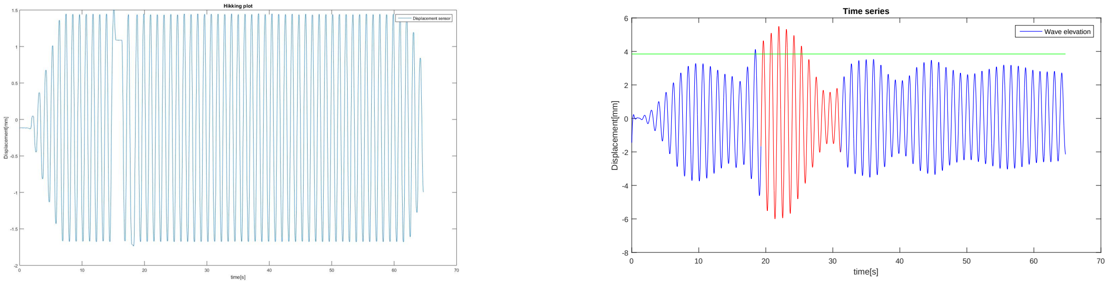

a *b*

Figure 4.4: Figure a) The actuator signal fault. Figure b) Original time series amplitude measurement.

Motion amplitude: The last problem regarding the actuator and its control system was that it didn't reach predetermined motion amplitude. Instead, the motions were about 10% lower than expected, i.e. if the input amplitude was 7.5mm, the actuator would oscillate the model with an amplitude of 6.9mm. The deviation was steady and a displacement sensor measured the actual magnitude, so this fault may not be characterized as a source of error.

It is also worth to mention that it was discovered enormous hikking in the time series for the forced heave experiments. This phenomenon was caused by contact between carriage metal and the metal in on the intersection between the wave probe cables and wave probes. The problem was overcome by taping the cable metal, and eliminate any contact between the metals. These experiments were conducted before Christmas, so they aren't directly an error source for this thesis. But it was decided to redo all the forced heave tests, which was done in January. An example of the hikking problem is displayed in figure 4.5.

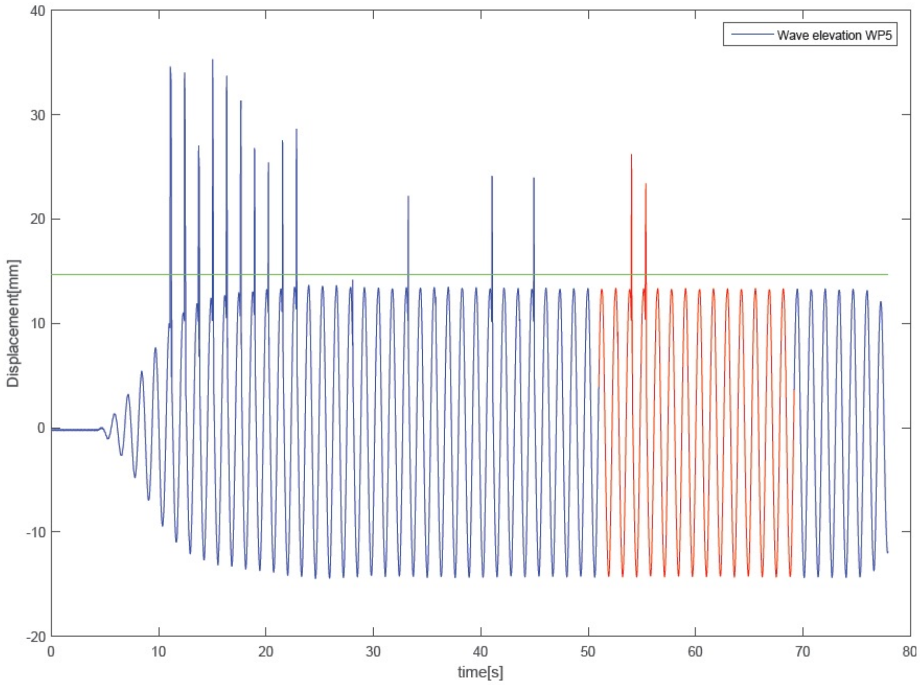

Figure 4.5: The figure display an example of hikking in time series results for forced heave motions, which were conducted before Christmas. These results were not satisfactory, and a new set of experiments were conducted in January.

4.2 Freely-floating Experiments

To quantify the model motions in two-dimensional incoming waves, a second set of experiments were carried out. During April 2016 over 900 different labs were conducted in the same tank as before. This included 30 different wave periods(0.7s - 1.3s), three different wave steepness(1/30, 1/45, and 1/60) and two different radii of gyration(0.3m and 0.5m). Also for these tests, all the bilge keels explained in the first paragraph of Chapter 4 were employed.

In order to generate incoming waves, it was necessary to remove the left beach in Figure 4.3a. Furthermore, several modifications from the forced oscillation set-up were needed. Firstly, the asymmetric model rig that connected the model to the oscillator and kept the different geometry sections together had to be removed. Instead, two L-profiles, of 3.97kg each, were used to connect them. The L-profiles also ensured sufficient stiffness to the structure. Secondly, since the weight of the model was insufficient, an external mass was included. In total 34kg was placed inside the boxes, making the total weight 79.92kg. At this state, the model reached the desired draft of 0.15m.

To restrain the model from drifting, springs from both sides of the hull were connected to racks mounted to the tank wall approximately 1.52m away from the hull. The model was free to move in surge, heave and pitch, and wouldn't touch the tank walls. The springs were horizontally connected 10cm above the water line.

Next, a displacement sensor from the left rack was attached to the model. This measured the drifting of the model during the experiments. On the right-hand side, another displacement sensor was installed. Though, its only function was to obtain symmetry and not utilized for measuring.

For these experiments, the rigid-body motions were not predetermined. In order to measure the movement of the model, three accelerometers were included; a_1, a_2 and a_3. Accelerometer one and three measured vertical movements, while number 2 determined horizontal geometry movement. All motions were measured in a body-fixed coordinate system. F_1 and F_2 in Figure 4.6a are force transducers placed between the mooring lines and the mounting.

The wave probes measuring the wave elevation had a slightly different arrangement compared to the forced oscillation tests. Here it was necessary to measure the wave height generated by the wavemaker, and a wave probe was therefore placed 3m downstream the wavemaker. Another wave probe was placed 1m upstream of the geometry to measure wave reflections. The wave elevation inside each moonpool was acquired through two wave gauges placed 6cm from each side of the walls. The last probe, measuring the transmitted waves, was positioned 1m downstream of the geometry. This is visualized in Figure 4.6b.

Lastly, the model was moved further away from the wavemaker. This was done to prevent reflections upstream the model to interfere and pollute the measurements. The distance could be determined by studying the formulas for linear waves presented in Chapter 2.8 and calculate the time spent for the waves to travel back and forth the wavemaker, and then back again to the model. The parabolic beach at the far end of the tank was another constraint, and the geometry was therefore placed at 7.8m from the wavemaker. This ensured no interference with the beach. For a wave period of 1.3s, this set-up gave approximately 23 waves before the reflections started to interact with the structure.

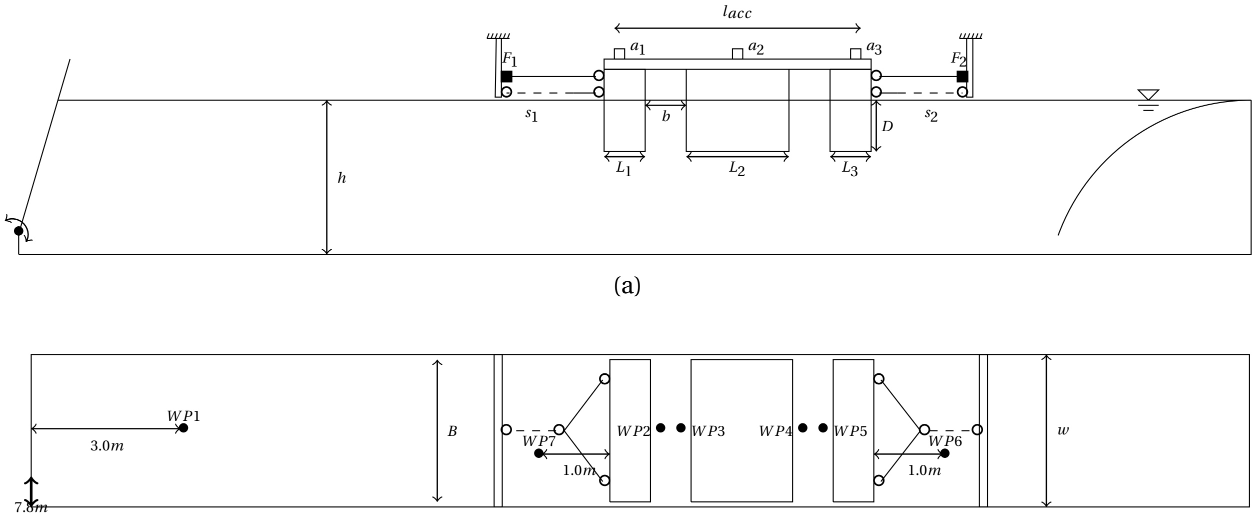

(a)

(b)

Figure 4.6: Experimental set-up of the freely-floating rigid motion model test. a) The geometry and instruments seen in xz-plane. b) Bird view plane of the tank displaying wave probes.

Table 4.2: Dimensions of model geometry for freely-floating experiments.

Quantity	**Term**	**Model scale**
Beam of boxes[m]	B	0.592
Moonpool gap[m]	b	0.2
Draft[m]	D	0.15
Water depth[m]	h	1.0m
Mass[kg]	m	79.92
Radii of gyration[m]	r_{yy}	[0.30,0.47]
Center of gravity[m]	CoG	0.17
Spring constant[N/m]	s_1	27.4
Spring constant[N/m]	s_2	32.14
Pre-tension[N]	F_1	6.75
Pre-tension[N]	F_2	6.91
Mooring length, left side[m]		1.52
Mooring length, left side[m]		1.52
Distance mooring line WL[m]		0.1

The last step before the test could be performed was to generate waves from the single flap wavemaker. Conveniently, the input files producing signals to the oscillator in the forced motion experiments could be used to generate sinusoidal waves for the wavemaker. The wave steepness was kept constant throughout the experiment while in total 30 different wave periods were tested. The wavemaker generated 27 waves for each period and was then held at rest for 210s before it executed a new wave period. The resting period was chosen based on the time it took for the waves to die out.

(a) (b)

Figure 4.7: Figure a) visualize the experimental set up for the freely-floating model. The white threads in lower left corner is a part of the spring mooring line. The cables are held up by a winch so that they won't introduce extra weights on the model. Figure b) display the model in xz-plane visualizing the moonpool and the bilge keels in grey.

4.2.1 Short Discussion of Error Sources

Some of the errors explained in the forced oscillation tests are also valid for the freely-floating experiments. Of course, the errors regarding the control system and carriage are not relevant, but errors from the measurement instrument and the geometry are of matter also for these experiments. For the freely-floating experiments, no water leakage was detected and the issue with the parabolic beaches penetrating the water could be disregarded.

In addition to these and the usual error sources, such as calibration factors and measurement instruments, a few additional error sources are identified.

The incident waves were calibrated beforehand, but they did not always obtain the required wave steepness. However, this discrepancy could be accounted for, since the wave amplitudes were measured through a wave probe near the wavemaker.

Ventilation: At wave period 30 for wave steepness 1/30 the video recordings displayed an occurrence of ventilation around the outer corners of the vessel. The author is not aware of the hydrodynamic effects. Since it only occurs for the highest period at wave steepness 1/30, the easiest approach would be to discard these measurements.

3D effects from wavemaker or the geometry were apparent during the experiments. A slight variation of moonpool width, b, for the moonpool closest to the wavemaker was detected after the model was mounted. The width deviated 3mm across the opening, and might have lead to a small 3D effect, but the significance is unknown.

This is also the case for the wavemaker, were small gaps on each side may have been a source of transverse waves in the wave flume. Investigation of video records, especially around the transverse eigenperiod of $T = 0.87s$, did not show any trace of significant 3D effects of the wavemaker.

The video recording discovered another 3D effect from the small gap between the geometry and the tank wall. The records indicated small 3D vortices from the gap corner into the geometry. It's not clear the importance of these 3D effects.

Longitudinal Sloshing: Another discovery was longitudinal sloshing modes inside the moonpool gap for certain wave periods. The number of wave probes inside the gaps was not enough to account for these effects. Nonetheless, the author conducted a sloshing test by bandpass filtering the wave elevation around the first sloshing mode. For a moonpool gap of 0.2m, this phenomena occurs at T=0.506s, i.e. $f = 1/0.506s$. The result of the test are displayed below, and as expected the sloshing effects increase linearly with increased wave steepness.

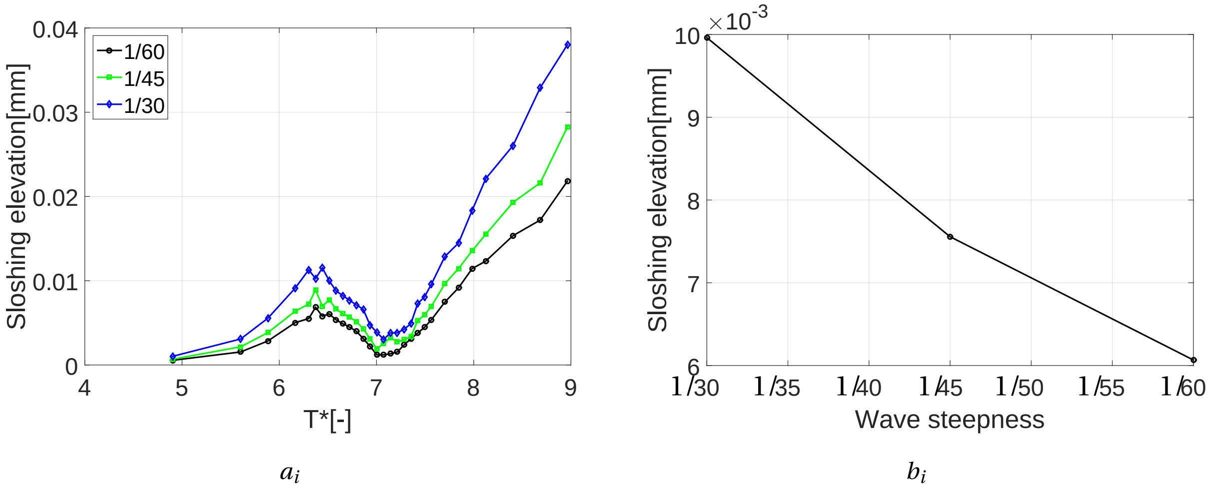

Figure 4.8: Figure a) display the occurrence of sloshing for different wave steepness. Figure b) display the sloshing at steepness 1/60,1/45,1/30 for wave period 15 in figure a. $T^* = T\sqrt{\frac{g}{b}}$

4.3 Analysis Procedures

All data from the experiments were collected in time series and needed to be processed before any results could be drawn. The data were collected in .bin-files with a sampling frequency of 200Hz. This frequency was chosen to ensure that no relevant data were excluded.

For the forced oscillation experiment, the following data were collected: displacement of geometry and wave elevation at each probe. In addition, the freely floating experiment included data from three accelerometers and forces from two force transducers. Before any equipment could start to record, it was necessary to calibrate the instruments.

The post-processing of raw data started once the calibration was done and the experiments were running. The adaption was done in MATLAB, further explained in Appendix B.

The purpose of the section is to give the reader an understanding of the process from the set-up of the experiments towards the results presented in Chapter 5. It includes the calibration process, the theory behind the post processing script in MATLAB and calculation of error sources.

4.3.1 Calibration of Instruments

Before it was possible to acquire any data, all equipment had to be calibrated from signals in Volts to signals in a relevant physical unit.

Conveniently, the employed transducers gave linear relation between the loads and the output voltage, and for all linear systems, the relations can be written as:

$$y = mx + b \tag{4.1}$$

Here m is the calibration factor found by measuring known loads between the voltage system and the desired physical measure, and b is a constant called the zero point, which figured as a reference point to the still water level, measured for each experiment and carried out after the calibration procedure were conducted.

An example of calculating the m-slope is given for the accelerometers: Here, the accelerometer was put on a horizontal table. There the zero gravity was measured. Next, it was turned 90^0, where 1G was found. Lastly, by turning the accelerometer upside down, it was possible to calculate 2G. From these three points, one could establish the calibration curve and find the calibration factor, m. Further, the force transducers were calibrated by measuring the gravity force from four different known weights.

As for the displacement sensors, MARINTEK had already performed the calibration, and no further action was needed.

The calibration of the wave probes was done by mounting them to a piece of wood with the probes penetrating the water, Figure 4.9. It was vertically moved eight times with an increment of 2 cm. For each increment, the voltage was measured for approximately 20 seconds.

This procedure was in total performed three times during forced oscillation experiments and two times during freely-floating model tests.

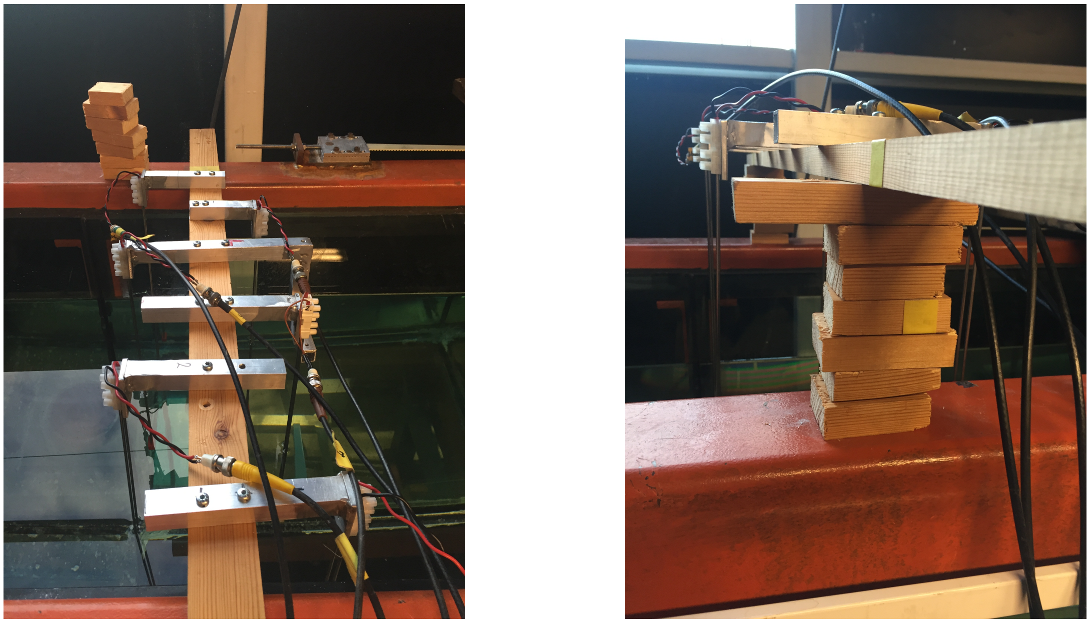

(a) (b)

Figure 4.9: Figure a display the rig for wave gauge calibration, while figure b display the increment bricks with a height of 2cm for each brick.

4.3.2 Calibration of Wavemaker

A part of the preparation for the freely-floating model test was to calibrate the wavemaker, such that the output waves had a satisfactory period and amplitude. The deviations between the theoretical wave from the input file and the output waves were corrected utilizing a mechanical transfer function.

The idea is to create an input file with the correct theoretical wave properties, ranging from small to big wave periods(0.5s:0.01:1.4s) and measure the actual output. The number of waves and resting time between each wave period followed the same pattern as described in Chapter 4.

Next, the establishment of the mechanical transfer function was done by calculating the ratio between the theoretical wave amplitude and the actual output wave measured by the wave probe. The new wave signals were then corrected with this ratio.

The test was performed for wave steepness 1/60 and 1/45 and visualized in Figure 4.10.

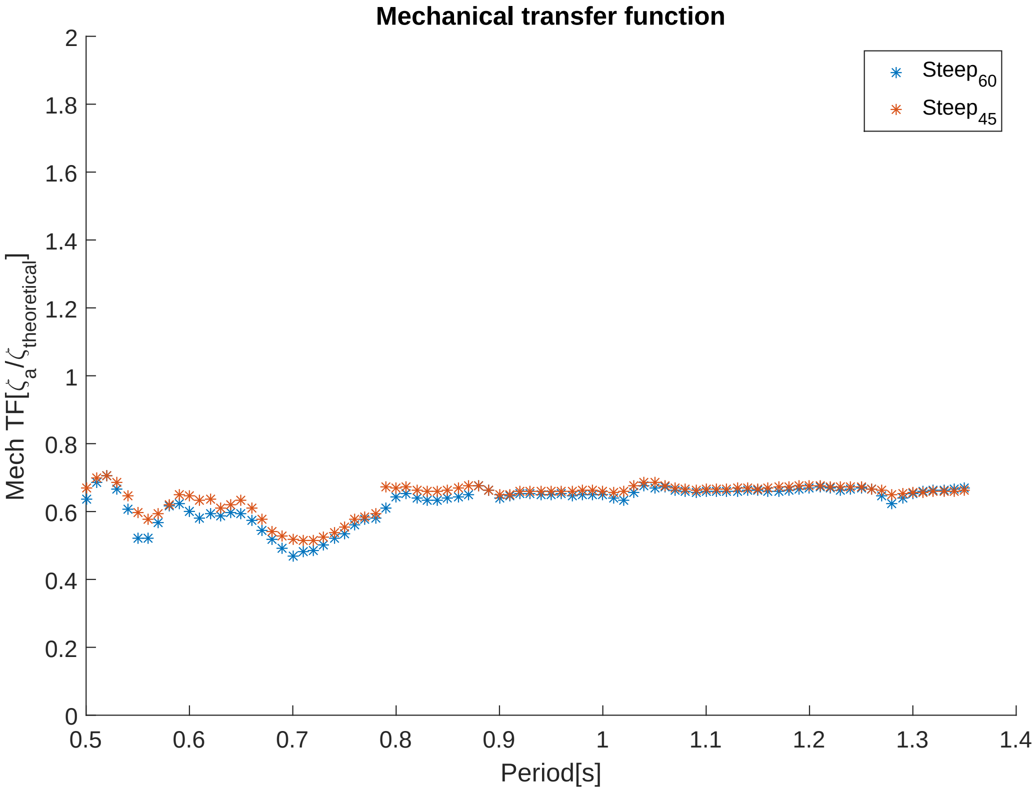

Figure 4.10: The figure display the mechanical transfer function establish for wave periods T=0.5-1.35s.

4.3.3 Time-series

The model test procedures in Chapter 4 describes that the oscillator or wavemaker created two hours runs with 30 different wave periods. These data sets are divided into 30 different time-series consisting of 60 forced oscillations or 27 wave periods, for the freely-floating experiment. The division into 30 time-series was done by detecting when the measured amplitude for each instrument exceeded a particular oscillation amplitude and stopped when the oscillations calmed down.

Take for instance the displacement sensor in Figure 4.6a. Once the waves hit the geometry, the sensor will oscillate with a distinct amplitude different from zero. MATLAB starts to record the oscillations and doesn't stop until the motions have passed the steady state oscillations and began to die out.

The result is 30 separate time-series of raw data with similar geometric properties but different oscillation period. In order to obtain results, these time-series needed further modifications.

4.3.4 Filtering

The raw data from the experiments displayed the occurrence of high-frequency noise. Thus, it was decided to employ a digital filter. A bandpass Butterworth filter was applied in MATLAB, where one of the features is to avoid phase shift that occurs for real time filtering.

It was constructed by utilizing the butter function, which returns the transfer function coefficients to an n-th order Butterworth filter. It was chosen to create a fourth order filter with the normalized cut-off frequency with respect to Nyquist frequency.

$$f_{nyquist} = \frac{f_{samp}}{2} = \frac{1}{2h} \tag{4.2}$$

where h is the time step of the unfiltered signal.

The advantage of using the normalization is that the Nyquist frequency is defined as the theoretical minimum of samples needed to avoid the signal to contain low-frequency part of the spectrum called fold-back. An illustration of this phenomenon is displayed in figure 4.11.

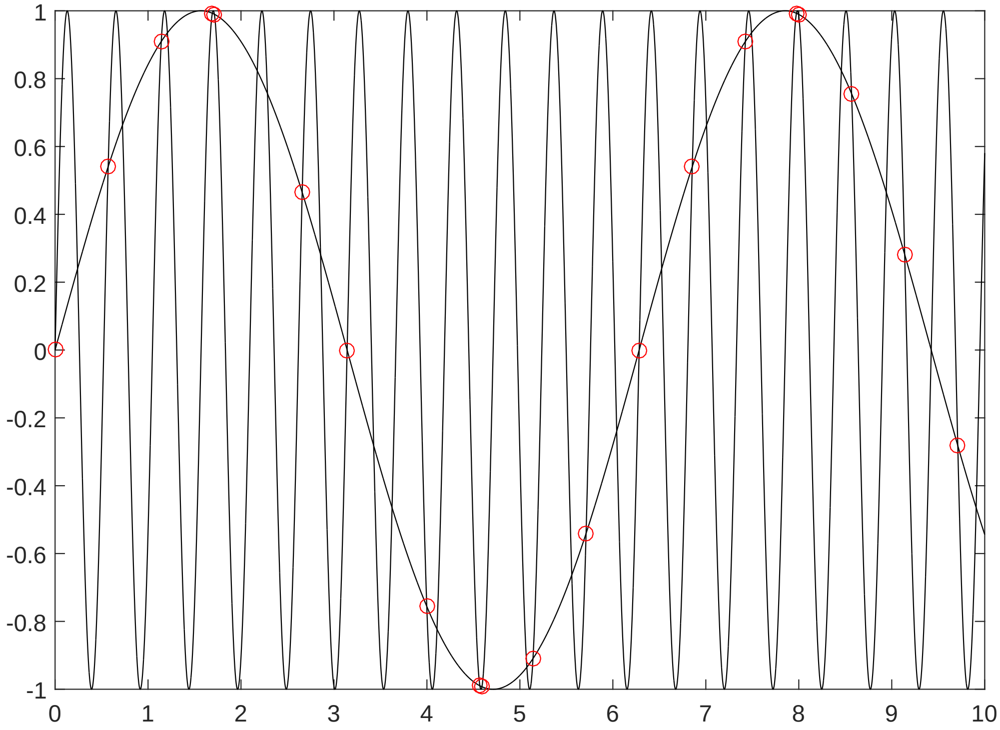

Figure 4.11: Illustration of the consequence of too low sampling frequency, i.e. foldback. (Steen, 2014)

4.3.5 Determination of Evaluation Interval and Beating Period

With the filtered time-series given for the instruments, it's possible to select an interval representing the steady-state response of the harmonic force.

However, for many of the time-series, it was detected a sequential variation in amplitude. This is called a beating period which is a physical phenomenon occurring for a dynamic system described in Chapter 2.9.

For the moonpool case, where the geometry starts from rest and the oscillations only continues for a limited amount time, one will experience beats in the transition towards steady state solution. These beats occur as a result of the interference between the steady-state motion, x_P from equation 2.31, that follows the forcing frequency, and the transient motion, x_H, following the frequency of the natural frequency of the system.

The occurrence of beats are seen in Figure 4.12c and the beating period is calculated as

$$T_{beat} = \frac{1}{|f - f_n|} \tag{4.3}$$

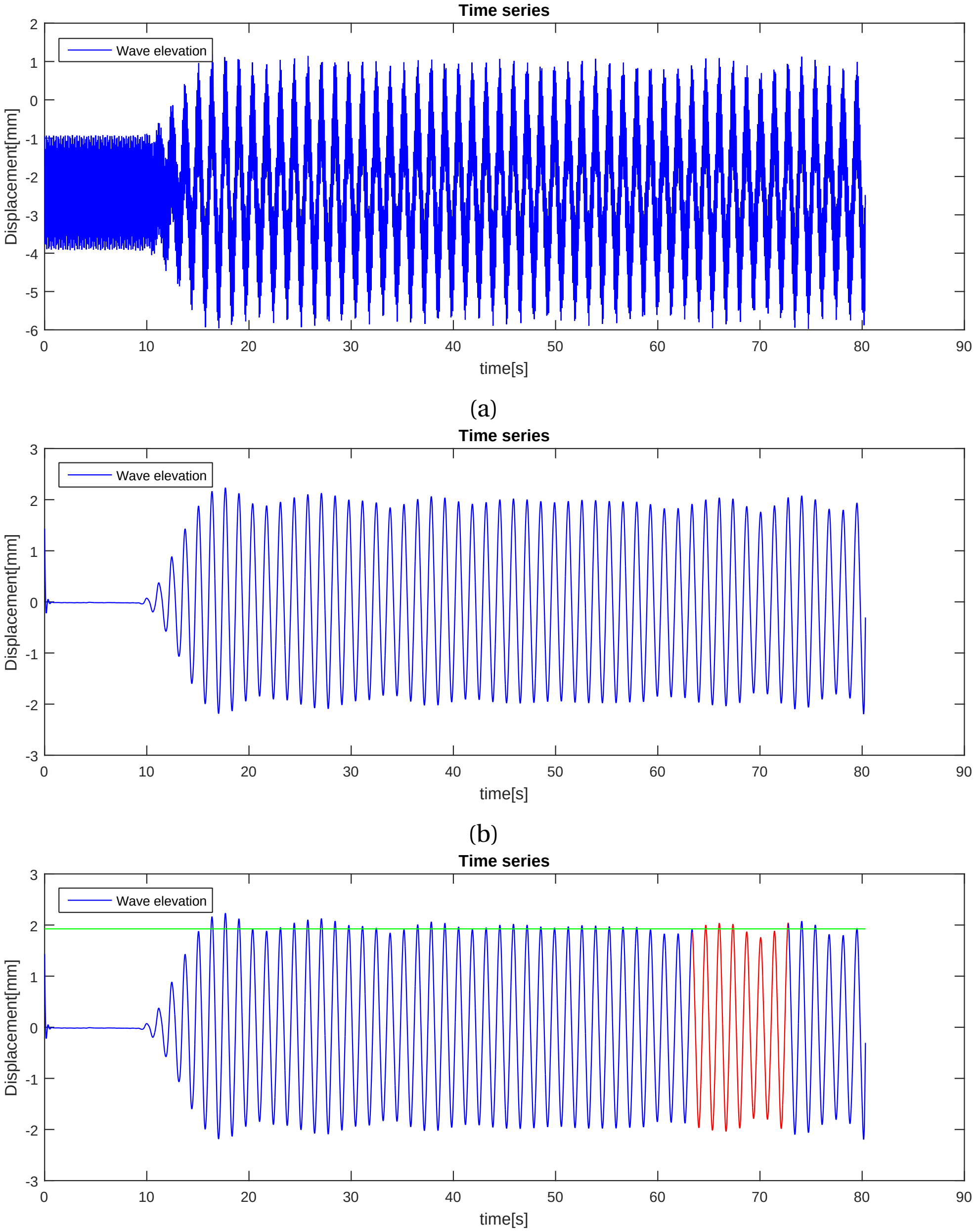

(a)

(b)

(c)

Figure 4.12: The figures display a typical time series for a forced moonpool motion. Figure a) shows a typical unfiltered function in blue, figure b) display the filtered function(the envelope for the beating period is clearly apparent). Figure c) shows the evaluated time slot in red and the calculated moonpool elevation in green.

4.4 Analysis Procedure

The next step after the calibration, filtering and the determination of evaluation period were to generate readable results for the analysis. From the time-series, it's possible to obtain results related to wave amplitudes in the tank, the geometry motions, RAO, phases and hydrodynamic coefficients.

4.4.1 Wave Amplitude

As for the wave probes, it was desirable to evaluate the wave amplitudes in an Earth-fixed coordinate system. For both experiments, wave probe 2 to 5 were mounted on the model. Hence, it was necessary to transform the outputs from a body-fixed to and Earth-fixed coordinate system. The other probes were already fixed to the tank, and no further modification was needed.

The wave gauges on the model measured relative motion between the geometry and the waves. Thus, the transformation was done through calculation of the geometry motion.

$$s = \eta_1 \vec{i} + \eta_2 \vec{j} + \eta_3 \vec{k} + \omega \times r \tag{4.4}$$

where $\omega = \eta_4 \vec{i} + \eta_5 \vec{j} + \eta_6 \vec{k}$ and $r = x\vec{i} + y\vec{j} + z\vec{k}$. This gives

$$s = (\eta_1 - \eta_6 y + \eta_5 z)\vec{i} + (\eta_2 - \eta_4 z + \eta_6 x)\vec{j} + (\eta_3 + \eta_4 y - \eta_5 x)\vec{k} \tag{4.5}$$

For this particular project, the geometry was evaluated in a two-dimensional frame, and it's possible to reduce the equation to:

$$s = (\eta_1 + \eta_5 z)\vec{i} + (\eta_3 - \eta_5 x)\vec{k} \tag{4.6}$$

Once the total vessel motion was found, one could calculate the moonpool wave height through equation 4.7.

$$\zeta = \eta_{RM} + s \tag{4.7}$$

where η_{RM} is the measured wave elevation at the wave probes.

For the forced motion model test, the vessel motions are predetermined from the oscillator and the s-value is therefore given. This is not the case for the freely-floating experiments, and the geometry motion had to be determined through the accelerometers. The procedure of finding the geometry motion is described next.

4.4.2 Rigid-body Motion for Freely-floating Experiments

The accelerometers were used to record the accelerations of the model exposed for incoming harmonic waves. Accelerometer 2 from Figure 4.6a measured horizontal accelerations, while the two others recorded the vertical accelerations. Since the vertical accelerometers were placed with a certain distance from the pitch rotation center, it was possible to calculate the pitch angular acceleration of the model, equation 4.8.

$$\ddot{\eta}_5 = \frac{a_{z1} - a_{z3}}{l_{acc}} \tag{4.8}$$

Further, the heave acceleration was calculated through,

$$\ddot{\eta}_3 = \frac{1}{2}(a_{z1} + a_{z3}) \tag{4.9}$$

Since the geometry was exposed for harmonic forces, it was reasonable to assume that the acceleration and the geometry motions also are harmonic functions. For an arbitrary harmonic function with an amplitude, A, it's possible to derive the acceleration as:

$$\begin{aligned} \theta &= A\cos(\omega t) \\ \ddot{\theta} &= -A\omega^2\cos(\omega t) \end{aligned} \tag{4.10}$$

Hence, to find the angular motion from the acceleration one have to multiply with $-\omega^{-2}$.

Once the angular motion is found, the horizontal acceleration of the geometry is given as

$$\ddot{\eta}_1 = a_{x2} - g\eta_5 \tag{4.11}$$

From the relationship in equation 4.7, 4.8, 4.10 and 4.11, the total motion, s, and all it's η-components can be determined.

4.4.3 Calculation of RAO and Phases

When all the motions and responses were known it's possible to obtain the transfer function for the model properties and wave elevations. For the subproblem dealing with forced motions, the moonpool wave elevations and phase angles were evaluated with respect on the forced motion, either in heave or pitch. The amplitude of the movements was found by following the procedure in Chapter 4.3.3, and the RAO are found from,

$$H_{mp}(\omega_j) = \left| \frac{\zeta_a}{\eta_{3a}} \right| \tag{4.12}$$

where ζ_a it the Earth-fixed moonpool water amplitude, determined by the green line in Figure 4.12c. And η_{3a} was the forced oscillator amplitude found from the displacement sensor.

For the forced pitch case, the RAO is done dimensionless by dividing the expression with the distance from geometry center to the middle of the moonpool, b', see Figure 4.3a.

$$H_{mp}(\omega_j) = \left| \frac{\zeta_a}{\eta_{5a}/b'} \right| \tag{4.13}$$

Further, for the freely floating case, all RAOs and phase angles were evaluated against the incoming waves, and the amplitudes were measured in a similar fashion as described in 4.3.3. The pitch RAO was done dimensionless by including the wavenumber k. Following formulas were used to calculate respectively surge, heave, pitch and moonpool motions:

$$\begin{aligned} H_1(\omega_j) &= \left| \frac{\eta_1}{\zeta_a} \right| \\ H_3(\omega_j) &= \left| \frac{\eta_3}{\zeta_a} \right| \\ H_5(\omega_j) &= \left| \frac{\eta_5}{k\zeta_a} \right| \\ H_{mp}(\omega_j) &= \left| \frac{\zeta_{mp}}{\zeta_a} \right| \end{aligned} \tag{4.14}$$

where the parameters are calculated based on the formulas presented in the preceding sections.

Lastly, the phase angle between load and the response was found through Fourier transform, where the complex argument of the signal is the phase offset from the regular sinusoid for that signal. By applying the Fourier transform to both signals, it was possible to find the phase difference between the two functions.

4.4.4 Hydrodynamic Coefficients

For determination of the added mass and potential damping coefficients of the moonpool structure, it was assumed that the hydrodynamic forces from the forced oscillations could be written in the following form,

$$F_{kj}(t) = -A_{kj}(\omega)\ddot{\eta}_j(t) - B_{kj}\dot{\eta}_j(t) \tag{4.15}$$

Here, $F_{kj}(t)$ is the radiation force in k-direction due to oscillatory motion in j-direction. Forces and moments due to hydrostatic pressure and instantaneous wetted surface are assumed neglected. By application of some trigonometric identities, it's possible to derive the added mass and potential damping term from equation 4.15. It is assumed that the force contribution to added mass are proportional to an harmonic sine function, while the force contribution to the potential damping is proportional to a cosine function. The harmonic motion, velocity and acceleration are respectively proportional to sine-, cosine-and sine-functions. By multiplication of either the harmonic velocity or acceleration, and then integration over whole periods the following properties can be deduced.

$$\begin{gathered}\int_0^{2\pi} \sin mx \cos mx dx = 0 \\ \int_0^{2\pi} \sin mx \sin nx dx = \begin{cases} 0, & \text{if } n \neq m. \\ \pi, & \text{otherwise.} \end{cases}\end{gathered} \tag{4.16}$$

For instance, by multiplication of $\ddot{\eta}_j$ it's possible to obtain,

$$\int_0^{nT} F_{kj}(t)\ddot{\eta}_j(t)dt = -\int_0^{nT} A(\omega)\ddot{\eta}_j(t)\ddot{\eta}_j(t)dt - \cancelto{0}{\int_0^{nT} B(\omega)\dot{\eta}_j(t)\ddot{\eta}_j(t)dt}$$

and the added mass coefficient is given by rearranging the equation

$$A(\omega)_{kj} = -\frac{\int_0^{nT} F_{kj}(t)\ddot{\eta}_j(t)dt}{\int_0^{nT}(\ddot{\eta}_j(t))^2 dt} \tag{4.18}$$

Similar procedure is used to show that the potential damping coefficient is written as

$$B(\omega)_{kj} = -\frac{\int_0^{nT} F_{kj}(t)\dot{\eta}_j(t)dt}{\int_0^{nT}(\dot{\eta}_j(t))^2 dt} \tag{4.19}$$

4.5 Calculation of Error Sources

Earlier sections have described typical bias errors for the experiments. The following paragraph will look into how to determine the precision error which is related to the random nature of the results.

The precision error can be estimated from repeated measurement, and ideally, one should do this for all conditions of an experiment. Though, because of the time constraints, this is seldom done. A common practice is to perform repetition for one given test condition and assume that the result is valid for the complete test.

For both model set ups, one test condition was repeated five times, and they made the foundation for the precision limit calculations, one for the forced oscillations and one for the freely-floating experiments. The idea is to measure the scatter of the results and establish a 95% confidence interval that the measurements are within this range.

The theory is based on choosing the Gaussian distribution as a parent distribution around the measured mean, i.e. if the measurement is repeated infinitely many times the measured values will follow the normal distribution around a mean. Mathematically it's written as:

$$f(X) = \frac{1}{\sigma\sqrt{2\pi}} e^{-\frac{(X-\mu)^2}{2\sigma^2}} \tag{4.20}$$

where σ is the standard deviation, μ is the mean and X is the stochastic variable. For a finite number of samples, N, the mean is given by:

$$\bar{X} = \frac{1}{N}\sum_{j=1}^{N} X_j \tag{4.21}$$

and the standard deviation can be calculated as:

$$S_x = \sqrt{\frac{1}{N-1}\sum_{j=1}^{N}(X_j - \bar{X})^2} \tag{4.22}$$

Further, it can be shown that sample mean of N observations is normal distributed with a mean μ and a standard deviation given as:

$$S_{\bar{X}} = \frac{S_X}{\sqrt{N}} \tag{4.23}$$

Following the Student's t distribution with N-1 degrees of freedom, one can obtain the precision limit of the mean with N repetitions.

$$P_{\bar{X}} = tS_{\bar{X}} \tag{4.24}$$

where t is given by the inverse cumulative density function of the parent distribution, $t = F^{-1}(\frac{1}{2}(1+\gamma))$. The gamma value is the confidence interval.

Chapter 5

Experimental and Numerical Results

The following chapter will present the observations and findings from the numerical study and the experimental setups described in Chapter 3 and 4. The sections are organized by displaying the results, before a short discussion of specific discoveries are included.

In general, it's focused to visualize as many experiments as possible, thus, a variety of graphs will be shown. Also, wherever feasible the tests will be compared against numerical results and findings from earlier research.

In addition, for all subsections, a geometry with the following properties are shown: draft= 15cm and squared moonpool inlets, which later is referred to as the reference geometry.

Further, the results will be presented in a dimensionless manner based on Froude scaling and geometrical similarities. In this fashion, it's easier to compare different experiments and numerical schemes. The moonpool width was chosen as the dimensional factor, giving rise to the dimensionless oscillation period, $T^* = T\sqrt{\frac{g}{b}}$, where g is the gravitation, and the dimensionless draft, $d^* = d/b$. Lastly, for the freely-floating experiments, the incoming waves are done dimensionless with the wave steepness, k. When utilized, the dimensionless factors will be included in the figure or table captions.

First, a comprehensive comparison between forced oscillation experiments and the numerical PVC3D scheme in both heave and pitch will be presented. The setups for these configurations are based respectively on Section 4.1 and Section 3.4. The graphs will capture the piston mode of motions inside the moonpools due to the radiation problem. Also, from the numerical scheme, forces and thereby the added mass and potential damping coefficients will be displayed. Further, from the added mass coefficients it's possible to obtain the eigenvalue problem.

Secondly, a section regarding the experiments on a freely-floating two-dimensional moonpool structure in incoming regular waves is visualized. The procedures around the experimental setup are found in Chapter 4.2. Also, for the reference geometry explained above, numerical results from Arnt Fredriksen's hybrid method are included.

5.1 Results From Forced Oscillations

A major part of the conducted piston mode experiments are presented in Figures 5.4-5.7 and display a moonpool geometry with a draft equal to 20cm. The first graph shows the RAOs for forced pitch motions, while the second figure is the corresponding standard deviation of the six different wave probe measurements. Figure 5.6 and 5.7 are structured in a similar fashion, but they represent the RAOs and standard deviations for the forced heave motion of the same geometry. Expect RAO for the reference geometry, which is display in Figure 5.1, are the rest of the 15cm draft results found in Appendix A and full size graphs are displayed in Appendix D.

An initial check of the quality of the experimental results is to compare the piston-mode resonance with the literature presented in chapter 2. This is done by simplifying the present geometry into a single moonpool case based on the method described in section 2.4, and the results must be understood accordingly.

The comparison is made with respect to experiments from Faltinsen et al. (2007) and Fredriksen (2015). In addition, Molin (2001) quasi-linear potential method, equation 2.19, is incorporated in the analysis. The results for heave and pitch considers rounded inlet corners found respectively in Figure 5.4 c_i and 5.6 c_i.

Included in the comparison is the eigenperiod for a U-tube tank, which is believed to exert somewhat similar flow pattern as forced pitch motions. The calculation is based on formula 2.13, where l= 1.1m and corresponds to the "tank length" between the interior free surfaces of the moonpools.

For forced heave oscillations, the resonance periods are found to be: T_{15} = 1.18s and T_{20} = 1.26s, while the natural pitch period is measured to T_{15} = 1.08s and T_{20} = 1.165s.

Table 5.1: Comparison of natural periods. Here $T^* = T\sqrt{\frac{g}{b}}$ and $d^* = \frac{d}{b}$. Based on (Fredriksen, 2015).

d^* \ Sources	Faltinsen et al. (2007)	Fredriksen (2015)	Molin (2001)	U-tube tank	Exp., heave	Exp., pitch
1.0	8.7	8.71	8.36	10.42	8.82	8.16

The table display that the piston mode resonance obtained from the experiments are in range with previous investigations of moonpool geometries, while the theoretical U-tube tank piston mode resonance has higher T^*-value than the forced pitch natural period.

Further, from Graph 5.1 it's observed that the asymptotic value, $T^* -> 0$, for the outgoing wave amplitude almost approach zero. The same asymptotic results cannot be seen inside the moonpools.

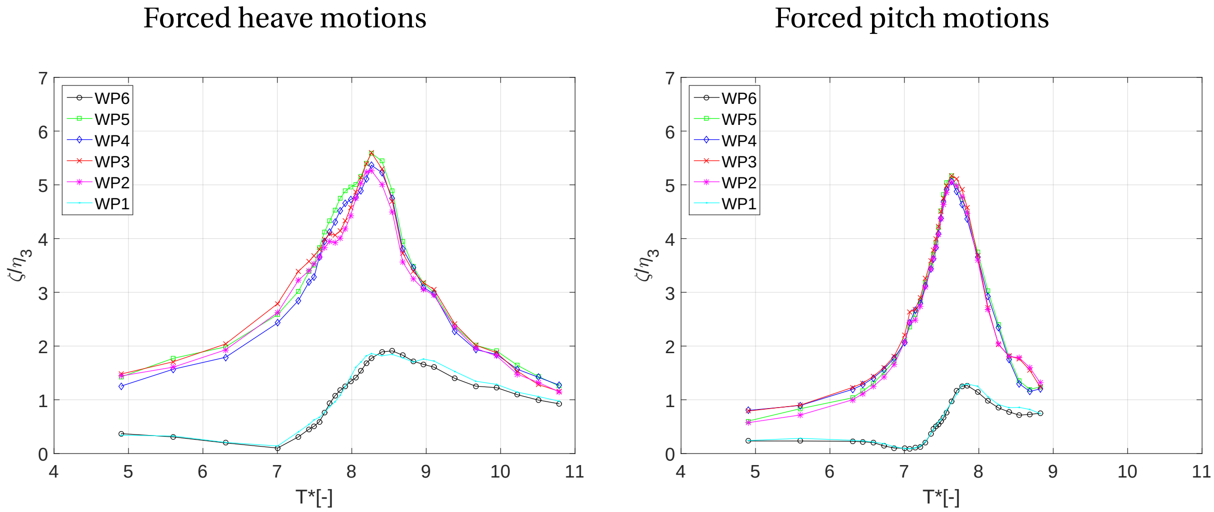

a_i b_i

Figure 5.1: The figure display the piston mode of motion for heave(a) and pitch(b) for the reference geometry, $D = 15$cm, squared corners and the highest forced motion amplitudes. The turquoise and the black line are wave probes located outside the geometry, while the rest measure wave elevation inside the moonpools. $T^* = T\sqrt{\frac{g}{b}}$.

The phase angles, α, between the Earth-fixed wave elevation inside the moonpools and the forced motions are displayed in Figure 5.2. The example shows the reference geometry, with $\eta_3 = 7.5$mm and $\eta_5 = 1.39^o$. Here, the positive pitch direction is defined through the right-hand rule of y-axis pointing into the paper.

For the pitching case: wave probe 2 and 3, located along the negative x-axis has a phase from 180^o to approximately 350^o, while wave probe 4 and 5, located along positive x-axis, display phases between 0^o to 160^o. The shift of 180^o between the moonpool is apparent due that they are located on the opposite sides of the x-axis.

By inspecting the phase angles and the RAO in Figure 5.1, it's observed that phase of the piston mode resonance and pitch motion are respectively 90^o and 270^o out of phase. Furthermore, for periods below the resonance, the motions are out of phase, and for higher periods they become in phase.

The same results are observed for forced heave motions, except that the water elevation inside the moonpool excites maxima and minima simultaneously. The phase angles pass through 90^o at piston mode resonance. For periods below it's out of phase, and correspondingly in phase for T^* above the natural period.

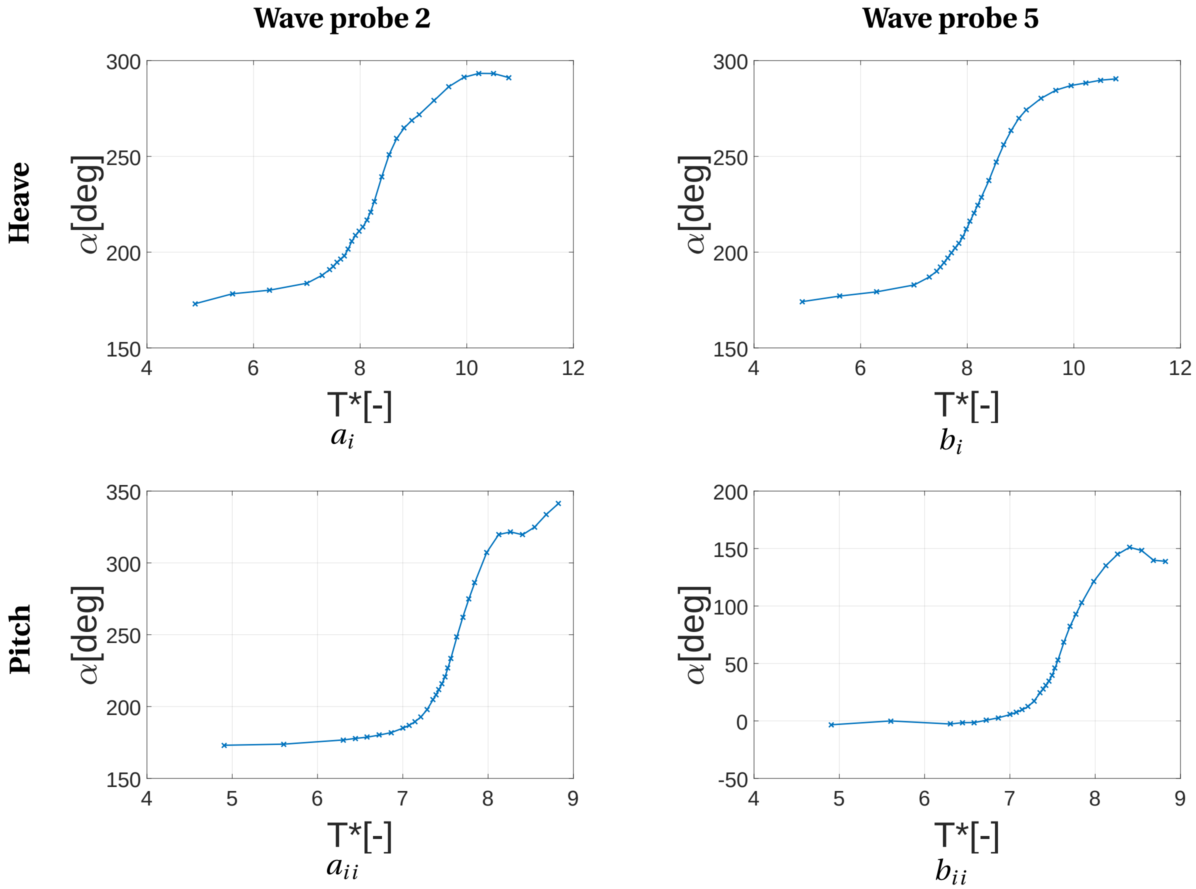

Figure 5.2: Phase angle for forced heave and pitch motions, for the reference geometry(D= 15cm and squared inlets) and motion amplitudes of respectively $\eta_3 = 7.5$mm and $\eta_5 = 1.39^o$. Left column display phase angle for left moonpool, and right column display for right moonpool. $T^* = T\sqrt{\frac{g}{b}}$

5.1.1 General Findings

Based on the RAO plots, Figure 5.4, 5.6 and 5.1, and the phase angles, 5.2, following discussion can be made.

Firstly, the theory states that the outgoing wave amplitude for asymptotic value, T->0s, should approach 0 for both forced heave and pitch motions. This is due that high frequency linearized combined free surface condition only generates vertical velocity components, and propagating waves are only observed if both horizontal and vertical contributions are present. Consequently, the velocity potential, ϕ, is therefore approximated to 0.

By inspection of Figure 5.1, the convergence of outgoing waves in forced heave and pitch is plausible, but not completely converged. A possible reason for the small deviations is because the dimensionless periods are too big, and do not approach T->0s.

The asymptotic analysis is different inside the moonpools since $\phi = 0$ allows vertical motions on the free surface.

Further, the layout for the phase angles is in compliance with the DAF analysis in chapter 2.9.1, where the phase angles for heave and pitch are 90^o out of phase with the wave elevation at resonant periods. As for the discrepancy between forced pitch motion and theoretical U-tube natural period, it's believed that outside effects of the moonpool section may have a contribution on the resonance motions. Thus, the natural periods do not coincide.

Figure 5.3 is a visualization of the numerical comparison between the piston modes of motion. The test condition is, draft equal to 20cm, largest forced motions and squared inlet geometries. Further, similar graphs are found in Figures 5.4- 5.7. Also, some of the test conditions are better visualized in Appendix D.

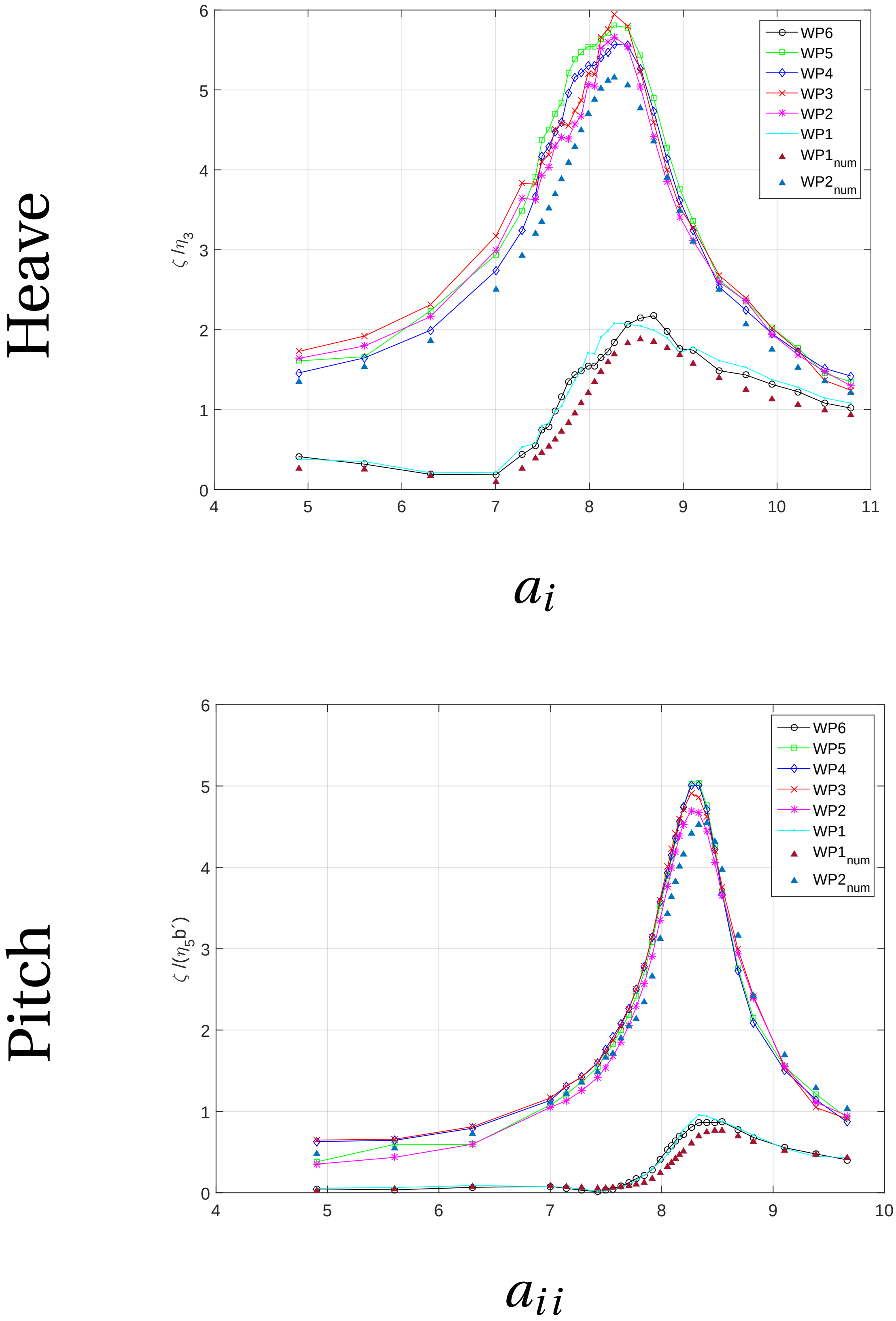

Figure 5.3: Comparison of the numerical study against the physical experiments. Both graphs display the largest forced amplitude respectively for heave and pitch for the squared inlet geometry with draft equal to 20cm. $T^* = T\sqrt{\frac{g}{b}}$.

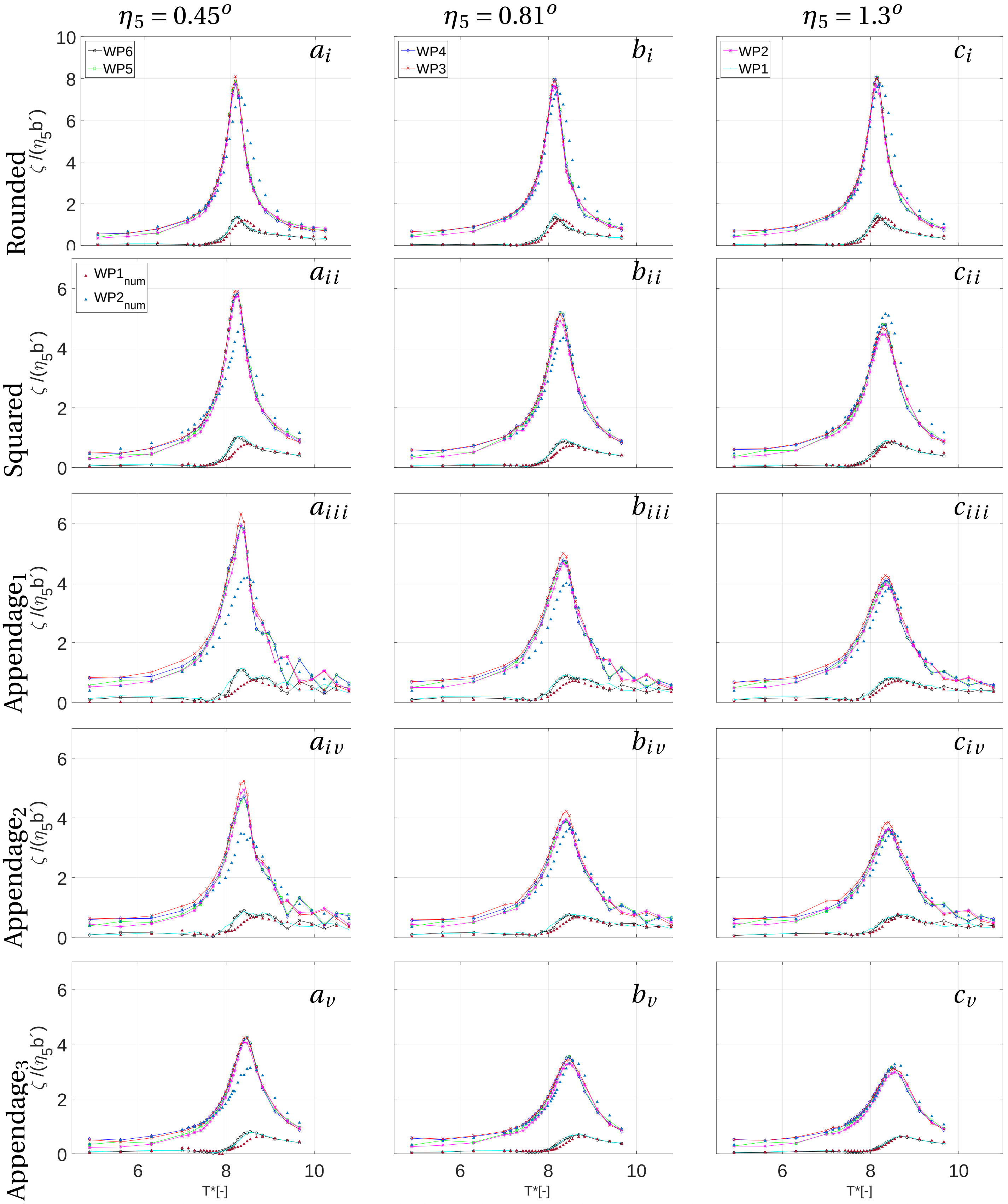

Figure 5.4: Forced pitch motion tests with draft equal to 20cm. The columns display respectively forced motion amplitudes $\eta_5 = 0.45^o$,$\eta_5 = 0.81^o$ and $\eta_5 = 1.3^o$, while the rows shows the different inlet configurations. The experimental results are display as lines while numerical RAO's are given as triangular scatter. The lower lines/scatter(turquoise, black and burgundy) are the outside wave probes. $T^* = T\sqrt{\frac{g}{b}}$

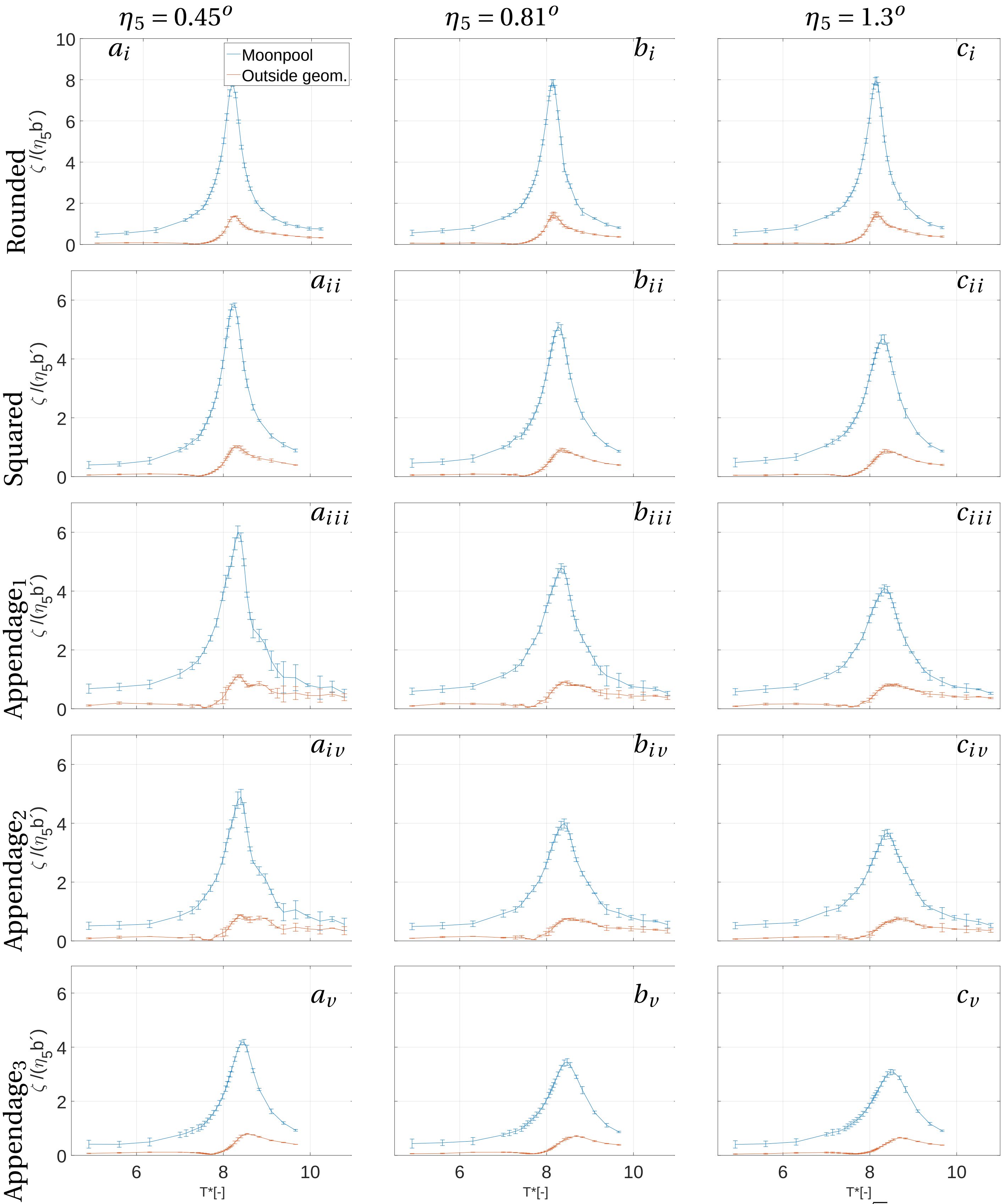

Figure 5.5: The corresponding standard deviation of the RAO's displayed in Figure 5.4. $T^* = T\sqrt{\frac{g}{b}}$.

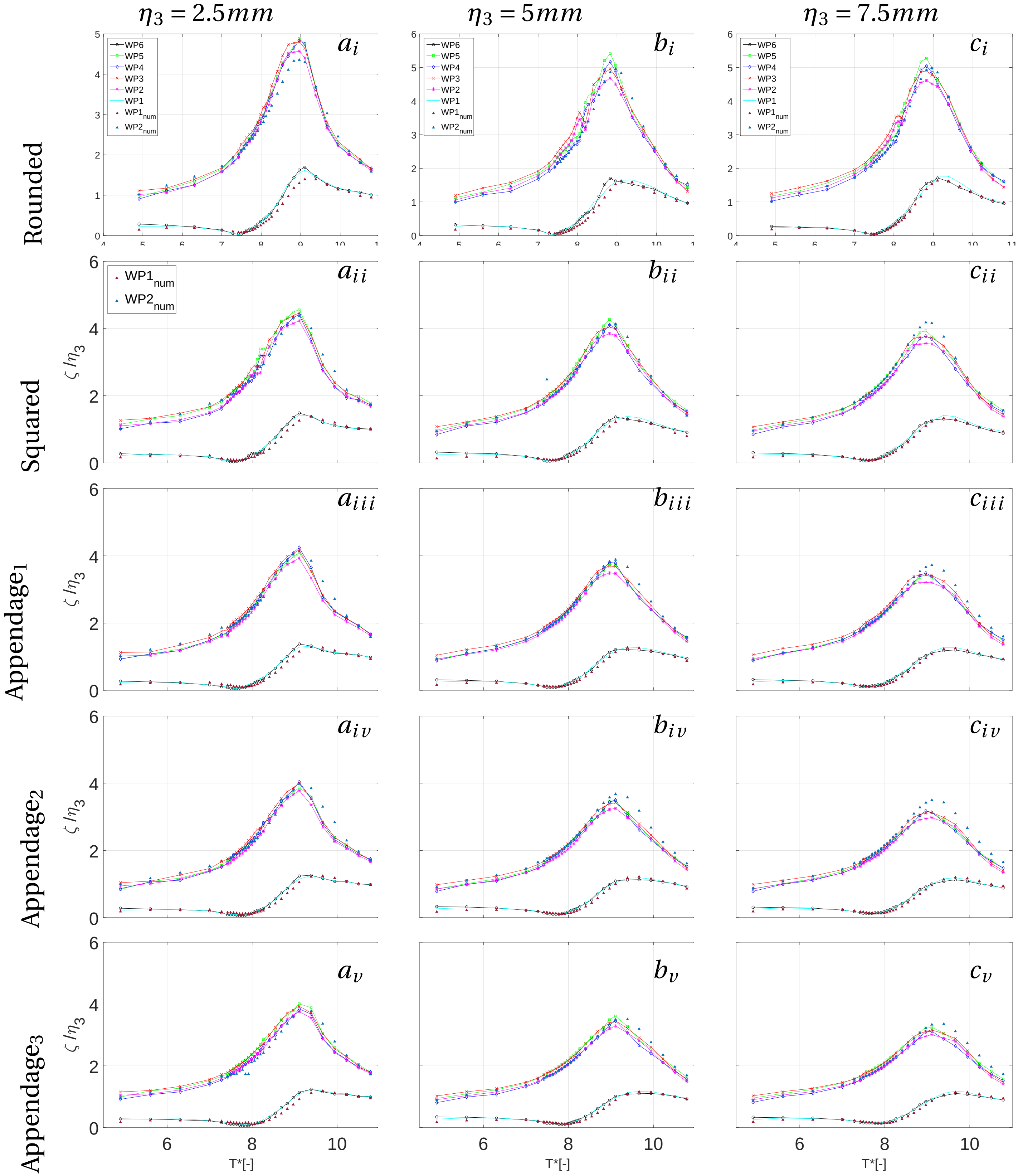

Figure 5.6: Forced heave motion experiments with draft equal to 20cm. The columns display respectively forced motion amplitudes $\eta_3 = 2.5$mm, $\eta_3 = 5$mm and $\eta_3 = 7.5$mm, while the rows shows the different inlet configurations. The experimental results are displayed as lines while numerical RAO's are given as triangular scatter. The lower lines/scatter(turquoise, black and burgundy) are the outside wave probes. $T^* = T\sqrt{\frac{g}{b}}$

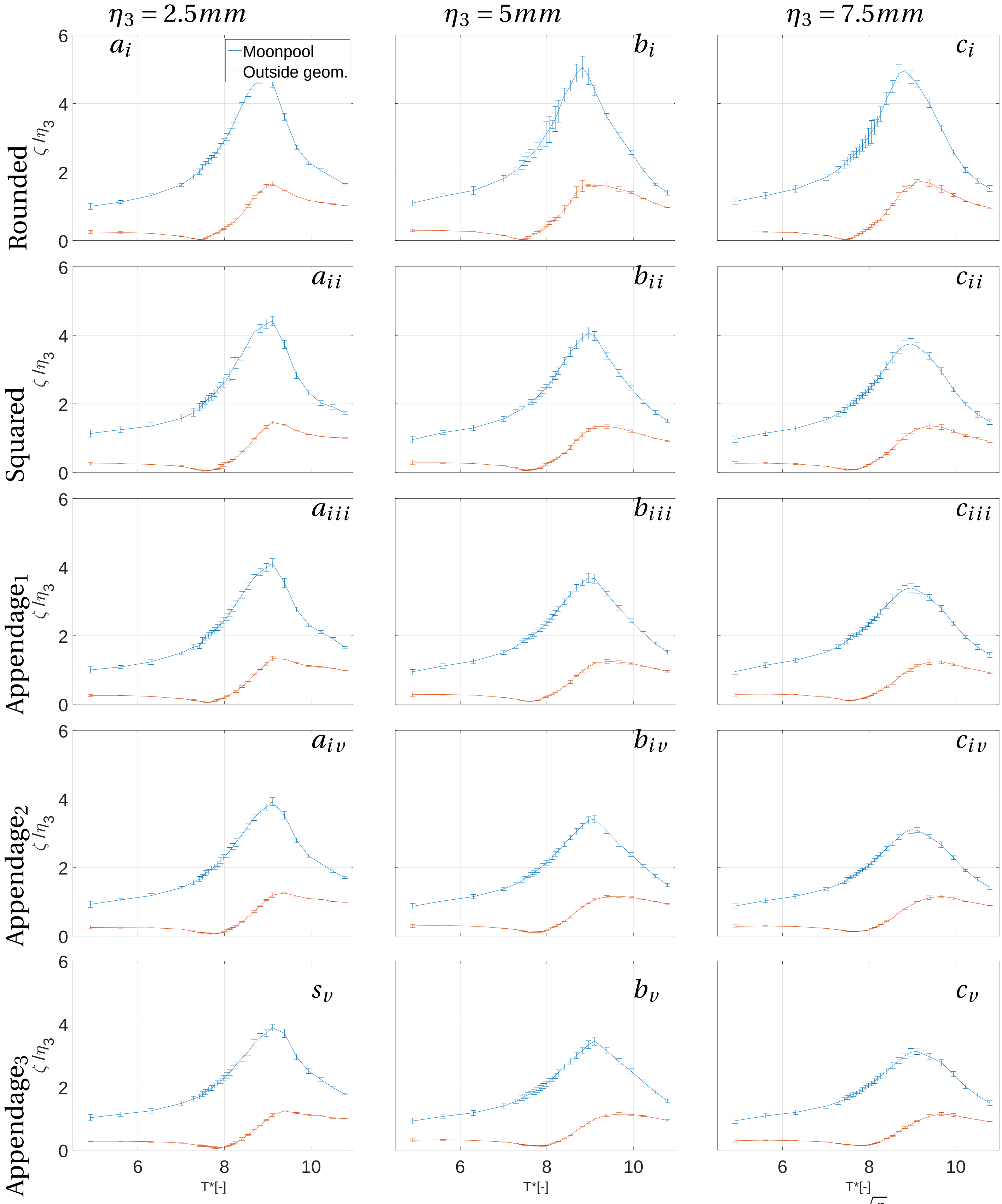

Figure 5.7: The corresponding standard deviation of the RAO's displayed in Figure 5.6. $T^* = T\sqrt{\frac{g}{b}}$.

5.1.2 Effect of Inlet Configuration

As stated in Chapter 4, five different moonpool inlet appendages were experimentally tested, and a comparison analysis for forced heave and pitch motions are included in Figure 5.8.

Mainly two observations are drawn from the graphs. First, the response amplitude is largest for rounded inlets and decreases with the appendage size, i.e. squared inlets have greater resonance peak than appendage 1 so on so forth. This is valid in both heave and pitch.

Secondly, the resonance period appears to shift towards higher natural periods, from the smallest T^*-value for rounded inlet towards the greatest period with appendage 3. This is apparent both for heave and pitch motions, but the trends are clearer for the rotational cases, see Table 5.2.

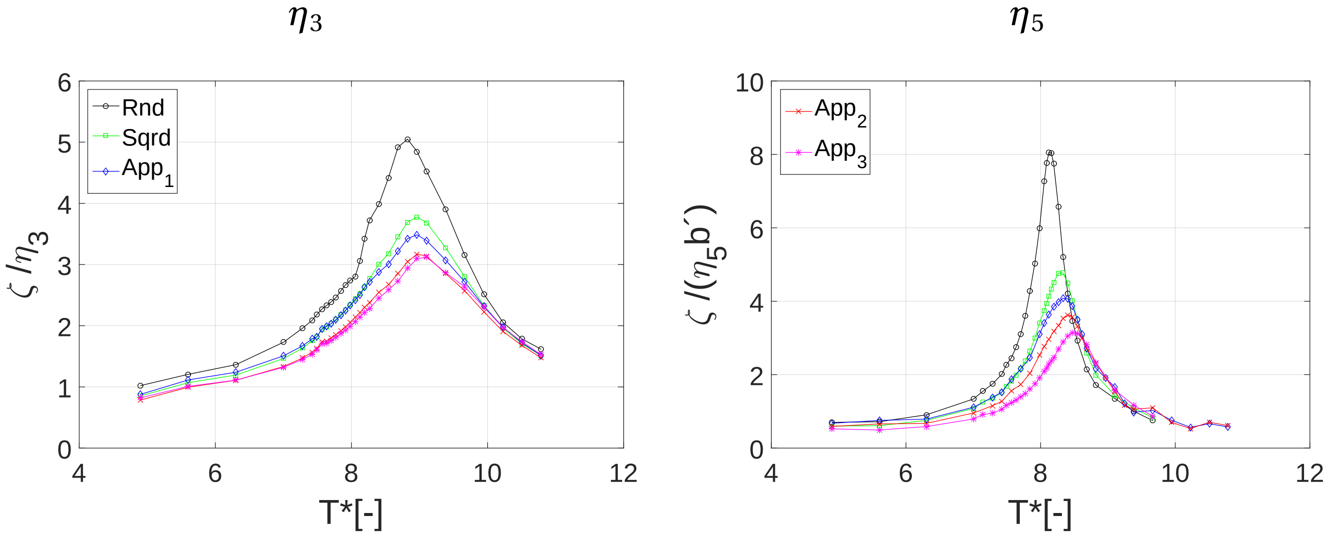

a_i b_i

Figure 5.8: Figure a) display RAO's for forced heave motion. Figure b) display results for forced pitch motion. Black line corresponds to rounded inlet, green for squared, while blue, red and pink are respectively appendage 1, 2 and 3. The analysis is done with the highest forced motion amplitude and Dr=20cm. $T^* = T\sqrt{\frac{g}{b}}$.

Table 5.2: Dimensionless natural periods of different moonpool configurations for forced heave and pitch motion. The period is given in $T^* = T\sqrt{\frac{g}{b}}$

Inlet DoF	Rounded	Squared	Appendage$_1$	Appendage$_2$	Appendage$_3$
η_3	8.82	8.96	8.96	9.10	9.10
η_5	8.16	8.26	8.33	8.40	8.54

For the configurations with the presence of a geometric singularity, it's experienced flow separation and vortex shedding, which give rise to a change in the pressure field and blockage effect of the water inflow inside the moonpools. These results contribute to an increased damping of the moonpool wave elevations, confirmed by the graphs in Figure 5.8. It is believed that the introduction of additional appendages will increase the shed vortices and hence increase the damping effects.

The rounded inlet does not have a geometric singularity, and the flow field had to be further investigated with respect to flow separation. The KC-and Reynolds number explained in Chapter 2.7 were employed to determine the position of flow separation, type of boundary layer and occurrence of separation due to oscillatory flow.

The characteristic length for determination of Reynolds-and KC-number was the diameter of the rounded inlet, and the highest relative water motion amplitude was found to be 4.8cm. Thus, the KC-number was calculated to 3.81. By comparison with Figure 2.10, it's believed that the geometry will not experience separation for oscillatory flow. According to the Reynolds number, the flow appears laminar upstream, and the separation point is thought to be further downstream than the inlet quadrant.

Consequently, the flow field for the rounded configuration is approximated as potential flow with no higher order damping effects present. This is also indicated in Figure 5.2, where the resonance amplitude is comparable much greater than the other inlets.

The second effect from the moonpool inlet analysis is the change in natural periods. Both Faltinsen (1990) and Molin (2001) have related the natural period to the draft of the moonpool inlet. The effective draft of the rounded configuration is believed to range from the free surface to the beginning of the inlet, i.e. 16cm. The squared design will experience a draft of 20cm, and the appendages will respectively have 21cm, 22cm, and 23cm draft. It is apparent from Graph 5.8 and Table 5.2 that the effective draft will reduce the T^*-value of the eigenperiods, which again supports the findings of Faltinsen (1990) and Molin (2001).

5.1.3 Effect of Forced Motion Amplitude

A review of forced motion amplitude variations displays following properties.

The response for the rounded inlet is proportional to the forced amplitude, and the RAO evolves with equal magnitude in both heave and pitch.

This is not the case for the square and the appended geometries, where the RAO's have a lower magnitude for higher forced motions.

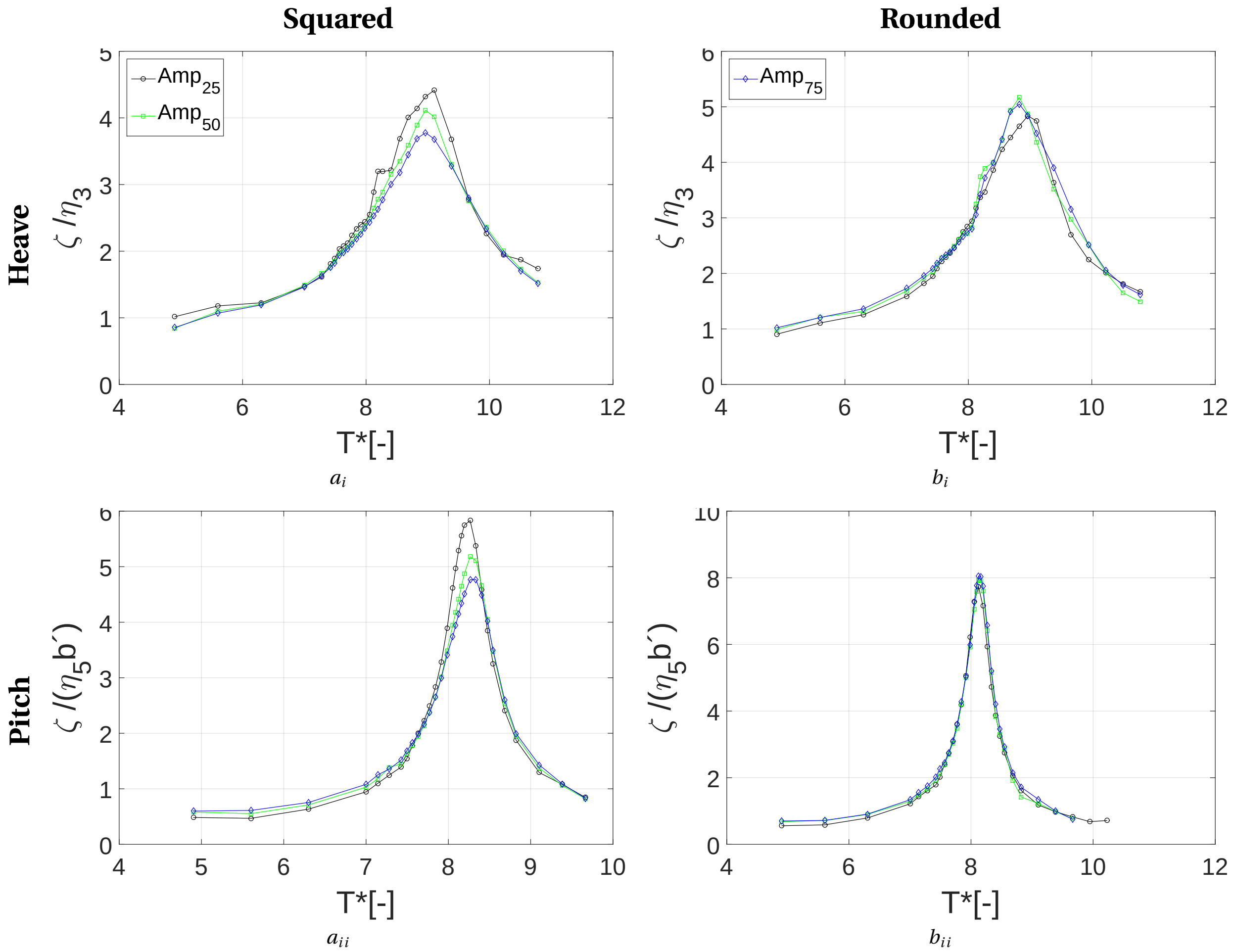

a_i b_i

a_{ii} b_{ii}

Figure 5.9: Comparison of forced motion amplitude. Column 1 display squared inlets, column two show rounded inlets and the rows are respectively for heave and pitch. Black, green and blue represents respectively the smallest, the middle and the largest motion amplitude. The analysis is done for Dr= 20cm. $T^* = T\sqrt{\frac{g}{b}}$.

The RAOs for the rounded inlet appear to be linearly dependent on the forced amplitude, which corresponds to the discussion from subsection 5.1.2 that claimed damping contributions in terms of radiated outgoing waves and no presence of higher order damping effects.

For the square and appended corners, the damping is clearly related to the amount of shed vortices around the inlets. Linearity cannot be assumed and, consequently, the vortex shedding and damping are greater for larger motion amplitudes. This is apparent for both heave and pitch motions, Figure 5.9.

5.1.4 Effect of Changing Draft

The draft analysis between 15cm and 20cm, display two main features; increasing draft give rise to resonance occurrence at higher periods, and the RAO decreases with increasing draft. These effects are shown in Figure 5.10.

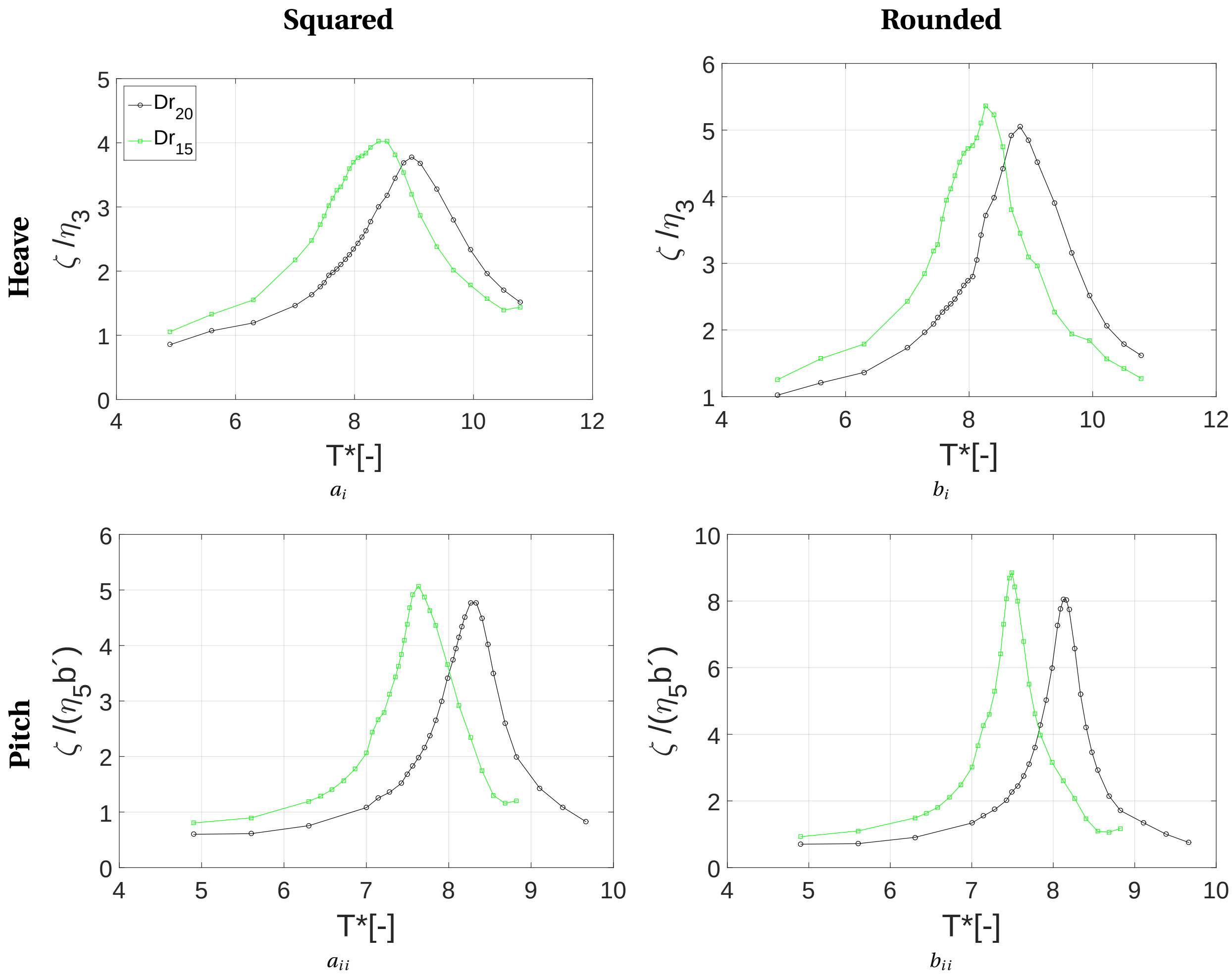

a_i b_i

a_{ii} b_{ii}

Figure 5.10: Column 1 consist of results in heave and pitch for a squared inlet. Column two display the same for rounded inlets. Green line is draft=15cm, black line is draft=20cm. The biggest forced motion amplitude is utilized. $T^* = T\sqrt{\frac{g}{b}}$.

First observation is in compliance with the formulas proposed in Molin (2001) and Faltinsen (1990) relating draft to natural frequency, meaning that the piston mode natural period could either be higher with a larger draft or lower for a smaller one.

Next, the comparison indicates that the RAO increase with a decrease in geometry draft. This is opposing results compared to what is found for single moonpool configurations. Fredriksen

(2015) believed that the draft change is negligible for the RAO magnitude. For the present case, the belief is that a decreasing draft will give greater access to flow effects outside the moonpool section, which again may contribute to a more significant response amplitude operator.

5.1.5 Added Mass and Potential Damping

From the radiation force obtained from PVC3D on the reference geometry with the highest forced motion amplitudes, it's possible to calculate the added mass and damping potentials. The theory behind this calculations is found in section 4.4.4. Figure 5.11 and 5.12 are the dimensionless added mass and damping potentials for the reference geometry.

Observations from Graph 5.11 display similarities between A^*_{15} and A^*_{51}, and B^*_{15} and B^*_{51}. Further, the surge - heave coupling and heave - pitch coupling have orders of magnitude lower values.

Comparison between the RAOs in Figure 5.1 and the added mass coefficients, Graph 5.11, shows a connection between negative added mass in heave to the piston mode resonance period. The same is observed between the pitch resonance and A^*_{55}.

The peak period for B^*_{33} and B^*_{55}, Figure 5.12, appears at the same periods as the maximum outgoing wave response in Figure 5.1.

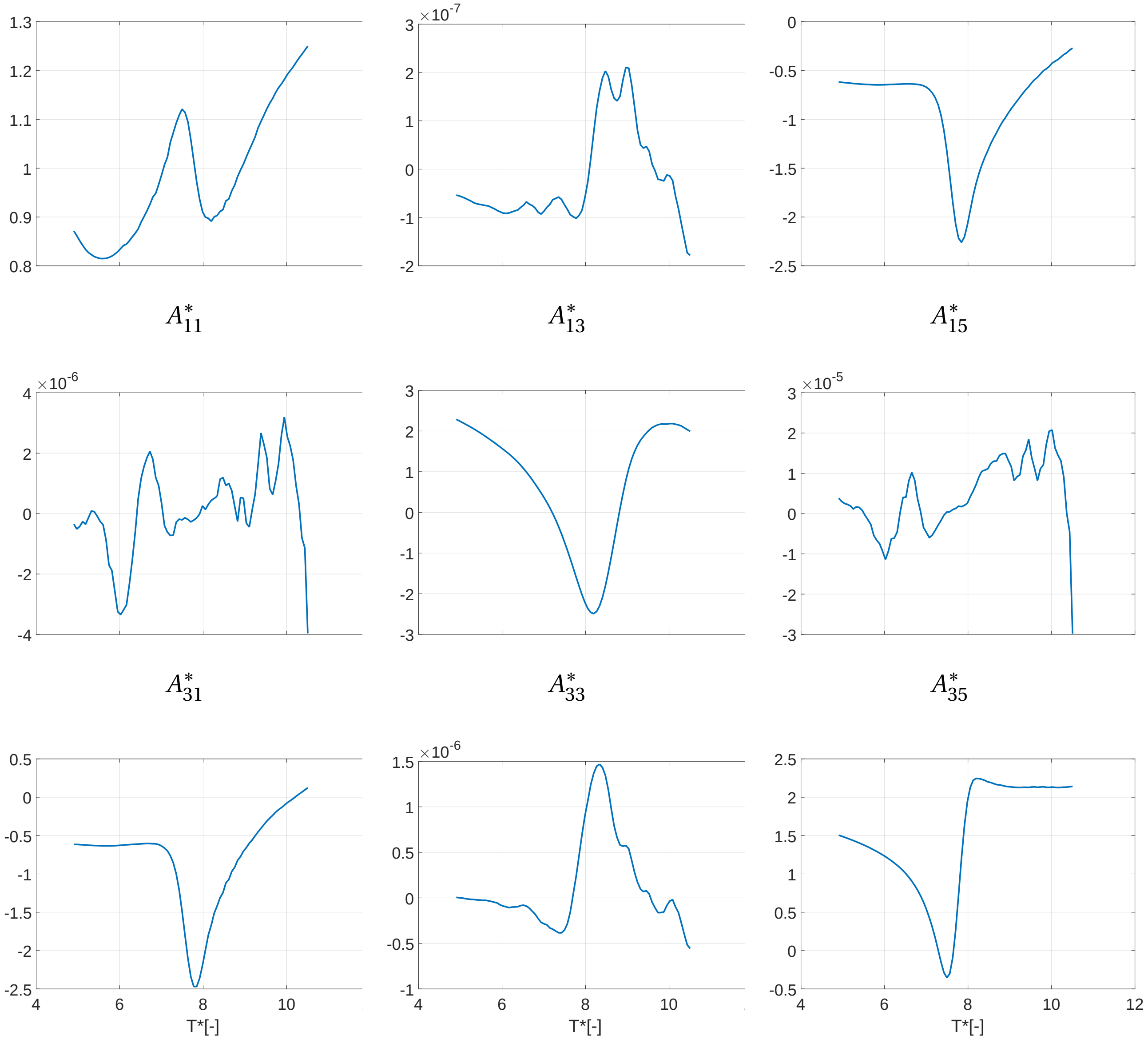

A^*_{11} A^*_{13} A^*_{15}

A^*_{31} A^*_{33} A^*_{35}

A^*_{51} A^*_{53} A^*_{55}

Figure 5.11: Added Mass coefficients obtained for a moonpool structure with squared corners and 15cm draft exposed for the highest forced motion amplitude. $T^* = T\sqrt{\frac{g}{b}}$ and the coefficients are done dimensionless wrt. formulas given earlier in section 2.9.2.

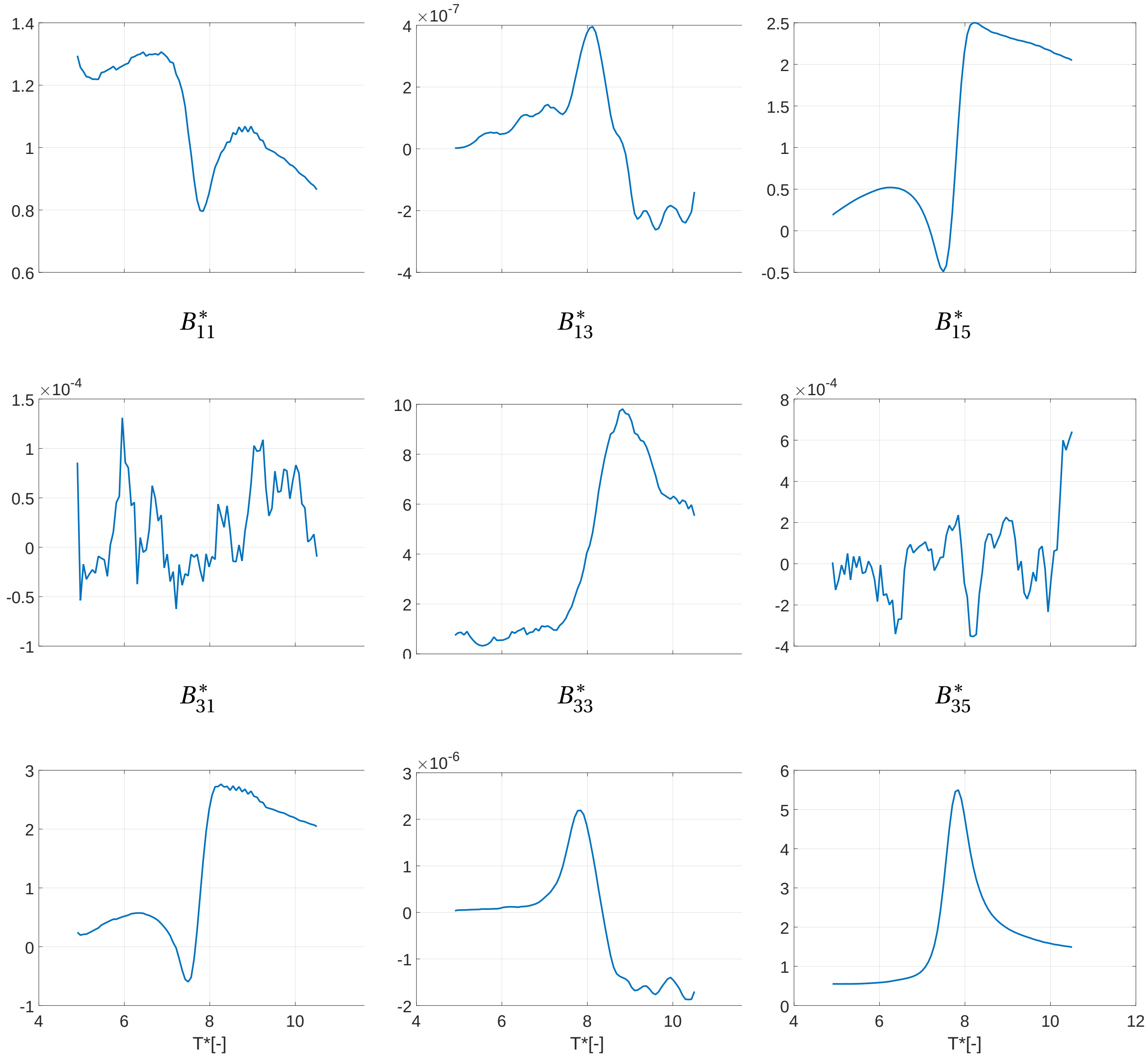

B^*_{11} B^*_{13} B^*_{15}

B^*_{31} B^*_{33} B^*_{35}

B^*_{51} B^*_{53} B^*_{55}

Figure 5.12: Potential Damping coefficients obtained for a moonpool structure with squared corners and and 15cm draft exposed for the highest forced motion amplitude. $T^* = T\sqrt{\frac{g}{b}}$ and the coefficients are done dimensionless wrt. formulas given in section 2.9.2.

From the added mass and the corresponding mass and stiffness coefficient from the freely-floating experiments, it's possible to calculate the eigenvalue problem of the moonpool geometry. The theory and procedure for this analysis are explained in Chapter 2.9.2.

Due to that the coefficients are frequency dependent, three different artificial solutions for each frequency dependent hydrodynamic added mass will be found. The real natural frequencies are found when the artificial ones correspond to the frequency used to calculate the frequency dependent added mass coefficient. Visually this corresponds to where the eigenperiod solution intersects with the straight period line. The solution is seen in Figure 5.13 and display the natural period in heave to be $T^* \cong 6.65$, and for pitch $T^* \cong 6.35$. The corresponding damping ratios are respectively $\beta = 0.12$ in heave and $\beta = 0.09$ for pitch motion.

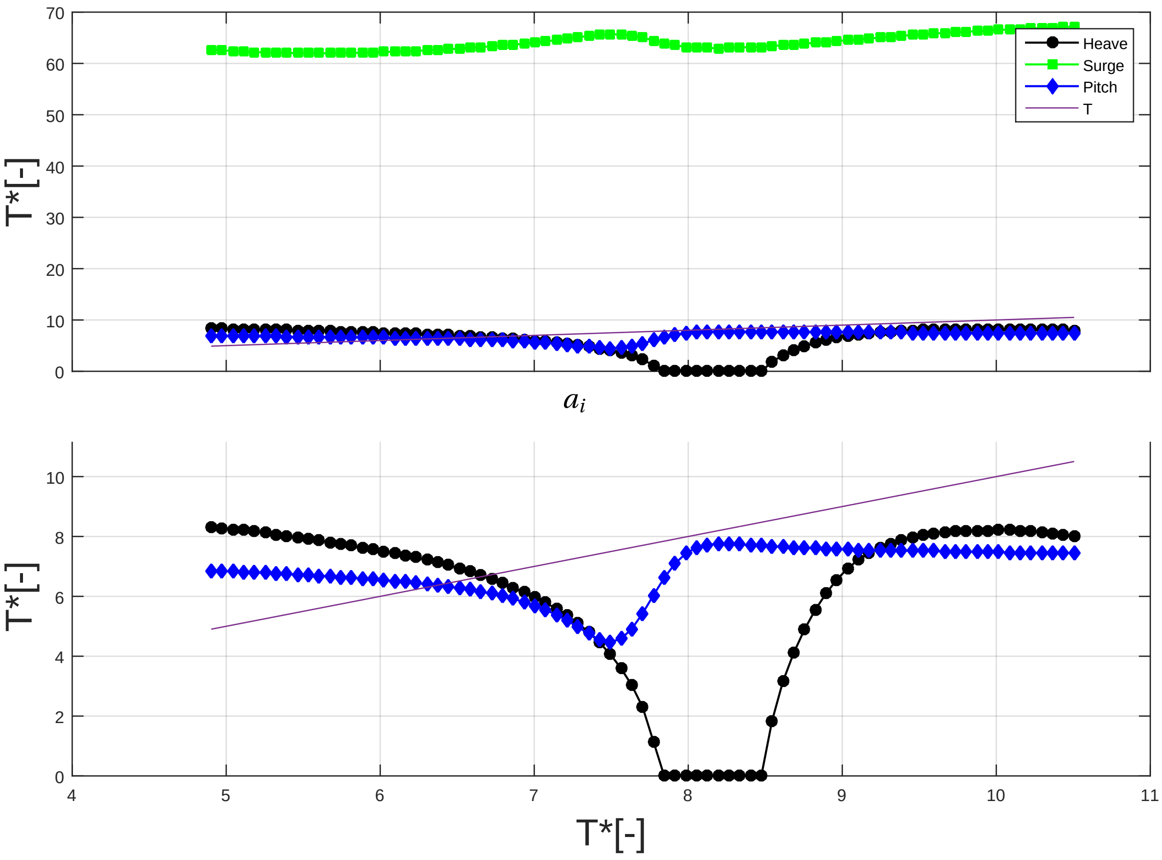

a_i

a_{ii}

Figure 5.13: The eigenvalue problem, figure a_i display the full problem, while figure a_{ii} zooms closer to the T^*-line. $T^* = T\sqrt{\frac{g}{b}}$.

Graph 5.11 confirms the coupling between surge and pitch motions, while heave is uncoupled to both surge and pitch. Further, the surge-heave coupling and heave-pitch coupling have orders of magnitude lower values. From the symmetry relation, they are expected to be zero.

The negative added mass for heave and pitch are connected to the resonance periods of the forced motion experiments. By inspection of respectively the heave and pitch resonance from Figure 5.1 a_i and b_i the negative added mass periods coincide with the resonance peak frequencies.

The potential damping graphs, 5.12, are related to the amount of energy radiated from the body. By comparing the resonance peaks of the outgoing waves in heave and pitch in the same figures as previous, it's evident that the damping maxima occurs for the periods with the highest amount of radiated waves.

A comment regarding the eigenvalue problem was that they were sensitive with respect to the inertia and the stiffness parameters. An increase in inertia or a decrease in the K_{55} would move the pitch eigenvalue plot such that it intersected with the $T*$-line three times instead of one. It would be of interest to perform a parametric study on the geometry, but this is not the scope of present work.

The practical meaning of the eigenvalue problem is further discussed in the chapter for freely-floating experiments.

5.1.6 Experimental Repetition Tests

Experimental repetition test was performed for two different conditions. Both repetition tests were done with rounded inlet corners and draft equal to 20cm. The only difference was the forced motion amplitude, one with 2.5 mm and one with 7.5 mm. Graphs 5.14 display the results and corresponding precision error. Here, the error bars follows a student-t distribution with a confidence interval of 95%.

The uncertainty for the moonpool wave elevation, blue line in Figure 5.14 b_i, varied between 4.8% for small oscillation periods to 1% for the highest periods. Around resonance, the uncertainty is calculated to be approximately 2%.

As for higher oscillation amplitudes, Figure 5.14 a_{ii}, the uncertainty varies from 3% to 1% over the frequency domain.

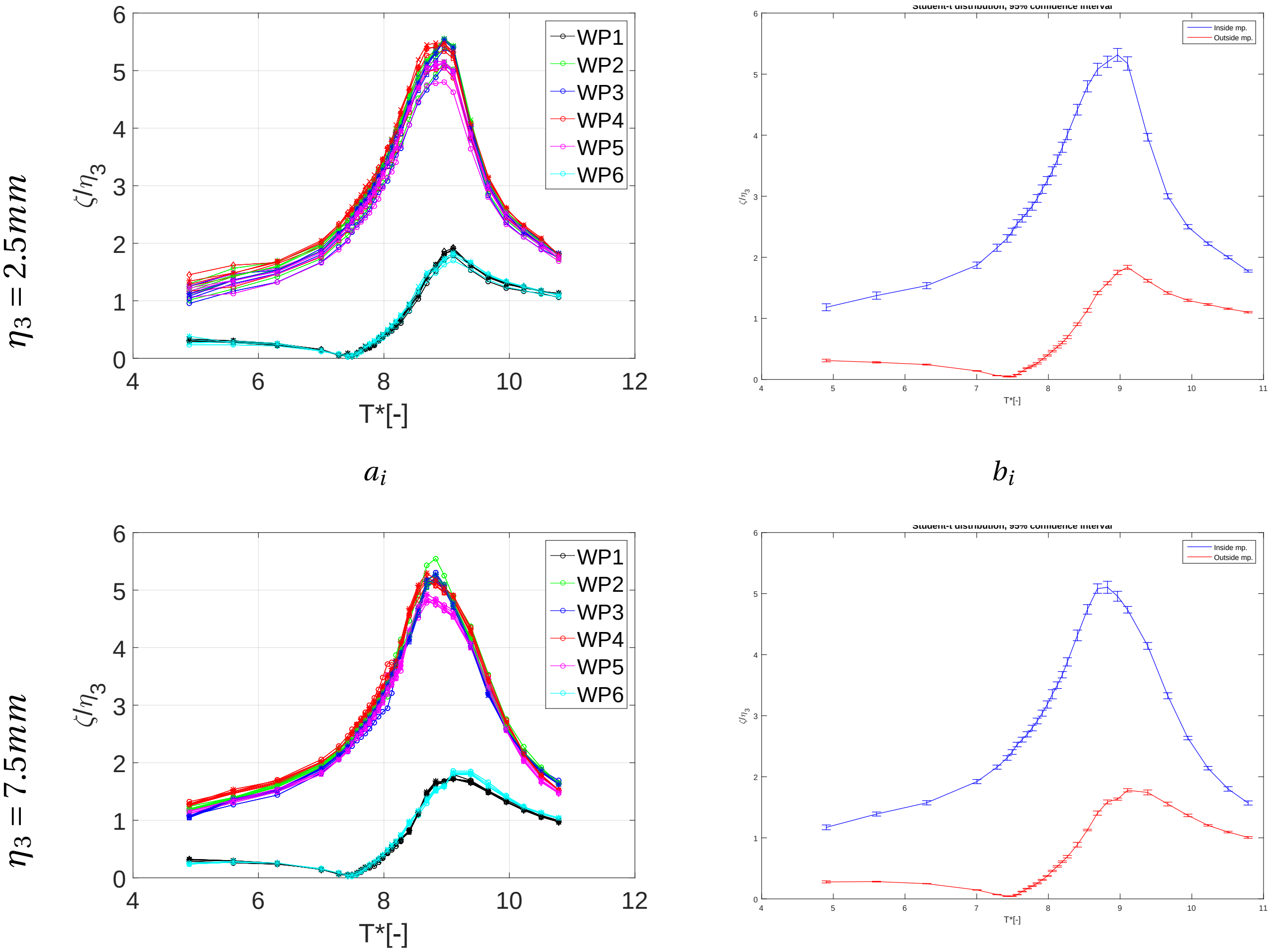

a_i b_i

a_{ii} b_{ii}

Figure 5.14: The repetition test in heave for a rounded inlet geometry with draft= 20cm. Column a display the repetition tests for $\eta_3 = 2.5$mm and $\eta_3 = 7.5$mm. Column b display the corresponding student-t precision limits for the repetition tests.

5.1.7 Comparison of Numerical and Experimental Study

The agreement between the numerical method and experiments in predicting the moonpool response are seen in Figure 5.3, 5.4 and 5.6. The results of the numerical scheme are in general satisfactory for the two largest amplitudes, while there is a discrepancy around piston mode resonance for the lowest pitch motion amplitude. In Figure 5.4 a_{ii}, the difference between numerical and experimental resonance for $\eta_5 = 0.45^o$ is 15%, while for $\eta_5 = 1.3^o$ in Figure c_{ii}, it's approximately 1%. The difference yields especially the moonpool configurations with the presence of geometrical singularities.

The similar discrepancy is evident for the 15cm draft, seen in Appendix A. Both the smallest and the intermediate forced amplitudes display a difference between numerical and experimental results.

In order to investigate these faults, a scheme test of a section exposed for forced pitch amplitude of $\eta_3 = 0.45^o$ was constructed. The inlets were squared, and the draft was 20cm. Results obtained for different numerical schemes, time steps and scaling of geometries for the forced pitch motion case are seen in Figure 5.15.

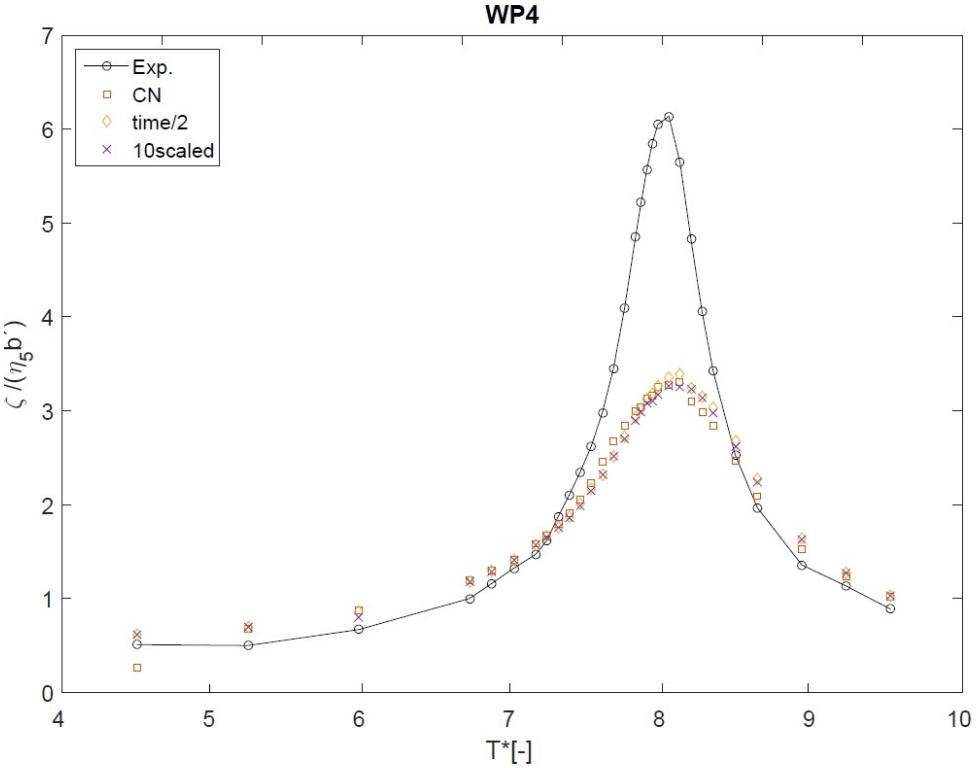

Figure 5.15: Visualization of the scheme test performed for a geometry with squared inlets, $\eta_3 = 0.45^o$, draft= $20cm$. The black line display the experiments, red scatter is the Crank-Nicolson scheme, yellow scatter is the reduced CFL-number and the purple scatter(x) is the scaled scheme. The period is done dimensionless with respect to $T^* = T\sqrt{\frac{g}{b}}$.

As the reader might have noticed, the scheme test have lower RAO magnitude than the final results seen in Figure 5.4. This is because the trial was done with a slightly coarser mesh than the final results. It's believed that the same trends are experienced for the final mesh as well.

First thought was that the numerical scheme suffered from numerical diffusion. Though, since the numerical RAOs for both low and high periods coincides with the experiments, this theory was rejected.

Possible reasons were proposed, and further investigations were needed. Since the results for higher forced motion amplitudes were in compliance with the experiments, a proposal was to scale the components in the domain and rerun the tests for a larger domain. Hence, the lengths were scaled ten times bigger with corresponding Froude scaling for the velocities and the forced motion periods.

It was also conducted an investigation of the numerical scheme where the method was replaced with a second order Crank-Nicolson scheme.

The last examination was performed with respect to the chosen time step size. This property depended on the CFL number and was dynamically changed during the simulations to obtain a CFL number less than 1. Hence, the time step was reduced by lowering the CFL condition to 0.5.

None of the applied methods gave any improvement, and the cause of error is beyond the author's knowledge. Though, since the error is not so dominant for rounded inlets, it's believed that the faults may be related to how the vortex shedding is simulated for small forced motion amplitudes, and a smaller mesh around the inlets may improve the results.

5.1.8 Processor Performance of Numerical Scheme

The CPU performance calculations are based on the theory proposed in Chapter 3.3.2, and the results are seen in table 5.3. The CPU performance appears in the interval between 600-850KNUPS, while the Simulation time is ranging from 310 to 375KNUPS.

Table 5.3: The table display the CPU performance of the numerical simulations given by formula $NUPS = \frac{n_x \cdot n_y \cdot n_{iter}}{T}$

Source Case	Elements	Iterations	Simulation Time	CPU Time	KNUPS/core Sim. Time	KNUPS/core CPU Time
1110	87568	1424	331s	147s	376.7	848.3
1140	85262	2399	328	296.2	310	690
1500	427730	1530	1743.0s	1088.8s	375.5	601.0

The difference in the clock time and CPU time indicates that there is a lag in the system caused either by a delay due to the time it takes to write output to file or that the CPUs ran in parallel.

5.2 Freely-floating Experiments

Up until now, the analyses have concerned a two-dimensional structure subjected to forced motions. The present section will provide results for a spring-moored 2D moonpool geometry exposed for incoming regular 2D waves. The experimental data are obtained from current work, while numerical plots are given from Arnt Fredriksen in Multiconsult. The properties are presented in Chapter 4.2: water depth = 1.0m, draft= 0.15m and moonpool gaps= 0.2m which corresponds to the reference geometry.

The model tests were performed for two different placements of external mass, which gave rise to various inertia. Also, an experimental repetition test of wave steepness 1/30 on a geometry with the largest inertia and squared corners was performed. All experiments are summeraized in Figure 5.20 and 5.21, and correspondig full scale graphs are found in Appendix D.

5.2.1 Decay Test

The decay test was conducted by displacing the structure and then released it, allowing a free decay of the geometry. This was done for both heave and pitch motions. The eigenfrequencies could be found through spectral analysis using a discrete Fourier transform of the resulting time-series, and the results were utilized in the construction of the incoming wave periods for the regular wave test.

All combinations of the geometric configurations were tested, and Figure 5.16 display eigenfrequencies for both DoFs. Here the reference geometry with the external mass placed near the flotation center is shown.

From the spectral analysis, it is seen that the configuration has natural heave period at $f \cong 1.1[1/s]$ which corresponds to the dimensionless periods of $T^* = 6.4$. The pitch spectral analysis gave one large and one small peak, resulting in dimensionless eigenperiods of $T^* = 6.43$ and $T^* = 9.1$. The lowest natural period for both DoFs are seen in the regular wave tests, Figure 5.17.

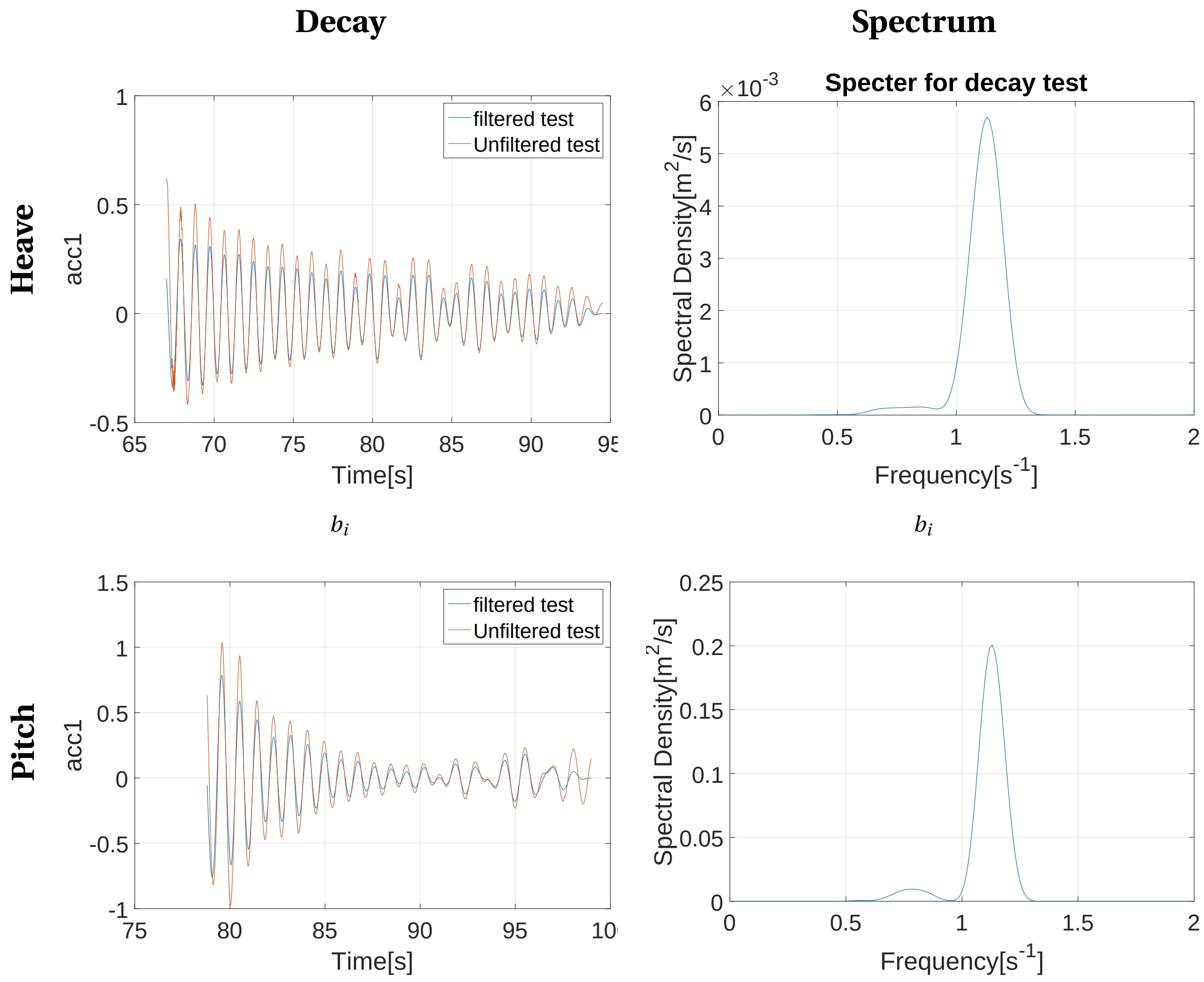

b_i b_i

b_i b_i

Figure 5.16: Decay test for the reference geometry. Column 1 display the decay for the accelerometer facing the wavemaker, and column 2 display the corresponding spectrum. Row one is obtained for heave motions, while row to is the results for pitch motions.

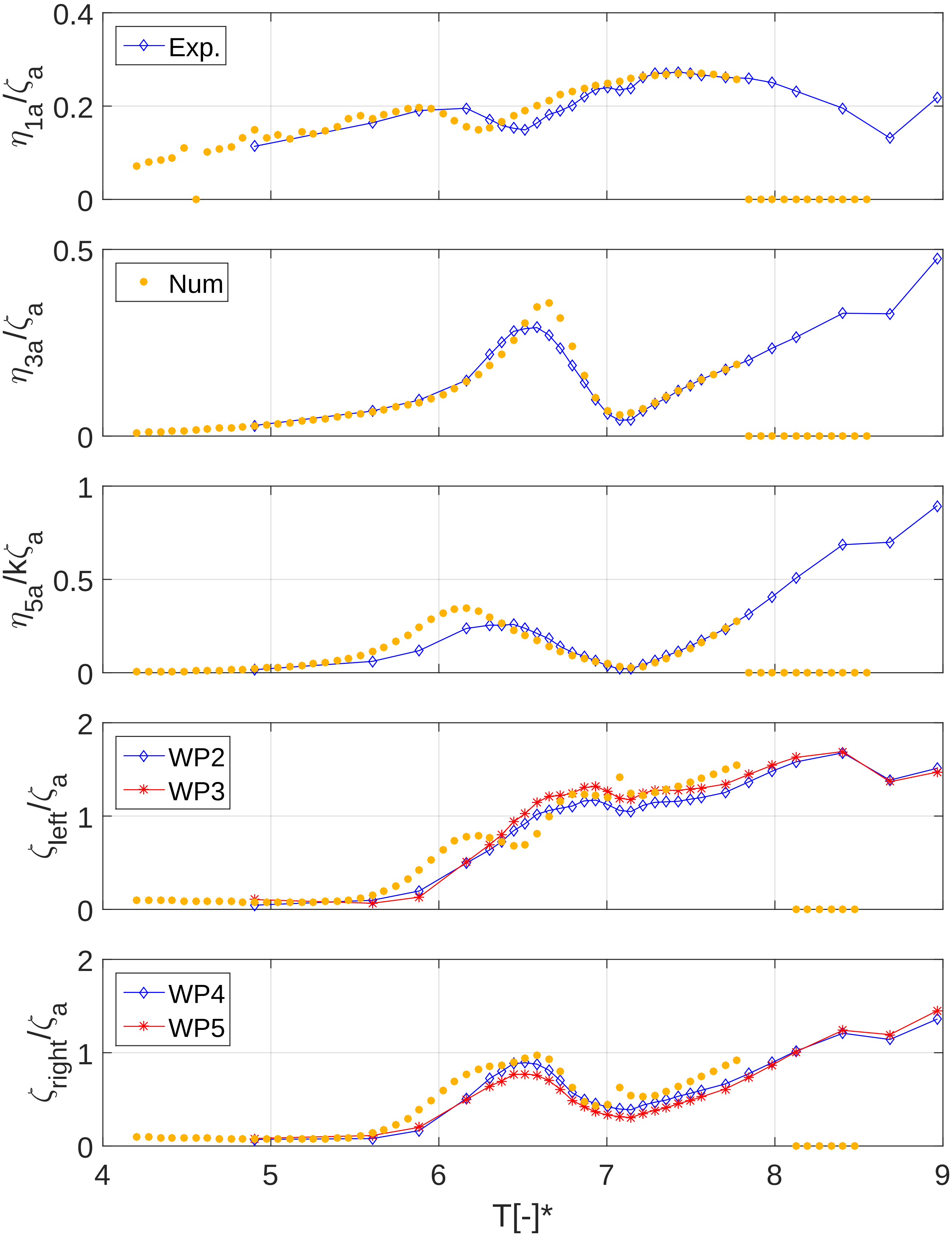

Figure 5.17: Freely-floating experiment exposed for incoming waves with steepness 1/60. The geometry has squared inlets, and tested for low inertia properties. Blue and red lines are experiments, yellow scatter is Fredriksen's numerical scheme. $T^* = T\sqrt{\frac{g}{b}}$.

5.2.2 Results for Freely-floating Structure

Figure 5.17 displays experimental and numerical results for a moonpool section with squared corners, the lowest inertia and an incoming wave steepness equal to 1/60. These graphs, together with plots displayed in Figure 5.20 and 5.21, lays the foundation for analyzing the freely-floating 2D experiments.

A general trend for the cases with low inertia is that the resonant motion has a cascading behavior between pitch, heave and moonpool wave elevation. From Graph 5.17 the resonant cascade moves the following. First, for wave period 5, 6 and 7, a pitch resonance peak is observed. At periods 7,8,9, maxima are seen both for heave motions and the moonpool facing away from the incoming waves. At last, the moonpool facing towards the incoming waves experience resonant behavior for period 12, 13 and 14. The same is not seen for rigid surge motions, where the RAO appears more or less as a linearly increasing line.

Around period 16 and 17, all RAOs display a decrease in response, and both heave and pitch rigid motion appears to cancel out. For higher periods, the response amplitudes are increasing.

Another observation is seen from the comparison of the radiation experiments and freely-floating tests. It's noticeable that the resonant behavior for pitch do not appear for any results in Figure 5.17, where the forced piston mode resonance for pitch is observed at $T^* = 7.7$. For the freely-floating case, the resonant water motions occur respectively at $T^* = 6.6$ in left moonpool and $T^* = 6.4$ in the right moonpool. The same tendency is as clear from forced heave motion, where the peak occurs at $T^* = 8.3$, where a RAO peak is observed for the heave, the pitch and the moonpool wave elevations.

Comparison with the eigenvalue analysis obtained from the radiation problem, Figure 5.13, and the freely-floating experiment RAOs, Graph 5.17, display compliance between the eigenvalue intersection points and the heave and pitch resonance periods. Further, no intersection points or resonance motions are experienced for the surge problem.

Inspection of phase angles give rise to following observations: The phase between moonpool wave motions and pitch are out of phase for small wave periods. At the cancellation period the phase shifts, through 90^o, and becomes in phase for higher periods. This is visualized in Figure 5.18 a_i, where β is defined as the phase angle between the pitch response and the moonpool water elevations. The same phenomenon is observed for the interaction between heave and the piston mode motion, 5.18 b_i.

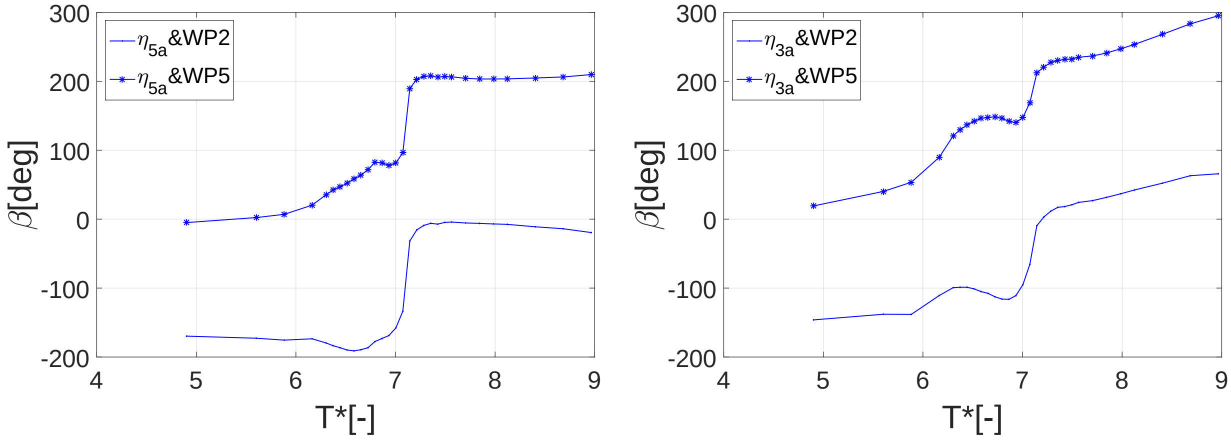

a_i b_i

Figure 5.18: Figure a display the phase angles between η_5 and the wave probes. WP2 is the wave probe located in left moonpool and WP5 is located in right moonpool. Figure b display phases for between have motion and piston mode.$T* = T\sqrt{\frac{g}{b}}$.

5.2.3 General Findings

The difference between the radiation and freely-floating RAOs also occurs within linear potential flow theory for steady-state motions (McIver, 2005). The phenomenon is described for rigid body motions in pitch. At steady-state, the main contributions from the diffraction and radiation potentials, equation 2.21, on the piston-mode are 180^o out of phase around the piston-mode natural period for the freely-floating body, and the main contribution from ϕ_d and ϕ_5 will cancel the response around this period.

Further, resonance values experienced for the heave and pitch RAOs, are supported by the solution of the eigenvalue problem. The surge motion which appears as a linearly increasing line, which is in a build up to a resonance peak occurring for higher oscillation periods. An estimation of the natural surge period is done by neglecting the asymptotic surge added mass contribution and calculate the eigenperiod by following the formula, $T_{1n} = 2\pi\sqrt{\frac{m}{k_{11}}}$, which is approximated to $T^* \cong 51$. Here, an additional added mass term would increase this value, and it is clear that the surge RAO for the freely–floating experiments are located in the inertia dominated domain according to Graph 2.12.

The cancellation period is explained through the discussion around phases, and can be compared to a mono-hull system with an anti-roll tank working 90^o out of phase with the resonant roll motion. For such system, the RAO will experience minima, and the anti-roll tank works as a vessel damping device.

The present arrangement is somewhat different, so to relate these problems one has to assume that the pitch cancellation periods appear where the pitch resonance is believed to occur for a mono-hull geometry. Such analysis is not performed in the present work, but by comparison with Fredriksen (2015) results, Chapter 2.3.3, it's evident that the mono-hull experience resonance at higher periods than the moonpool section. The same finding is apparent from the pitch equation of motion. For the two sections, it's assumed that they have equal length and similar radii of gyration. I.e. the mono-hull will experience a greater mass, and the inertia must increase to keep the radii of gyration constant. With an increased inertia, I_5, the uncoupled natural period in pitch, $T_5 = \sqrt{\frac{A_(55)+I_5}{C_(55)}}$, will increase, and it's plausible that the cancellation of the current system appears at the mono-hull resonance period.

From the author's view, the moonpools are therefore believed to work as an integrated "anti-pitch tank," canceling out resonant pitch motions for particular periods. The effect is illustrated for both heave and pitch in Figure 5.19.

5.2.4 Time Series of Cancellation period

The time series corresponding to the cancellation periods in heave and pitch are seen below. Initially, both the heave and the pitch response builds up faster than the water motion inside the moonpools. After the initial seconds, the geometry motions are decreasing, while the moonpool responses still increase. It is evident that the initial displacement are greater than the steady state.

Also, the moonpool motion facing away from the incoming wave, experience a decrease after an initial build-up.

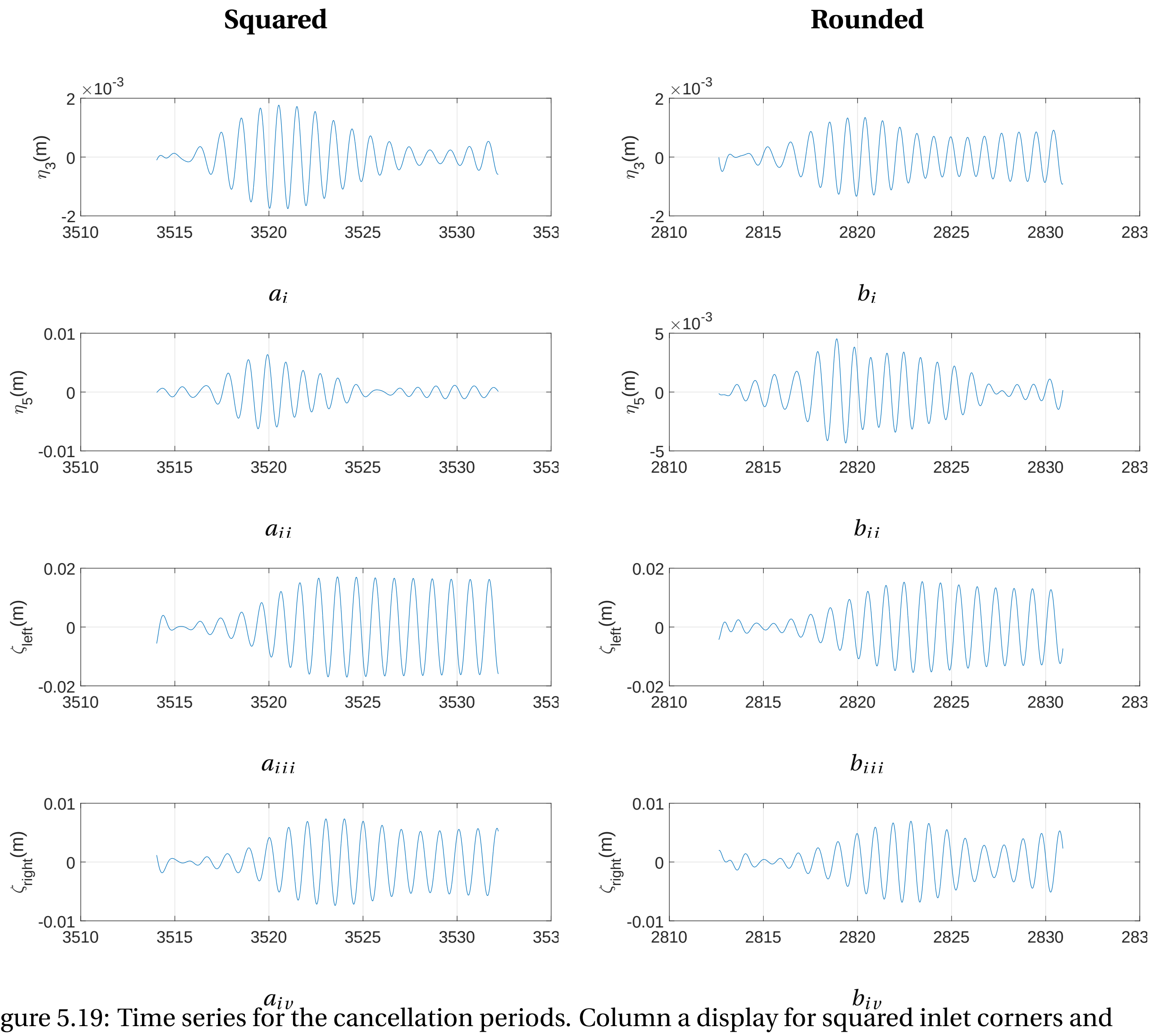

Figure 5.19: Time series for the cancellation periods. Column a display for squared inlet corners and column b is the same for rounded configurations. wave steepness = 1/60.

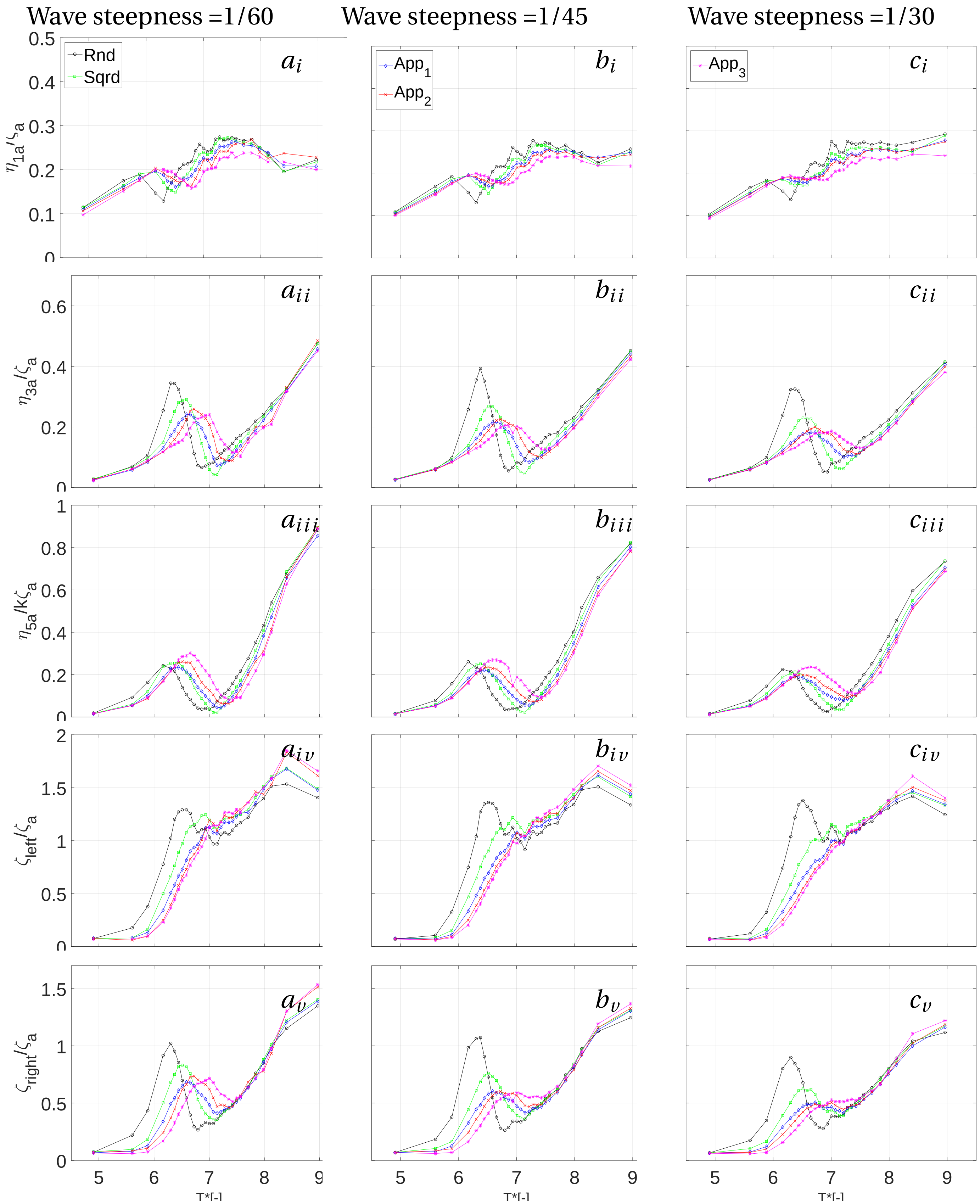

Figure 5.20: Comparison of free-floating test with five different inlet geometries for mass placed in geometry center. Column 1, 2 and 3 display respectively the wave steepness 1/60, 1/45 and 1/30.
$T^* = T\sqrt{\frac{g}{b}}$

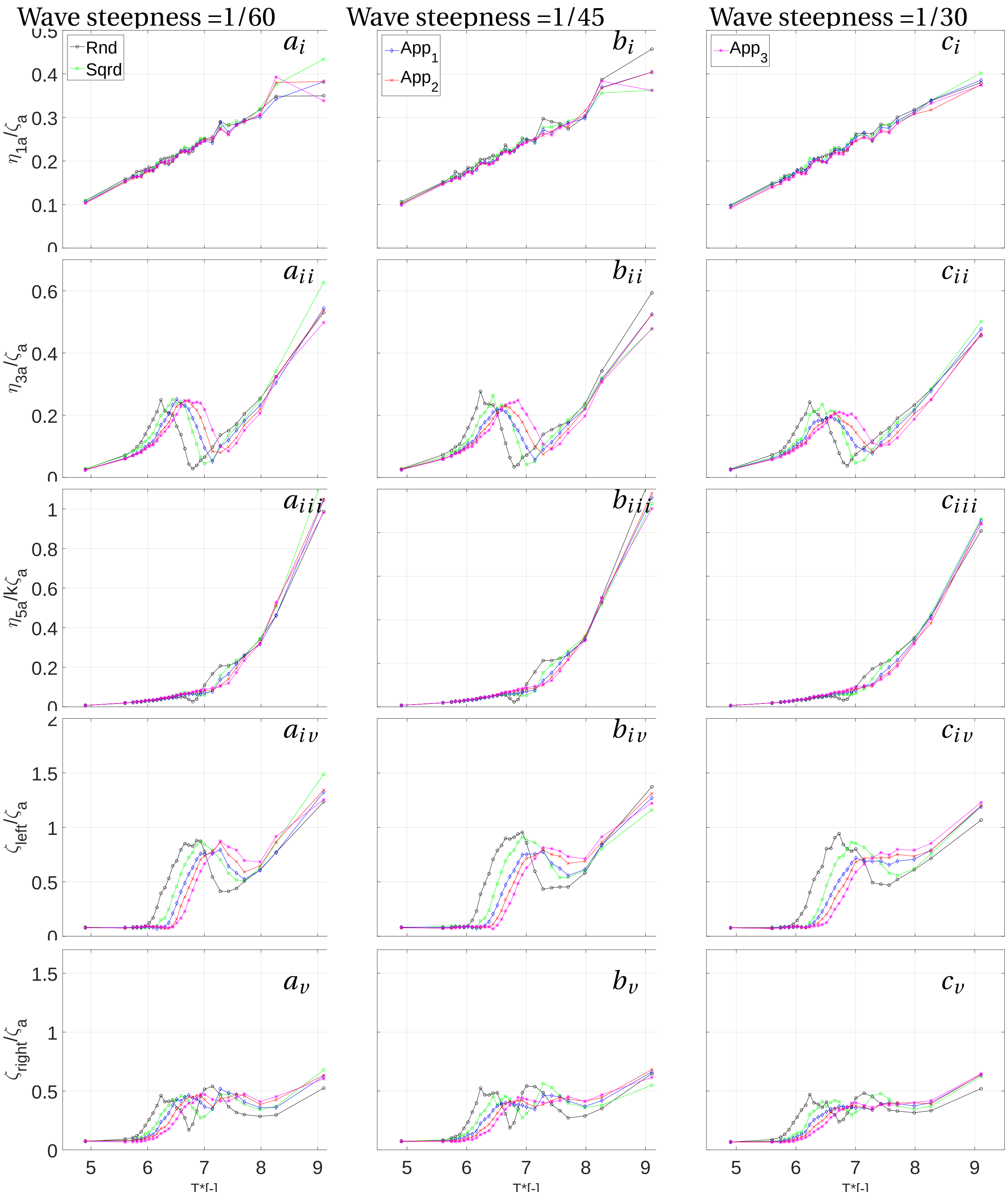

Figure 5.21: Comparison of free-floating test with five different inlet geometries for mass placed away from geometry center. Column 1, 2 and 3 display respectively the wave steepness 1/60, 1/45 and 1/30. $T^* = T\sqrt{\frac{g}{b}}$

5.2.5 Effect Changing Moonpool Inlet

The influence of the inlet configurations was also investigated for the freely-floating case. The results are displayed in Figure 5.20 and 5.21, and the trends are as follows.

For the both low and high inertia cases, responses seem to shift towards greater periods with increasing appendages. For instance, the RAO for the rounded configuration experience both the resonance and the cancellation for lower T^*-values than the square inlet geometry. This is the trend for the surge, heave, pitch and the wave elevation inside the moonpools.

Next, the heave response for low inertia are largest for the rounded configuration and decreases with increasing appendage. For the pitch RAO, this is not the case since the resonance peak values are of similar magnitude irrespective of inlet configuration.

The cancellation period is most evident for square and round geometries, and this effect decreases with the size of the appendages.

Figure 5.22: The figure display three of the five tested moonpool inlet configurations. 1. Rounded, 2. Squared, 3. Appended.

The moonpool inlet effect argumentation is somewhat similar to the discussion regarding the moonpool corners from the forced motion experiments.

By inspection of the low inertia case, it's seen that the heave and the piston mode of motion inside the moonpools are significantly higher for the rounded inlets than the structures with geometrical singularities in the moonpool entrance. Again this is explained by the amount of shed vortices for the squared and appended sections, which leads to greater non-linear damping contributions and smaller responses.

The pitch RAOs evolves differently, where the resonance amplitudes are of equal magnitude irrespective of the moonpool inlet. A theory is that the squared corners, on the outer hull of all configurations, shed vortices regardless of the design of the moonpool entrance. Since the outer corners have large distance from the pitch center, it's believed that they are dominant for the pitch damping contributions and the resonances exert similar magnitudes.

Next, the moonpool draft controls when the natural periods occur. The rounded configuration, i.e. the smallest effect draft, experience resonance and cancellation for lower periods than for instance the square inlet design. This phenomenon is in accordance the forced motion experiments, i.e. smaller draft trigger resonance at lower periods.

Also, with increasing vertical appendage length, the cancellation effects are also reduced.

Some the above mentioned tendencies are also seen in the case of high inertia. Here, the RAOs are in general different, which is further discussed in Section 5.2.6.

5.2.6 Inertia Effects

Two different mass moments of inertia were utilized for the freely-floating experiments. By comparison in Figure 5.23, following observations can be made.

The heave RAO for the squared configuration is not affected by the inertia changes. This is not the case for the pitch response. For a low radius of gyration, there is a resonance peak for small periods, followed by a distinct cancellation period. For larger inertia, the response for small periods is insignificant, and no particular cancellation period is observed. For higher periods, the responses are coinciding.

The hydrodynamics inside the moonpool are also changed with different inertia, where larger responses are observed for small inertia. Also, a distinct decrease in moonpool response is seen around heave cancellation period both for the small and the large inertia configurations.

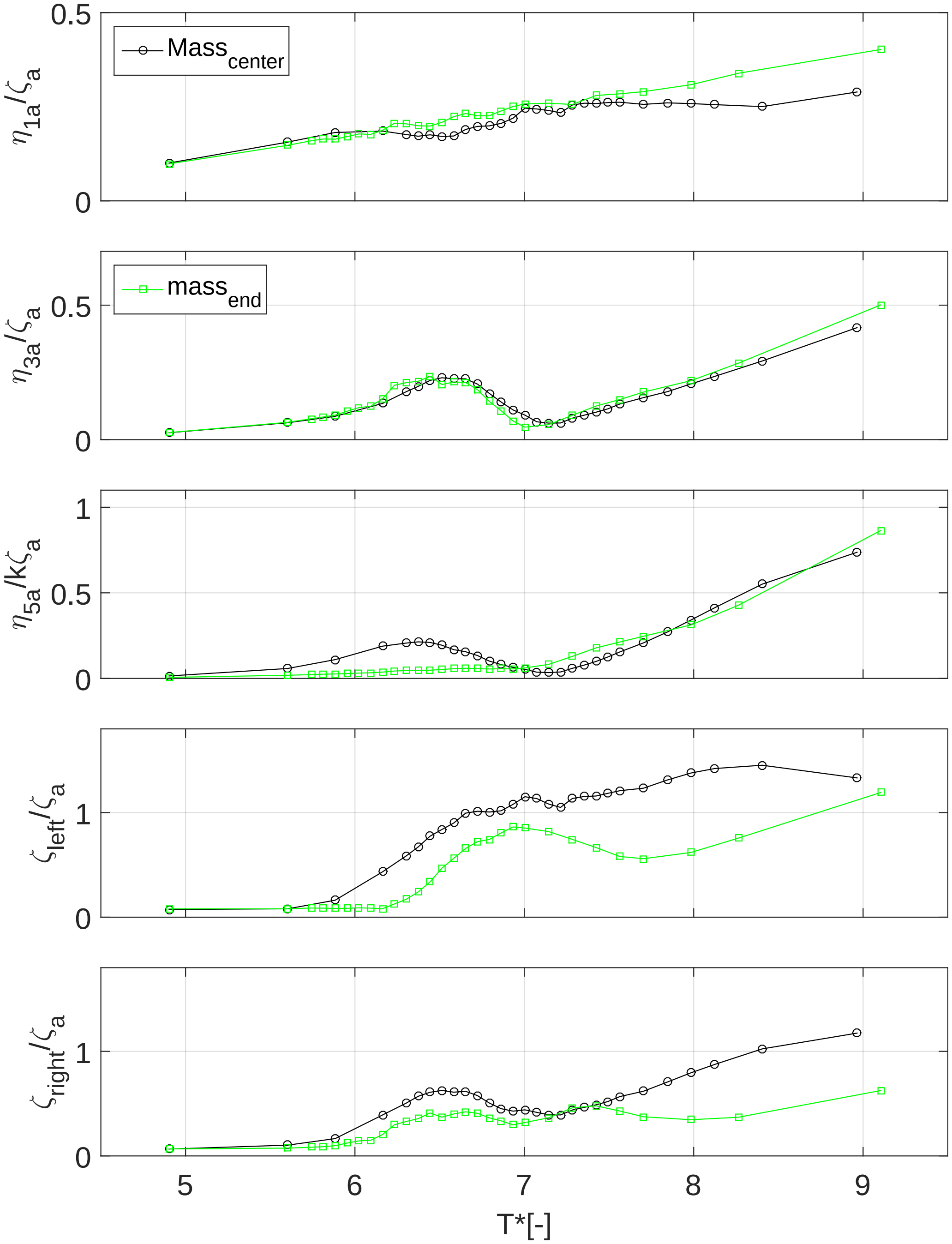

Figure 5.23: Comparison of the effect of Mass placement, for the reference geometry with wave steepness 1/60. $T^* = T\sqrt{\frac{g}{b}}$.

A comparison of the graphs with the equation of motion, formula 2.44, it's evident that the mass variable inside the heave equation is not affected by the change in mass placement. The same conclusion cannot be drawn regarding the inertia coefficient that appears in pitch equation of motion. An increase in I_5 will decrease the natural frequency, and the resonance peak will shift towards higher periods.

For the geometry configuration with the mass placed away from the flotation center, it appears that the inertia is dominant for small periods and restricts the response amplitudes in pitch, which again decreases moonpool motions. This corresponds to the dynamic amplification factor from Section 2.9.1, whereas in the inertia dominated part of the RAO, the amplification factor is insignificant.

As for the surge RAO, the natural periods is already much higher than the evaluated period, and will not experience significant effects by the change of inertia.

5.2.7 Effect of Wave Steepness

Figure 5.24 display the wave steepness effect of the rounded and squared inlet configuration. Here, the pitch RAOs are plotted and following observations can be made:

For squared inlet corners, Figure a, the RAO decreases with increasing wave steepness. The same tendency is not clear for the rounded geometry, where the RAO display similar magnitudes around the resonance, this is different for higher periods.

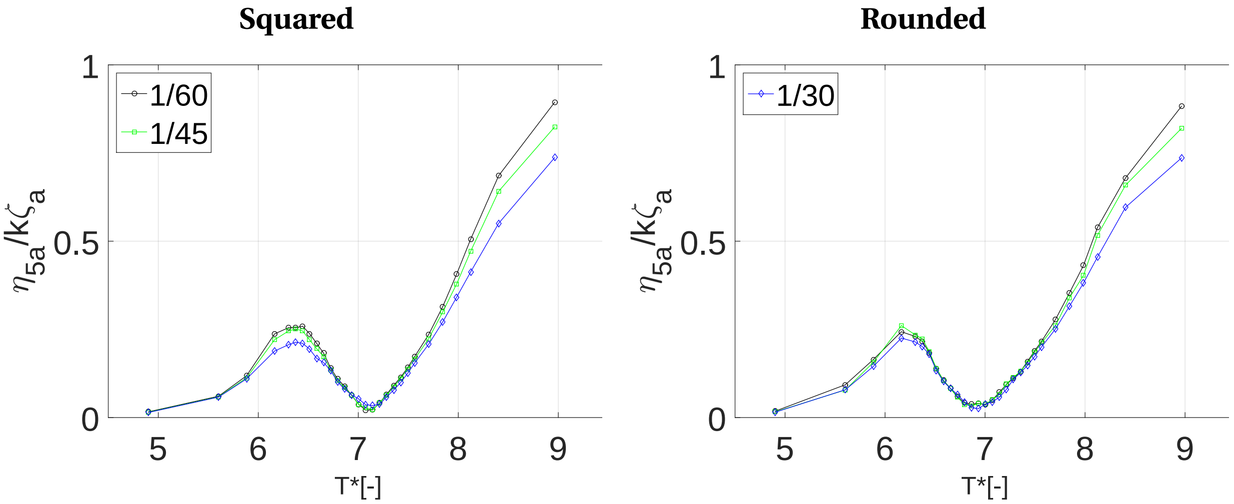

a_i b_i

Figure 5.24: The effect of wave steepness for the freely-floating experiment, $T^* = T\sqrt{\frac{g}{b}}$.

By comparing the results from Figure a and b, 5.24, it's evident that for square inlet corners, the RAO decreases with increasing wave steepness. The vortex shedding rises the nonlinear damping effects for higher motions. Thus, the RAO decreases.

For round corners, it's observed that the RAO does not change similarly, which is connected to the potential theory explained for the forced motions results. For the highest periods, a discrepancy is also seen for round corners. Here, the motions are large, and the corners facing out of the structure are squared, which might result in vortex shedding and viscous damping effects.

5.2.8 Cancellation Interval

An investigation of the cancellation intervals was done by the creation of a 3rd order polynomial for the different moonpool inlet configurations. The results are displayed for the low inertia moonpool case with wave steepness 1/60. From Figure 5.25 it's evident that the rounded configuration experience greatest cancellation effects with a value of 0.0398, while the squared value is 0.0448.

The other graph, Figure 5.26, compare the width of the cancellation interval between the configurations. This figure is based on the real plots. In order to investigate the width trends, the minima for each design are moved to a reference point such that they coincide. From this graph, it's seen that the rounded geometry has a slightly wider cancellation interval than the other sections.

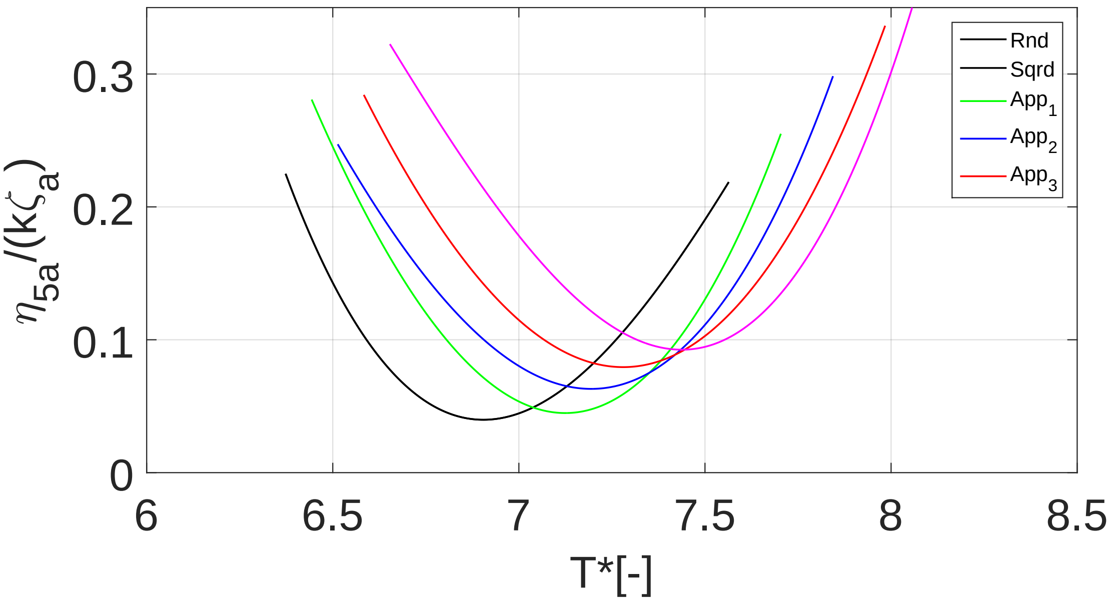

Figure 5.25: Cancellation period for the geometry exposed for wave steepness 1/60. The inlet configurations are evaluated with small inertia.

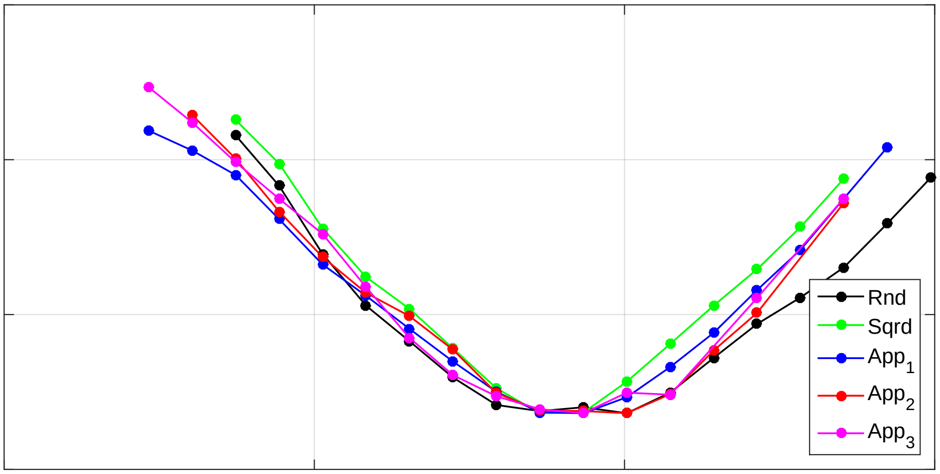

Figure 5.26: Cancellation width for the geometry exposed exposed for waves with steepness 1/60. The inlet configurations are evaluated with small inertia.

5.2.9 Comparison with Fredriksen's Numerical Scheme

Figure 5.17 displays result for the model tests and Fredriksen's hybrid scheme.

A first observation is that the experimental responses for the surge, pitch, and the moonpool wave elevations appear with an offset compared to the numerical scheme. Furthermore, there is a difference in the response magnitudes for both the heave and the pitch RAO. They are summarized in Table 5.4.

Further, the cancellation periods in heave and pitch are in compliance between the two methods.

Table 5.4: Percentage difference between the resonance peaks between Fredriksen's numerical scheme and experiments.

DoF	**Difference**
Heave[%]	16.7
Pitch[%]	15.4

To obtain higher agreement between the numerical and experimental results, a more extensive sensitivity- and convergence study is needed.

The response offset indicates that there is a discrepancy between the inertia values applied for the numerical scheme and the inertia used for the experiments. The difference may occur because the inertia values from the model tests were theoretically approximated based on the mass placement of the freely-floating structure and not a measured during the experiment.

Thus, the input inertia to the numerical program may differ from the actual property.

Further, the response peak discrepancies seen in heave and pitch are also thought to improve by through the extensive sensitivity analysis. Though, it should be mentioned that Arnt Fredriksen has reported similar faults from other investigations that utilize the same hybrid scheme.

5.2.10 Experimental Repetition Test

An experimental repetition test was performed at the end of the freely-floating experiments. The wave flume and model arrangements were the same, and the only replicated property was the incoming waves. The test was conducted five times with wave steepness equal to 1/30, squared inlet corners and the exterior mass placed away from the flotation center.

The uncertainty of the experiments was calculated with the confidence interval of the Student-t distribution equal to 95%. The errors are shown in Figure 5.27, where the error bars at each period display the given uncertainty at that particular oscillation frequency. In Table 5.5 some main features regarding the error analysis are displayed, namely maximum and minimum uncertainty over the frequency domain, and also the uncertainty around the resonance peak in heave.

From the graphs, it's observed that the first test deviates slightly from the others. This is especially seen for the heave resonance period.

Table 5.5: The table display some features regarding the student-t error analysis. Column 2 display the uncertainty for the different DoF's at heave resonance. Column 3 and 4 display respectively the maximum and the minimum uncertainty over the frequency domain.

DoF	**Uncertainty at heave resonance**	**Max. uncertainty**	**Min. uncertainty**
Surge[%]	0.8	5.1	0.4
Heave[%]	5.0	9.3	0.5
Pitch[%]	2.4	9.0	0.4
Left Moonpool[%]	3.1	11.7	0.7
Right Moonpool[%]	3.3	8.6	0.4

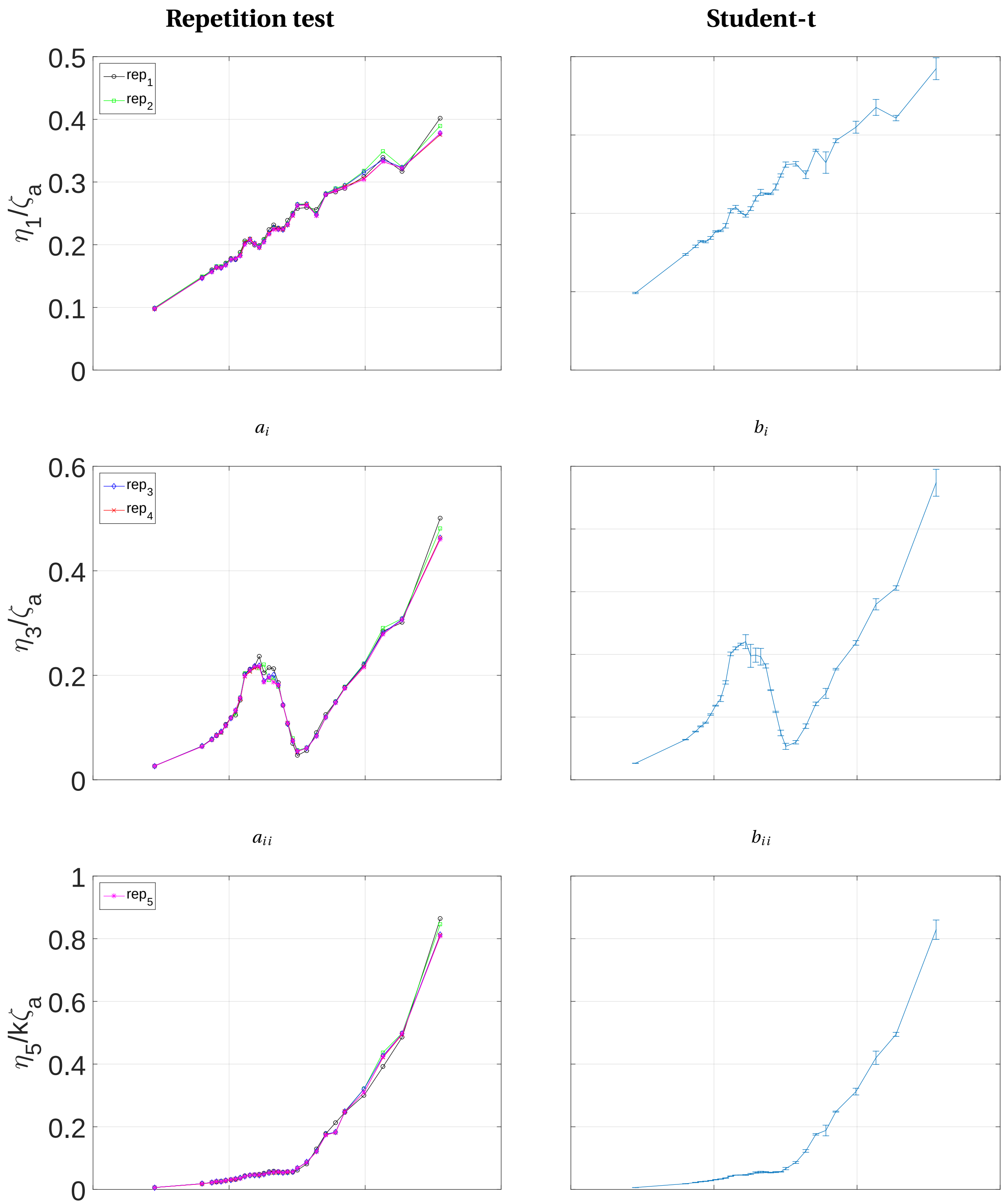

Repetition test

Student-t

a_i b_i

a_{ii} b_{ii}

a_{iii} b_{iii}

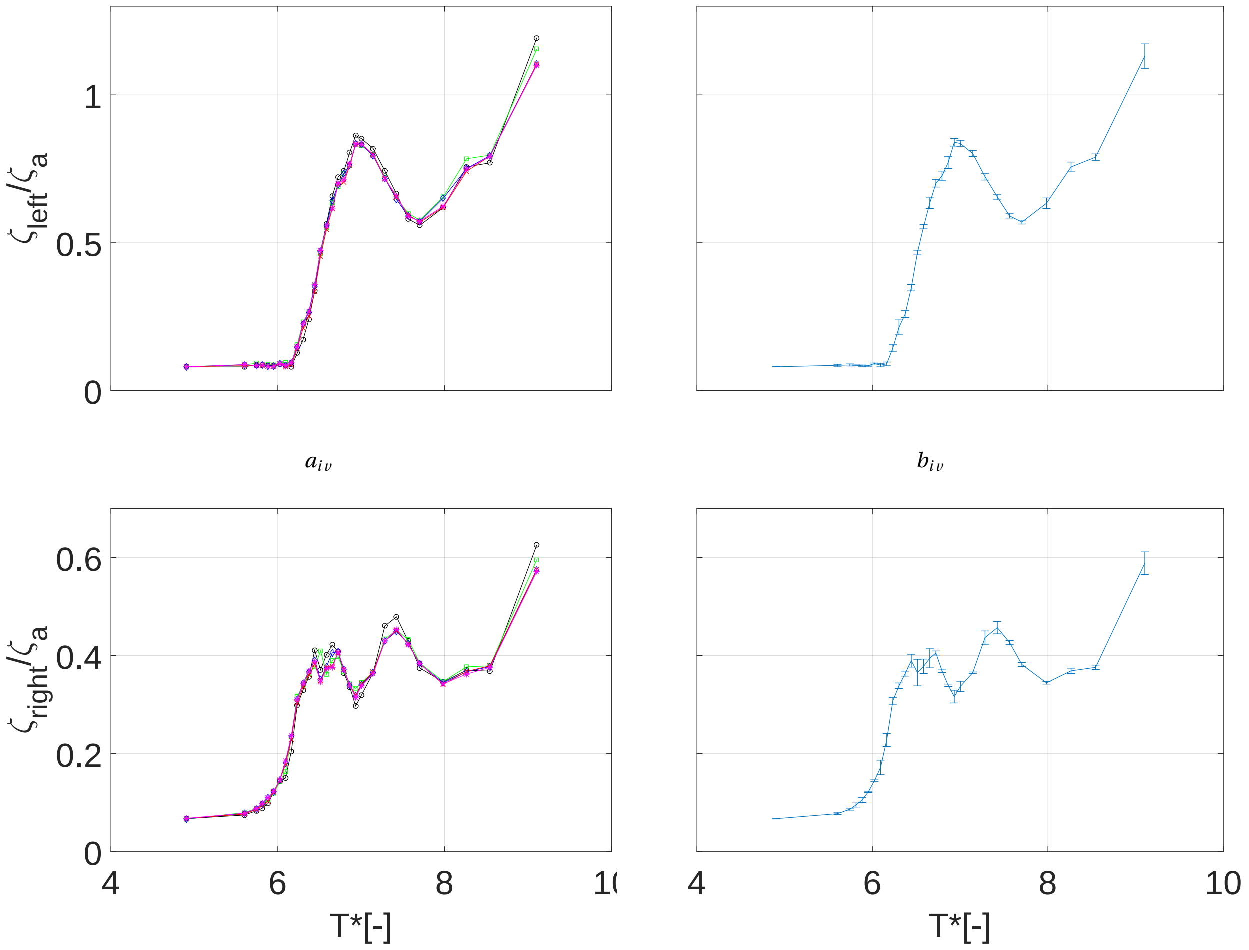

a_{iv} b_{iv}

a_v b_v

Figure 5.27: Column 1 display the RAO's for the different repetitions, while column 2 show the corresponding student-t distribution with 95% confidence interval. The repetition is performed for the reference geometry with high inertia. $T^* = T\sqrt{\frac{g}{b}}$

5.3 Applicability of Moonpool as Damping Device

So far, this thesis has discussed the flow field and rigid body motions of a model scale moonpool experiment, and not the advantages it may have for a practical case.

As stated in the introduction, this work has been concerned with a two-dimensional moonpool case. In reality, the bridge floater will be a three-dimensional structure 256 times bigger than the model. Thus, is necessary to account for the 3D flow effects. As for the incoming wave problem, the 2D approximation might not be a rough simplification, since the bridge will cross a fjord where the majority of the waves that enter the bridge floaters will be long crested ocean swells.

If we, for now, accept the results from the 2D flow, there are mainly two parameters that define the utilization of the moonpool device as a pitch damping device. This is the values of the pitch RAO cancellations and the width of the interval with beneficial cancellation effects.

Analyses of the width of the cancellation intervals, Figure 5.26, does not show any great difference between the configurations, but the round inlet design may have a slightly wider advantageous range.

Further, the cancellation effects are found to be most pronounced for the round and square inlet configurations. This is observed from Figure 5.25. Though, from Figure 5.20 it's also evident that the introduction of moonpools also gives rise to resonant behavior for lower periods, particularly for the geometry with low inertia and round inlets.

A proposal has been to include a device that can reduce the resonant effects. For instance, an anti-pitch tank working 90^o out of phase on the geometry motion around the resonant periods. Though, it has not yet been investigated in present work.

As for the heave cancellations, it's evident that the round inlet design experience a large resonance peak close to the cancellation period, which indicates that a small difference in the incoming wave periods may amplify the motions. This must be seen in the context of the dynamic amplification factor from section 2.9.1 and the full scale damping contributions for the bridge in the areas around the resonance peak and cancellation periods.

Another configuration that affects the dynamic behavior is the mass placement of the structure. As of today, the author is not aware of the inertia effects of the bridge superstructure. Hence, a broad discussion is not necessary. Though, if we consider the 3D bridge floaters exclusively, the concrete mass will be concentrated near the flotation center, and the model test with the small inertia configuration is the most realistic design. This is also the property which gives the clearest pitch cancellation at certain periods.

The metocean data of the specific fjord is given in Figure 5.28, and the highest swell density occurs of wave period around $T_p = 10s$. The cancellation period for the model scale, 1:265, was approximate $T^* = 7$, which corresponds to T~16s in full scale, and indicates that further geometrical optimization will be needed at a later stage.

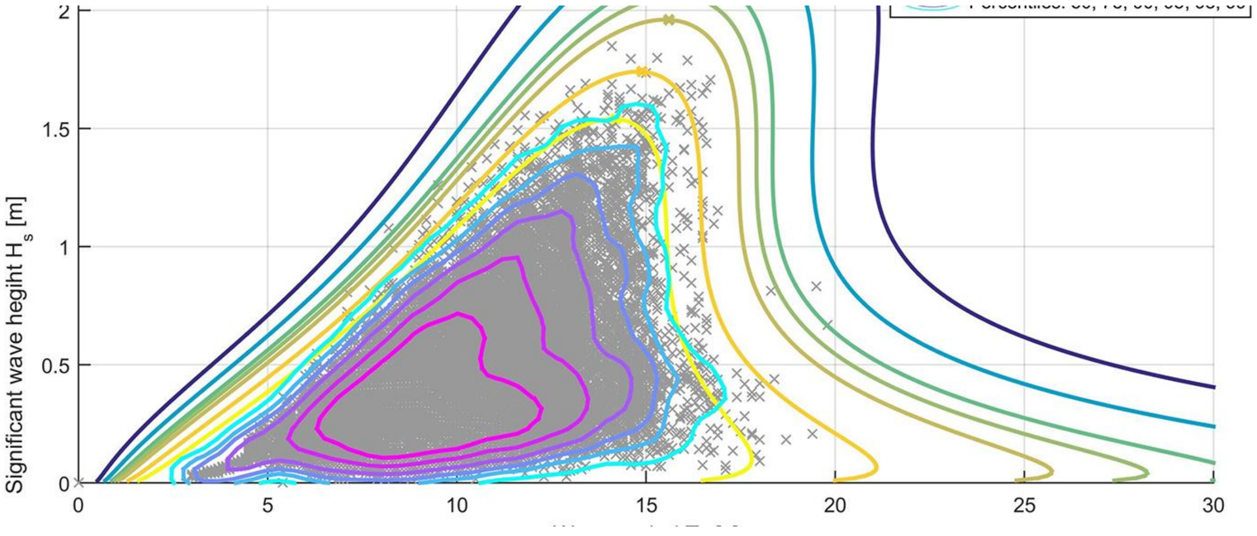

Figure 5.28: Metocean data for Sulafjorden obtained from Multiconsult. (Mul, b)

Chapter 6

Conclusive Summary and Future Work

In this thesis, several aspects regarding hydrodynamics of a vessel equipped with two moonpools have been addressed. The starting point was to give a brief introduction of theories to determine the hydrodynamics around such vessel. This led to a discussion of potential and viscous flow formulations for the fluid domain around the structure, and the viscous approach provided the most consistent results. Secondly, the dynamics of a 2D section free to move in three degrees of freedom was described in detail, leading to the coupled equation of motion for a floating vessel and the corresponding eigenvalue problem.

The next objective of the thesis was to perform a numerical study, describing the CFD problem, and how it can be utilized to compare the physical experiments. This chapter leads to an explanation of numerical simulations performed in PVC3D and employed in connection with the radiation experiments carried out on a two moonpool geometry with different properties.

The second set of experiments were done regarding a spring moored freely-floating section with same geometrical properties as before.

My contributions to the field are presented in Chapter 5. Here, the results from the numerical study, the forced piston mode of motion and the freely-floating experiments are displayed. First, a comparison between numerical and forced oscillation model test are shown. Overall satisfactory results are obtained, with an exception for the lowest forced pitch motion with draft equal to 20cm and the two lowest pitch motions for draft equal to 15cm.

Further, the experiments were found to be in compliance with theory and the literature of the similar field. The parameter study displayed that the round inlet corners had the highest resonance peaks which occurred for lower periods than the other configurations with geometrical singularities present. These trends correspond to the larger damping effects from shed vortices introduced with geometrical singularities, while the appearance of the natural periods is related to effective moonpool draft. This finding is in compliance with the draft comparison, where a smaller draft gave rise to lower natural periods. Another effect was that the low draft configuration resulted in higher RAO peaks. The forced motion amplitude shows linear relation for rounded corners and non-linear effects for the other settings.

Same tendencies are observed from the freely-floating experiments and the experiments of the low inertia structure, following findings are made. Comparison of the radiation problem and the freely-floating experiment display that no resonant water motions occurs for the piston-mode resonance frequency. Here, the radiation- and diffraction potential cancels each other out. This is apparent in both the have and the pitch RAO.

Further, the heave and pitch RAOs experience cancellation for particular incoming wave periods, which is related to the pressure- and flow field between the moonpools and the rigid-body motion of the structure. The moonpool device can be thought of as an integrated anti-pitch tank, having cancellation effects on the heave and the pitch resonance motions when they are 90 degrees out of phase with the moonpool water elevations. The bridge floaters are believed to exert advantageous pitch cancellation properties in a given range of the incoming ocean swells.

6.1 Future Work

Even though a great effort have been made to explore the hydrodynamics of a double moonpool section, further studies should be done regarding both the numerical and the experimental processes.

The first proposal is to carry out a mesh convergence- and sensitivity analysis for the forced motion experiment. The attempt should be to adequately capture the phenomenon around the inlet corners of the moonpool. This is believed to improve the precision of the numerical study for the smallest amplitudes of the forced motion experiments.

The same lines can be drawn regarding the numerical studies of the freely-floating model, and the results of the resonance periods are believed to improve through a convergence- and sensitivity study.

Further, a parameter study regarding the eigenvalue problem is something that should be further looked into, and an inspection of this problem will be conducted during July 2016.

As for the applicability of the findings, several other studies are needed before the moonpool design can be utilized as supports for a floating suspension bridge. Further studies should include 3D parametrization of the 2D results of the present work. Secondly, a 3D model must be investigated with regards to the 3D flow effects. Also, cancellation periods of the system should be tuned to match the metocean data proposed by Multiconsult. It is believed that a parametric study of the draft and moonpool gap sizes can be utilized in this process, and hence should be performed.

The last suggestion is to investigate the possible benefits of installing an anti-pitch tank on top of the bridge floaters. This device will work 90^o out of phase of the resonance periods in pitch.

Appendix A

Graphs from Forced Motion Experiments

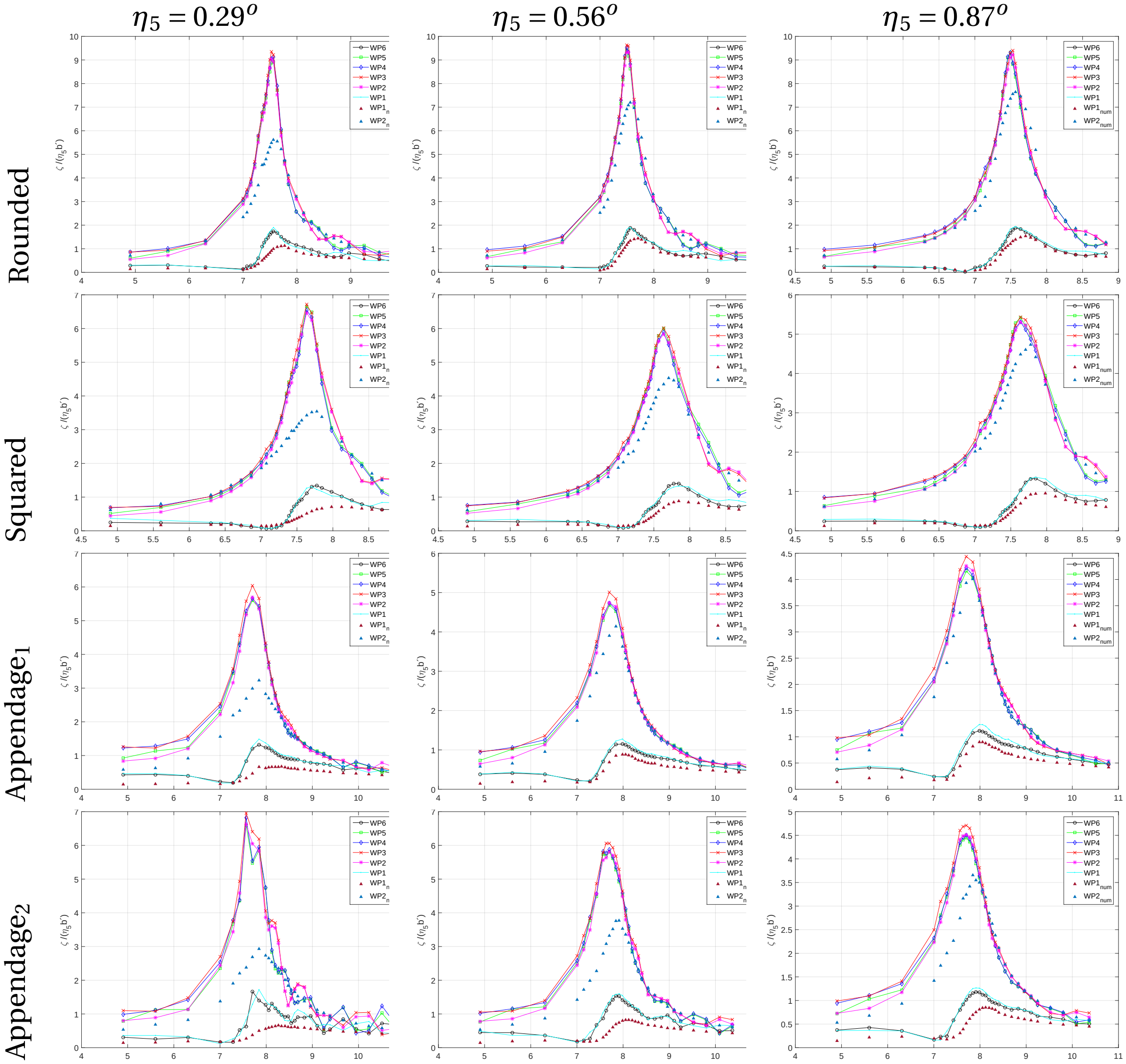

Figure A.1: Forced pitch motion tests for 15cm draft geoemtry. The columns display respectively forced motion amplitudes $\eta_5 = 0.29^o$,$\eta_5 = 0.56^o$ and $\eta_5 = 0.87^o$, while the rows shows the different inlet configurations. Scatter are numerics. The lower lines/scatter(turquoise, black and burgundy) are the outside wave probes. $T* = T\sqrt{\frac{g}{b}}$

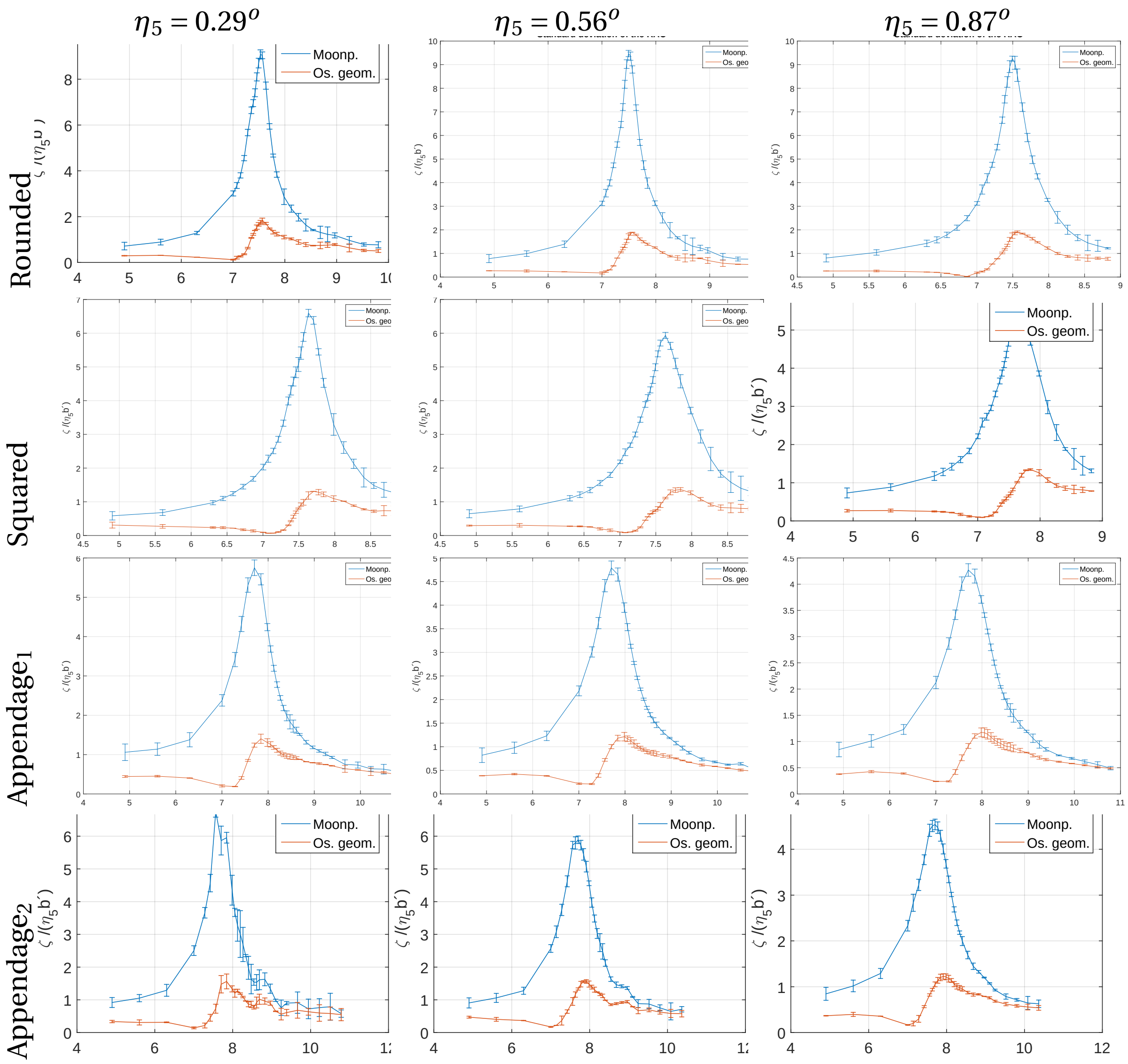

Figure A.2: The corresponding standard deviation of the RAO display in figure A.1. $T^* = T\sqrt{\frac{g}{b}}$.

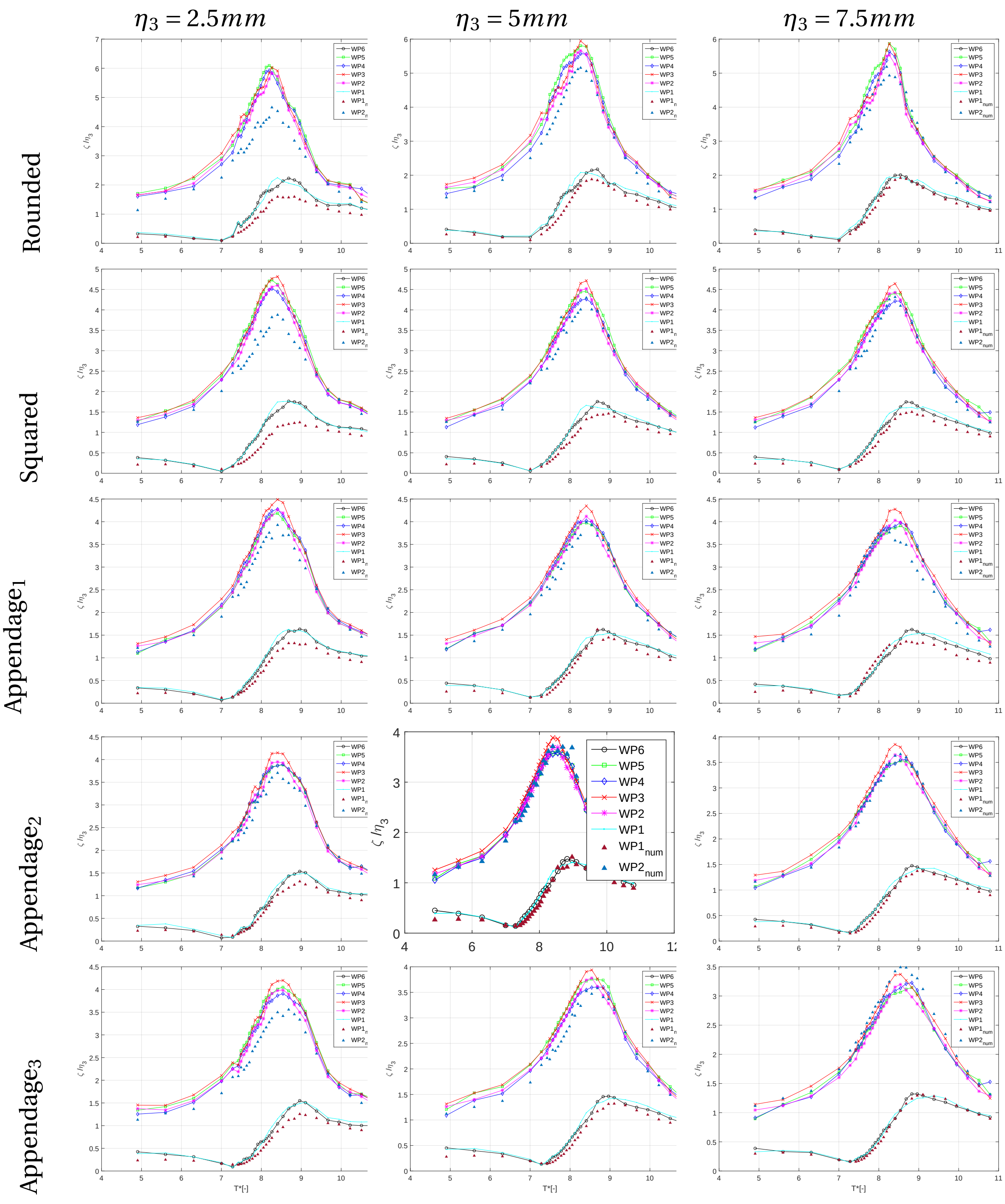

Figure A.3: Forced heave motion experiments for 15 cm draft geometry. The columns display respectively forced motion amplitudes $\eta_3^* = 2.5mm$,$\eta_3^* = 5mm$ and $\eta_3^* = 7.5mm$, while the rows shows the different inlet configurations. The experimental results are display as lines while numerical RAO's are given as triangular scatter. The lower lines/scatter(turquoise, black and burgundy) are the outside wave probes. $T* = T\sqrt{\frac{g}{b}}$

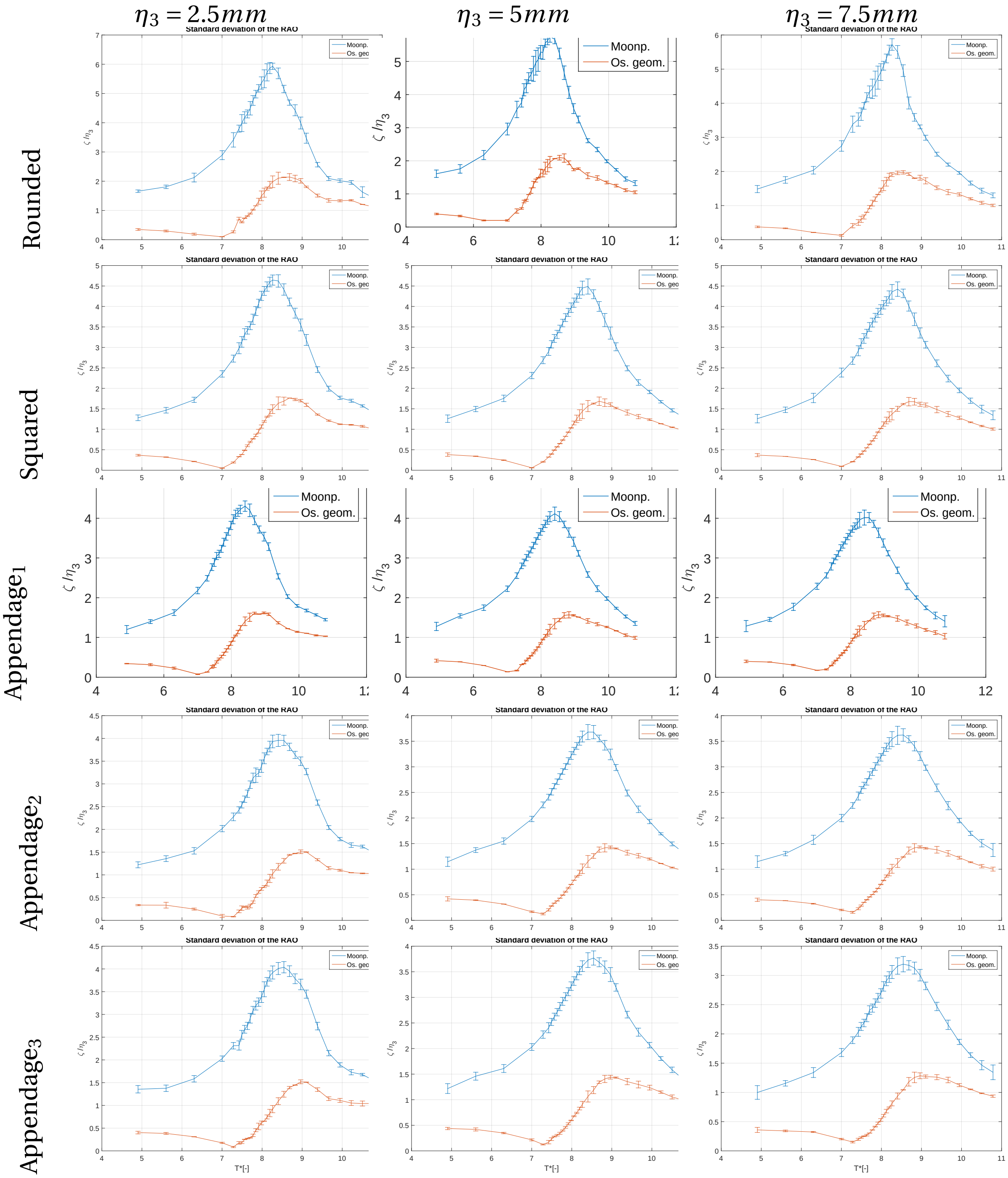

Figure A.4: The corresponding standard deviation of RAO's displayed in graph A.3, $T^* = T\sqrt{\frac{g}{b}}$.

Appendix B

MATLAB Program

This appendix aims to describe design of the post-processing MATLAB program.

The ultimate goal was to output the hydrodynamics of the moonpool geometry through different graphs representing both numerical and experimental tests. The result could for instance be RAO's of wave height inside moonpool, RAO's of geometry motions, undamped eigenperiods in three dofs, added mass and potential damping coefficients or time series.

Initially, every experiment had its own ID representing that specific case. Both the text file, containing test properties, and the experimental results were stored with this ID name, respectively in a .txt- and .bin-file. Different from the physical experiments, where all the results from 30 oscillation periods were stored in the same .bin file, were the results obtained from numerical simulations split into 30 different results folders for each oscillation period. For instance, for experiment ID 1030, were the physical results stored in 1030.bin, while the numerical experiments were stored in files containing both ID and oscillation period, i.e. 1030T0700...1030T1460.

The MATLAB post-processing procedure started by running a pre-analysis script, "a1_ pre_ run.m", where the user defined which experiment to be analyzed. It was also possible to define more than one experiment, so that several analyses could be performed without any new user input. Next, the user had to define what kind of experiment it was(forced oscillation, freely floating or hydrodynamic properties).

The next step was to run the main script, "a2_ run.m". Firstly, all global constant were defined. Then the program started to run through all the user-given experiments by opening the text-file and the .bin-file. Next, it navigated to the appropriate post-processing scripts, which are further explained in the following sections.

Lastly, the main-program visualize the results from the post-processing by entering the "plot_graphs.m" script. The structural layout is display in figure B.1.

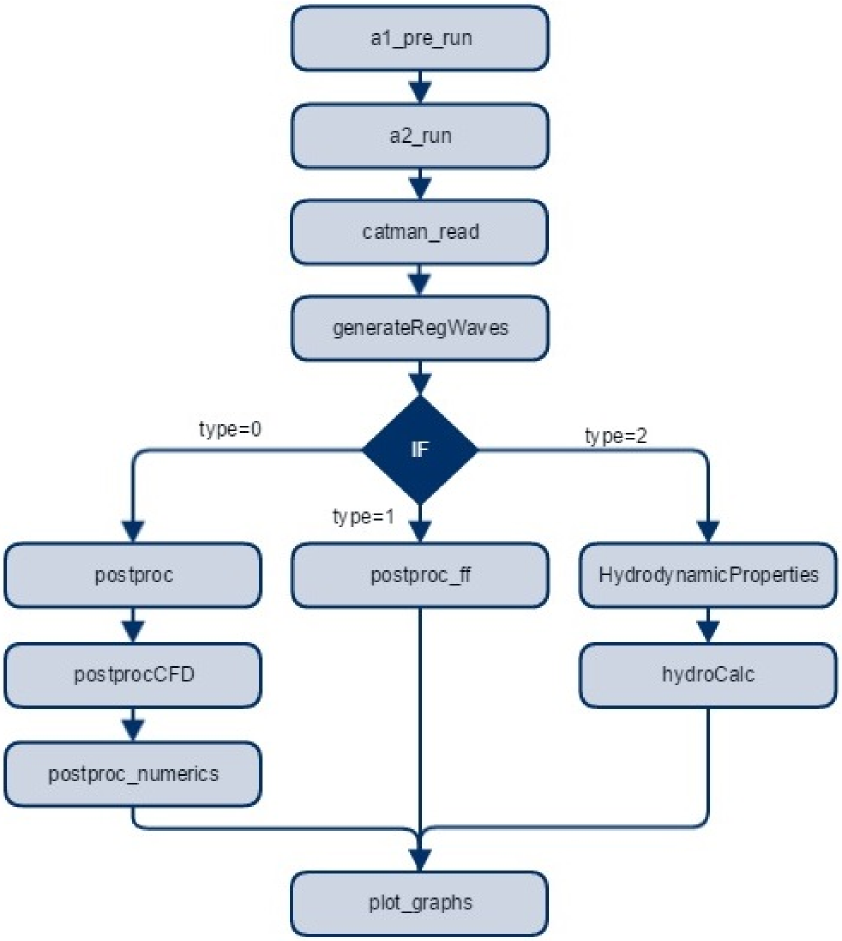

Figure B.1: An overview of the MATLAB program designed to post-process both numerical and experimental model tests.

B.1 Layout for Numerical Simulations and Forced Oscillation Experiments

The first type of post-processing application was forced oscillation experiments. Since these results should be used to verify the numerical simulations, results from the CFD-analyses were also included.

After the specific .txt- and .bin-file was opened, the program executed the "postproc.m" script. Here, it started the procedure of post-processing data from the experiment based on the theory presented in chapter 4.3. First, it stored the raw data time series of the wave heights for the thirty different oscillation periods into a structure. The final structure contained thirty different entries of each wave probe where all the Wave probes consisted of a vector with the sampling data for the specific period of the experiment.

The relevant wave probes, i.e. those mounted on the geometry, was then modified to measure the Earth-fixed wave elevation by entering a function called "motionfunc.m".

Once all the wave probe measurements were properly stored and transformed, a filtering procedure was performed following the instructions given in chapter 4.3.

Next, the evaluated interval of the time series were picked based on the theory regarding beating periods. This was done through the function "oscillatioint.m". Thus, the remaining vectors consisted of smooth harmonic oscillations, with approximately constant oscillation amplitude, which were the basis for calculating the wave elevation and geometry displacement. These properties were found through "findAverageHeight.m".

From the resulting wave elevation and geometry motion, the RAO, phases and standard deviations for the different oscillation periods were calculated. This was done in compliance with theory presented in section 4.4. An additional feature for geometry with rounded inlet was the determination of KC-number.

Also, if the user defined visualization of time series in the the pre program, this was at the end of this subroutine.

At this point, the program had calculated results regarding the physical experiments. Now, it started post-processing the results from the numerical simulations, which took place in subroutine "postproCFD.m". First, the script navigated to the directory containing the results from all the numerical simulations. Here it compared the input file ID, given by the user with the corresponding numerical simulations. Once these folders were located it started to collect and store the output data from each of the thirty oscillation period folders into a MATLAB structure equal to the one explained in preceding paragraph.

From this subroutine, the program entered a new one, "postproc_ numerics.m" where the same post-processing procedures as for the physical experiment were performed except that all the numerical wave probes were employed an Earth-fixed coordinate system and did not need to be transformed in "motionfunc.m".

Lastly, results from both the physical and numerical experiments were processed and could be visualized in the same graph. This was done in "plot_ graphs.m" shown in figure B.2.

The subroutine design is displayed below.

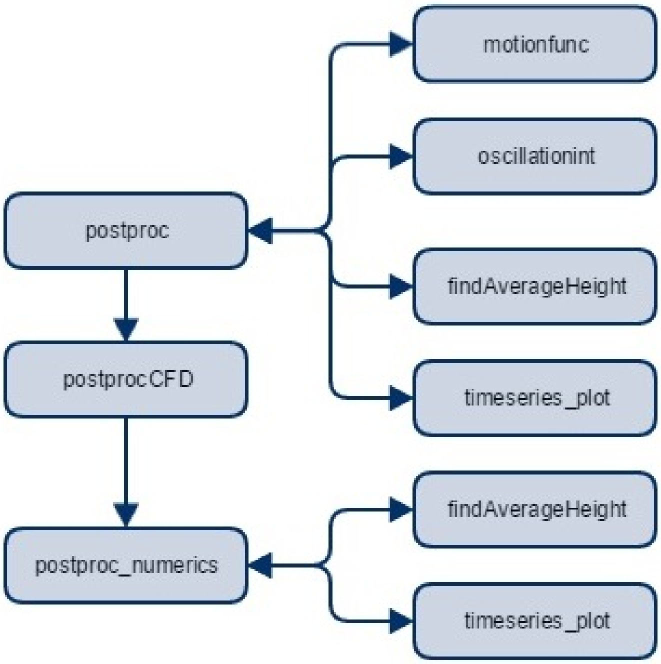

Figure B.2: Subroutine structure over forced oscillations

B.2 Layout for Freely Floating Experiments

The second type of experiments were the freely-floating structure exposed for incoming waves. Because of the different nature of these tests, it was decided to create an add on to the post-processing program, type= 1 in figure B.1.

After the intial pre programs it entered the "postporc_ ff.m" subroutine and started to analyze the experiments. First, a new set of constant relevant for these tests were defined. Next, the start point of the time series was to be determined. Different for the forced tests, where the motions responded almost immediately to the oscillator movement, the motions for these experiments was dependent on when the incoming waves reached the certain point in the wave tank. In figure 4.6b the different distances in the wave tank are given. It is observed that wave probe 1 is located near the wavemaker. Besides measuring the wave height from the wavemaker it also worked as a trigger for recordings. Once, the wave probe measured that the wave height started to fluctuate around the still water level the MATLAB program started to record the time series. Since the geometry was located 5m further down stream, a recording time lag was required for the measurement at the geometry. The time lag was calculated through linear wave theory, covered in chapter 2.8. The mentioned procedure took place in the function "startWaveGen.m".

Next up were a similar filtering and evaluation interval procedure as in the forced oscillation-subroutine. After the representative time series were carefully selected, calculations of geometry motions and wave heights could be done. The foundation of the motion theory is further described in chapter 4.4. The amplitudes needed for the different RAO's was again calculated through "findAverageHeigth.m" and the phase angles between geometry motion and incoming waves was determined through the "findphase.m" function.

Once all these properties were determined, it could be visualized in the global "plot_ graphs.m" subroutine.

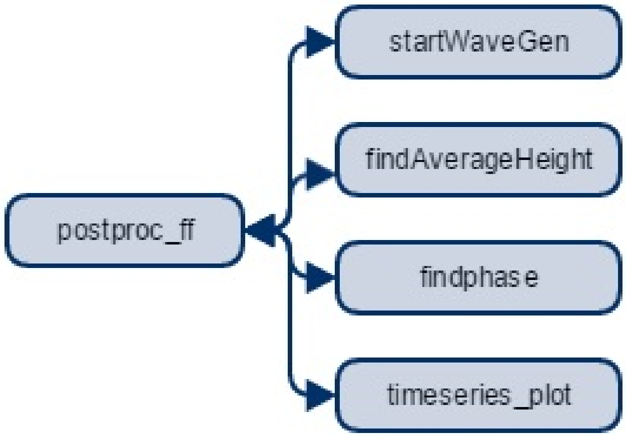

Figure B.3: An overview of the post-processing structure for the freely floating experiments.

B.3 Layout for the Eigenperiod Problem

The eigenperiod calculation subroutine was the last attribute added to the MATLAB program. This script determined the eigenperiods of the three dof system by solving the determinant of coupled equation of motion. Since the added mass coefficients are highly frequency dependent, this had to be done for every single period of the thirty different oscillation periods.

The analysis required added mass coefficients from three different forced oscillation tests, respectively the separate simulations of forced oscillations in surge, heave and pitch. The calculation procedure of the added mass and potential damping coefficient is further described in chapter 4.4.4, and was the foundation of the subroutine "hydrodynamicProperties.m".

The subroutine was designed in following manner. First, the script was directed to the case folder and compared the file ID with the folder names. Once the corresponding folder was located, it opened each of the thirty oscillation periods, and collected the force and time output for the specific case. This information was used to determine the added mass and damping coefficients for the specific frequency, and was calculated in the "forceIntegration.m" function. This was repeated for all thirty periods in surge, heave and pitch.

Next, the program entered another subroutine "hydroCalc.m" Here, the rest of the matrices included in the undamped equation of motion were defined, i.e. mass and stiffness matrix.

Now, the program calculated the cubic eigenvalue problem which occurs from the determinant of the 3x3-matrix system. This was done for all thirty periods and performed by the "determinanttest.m" function.

Lastly, the output were visualized in the "plot_ graphs.m" subroutine.

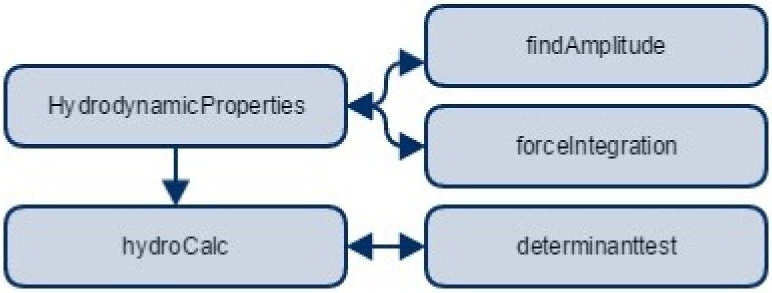

Figure B.4: An overview of the eigenperiod subroutine.

Appendix C

OpenFOAM

For the scope of this thesis, OpenFOAM and its extension, PVC3D, was the preferred software. OpenFOAM is a free open source CFD software developed primarily by OpenCFD Ltd. The software and its packages are written in C++ and runs on Linux operating system, which gives it a wide range of solvers, utilities and libraries. The advantage with OpenFOAM is the ease of customizing own solvers.

In addition to the solver, OpenFOAM is supplied with pre-and post-processing environment displayed in figure C.1.

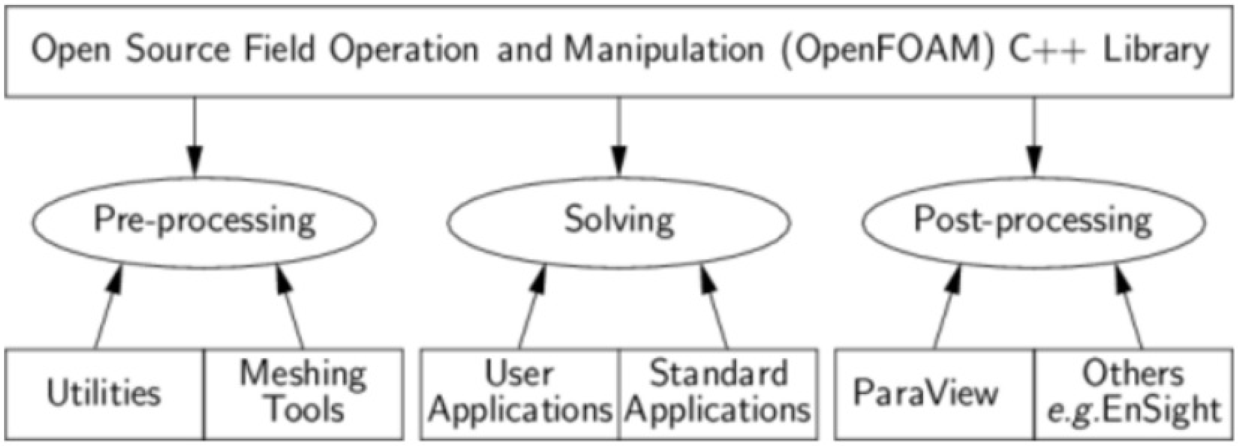

Figure C.1: Overview of OpenFOAM structure (OF).

C.1 Pre-processing

In order to run an application in OpenFOAM, it requires a minimum set of inputs arranged in directories and sub-directories, figure C.2. The "case" parent folder contains three sub-directories: 0, constant and system. Inside the 0 folder are all the initial field condition regarding velocities and pressure at the boundaries. The constant folder includes information regarding the fluid- and turbulence-properties. It also contains a sub-directory specifying the geometry and the mesh. Also, a system directory with parameters associated with the solutions procedure is included. This yields the solver and solution scheme, start and end time, time step and tolerances for implicit schemes. In addition, as the application runs, multiple of time step folders are created containing field solutions for fixed iteration intervals.

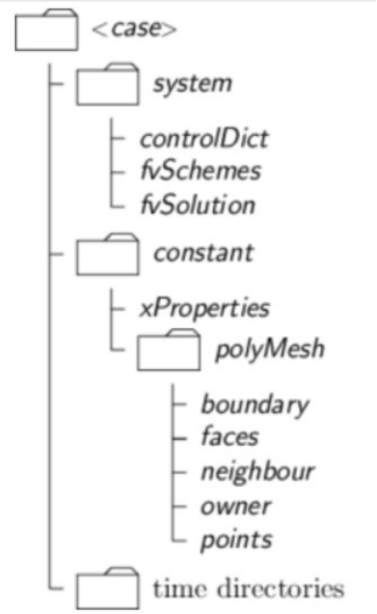

Figure C.2: Case directory structure in OpenFOAM (OF2).

C.1.1 System Directory

The system directory contains four essential files regarding the solution procedure: ControlDict, fvSchemes, fvSolution and SampleDict.

In the ControlDict file the user is able to input the solver(further explained in ch. 3.3.1), time step, start and end time for the simulations and the measurement functions calculating the output of the simulations. The relevant output functions applied in this project was forces on the hull and six wave probes located inside the moonpool or in the surroundings of the geometry. Their placement corresponds with the wave probe locations for the forced experiments, discussed in chapter 4.

For the simulations it was desirable to run 25 oscillation for each specific case. The start time was always 0, and the end time was dynamically changed for each specific forced oscillation period, ranging from 0.7s-1.54s. As an example, for an oscillation period of 0.7s the simulations ran for $0.7s \cdot 25 = 17.5s$. The procedure of changing the input parameters are further explained in chapter C.2. Next, an adjustable time step was implemented, restricted by the CFL-number.

The numerical schemes applied for the simulations are displayed in table C.1.

Table C.1: The numerical solutions schemes

Property	**Numerical Schemes**
Time scheme	Euler, Backward Euler
Gradient	Gauss linear
Divergence	Gauls linear, Gauss upwind
Laplacian scheme	Gauss linear
Interpolation scheme	linear

The numerical schemes for time differentiation is by default an implicit forward Euler method. As we shall see in chapter 3.3.1 is the fluid domain divided into a potential domain and an interior domain. For the potential domain, covering the free-surface waves, a second order implicit backward Euler schemes is utilized.

Since the solution schemes are of implicit type, the sparse matrix solvers are iterative. In other words, the residual of the solution is evaluated by substituting the current solution into the equation and taking the magnitude of the difference between the left and the right hand side and compared against the tolerance determined by the user in fvsolution. The tolerance in this thesis was set to 10^{-7}. The iteration stop if:

- the residual falls below the solver tolerance
- the ratio to initial residuals falls below the solver relative tolerance
- the number of iterations exceeds a maximum number of iterations

C.1.2 Constant Directory

The fluid properties included in the constant directory are summarized in table C.2.

Table C.2: The fluid properties

Property	**Value**
Gravitation$[m/s^2]$	9.81
Kinematic Viscosity$[m^2/s]$	10^{-6}
Turbulence model	Laminar
Motion dictionary	Follows motion given in 0-folder

The second content was the polyMesh folder containing all the geometrical properties of the fluid domain. The creation of the polyMesh folder is further explained in chapter 4.

Time Directories

The time directories initially consists only of one sub-folder, the 0-file, that contains the properties of the fluid domain at initial state. Here, the user must specify the initial conditions at the boundaries regarding the pressure field, p, and the velocity field, U. For the numerical case inspected in present work, a free surface initial condition file was also included. The structure and layout of these files are displayed in appendix ...

C.2 Dynamic Pre-processing Code

It was planned to execute over 1800 numerical simulations. Manually changing the properties for each case was not time efficient, hence a MATLAB program producing all the different variation were implemented.

The changeable variables included 30 different oscillation periods, three oscillation amplitudes, two degrees of freedom, five inlet geometries and two drafts. Information for each specific case was stored inside text files in advance of the simulations. Here, all 30 oscillation periods were included in each file, reducing the numbers of text files from 1800 to 60.

Next, a template folder was made. This folder consisted of all directories and files needed to run the OpenFOAM application, i.e. system-, constant- and 0-folder. The only difference between the template folder and an executable case directory, was that the variable inputs inside the template consisted of dummy variables which were changed before each simulation. An example of such variable is the time duration of each case, which is given as an input in the controlDict file. As earlier mentioned, this variable was different for each of the thirty oscillation periods. Instead of changing it manually, a dummy variable was introduced in the template: __endTime__.

The dummy variable worked as an ID for the MATLAB program, such that it knew where it should swap the dummy variable with the for instance calculated end-time for the specific case.

Since the underwater geometry of the moonpool geometry depended on moonpool inlet corners and draft, it was necessary to manually create ten different meshes reflecting all the different combinations of draft and corners.

Once the meshes, text files and template directory were made, the process of constructing the MATLAB program started. The schematically layout and flow chart of the program are display in figure C.3. The step wise explanation is given below:

1. The script navigates to the text-file folder and count the number of text-files inside
2. It then runs through one text-file at a time, collecting the information regarding degree of freedom, oscillation amplitude, mesh ID and a string with different oscillation periods.
3. The program will run through the oscillation periods. For each period it starts by calculating the forced motion amplitude, determined by measuring the amplitude from the .bin-files that corresponds to the specific physical experiment.
4. Furthermore it will create the case folder, named after the text-file name, oscillation period and oscillation amplitude, i.e. 1030T110A75 which corresponds to text-file 1030, oscillation period 1.1s and amplitude 7.5mm.
5. Next, the template directory and the mesh folder are imported into the case folder.
6. It now starts to change the dummy variables, respectively the frequency and oscillation amplitude in the U-file and the end-time, time step and the maximum time step in the controlDict-file.
7. Once the dummy variables are changed, the MATLAB program call OpenFOAM and it starts executing the simulation.

8. This procedure is repeated for all the periods and all different geometry configurations.

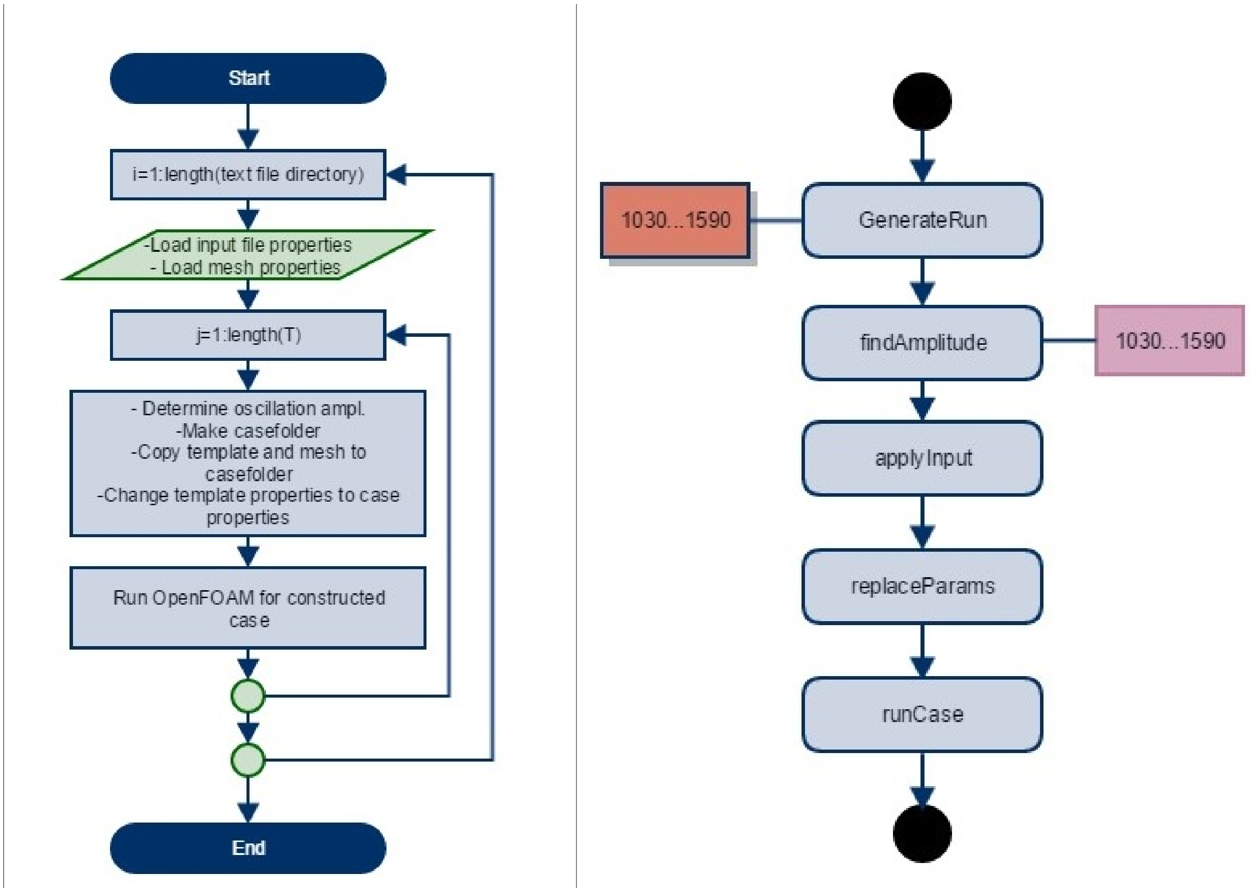

a_i b_i

Figure C.3: An overview of the program structure and the flow chart for the dynamic MATLAB code.

Appendix D

Experimental Graphs

D.1 Forced Motion Experiments

D.1.1 Rounded Inlet Corners in Heave

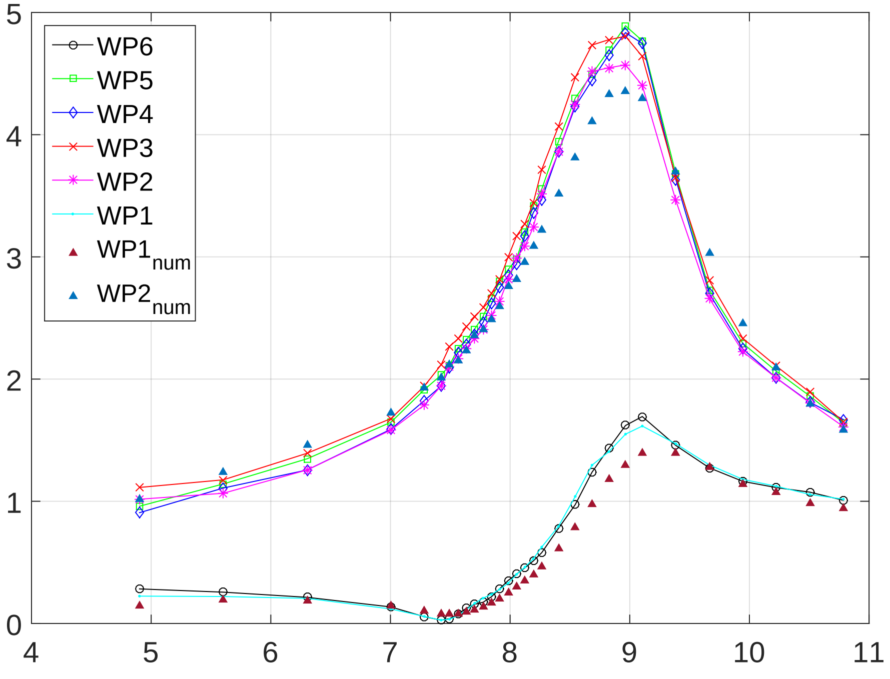

Figure D.1: Rounded inlets, $\eta_3 = 2.5mm$,dr=20cm

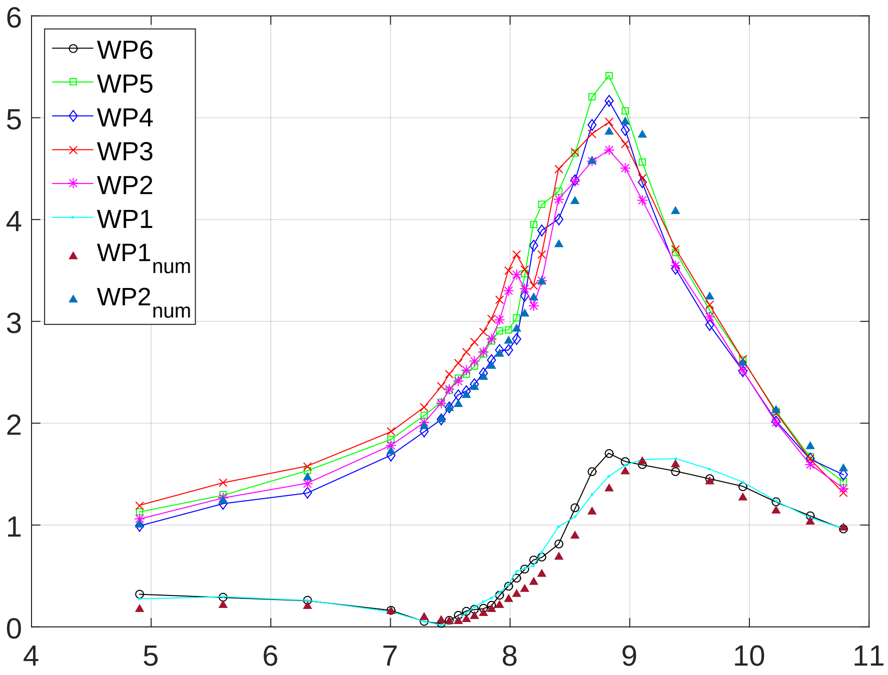

Figure D.2: Rounded inlets, $\eta_3 = 5mm$,dr=20cm

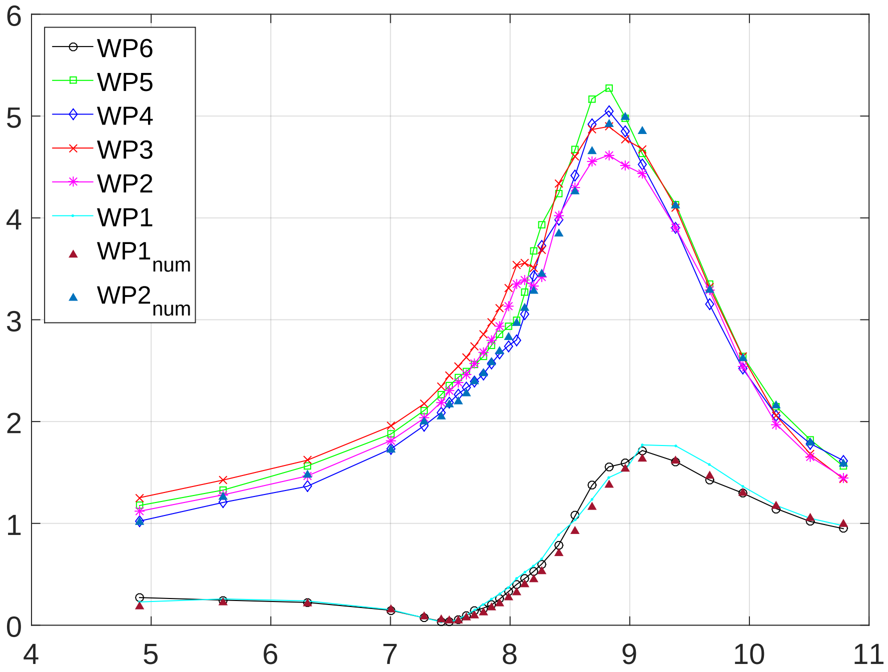

Figure D.3: Rounded inlets, $\eta_3 = 7.5mm$,dr=20cm

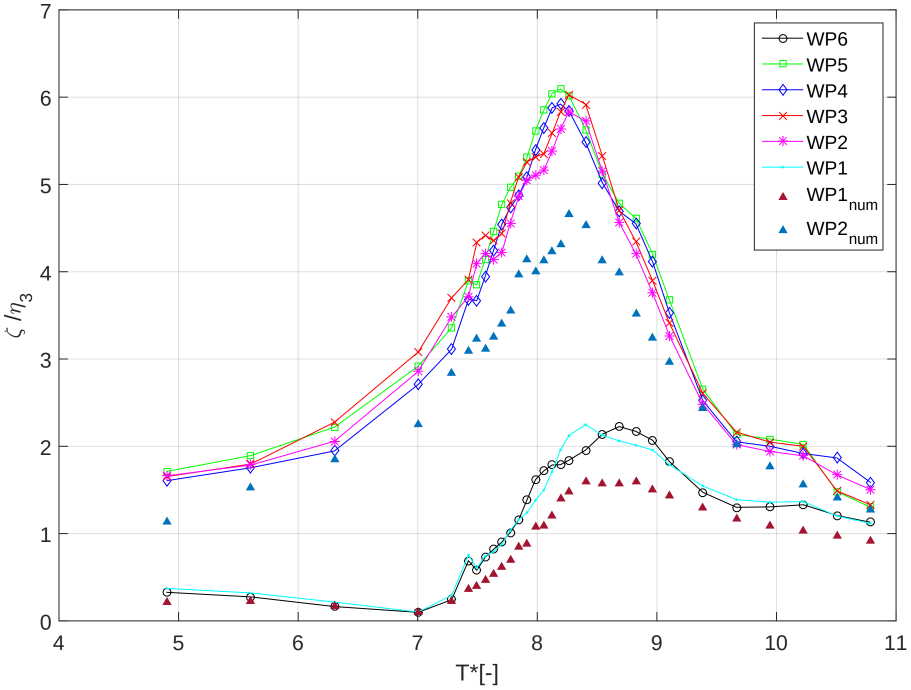

Figure D.4: Rounded inlets, $\eta_3 = 2.5mm$,dr=15cm

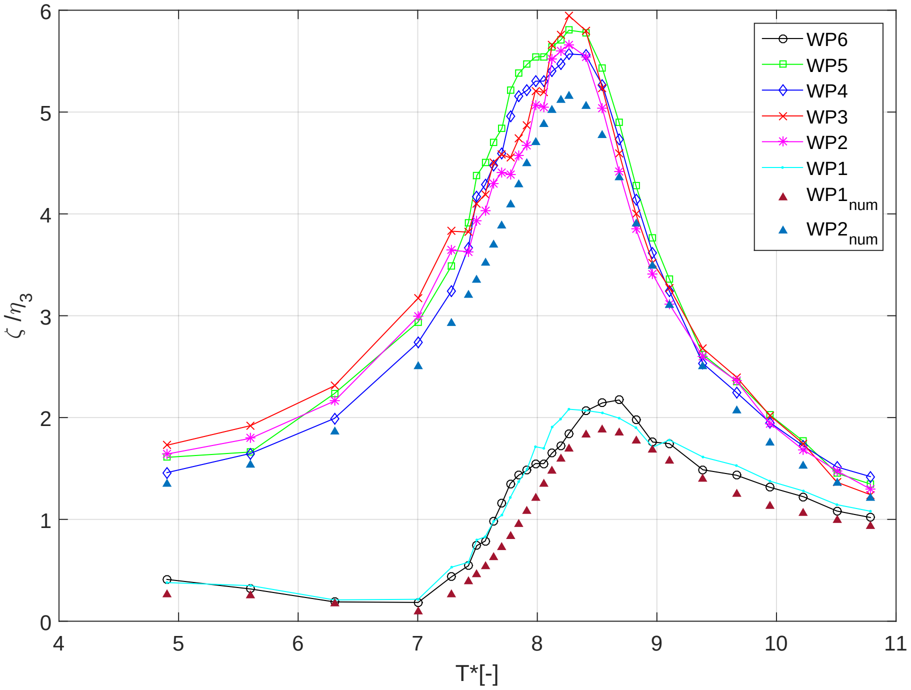

Figure D.5: Rounded inlets, $\eta_3 = 5mm$,dr=15cm

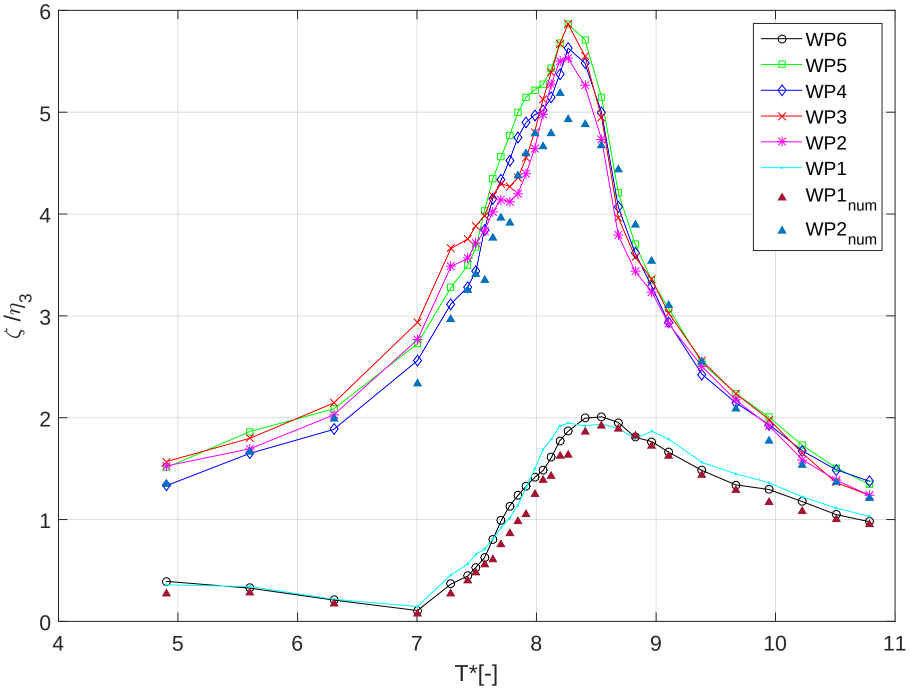

Figure D.6: Rounded inlets, $\eta_3 = 7.5mm$,dr=15cm

D.1.2 Squared Inlet Corners in Heave

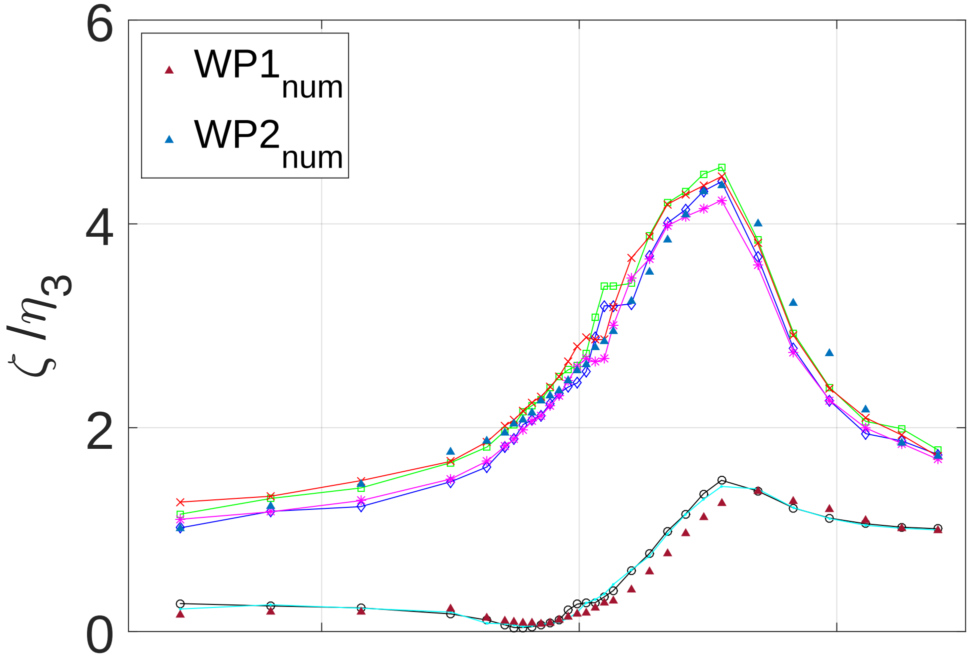

Figure D.7: Squared inlets, $\eta_3 = 2.5mm$,dr=20cm

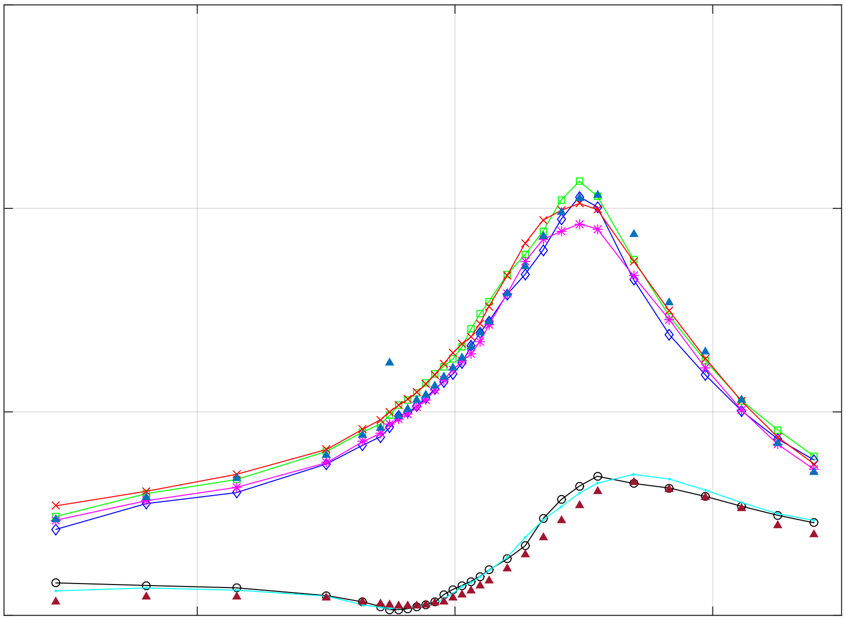

Figure D.8: Squared inlets, $\eta_3 = 5mm$,dr=20cm

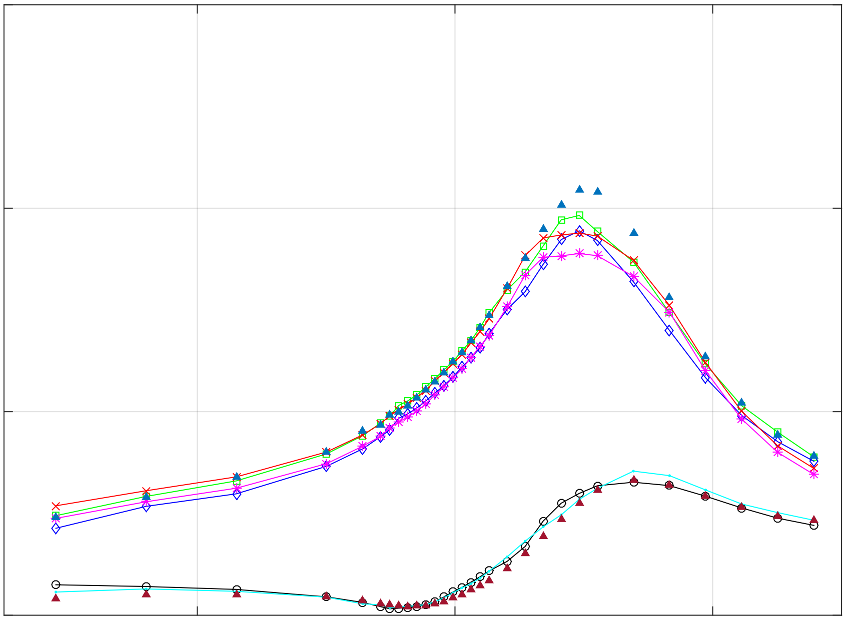

Figure D.9: Squared inlets, $\eta_3 = 7.5mm$,dr=20cm

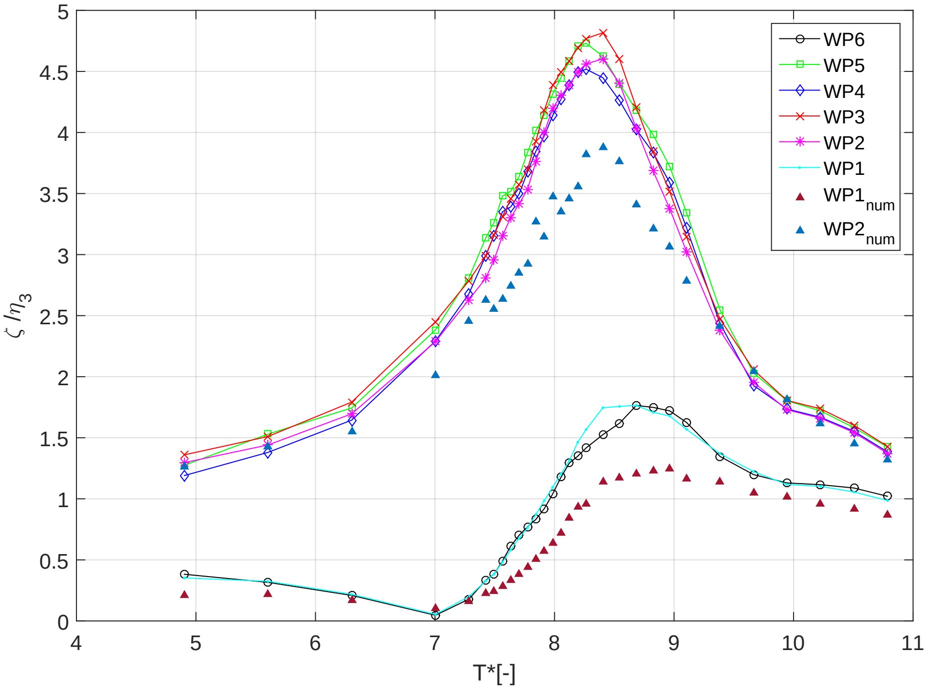

Figure D.10: Squared inlets, $\eta_3 = 2.5mm$,dr=15cm

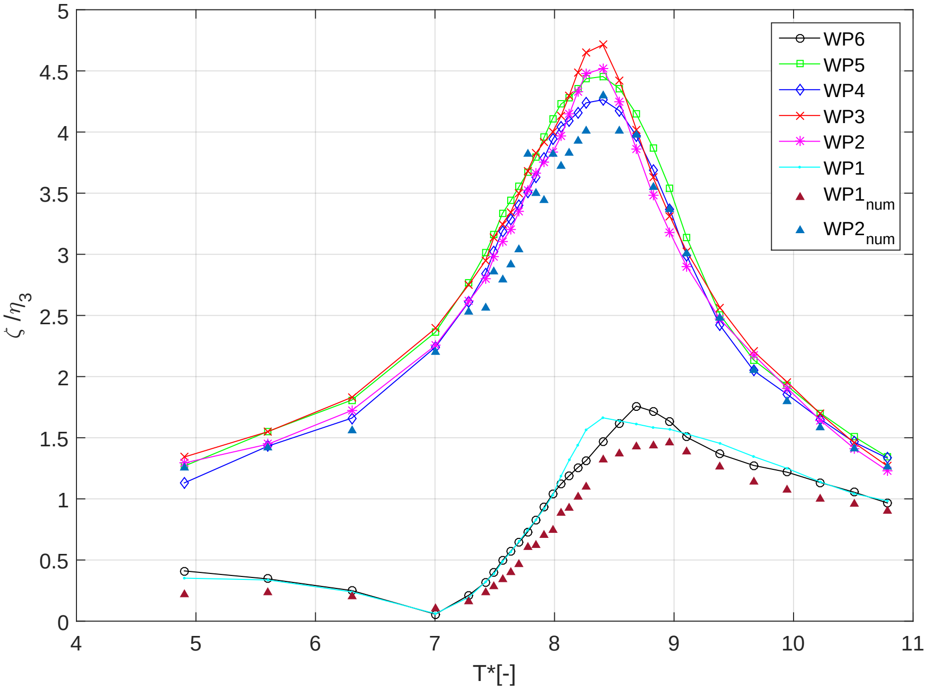

Figure D.11: Squared inlets, $\eta_3 = 5mm$,dr=15cm

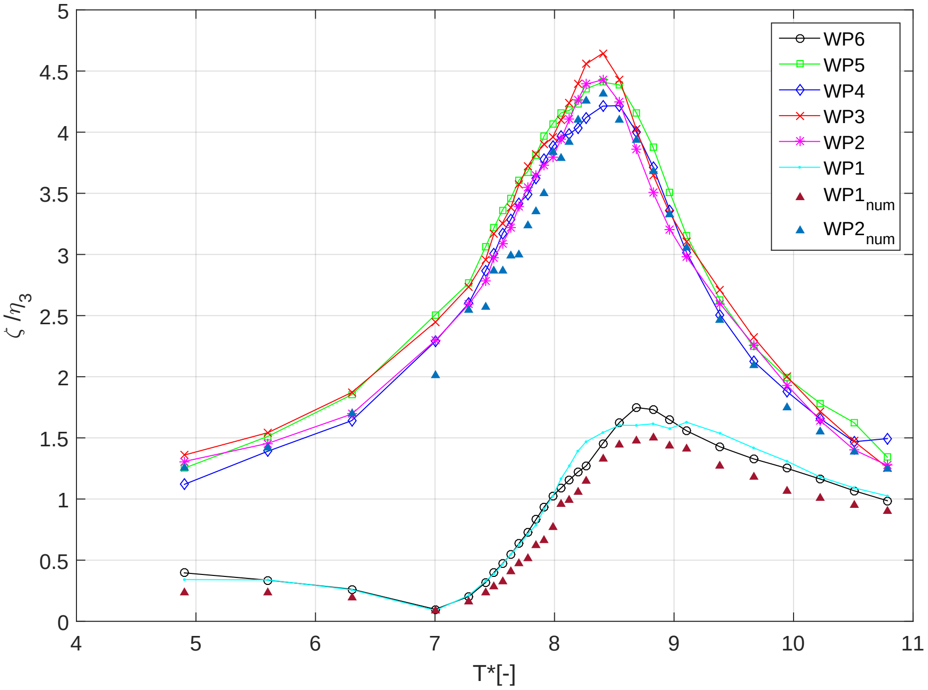

Figure D.12: Squared inlets, $\eta_3 = 7.5mm$,dr=15cm

D.1.3 Appended Inlet Corners in Heave

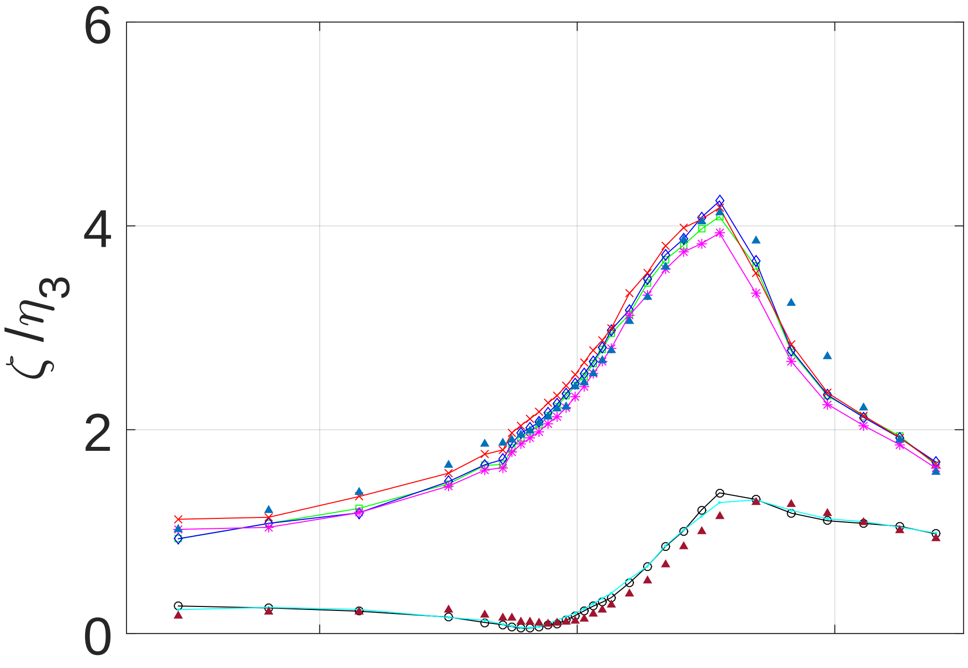

Figure D.13: App. 1 inlets, $\eta_3 = 2.5mm$,dr=20cm

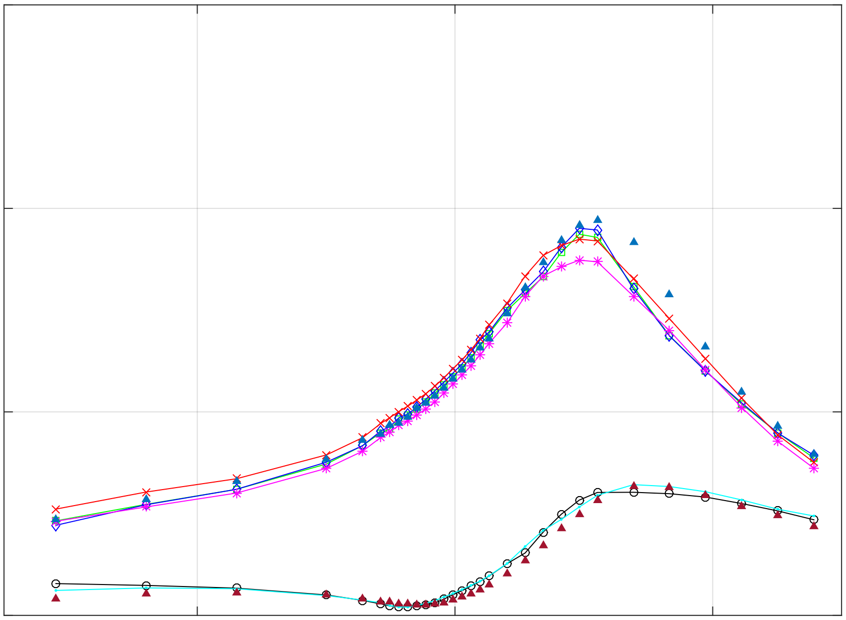

Figure D.14: App. 1 inlets, $\eta_3 = 5mm$,dr=20cm

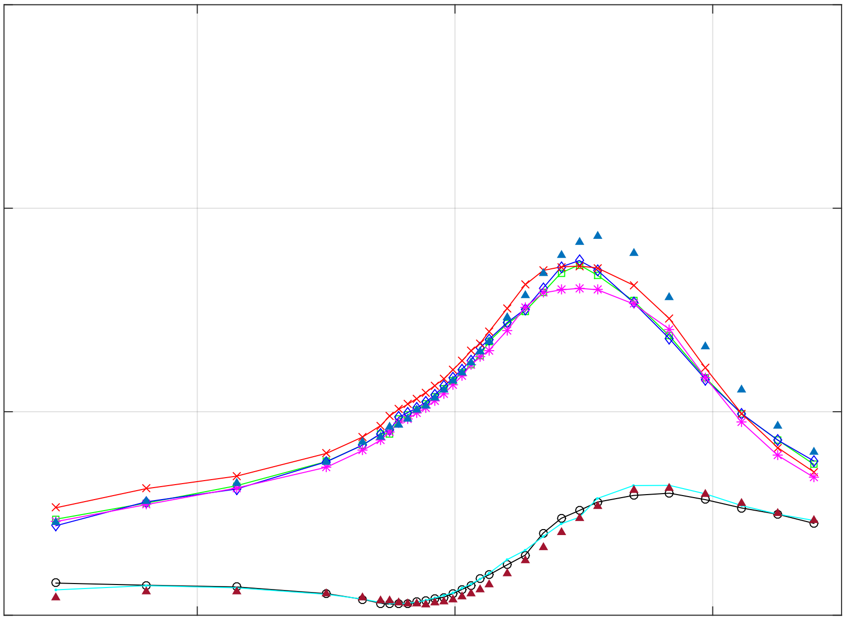

Figure D.15: App. 1 inlets, $\eta_3 = 7.5mm$,dr=20cm

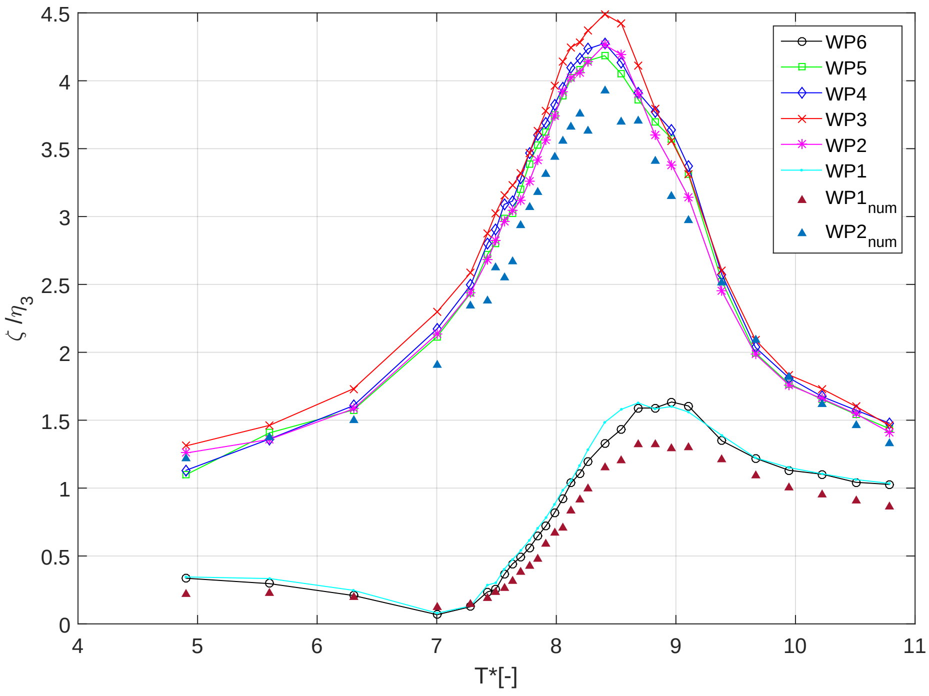

Figure D.16: App. 1 inlets, $\eta_3 = 2.5mm$,dr=15cm

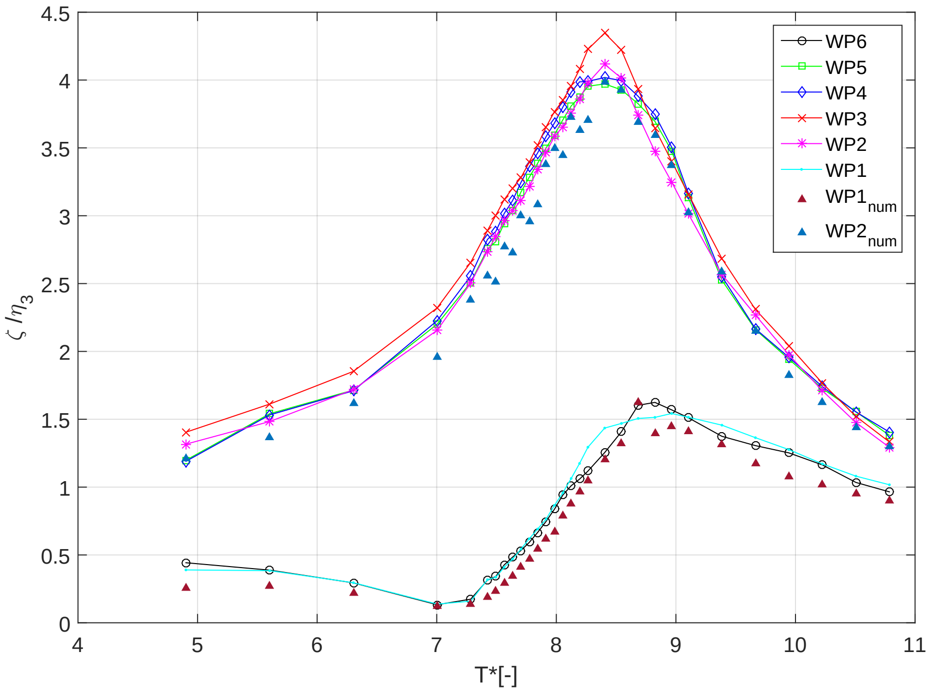

Figure D.17: App. 1 inlets, $\eta_3 = 5mm$,dr=15cm

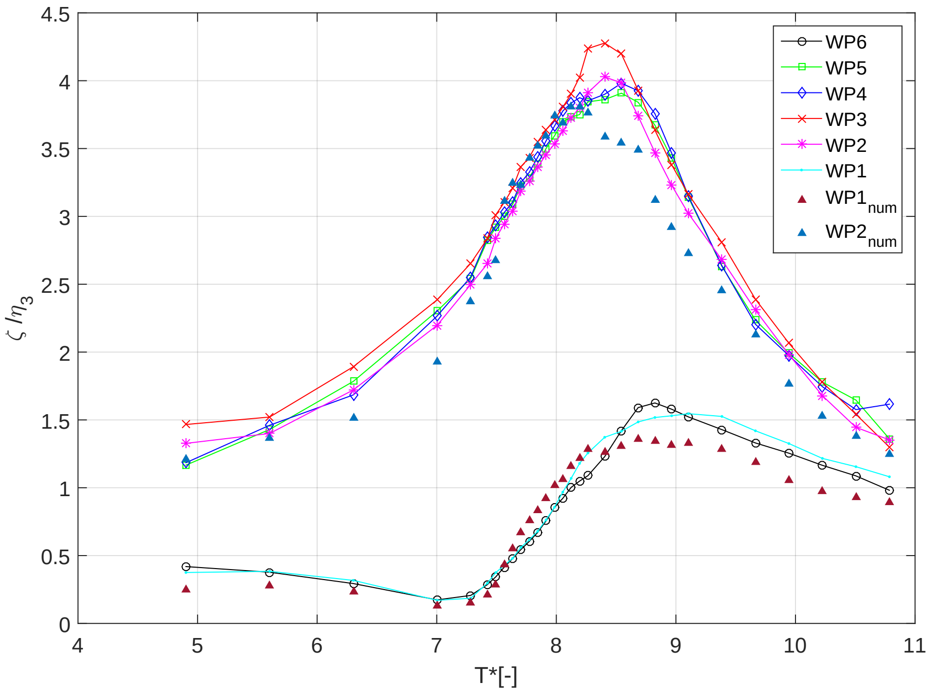

Figure D.18: App. 1 inlets, $\eta_3 = 7.5mm$,dr=15cm

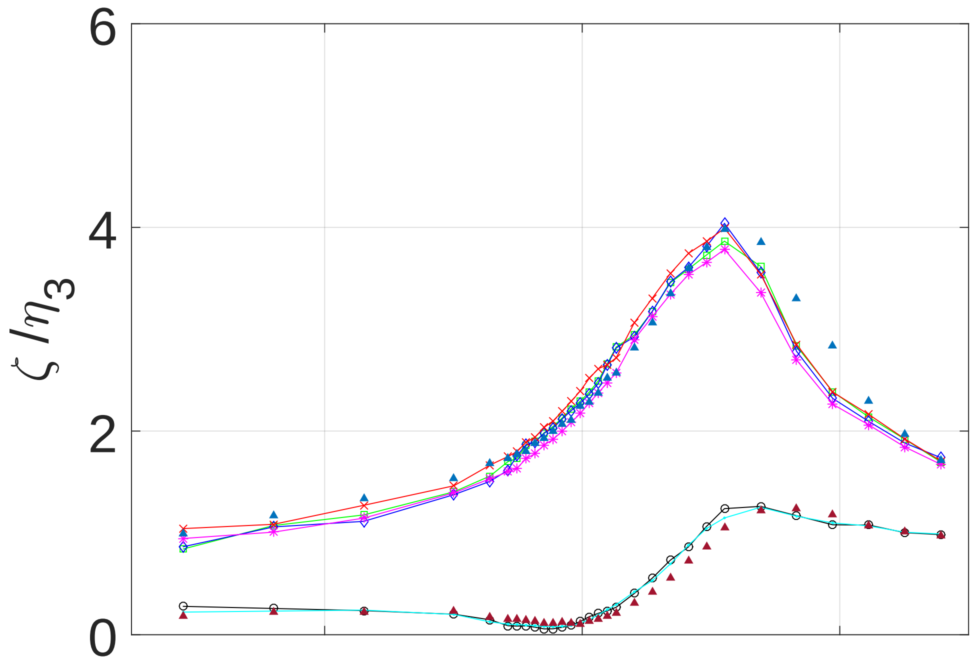

Figure D.19: App. 2 inlets, $\eta_3 = 2.5mm$,dr=20cm

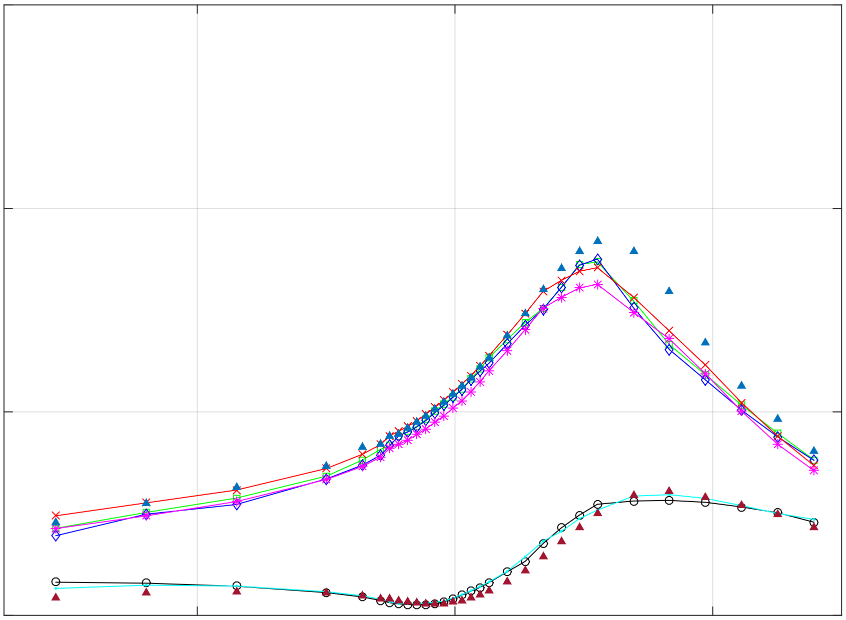

Figure D.20: App. 2 inlets, $\eta_3 = 5mm$,dr=20cm

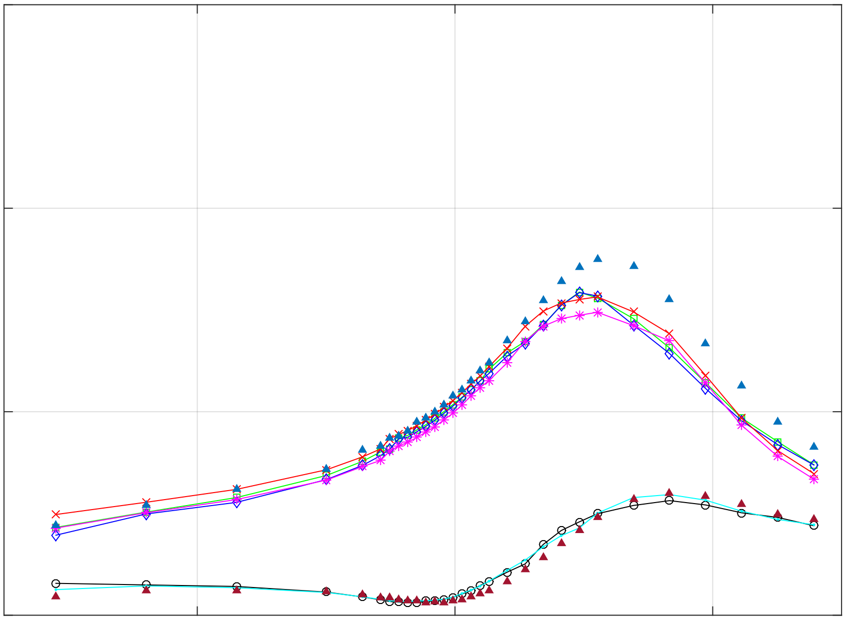

Figure D.21: App. 2 inlets, $\eta_3 = 7.5mm$,dr=20cm

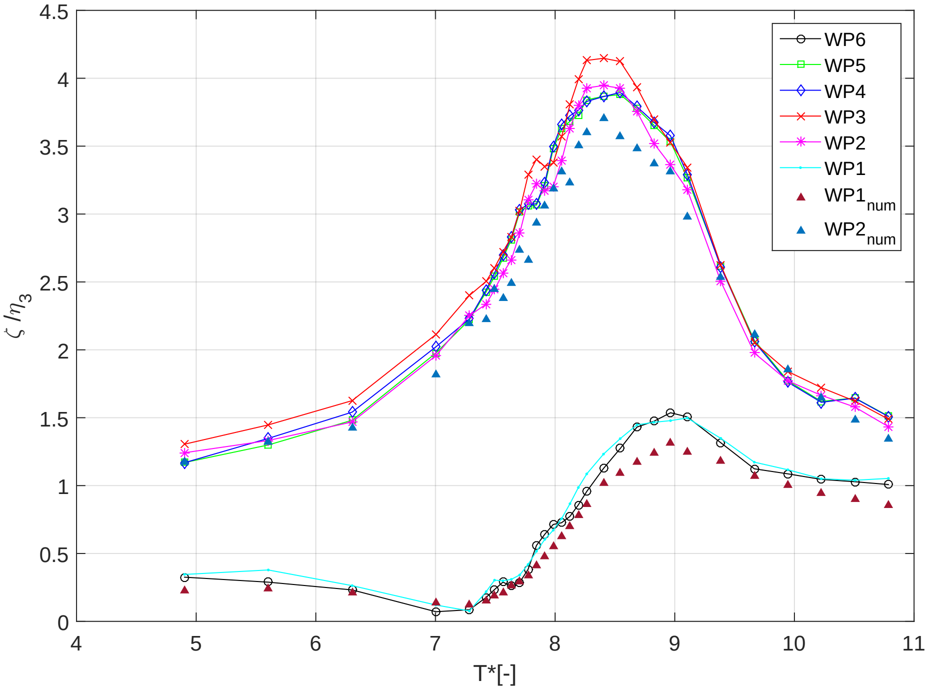

Figure D.22: App. 2 inlets, $\eta_3 = 2.5mm$,dr=15cm

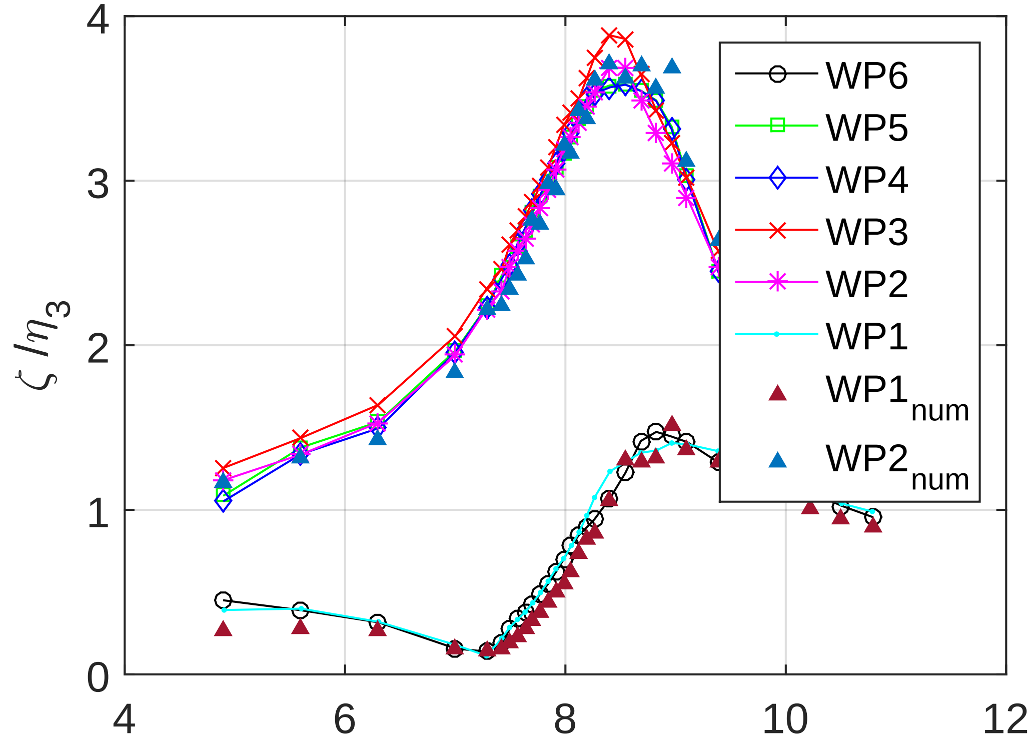

Figure D.23: App. 2 inlets, $\eta_3 = 5mm$,dr=15cm

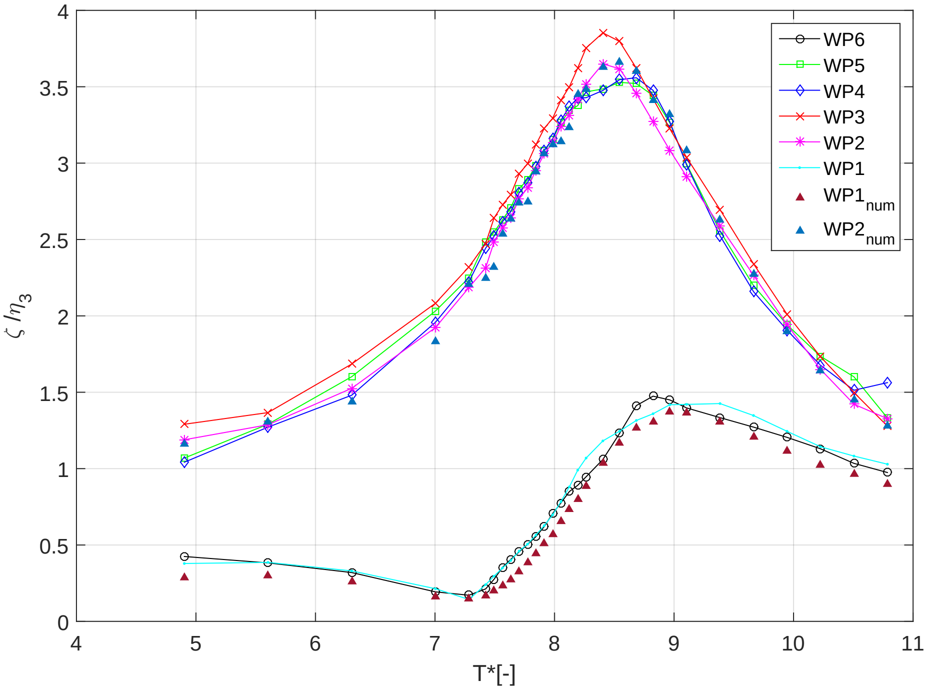

Figure D.24: App. 2 inlets, $\eta_3 = 7.5mm$,dr=15cm

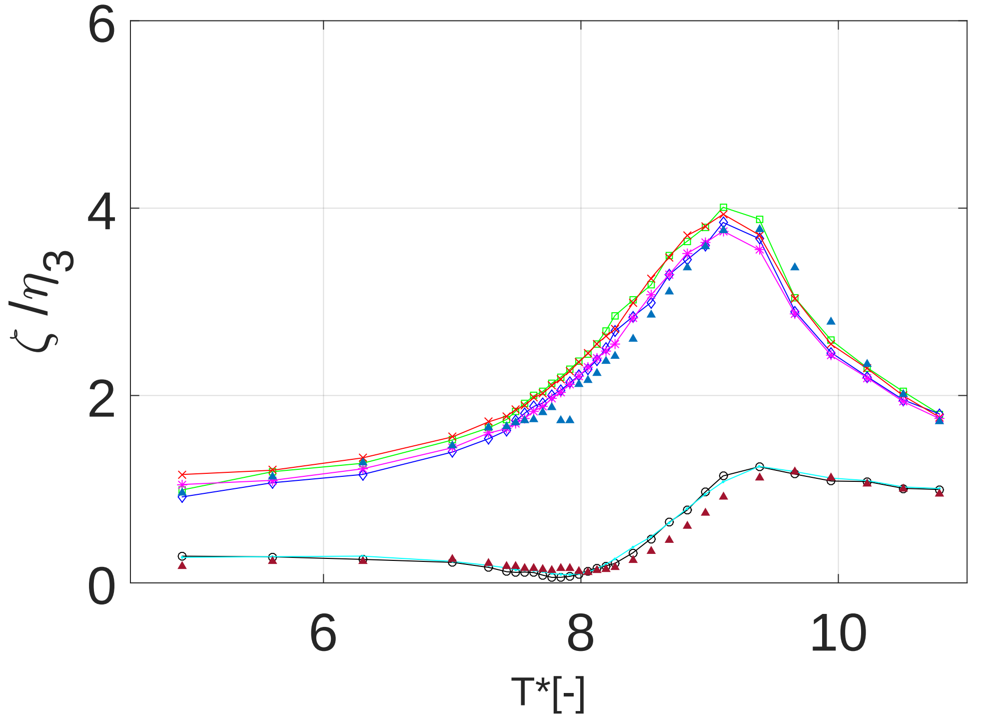

Figure D.25: App. 3 inlets, $\eta_3 = 2.5mm$,dr=20cm

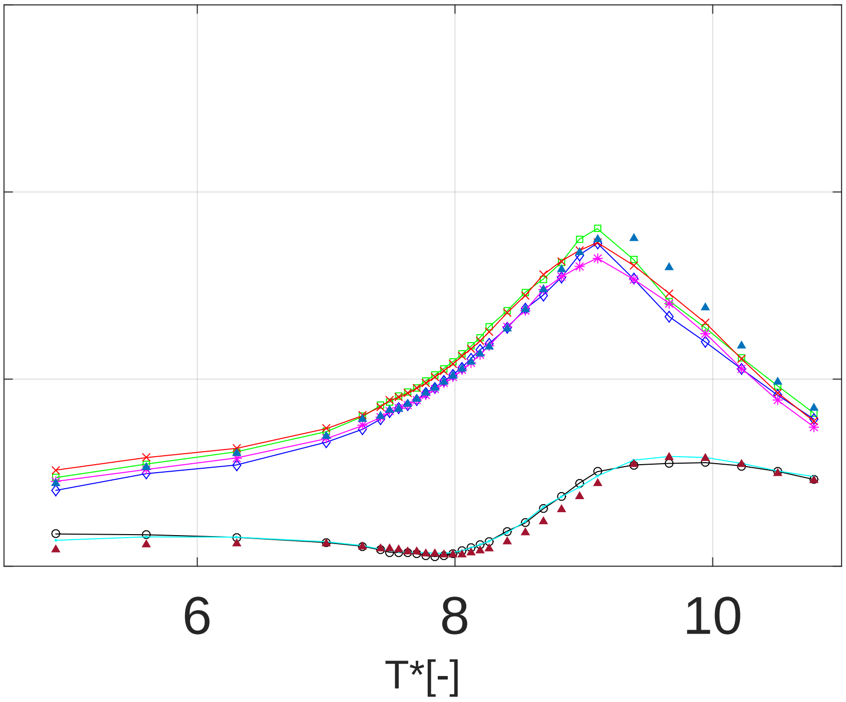

Figure D.26: App. 3 inlets, $\eta_3 = 5mm$,dr=20cm

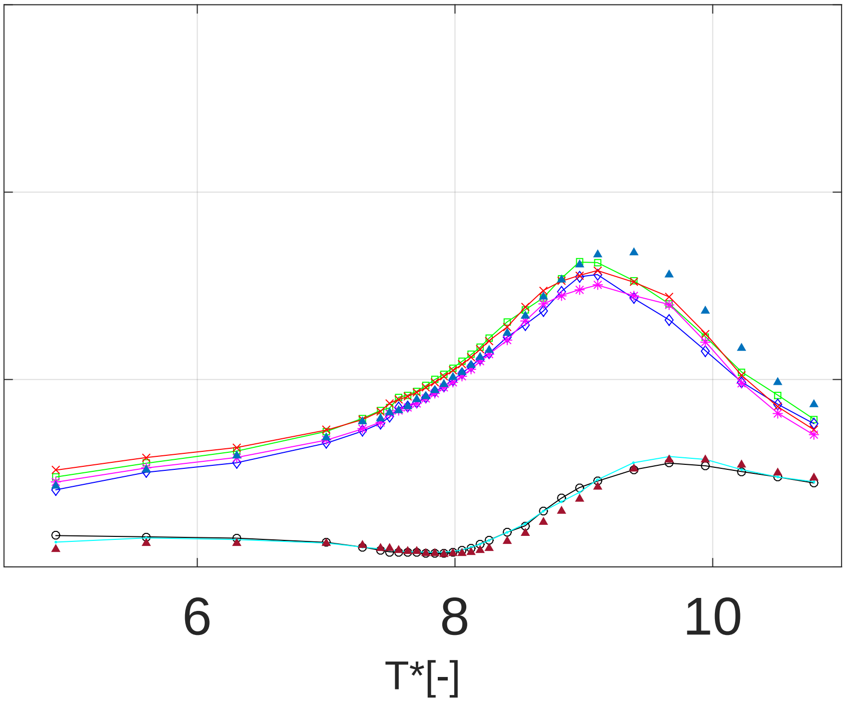

Figure D.27: App. 3 inlets, $\eta_3 = 7.5mm$,dr=20cm

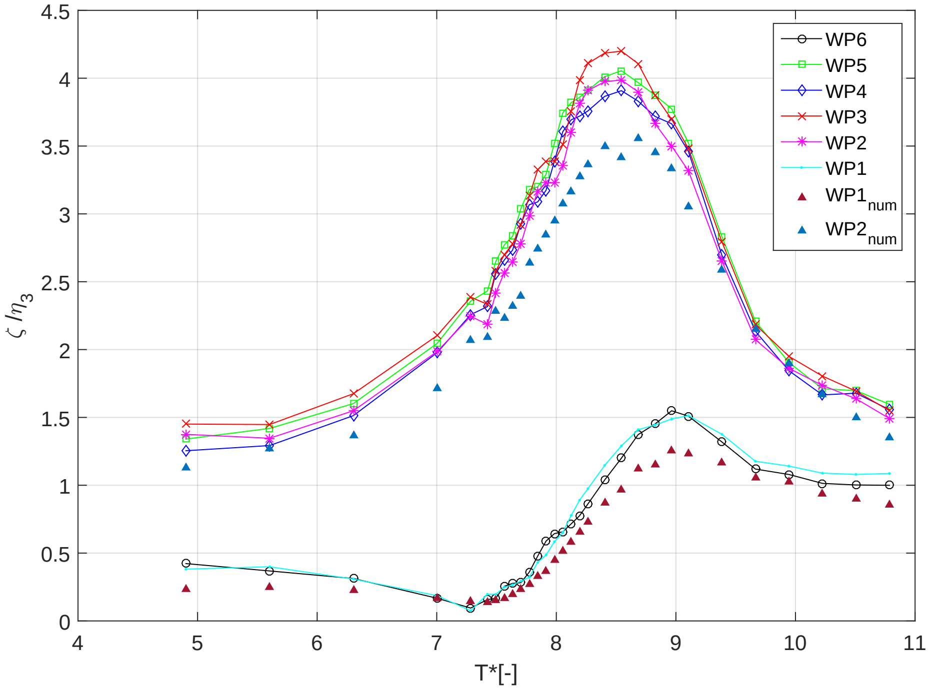

Figure D.28: App. 3 inlets, $\eta_3 = 2.5mm$,dr=15cm

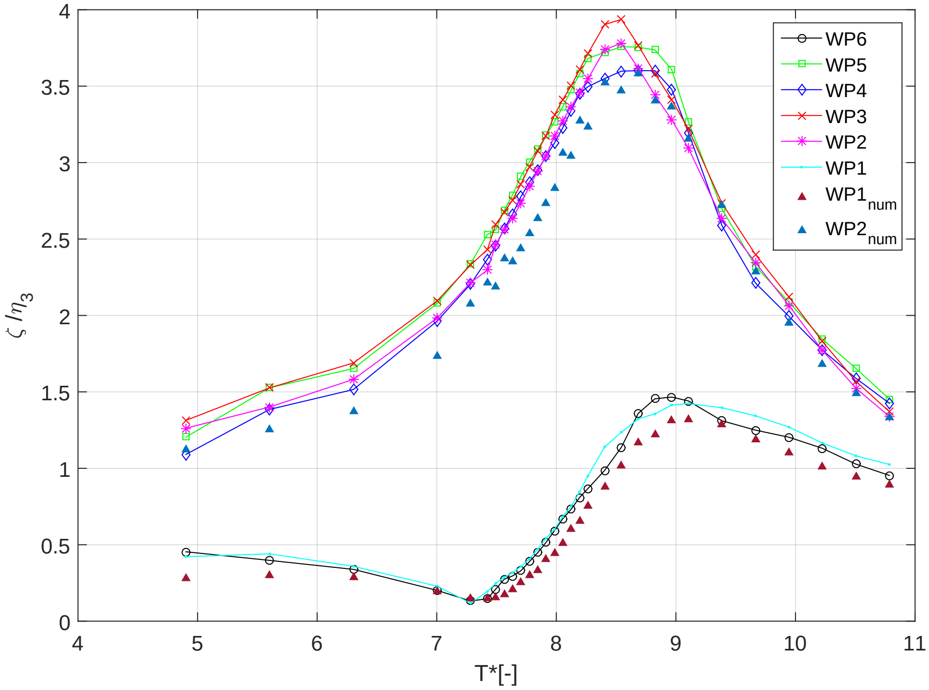

Figure D.29: App. 3 inlets, $\eta_3 = 5mm$,dr=15cm

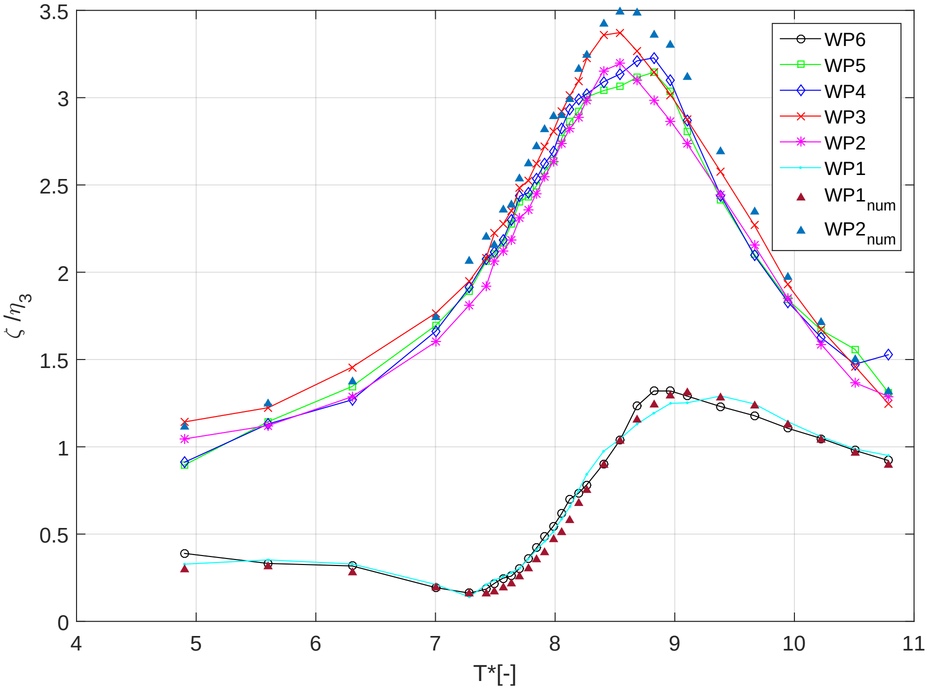

Figure D.30: App. 3 inlets, $\eta_3 = 7.5mm$,dr=15cm

D.1.4 Rounded Inlet Corners in Pitch

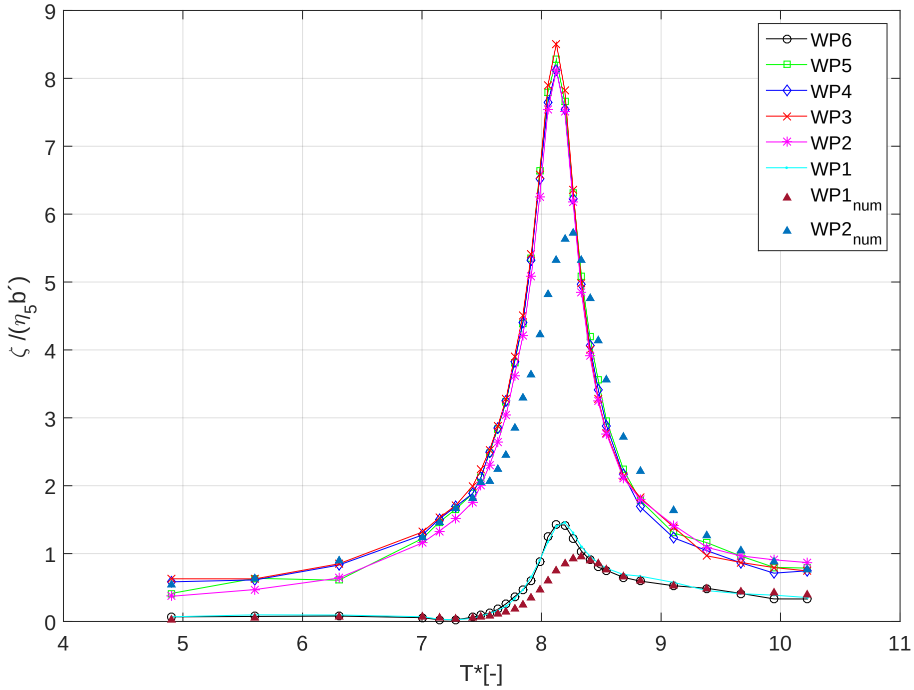

Figure D.31: Rounded inlets, $\eta_5 = 2.5$,dr=20cm

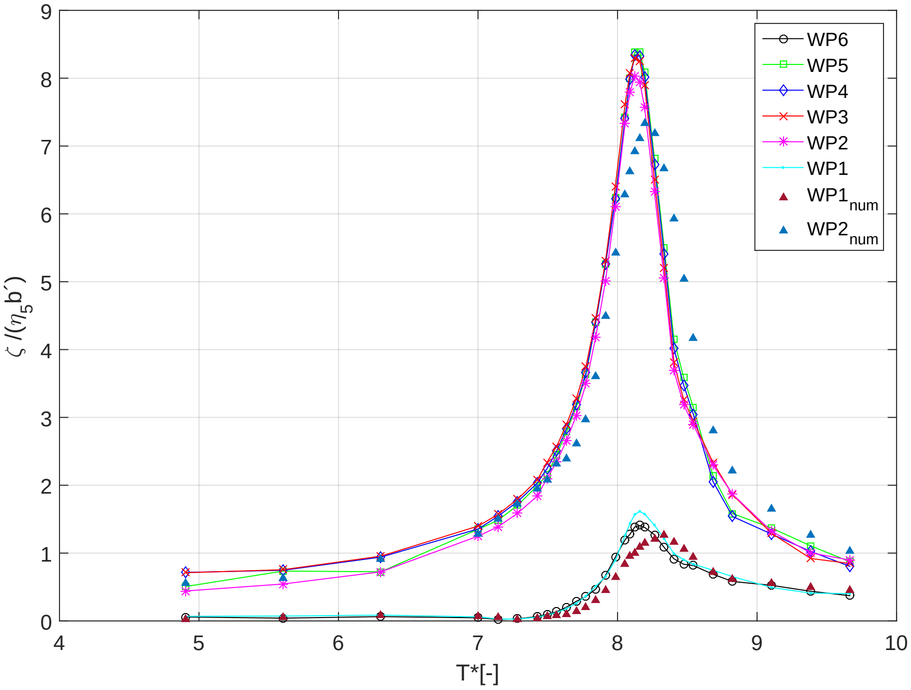

Figure D.32: Rounded inlets, $\eta_5 = 5$,dr=20cm

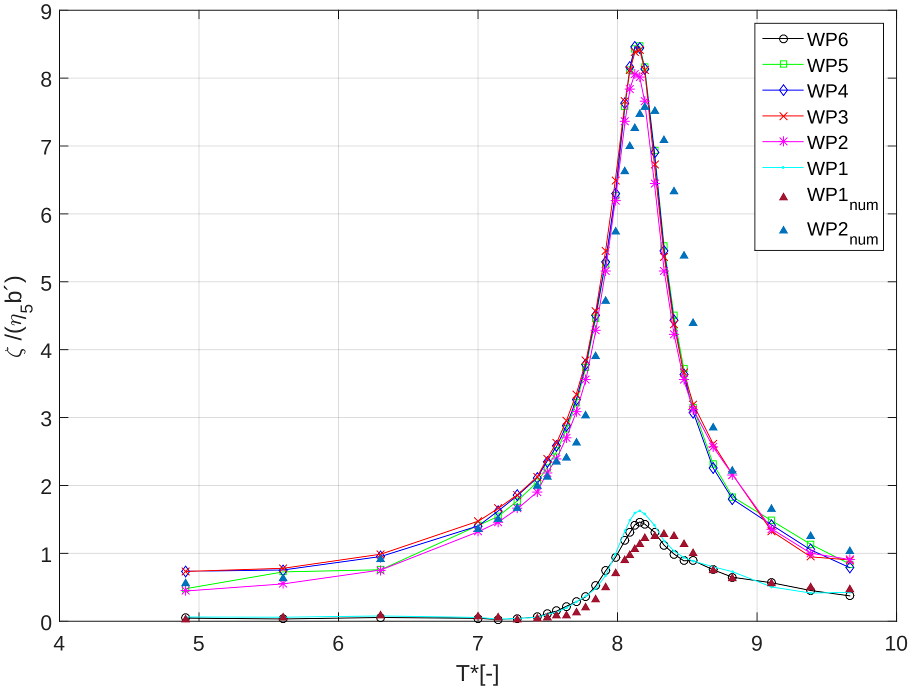

Figure D.33: Rounded inlets, $\eta_5 = 7.5$,dr=20cm

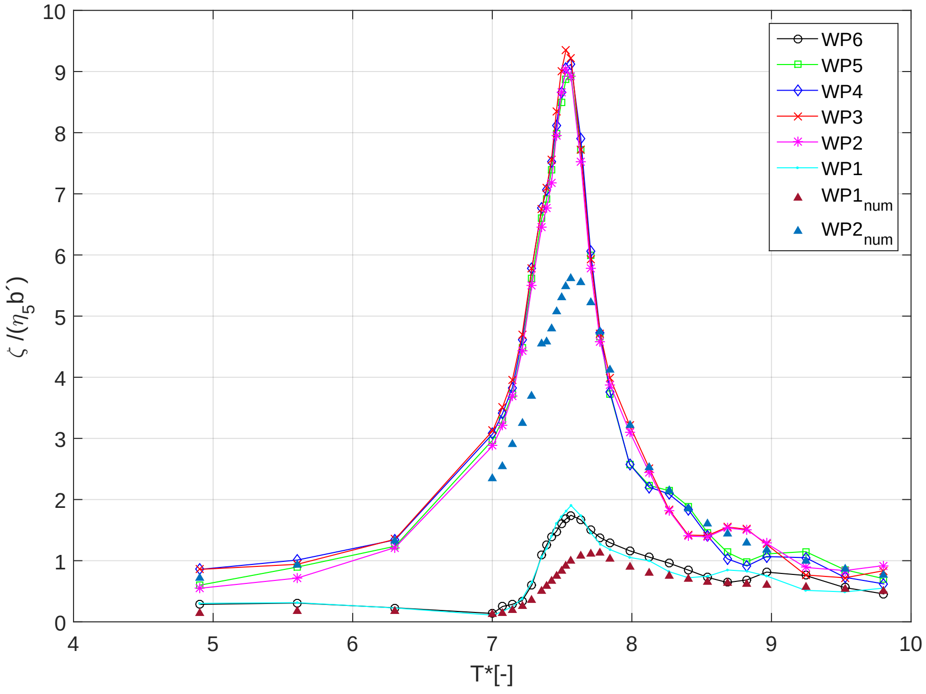

Figure D.34: Rounded inlets, $\eta_5 = 2.5$,dr=15cm

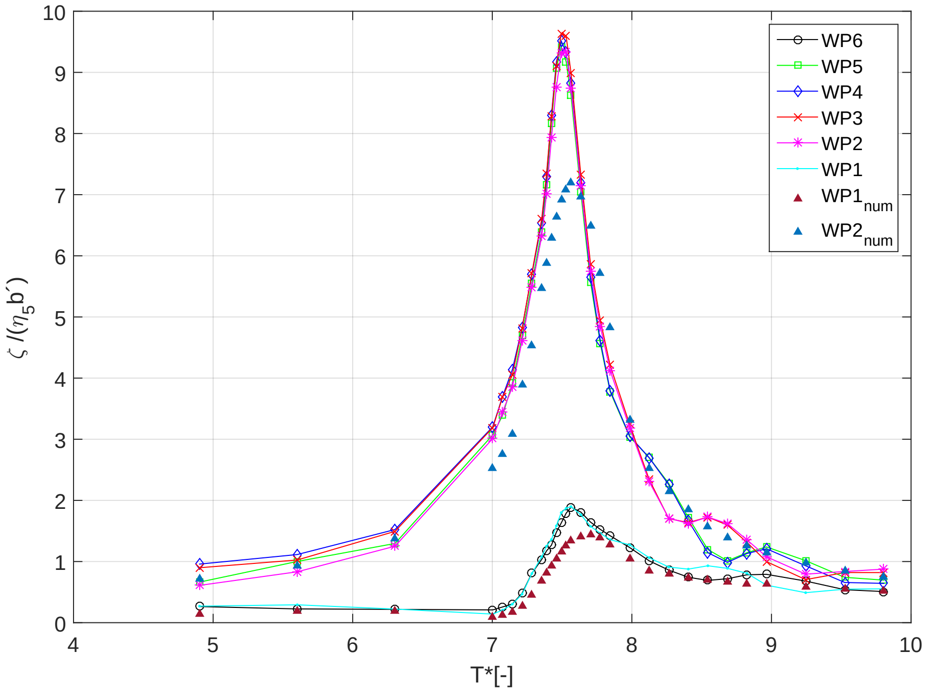

Figure D.35: Rounded inlets, $\eta_5 = 5$,dr=15cm

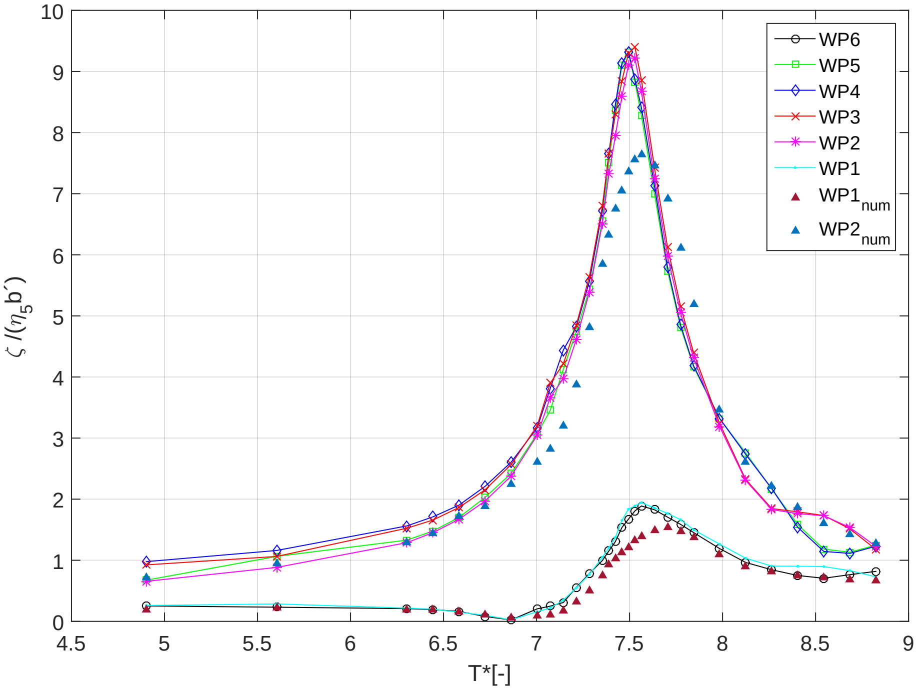

Figure D.36: Rounded inlets, $\eta_5 = 7.5$,dr=15cm

D.1.5 Squared Inlet Corners in Pitch

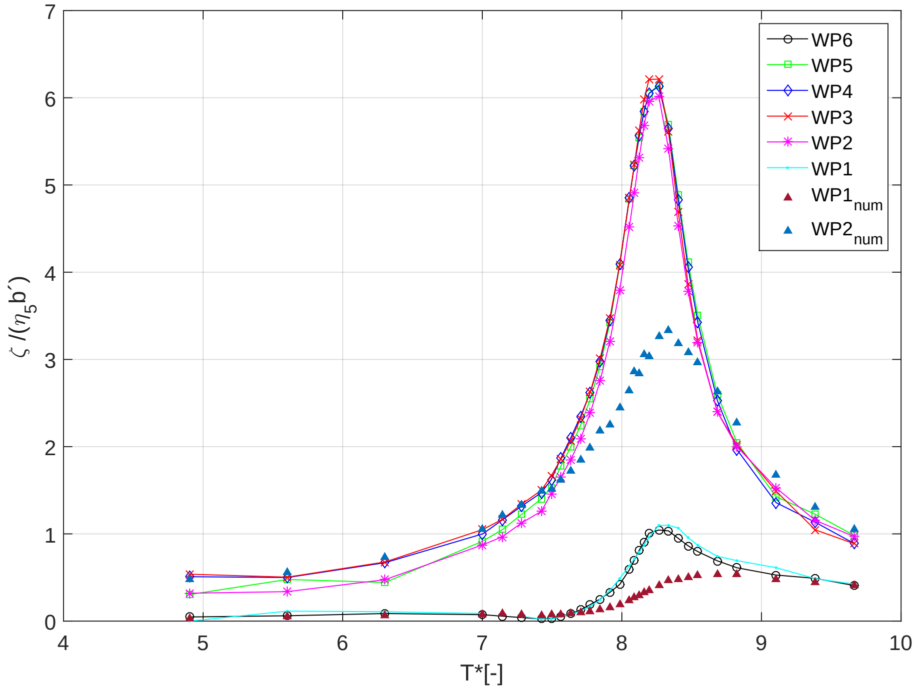

Figure D.37: Squared inlets, $\eta_5 = 2.5$,dr=20cm

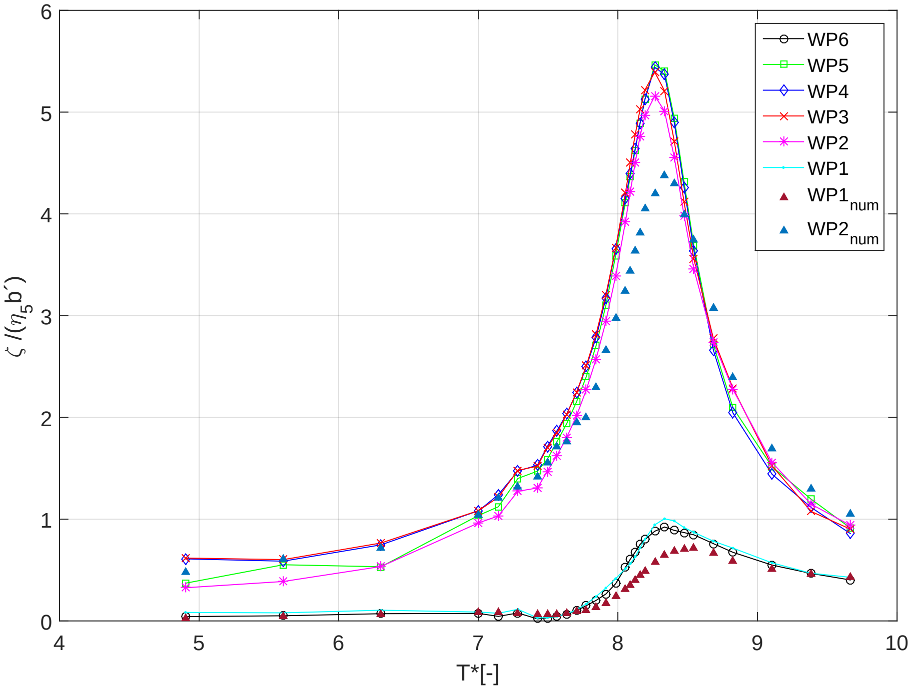

Figure D.38: Squared inlets, $\eta_5 = 5$,dr=20cm

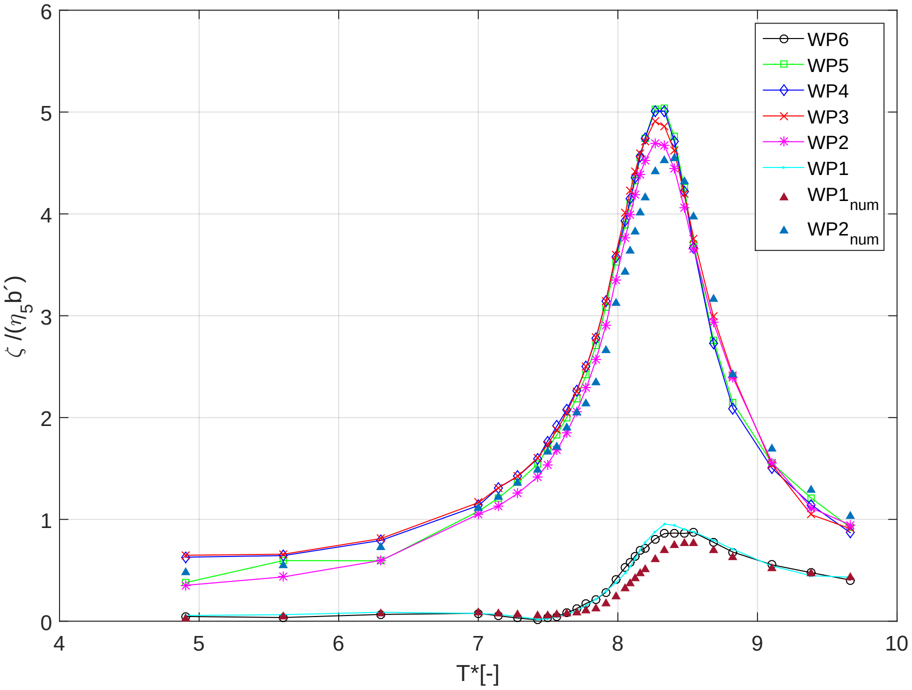

Figure D.39: Squared inlets, $\eta_5 = 7.5$,dr=20cm

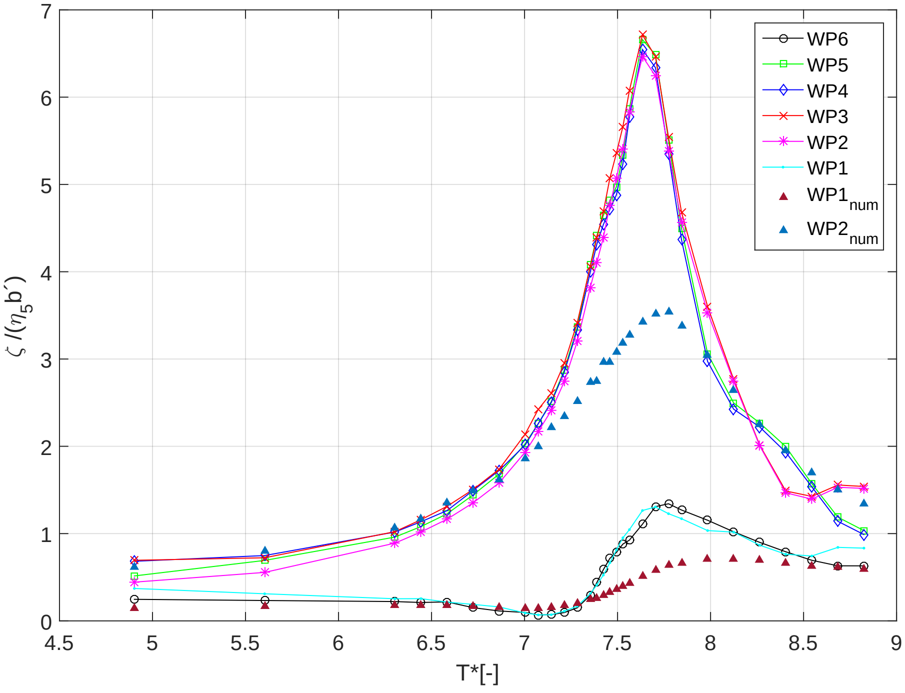

Figure D.40: Squared inlets, $\eta_5 = 2.5$,dr=15cm

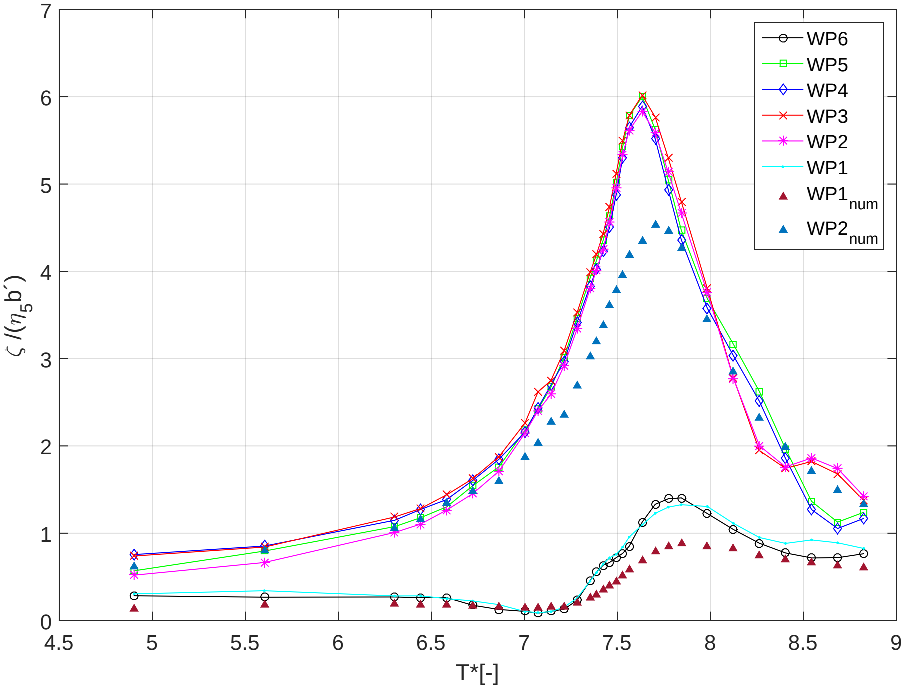

Figure D.41: Squared inlets, $\eta_5 = 5$,dr=15cm

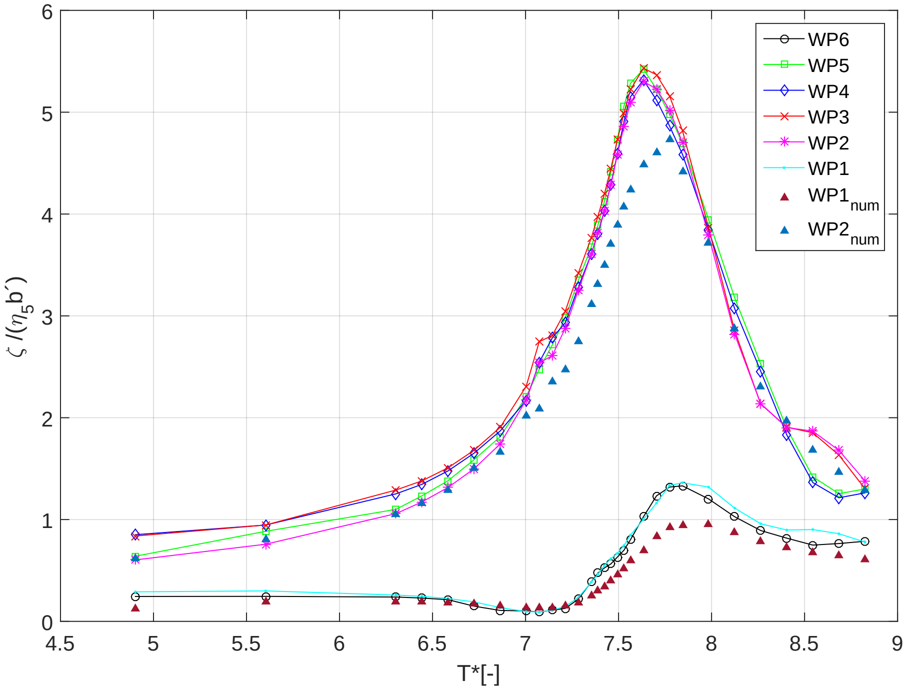

Figure D.42: Squared inlets, $\eta_5 = 7.5$,dr=15cm

D.1.6 Appended Inlet Corners in Pitch

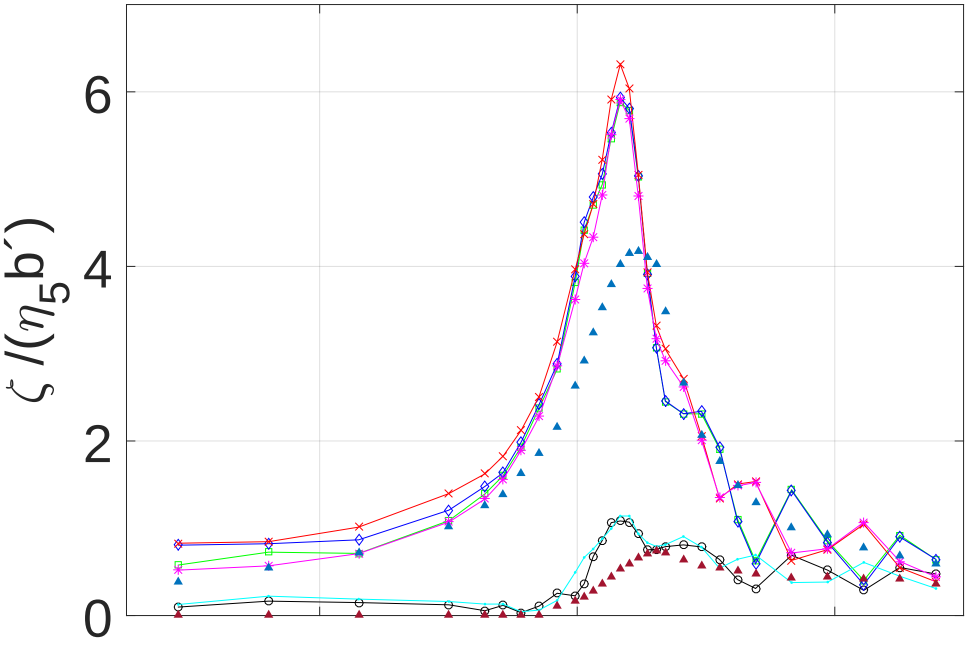

Figure D.43: App. 1 inlets, $\eta_5 = 2.5$,dr=20cm

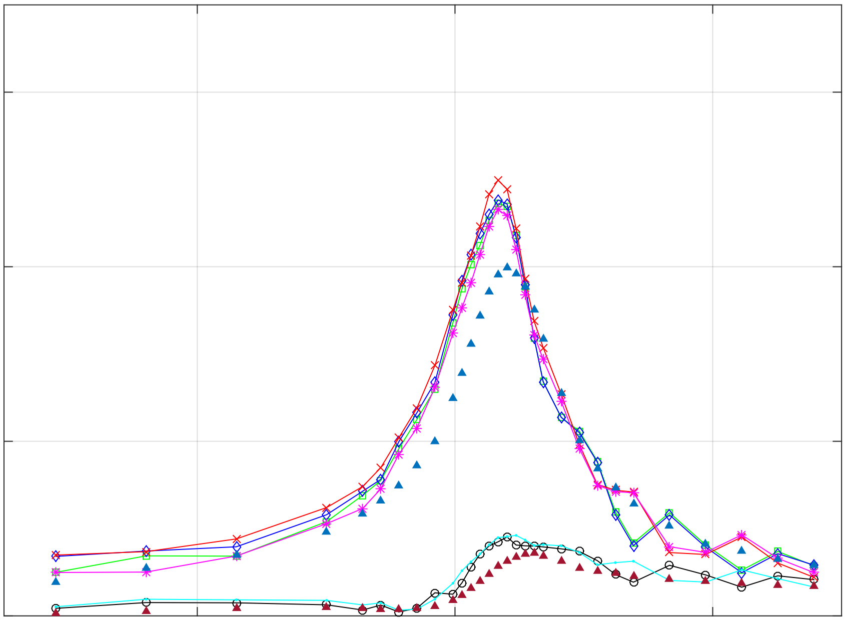

Figure D.44: App. 1 inlets, $\eta_5 = 5$,dr=20cm

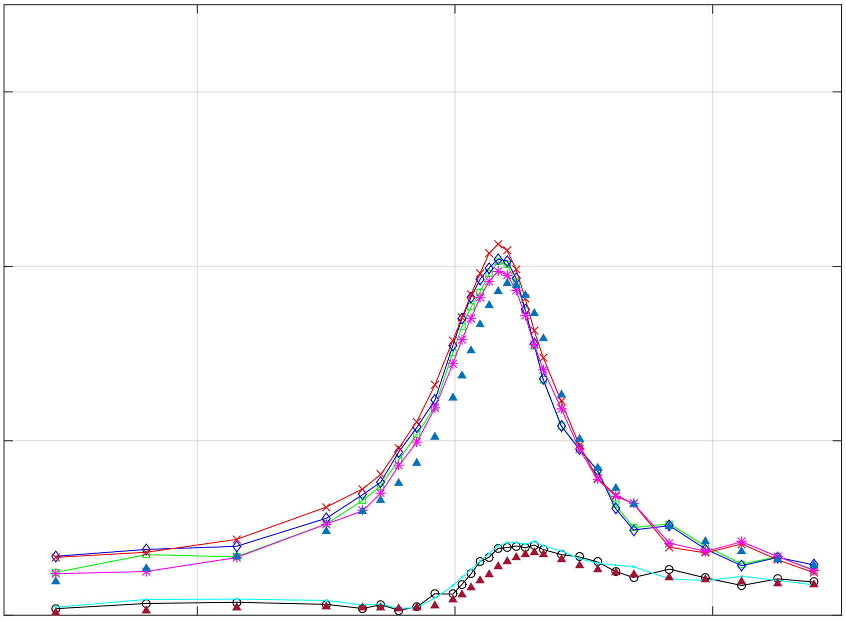

Figure D.45: App. 1 inlets, $\eta_5 = 7.5$,dr=20cm

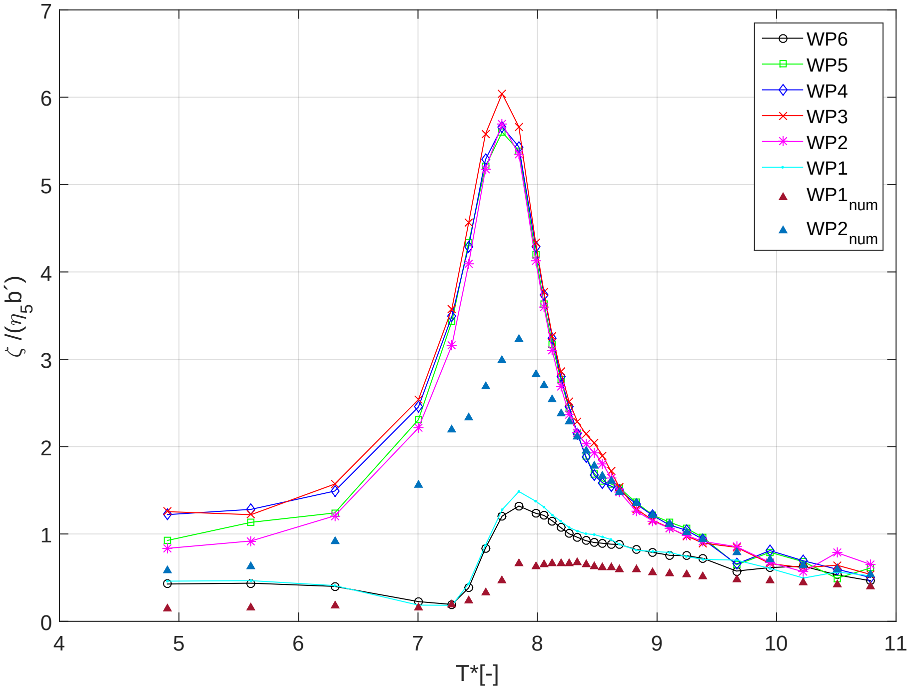

Figure D.46: App. 1 inlets, $\eta_5 = 2.5$,dr=15cm

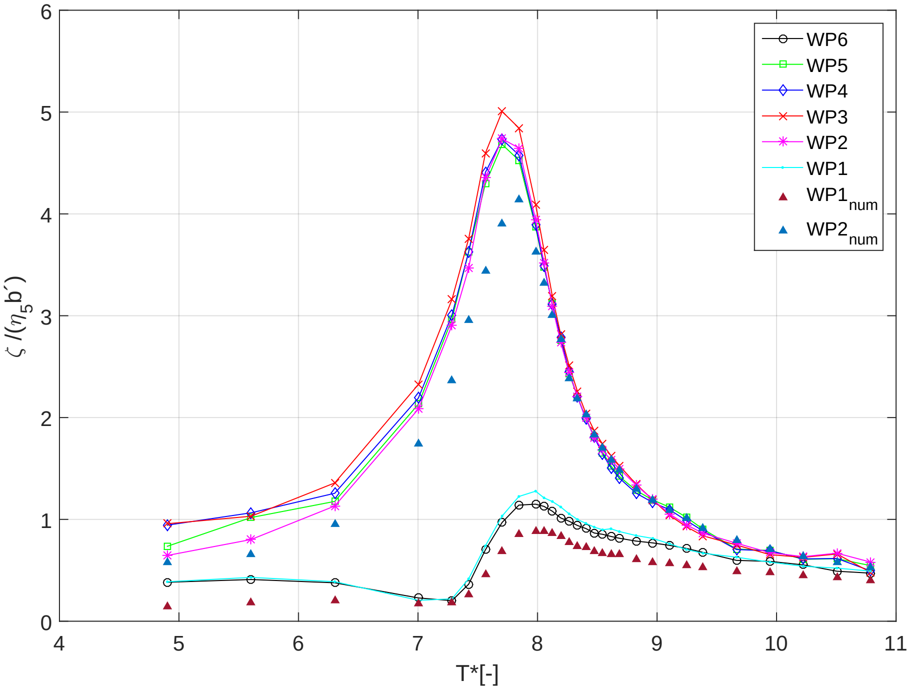

Figure D.47: App. 1 inlets, $\eta_5 = 5$,dr=15cm

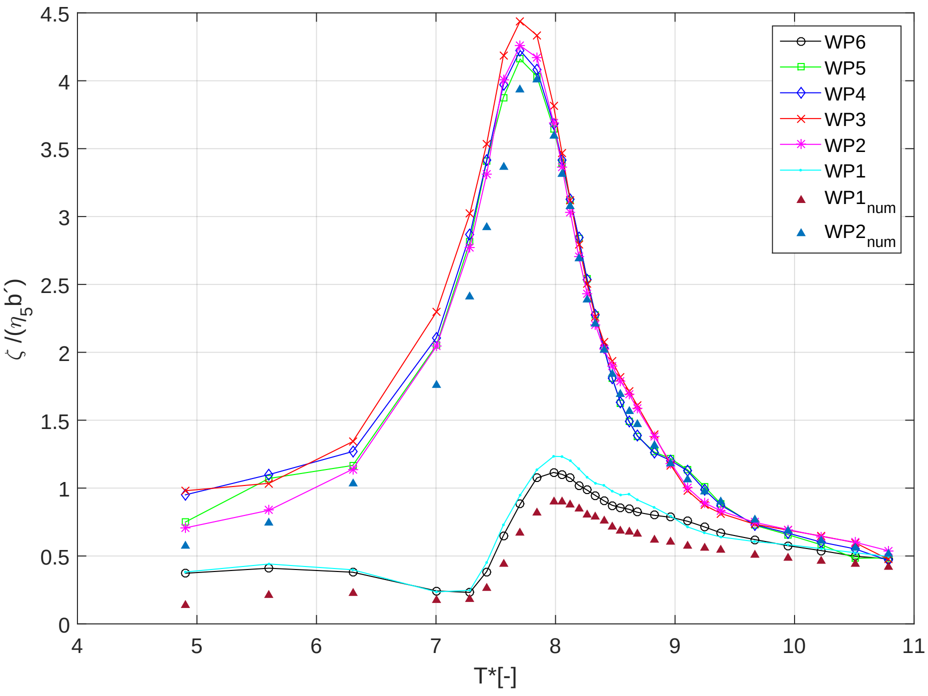

Figure D.48: App. 1 inlets, $\eta_5 = 7.5$,dr=15cm

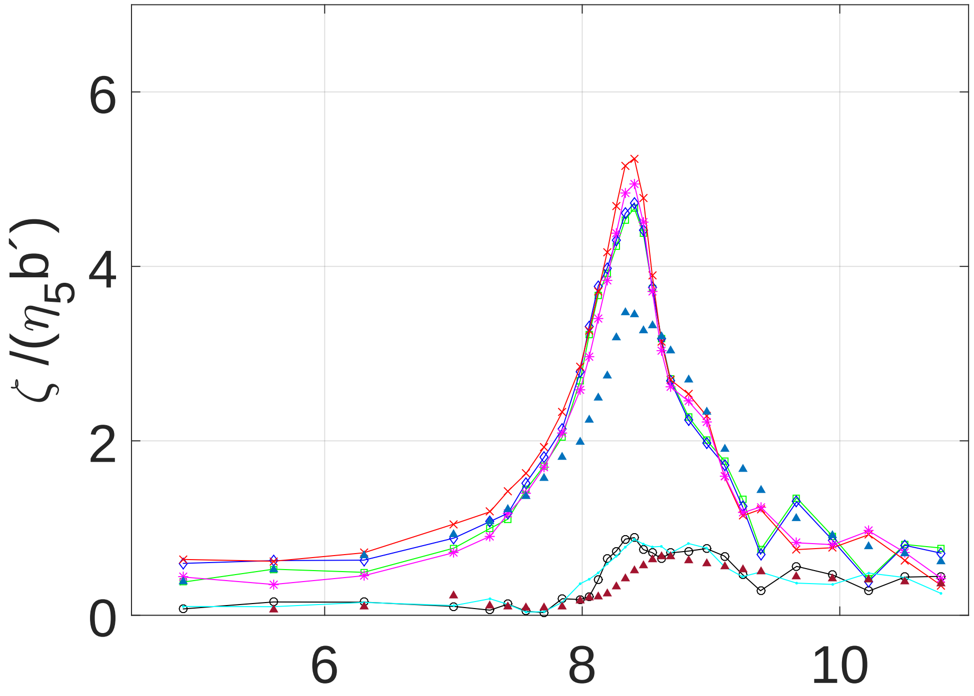

Figure D.49: App. 2 inlets, $\eta_5 = 2.5$,dr=20cm

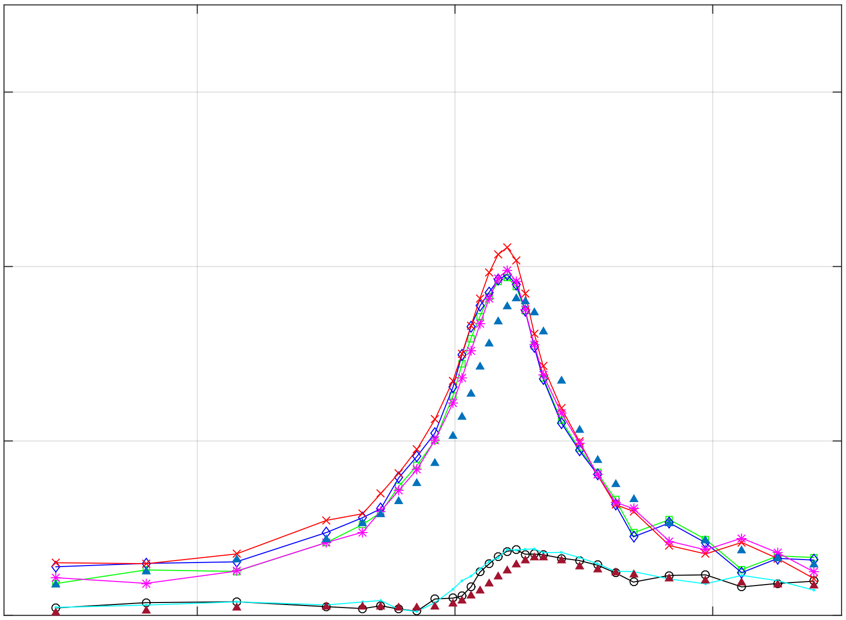

Figure D.50: App. 2 inlets, $\eta_5 = 5$,dr=20cm

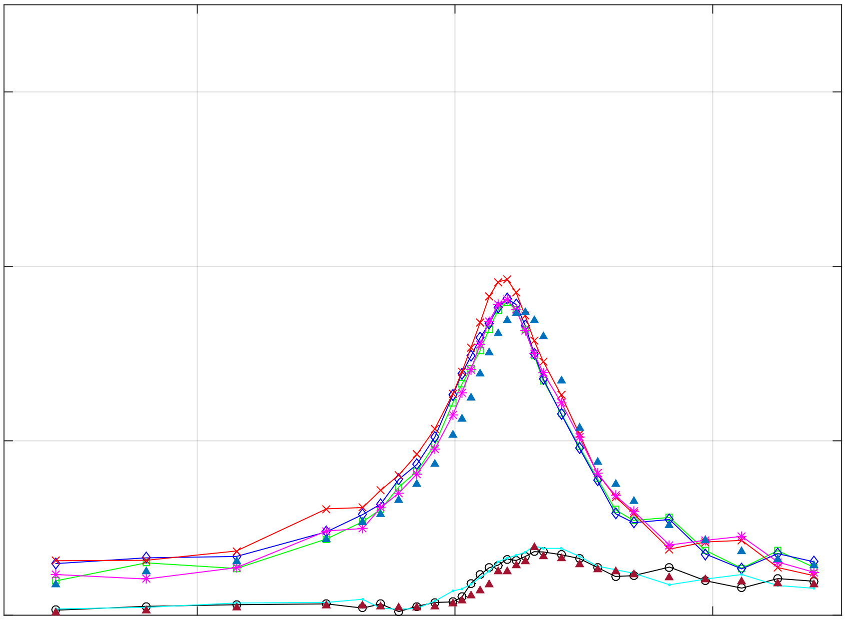

Figure D.51: App. 2 inlets, $\eta_5 = 7.5$,dr=20cm

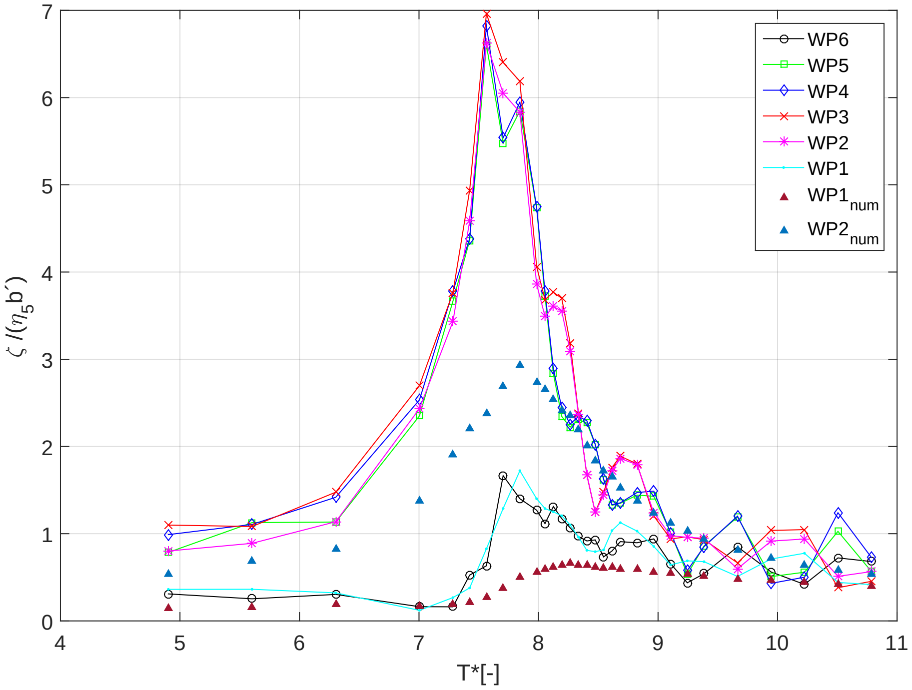

Figure D.52: App. 2 inlets, $\eta_5 = 2.5$,dr=15cm

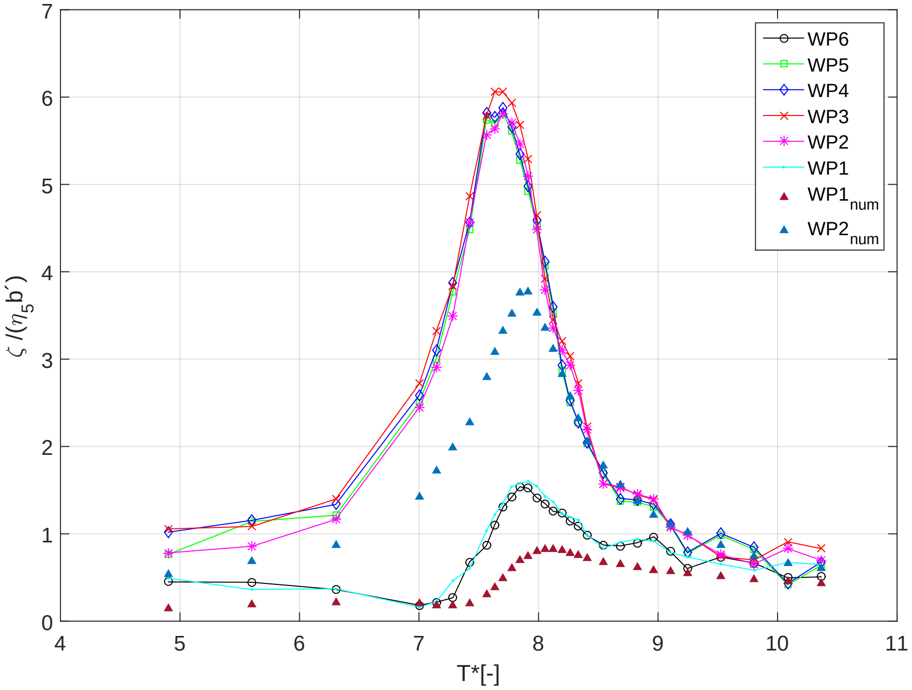

Figure D.53: App. 2 inlets, $\eta_5 = 5$,dr=15cm

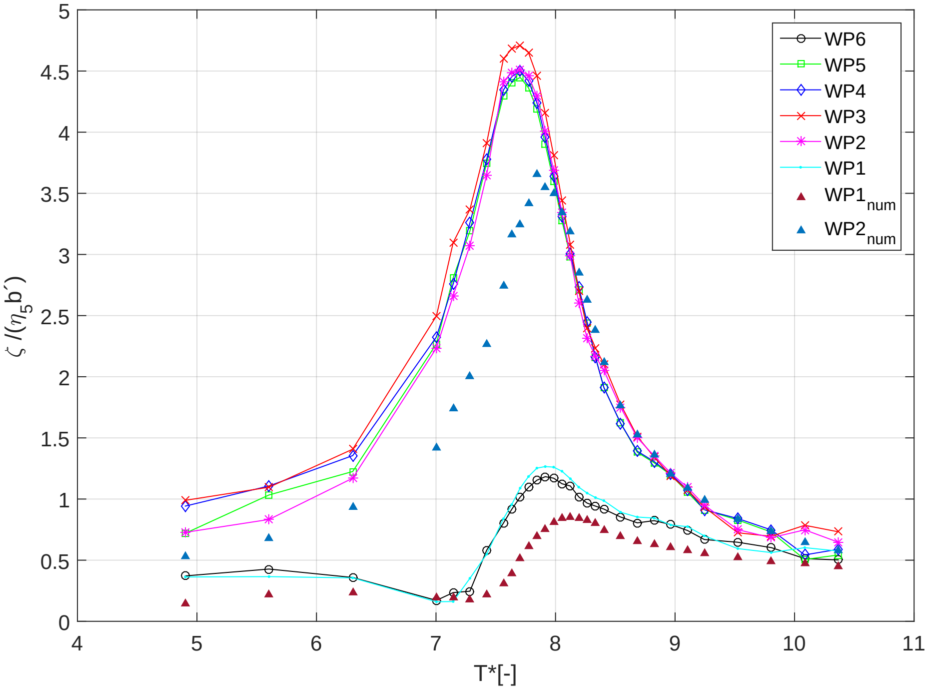

Figure D.54: App. 2 inlets, $\eta_5 = 7.5$,dr=15cm

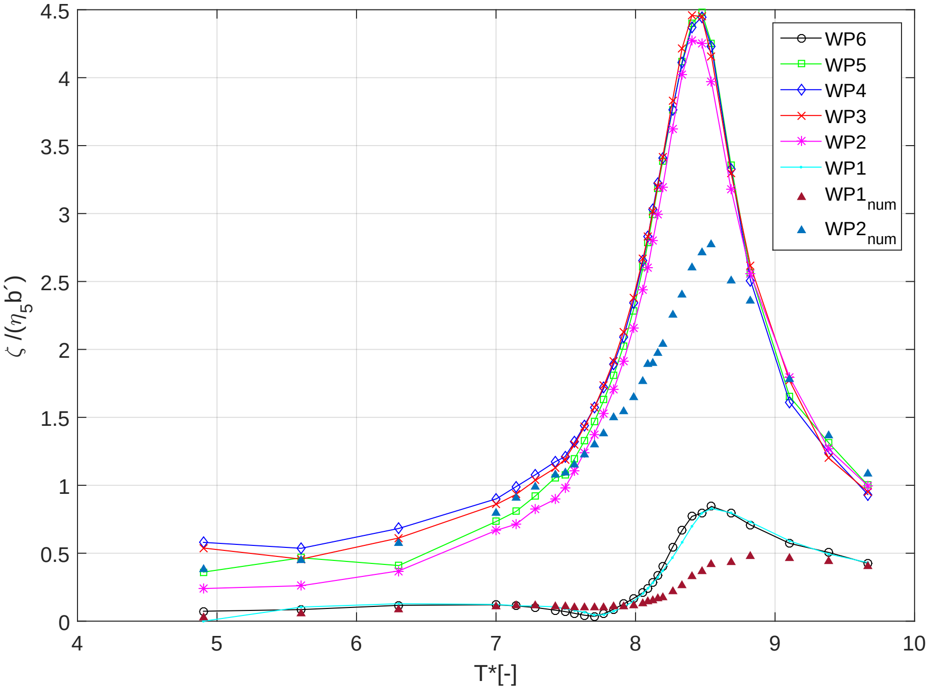

Figure D.55: App. 3 inlets, $\eta_5 = 2.5$,dr=20cm

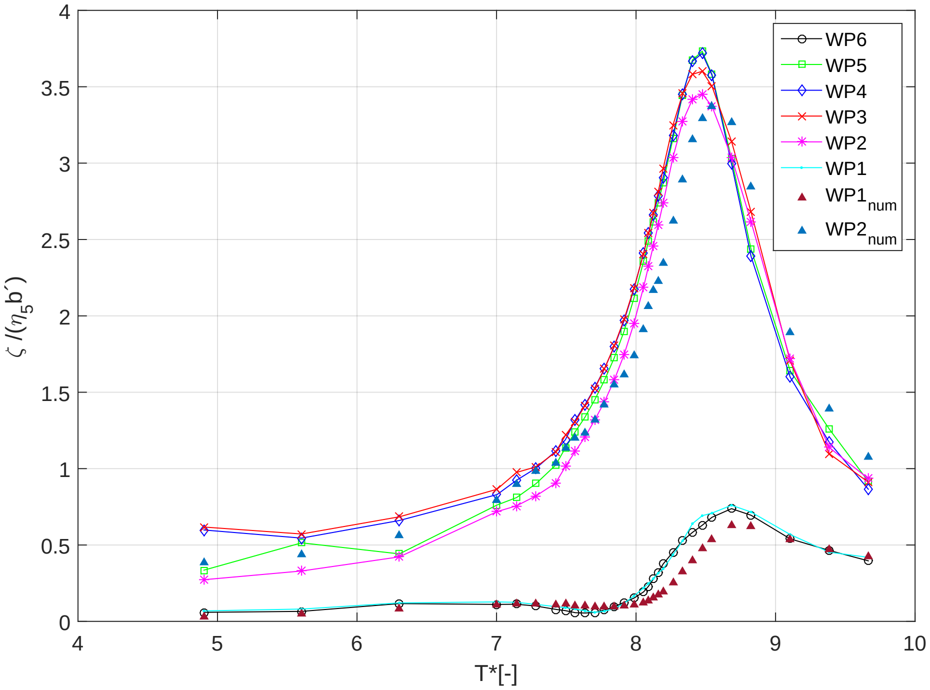

Figure D.56: App. 3 inlets, $\eta_5 = 5$,dr=20cm

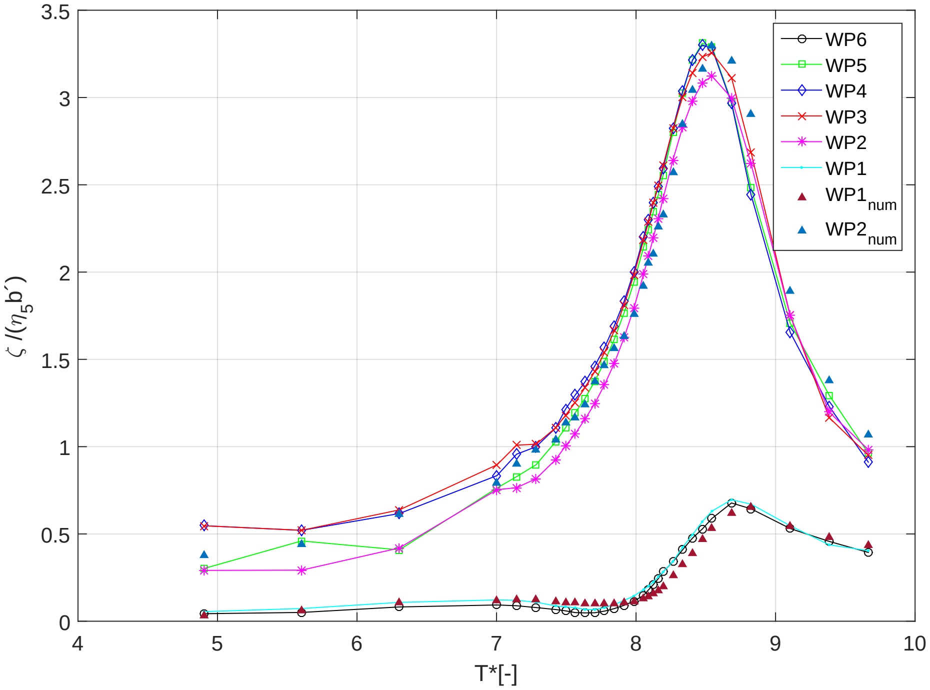

Figure D.57: App. 3 inlets, $\eta_5 = 7.5$,dr=20cm

D.2 Freely-floating Experiments

D.2.1 Rounded Inlet Corners

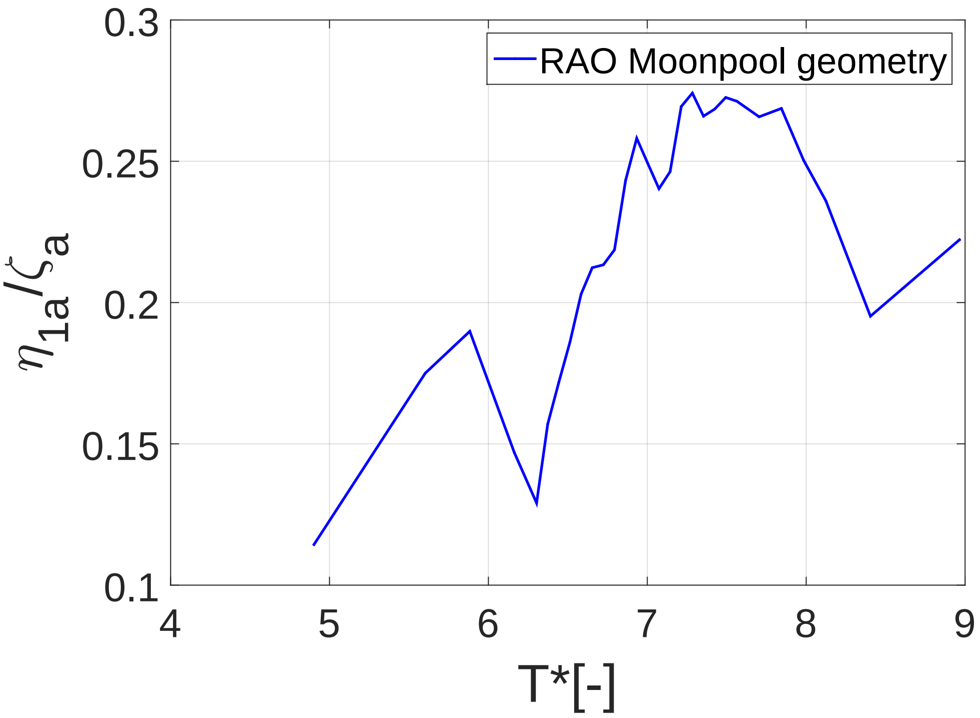

Figure D.58: Surge, wave steepness 1/60, rounded inlet, Mass in center

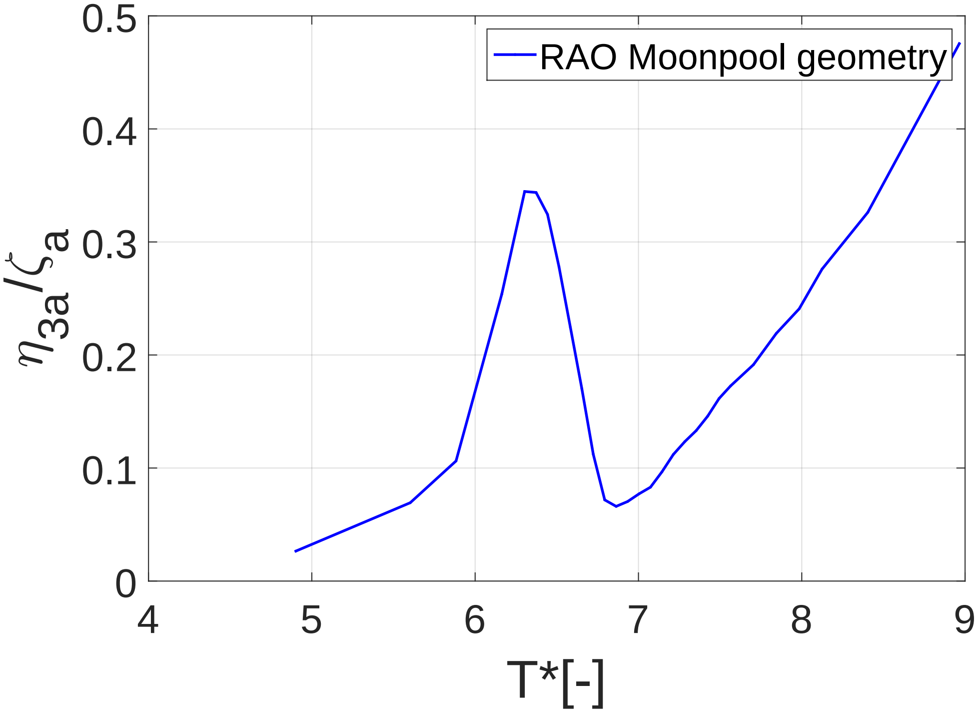

Figure D.59: Heave, wave steepness 1/60, rounded inlet, Mass in center

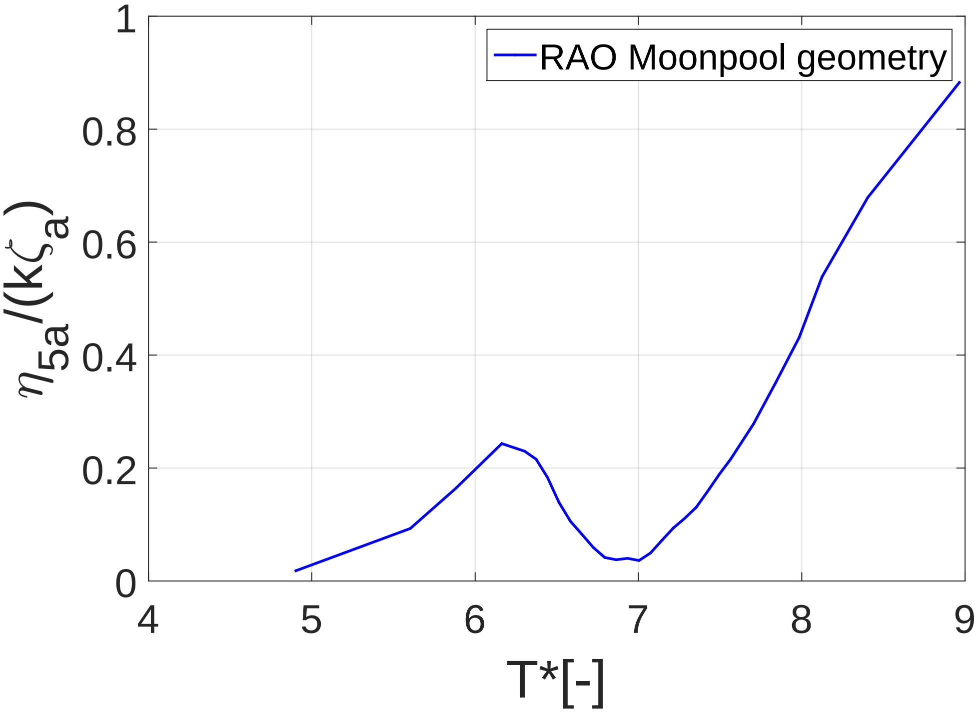

Figure D.60: Pitch, wave steepness 1/60, rounded inlet, Mass in center

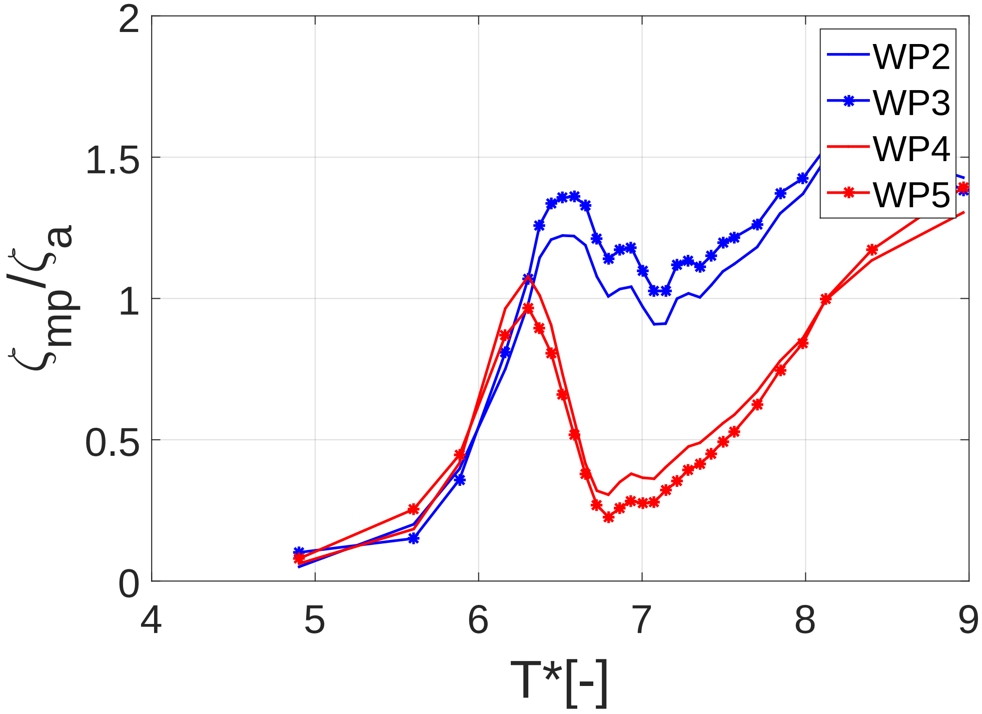

Figure D.61: Moonpools, wave steepness 1/60, rounded inlet, Mass in center

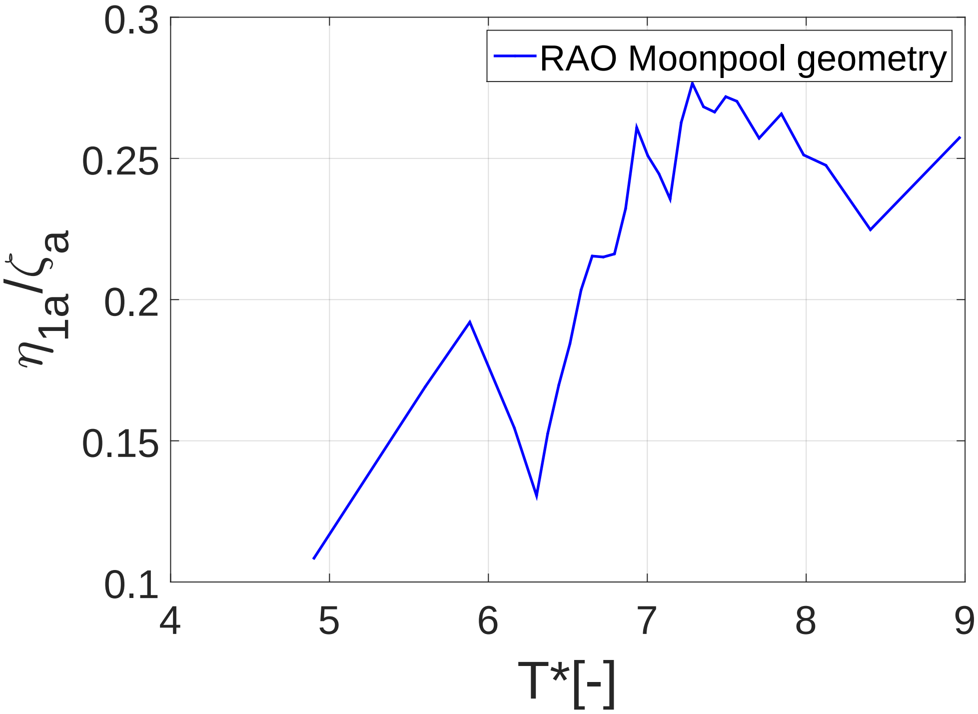

Figure D.62: Surge, wave steepness 1/45, rounded inlet, Mass in center

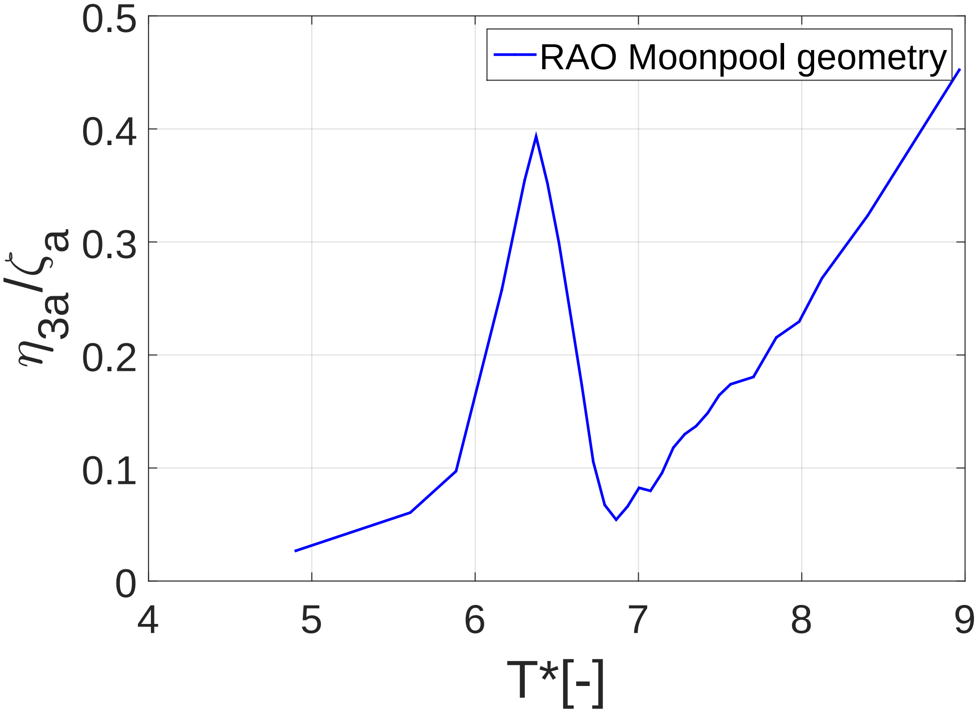

Figure D.63: Heave, wave steepness 1/45, rounded inlet, Mass in center

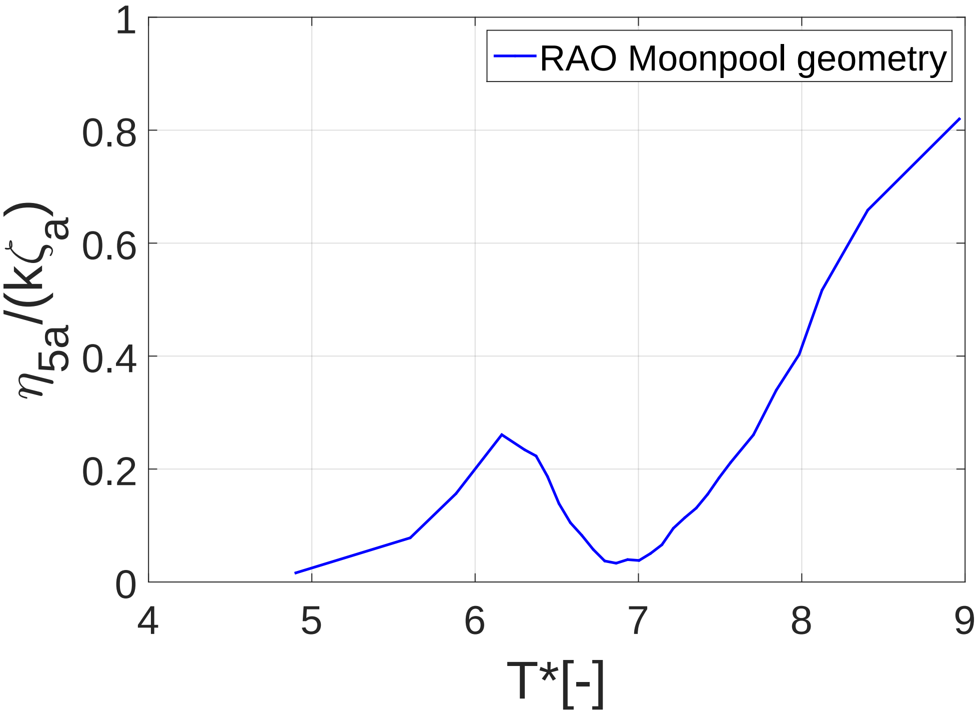

Figure D.64: Pitch, wave steepness 1/45, rounded inlet, Mass in center

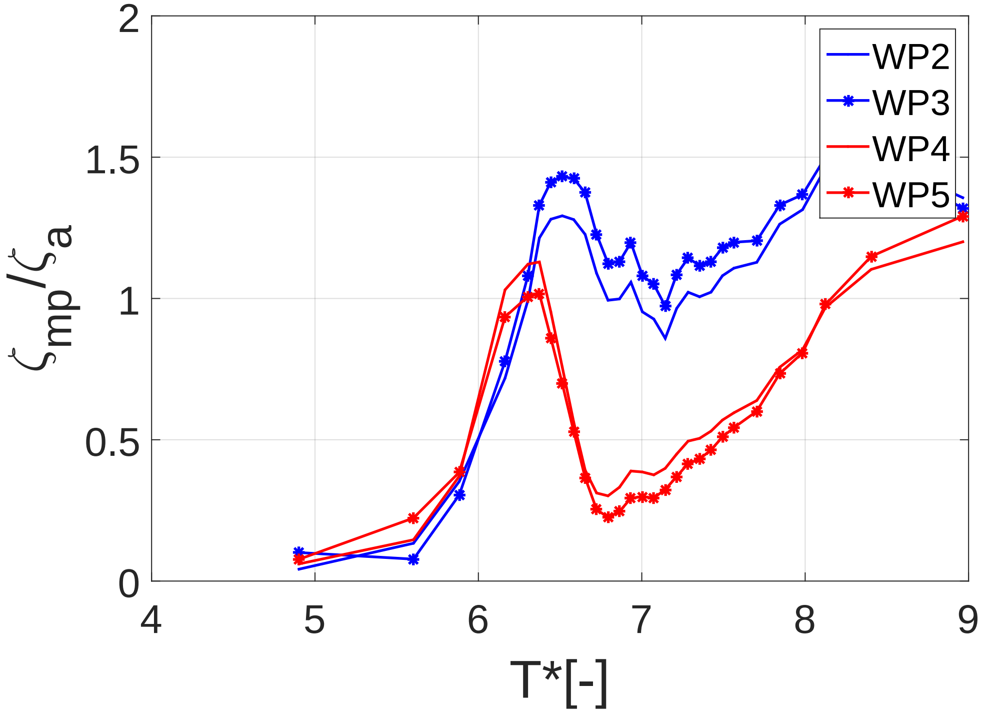

Figure D.65: Moonpools, wave steepness 1/45, rounded inlet, Mass in center

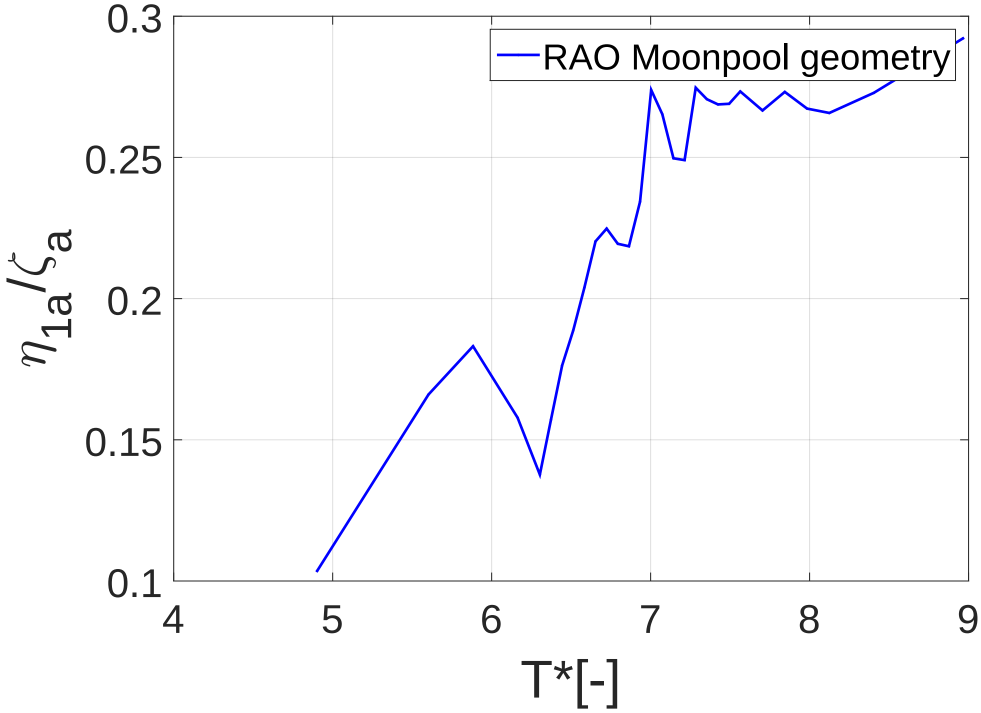

Figure D.66: Surge, wave steepness 1/30, rounded inlet, Mass in center

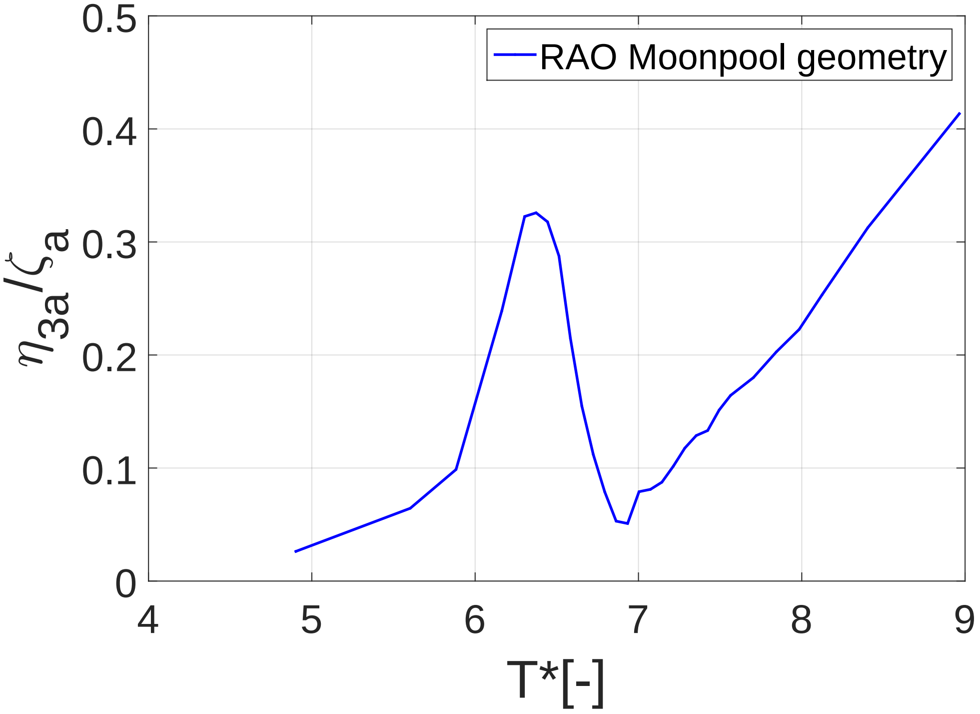

Figure D.67: Heave, wave steepness 1/30, rounded inlet, Mass in center

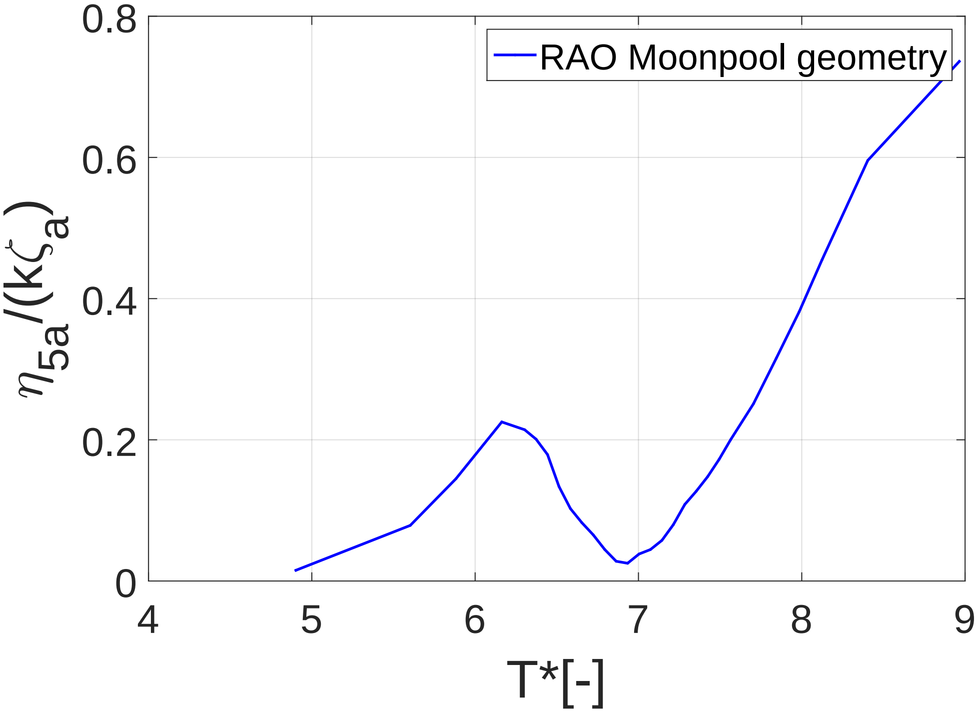

Figure D.68: Pitch, wave steepness 1/30, rounded inlet, Mass in center

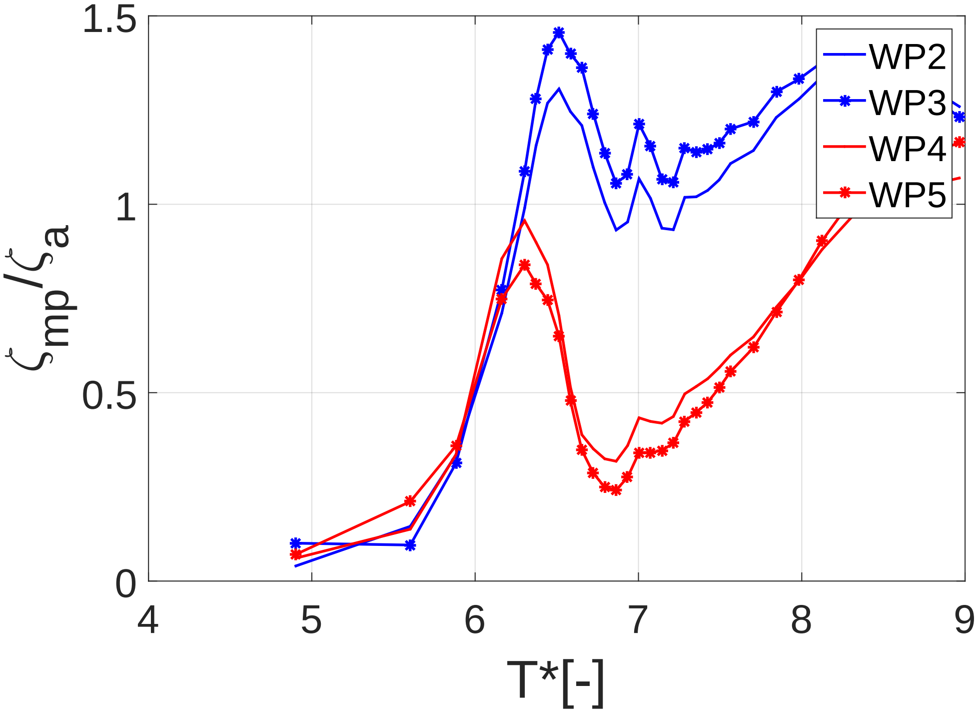

Figure D.69: Moonpools, wave steepness 1/30, rounded inlet, Mass in center

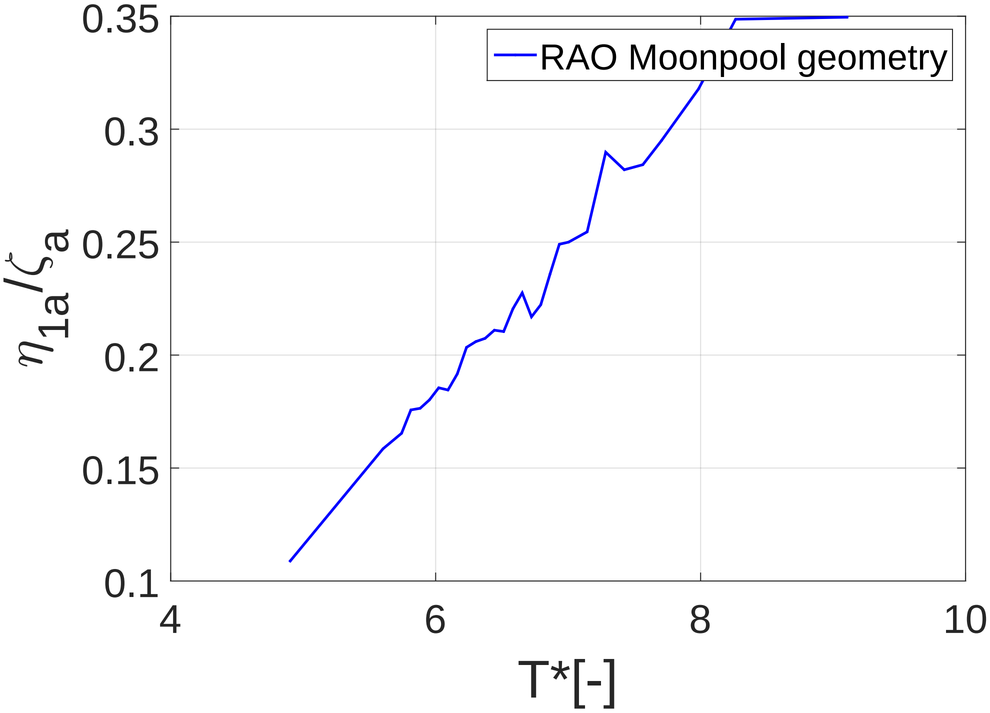

Figure D.70: Surge, wave steepness 1/60, rounded inlet, Mass at ends

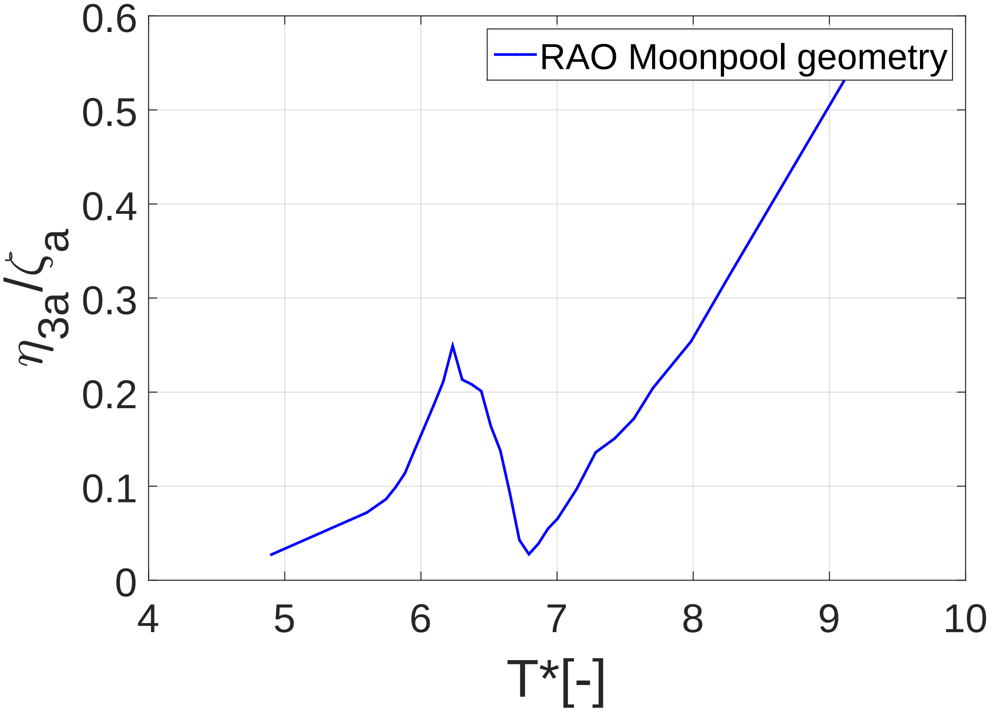

Figure D.71: Heave, wave steepness 1/60, rounded inlet, Mass at ends

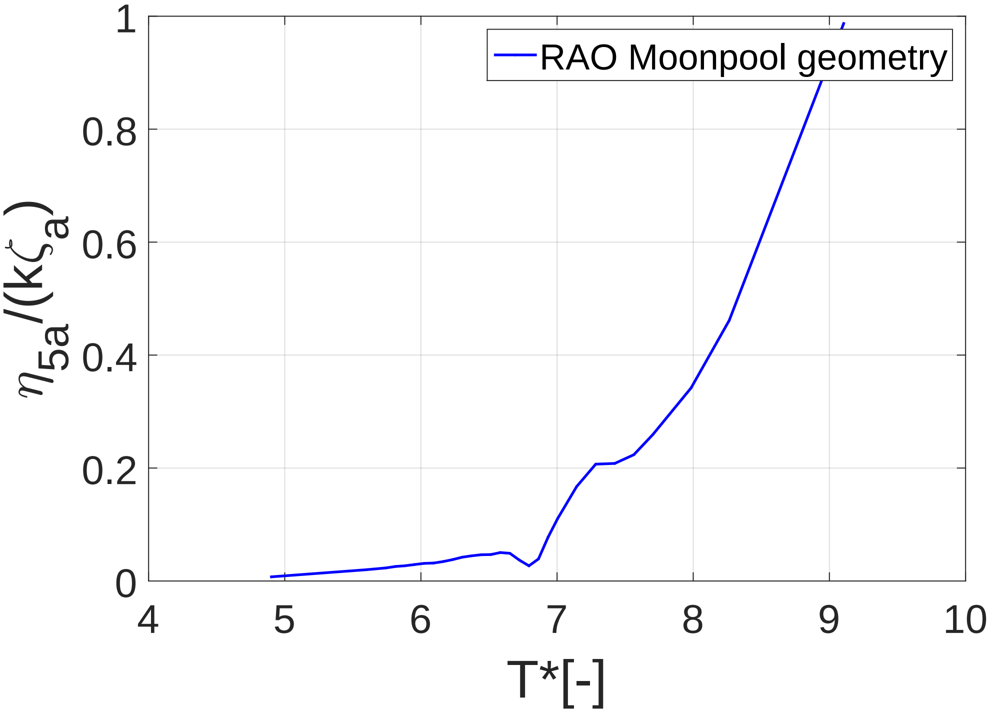

Figure D.72: Pitch, wave steepness 1/60, rounded inlet, Mass at ends

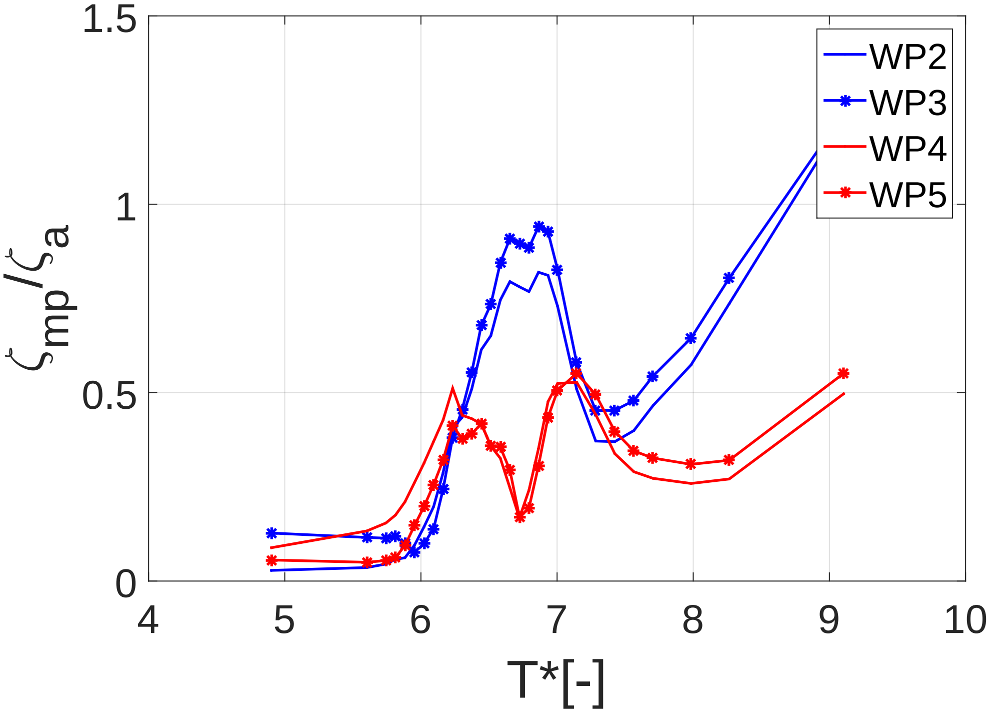

Figure D.73: Moonpools, wave steepness 1/60, rounded inlet, Mass at ends

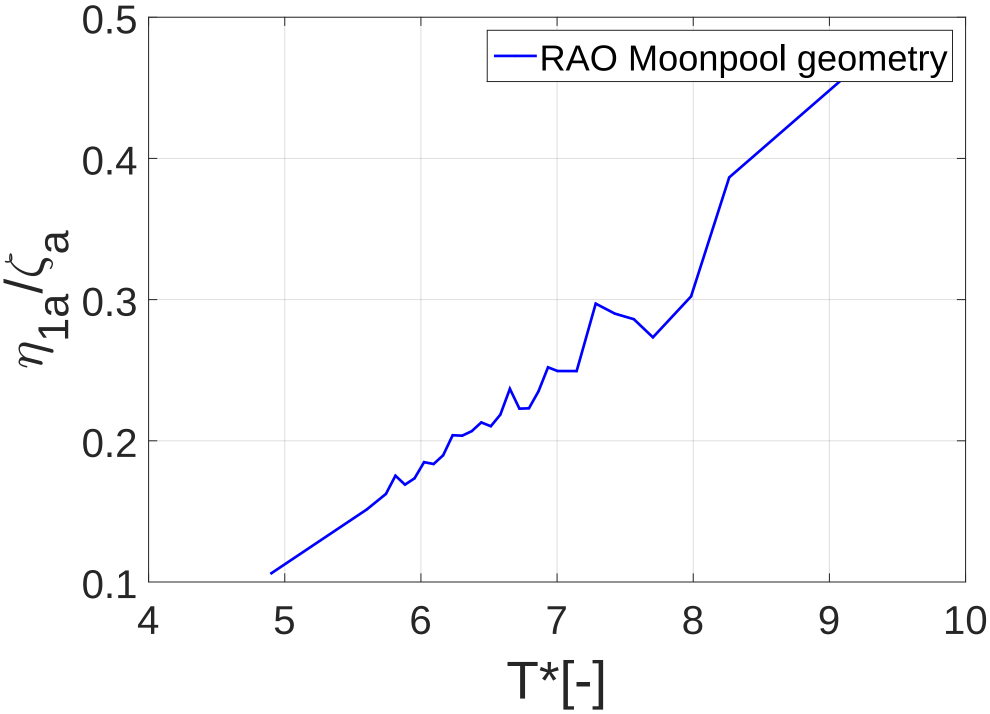

Figure D.74: Surge, wave steepness 1/45, rounded inlet, Mass at ends

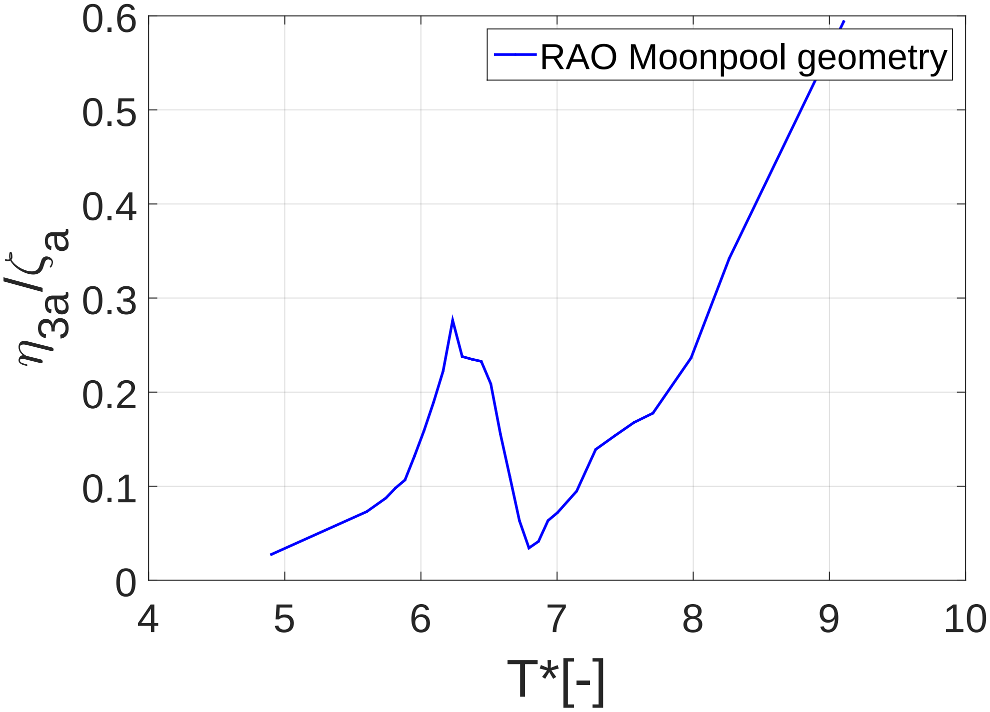

Figure D.75: Heave, wave steepness 1/45, rounded inlet, Mass at ends

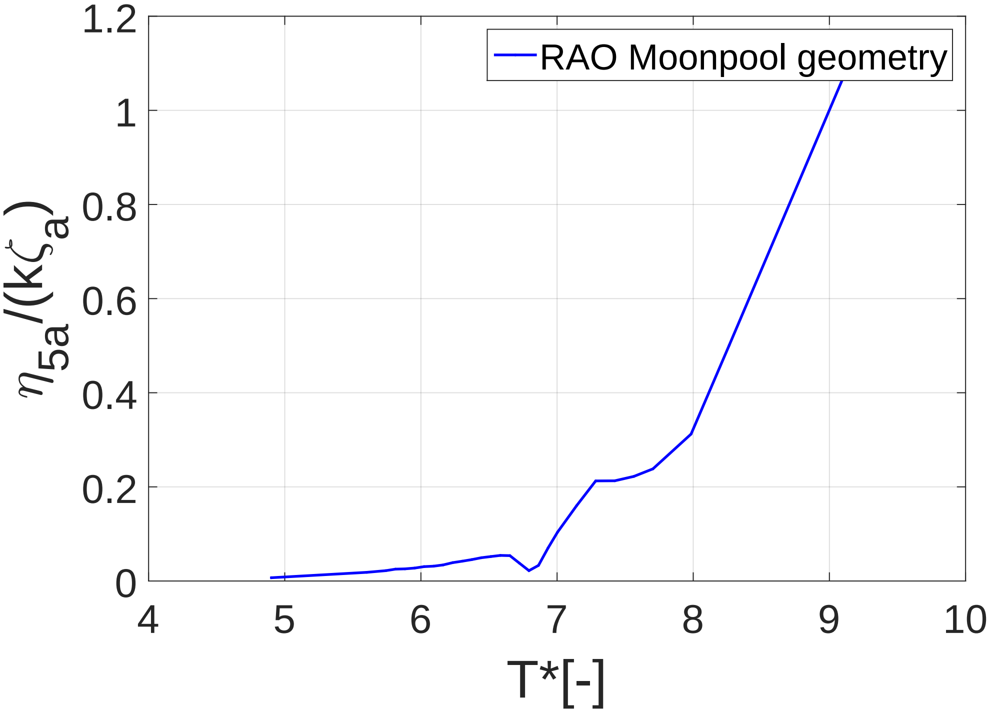

Figure D.76: Pitch, wave steepness 1/45, rounded inlet, Mass at ends

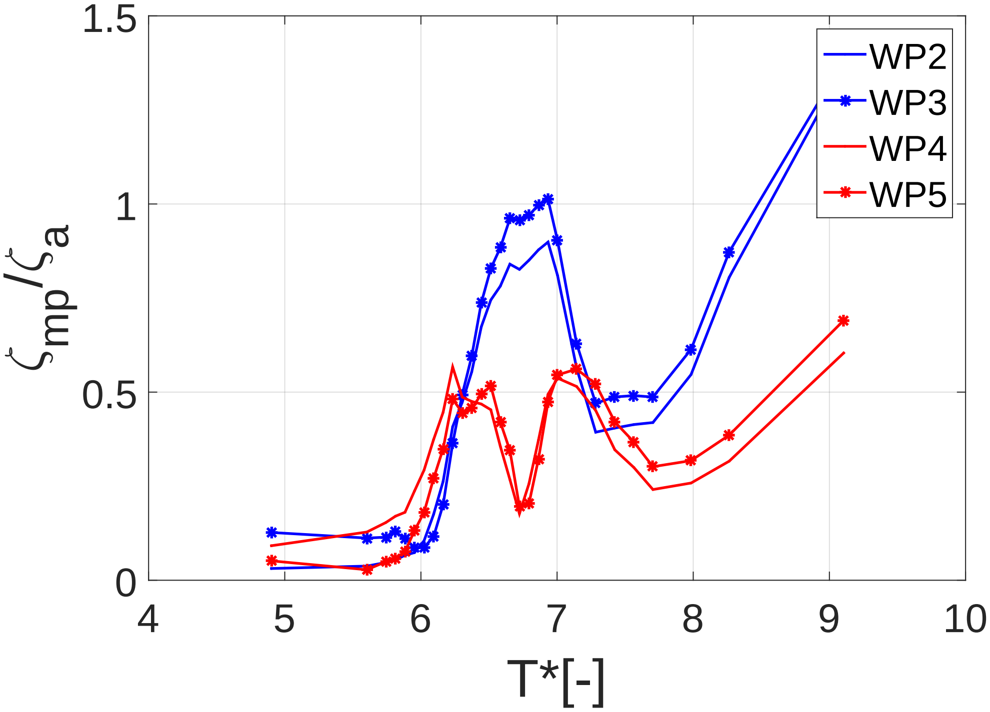

Figure D.77: Moonpools, wave steepness 1/45, rounded inlet, Mass at ends

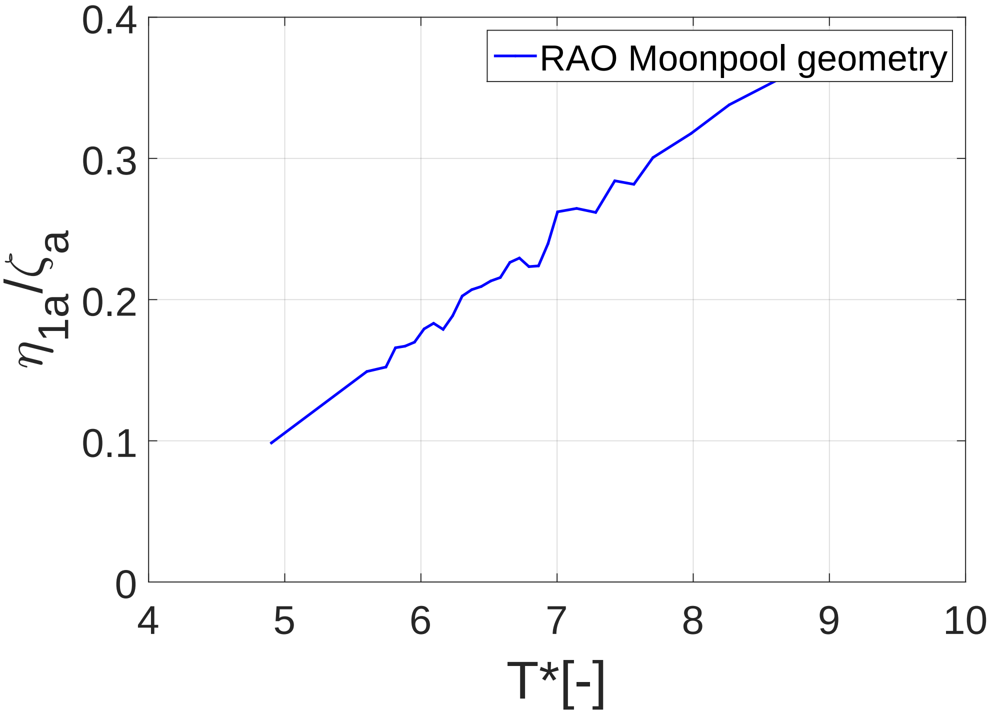

Figure D.78: Surge, wave steepness 1/30, rounded inlet, Mass at ends

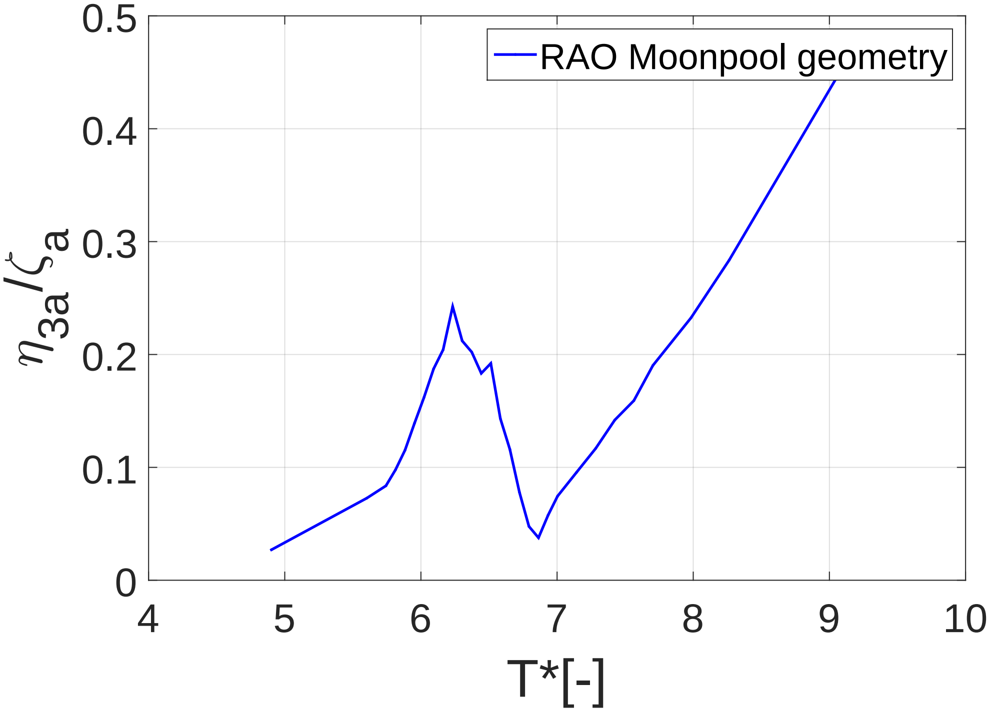

Figure D.79: Heave, wave steepness 1/30, rounded inlet, Mass at ends

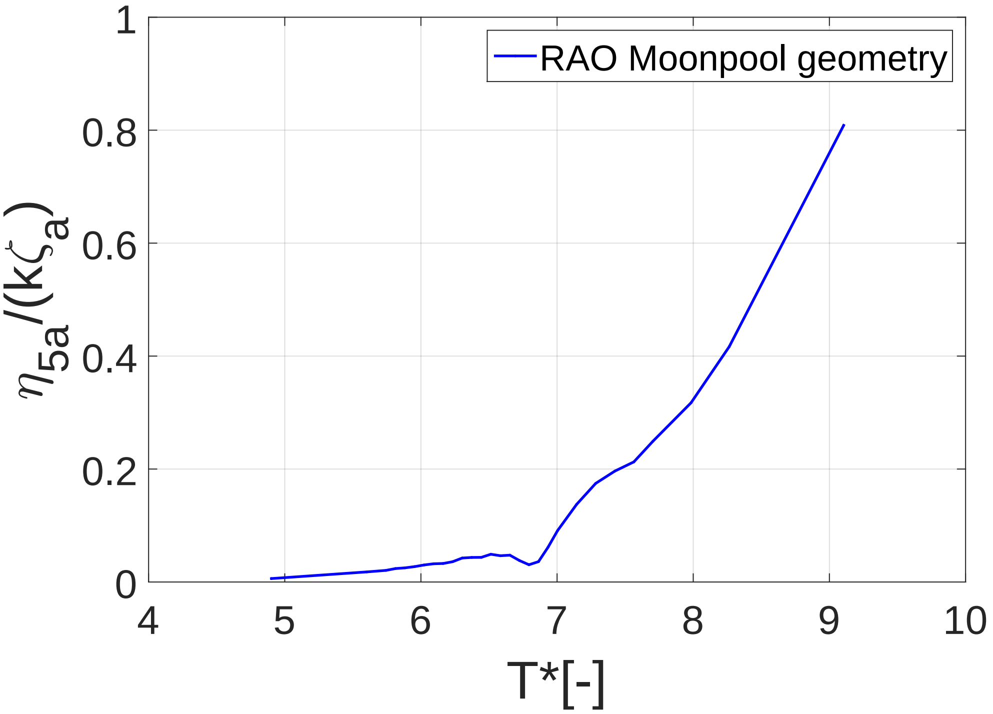

Figure D.80: Pitch, wave steepness 1/30, rounded inlet, Mass at ends

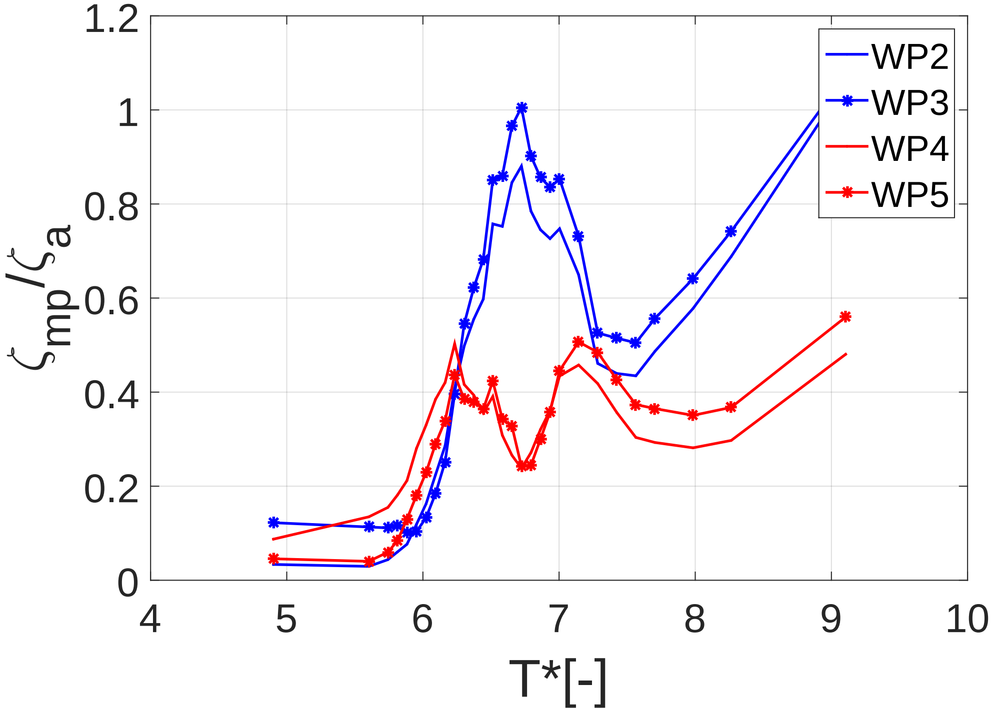

Figure D.81: Moonpools, wave steepness 1/30, rounded inlet, Mass at ends

D.2.2 Squared Inlet Corners

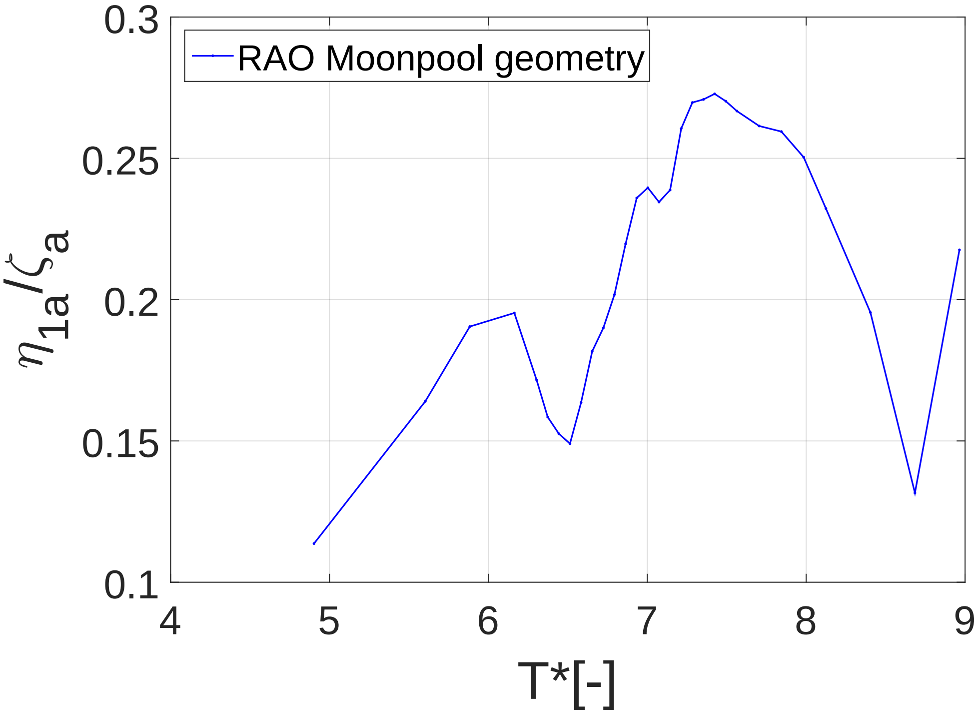

Figure D.82: Surge, wave steepness 1/60, squared inlet, Mass in center

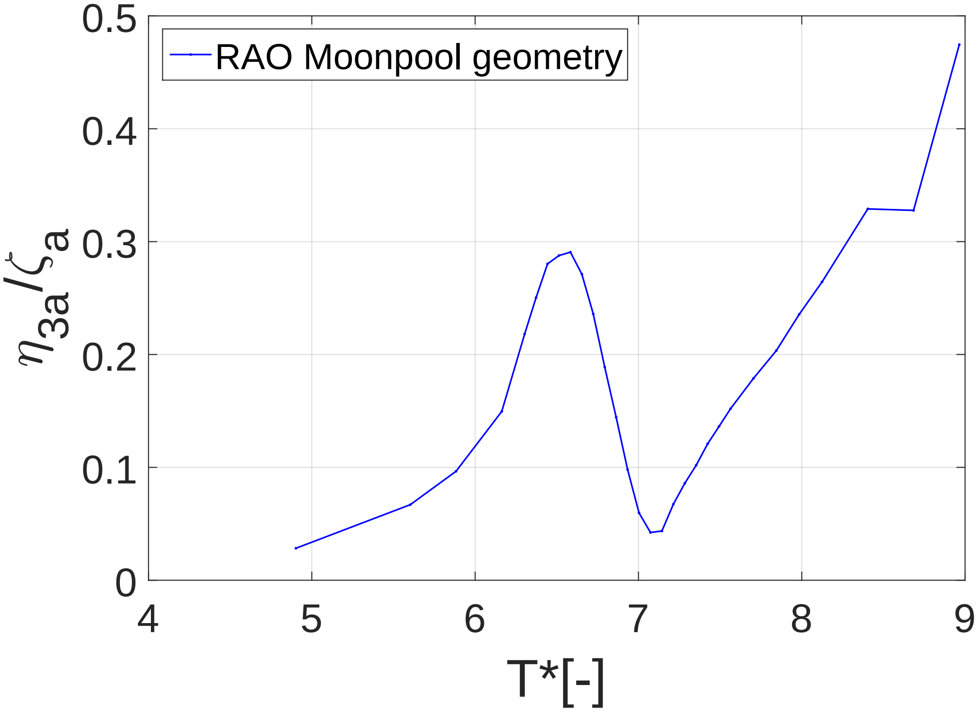

Figure D.83: Heave, wave steepness 1/60, squared inlet, Mass in center

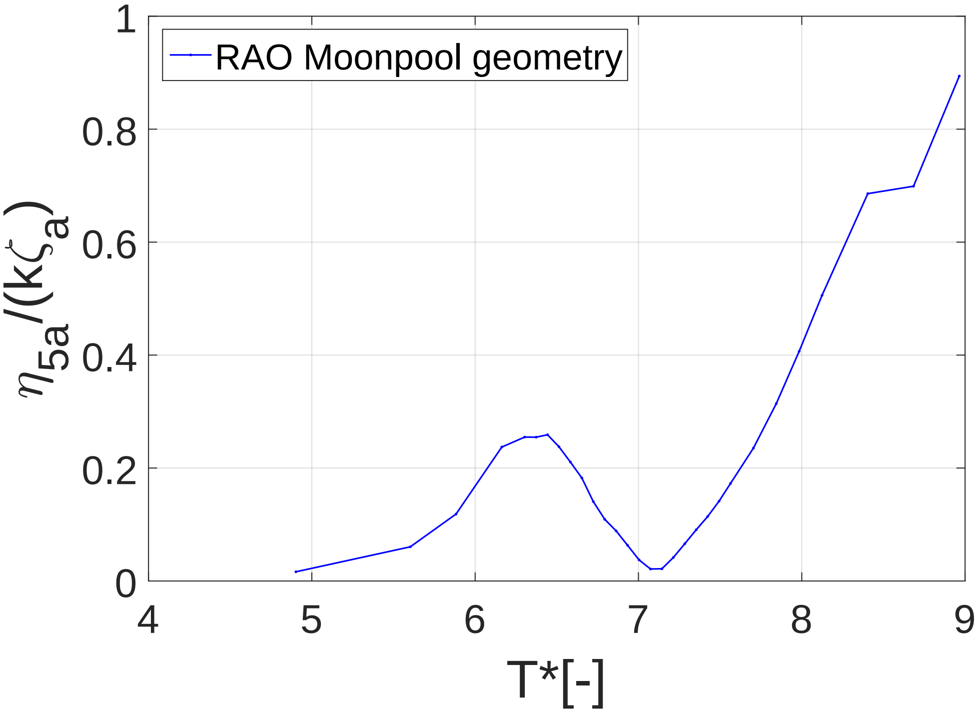

Figure D.84: Pitch, wave steepness 1/60, squared inlet, Mass in center

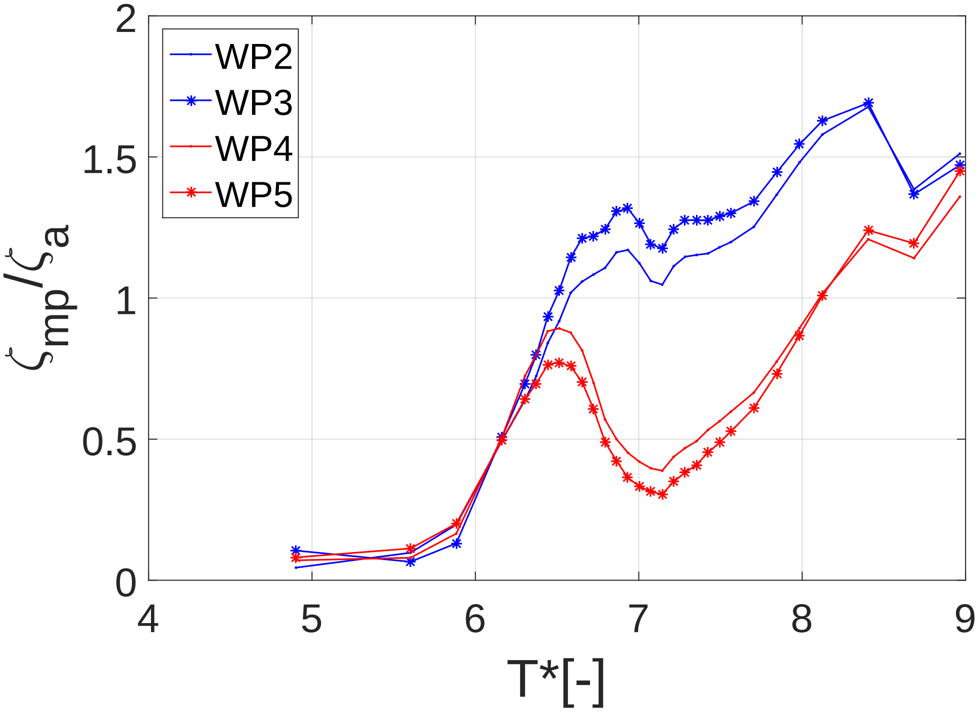

Figure D.85: Moonpools, wave steepness 1/60, squared inlet, Mass in center

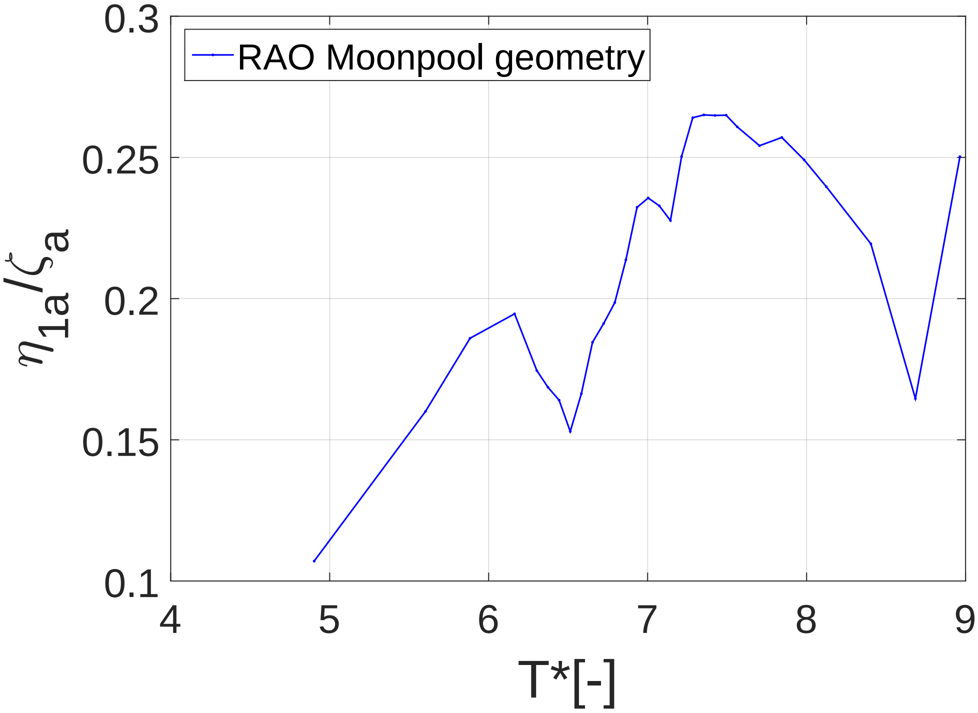

Figure D.86: Surge, wave steepness 1/45, squared inlet, Mass in center

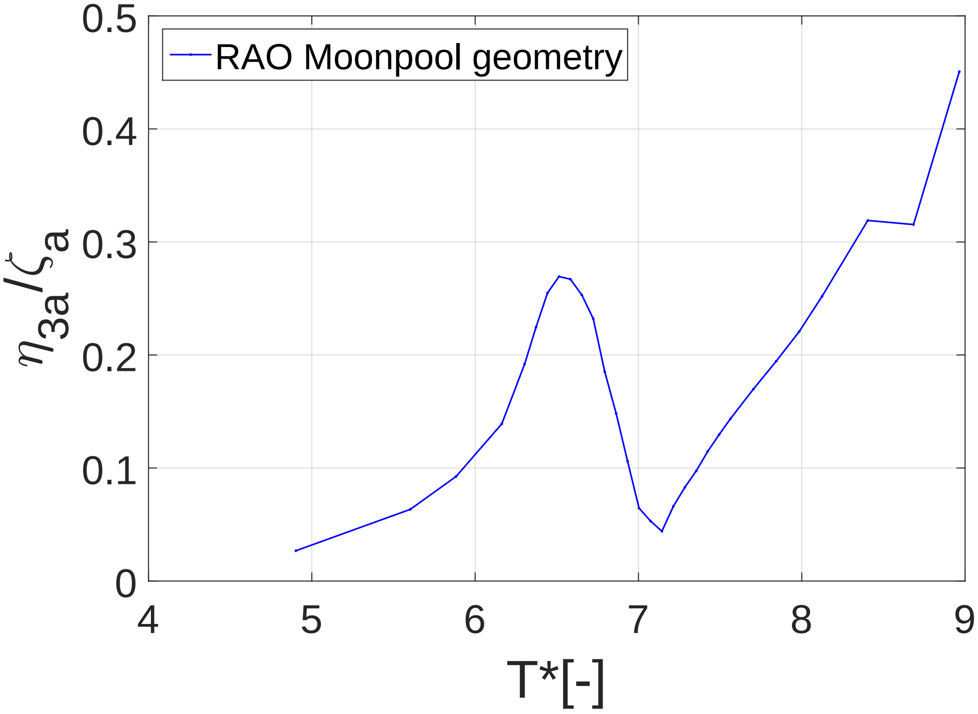

Figure D.87: Heave, wave steepness 1/45, squared inlet, Mass in center

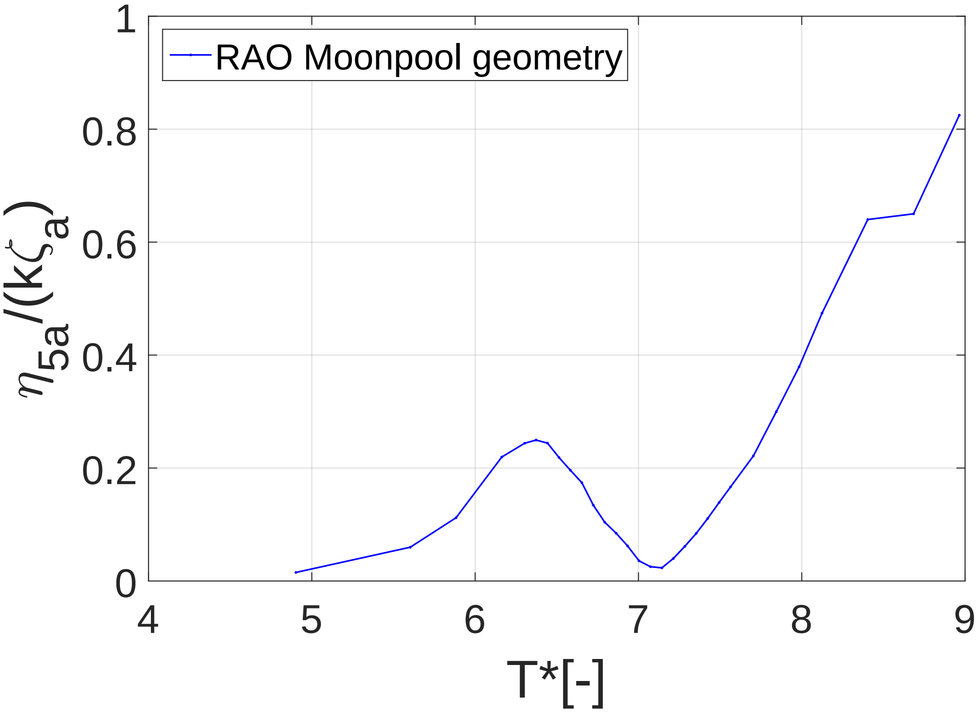

Figure D.88: Pitch, wave steepness 1/45, squared inlet, Mass in center

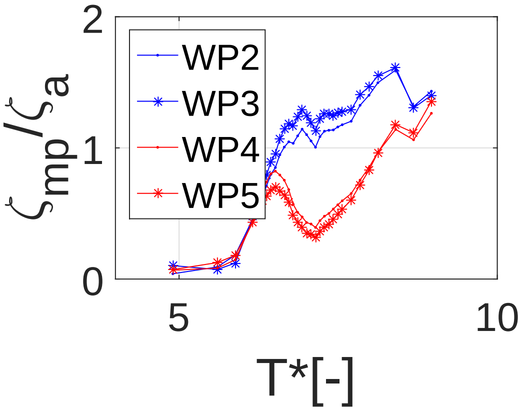

Figure D.89: Moonpools, wave steepness 1/45, squared inlet, Mass in center

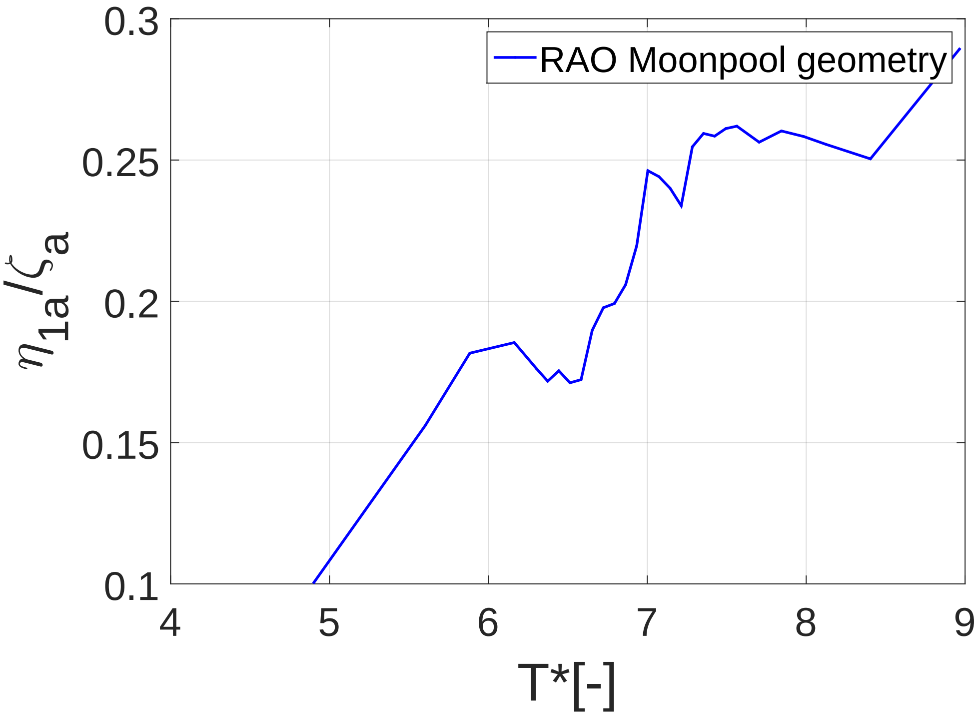

Figure D.90: Surge, wave steepness 1/30, squared inlet, Mass in center

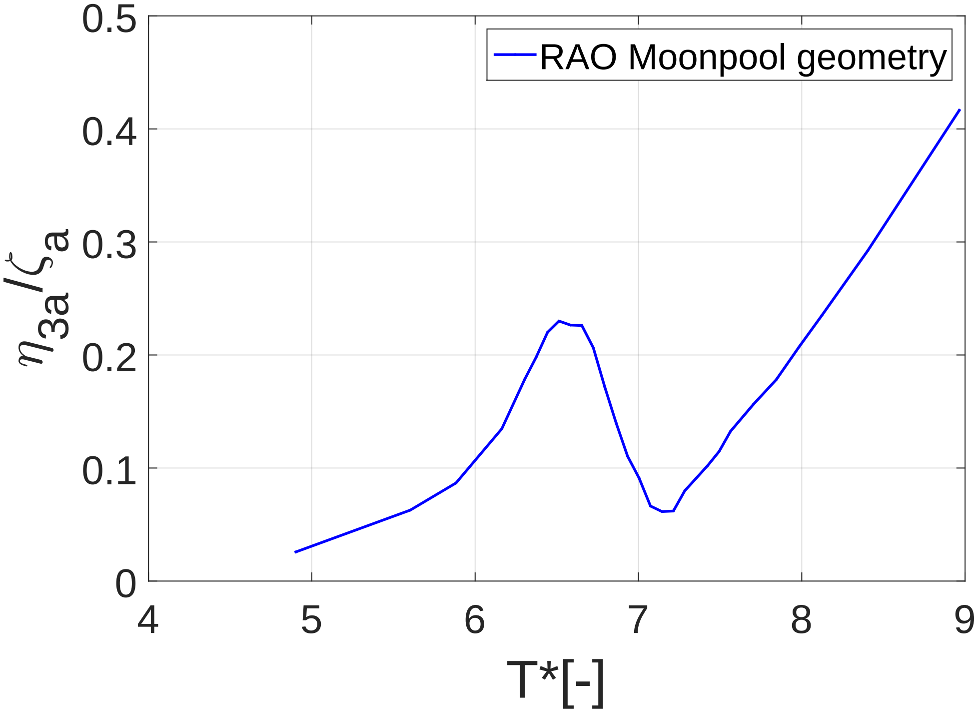

Figure D.91: Heave, wave steepness 1/30, squared inlet, Mass in center

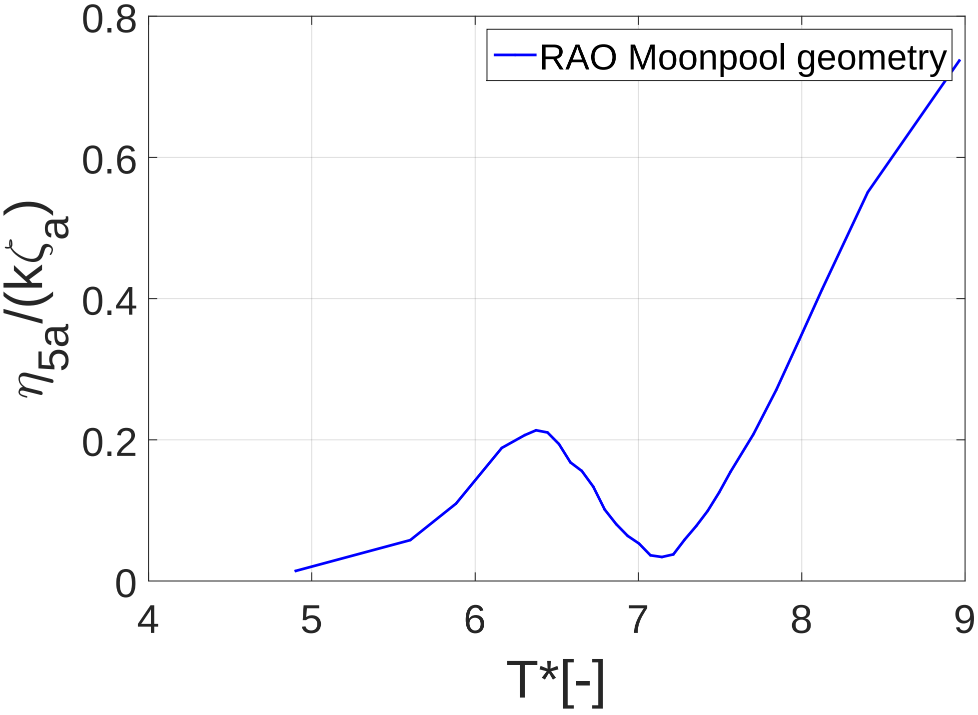

Figure D.92: Pitch, wave steepness 1/30, squared inlet, Mass in center

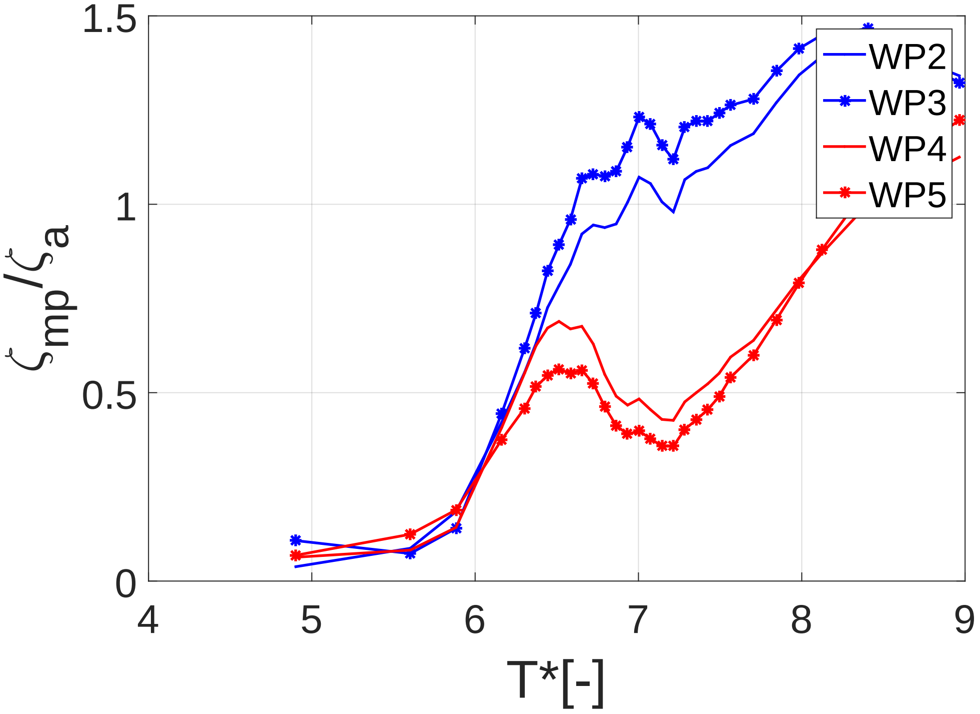

Figure D.93: Moonpools, wave steepness 1/30, squared inlet, Mass in center

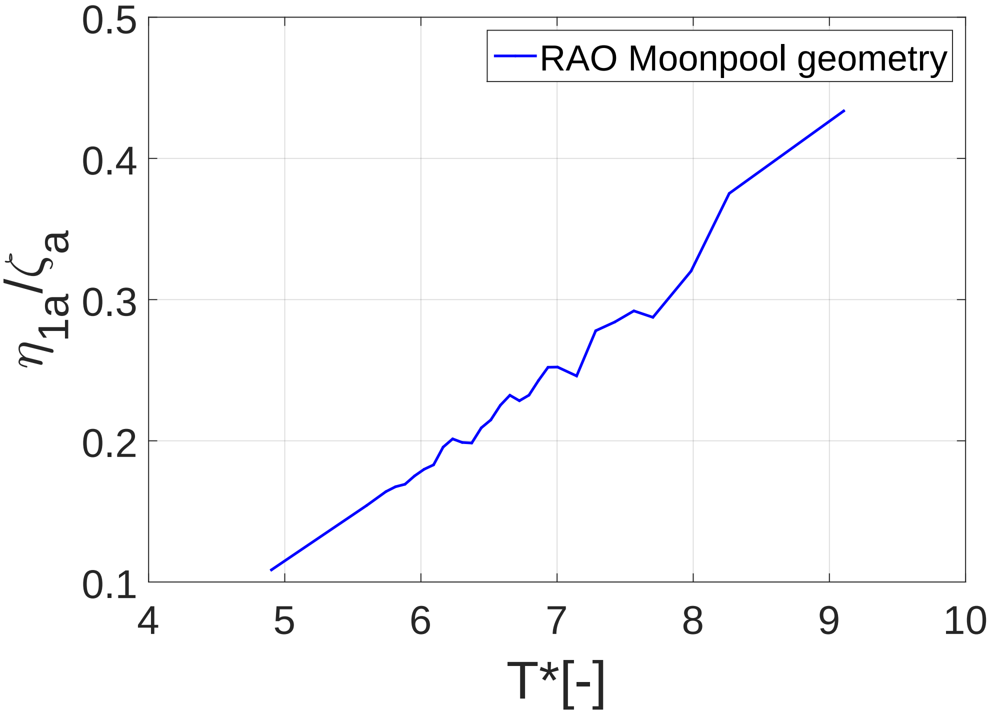

Figure D.94: Surge, wave steepness 1/60, squared inlet, Mass at ends

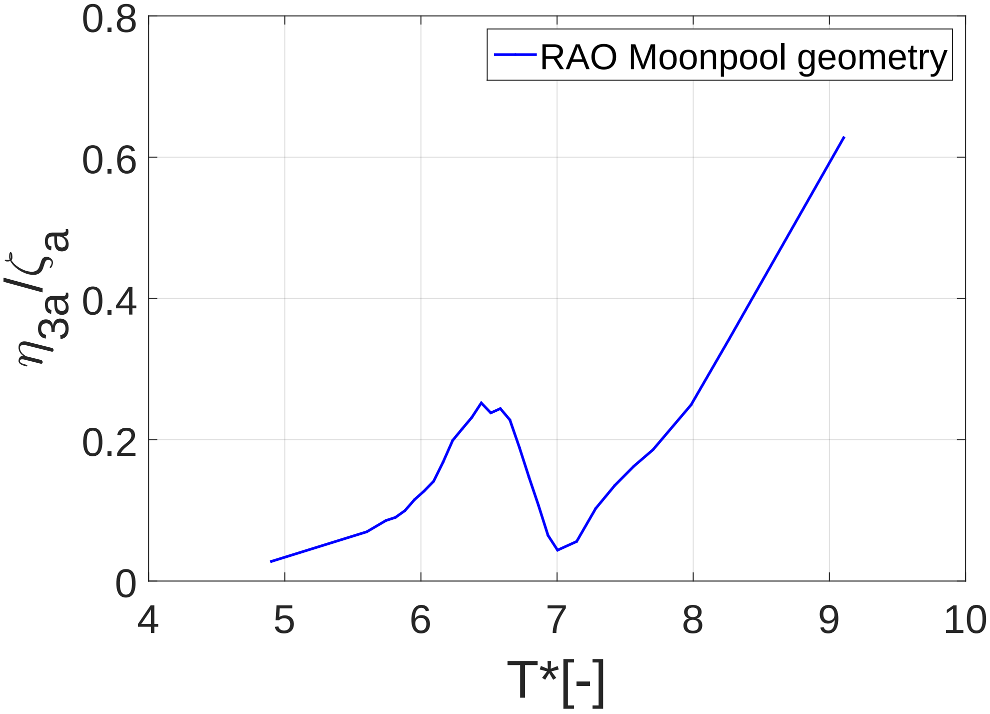

Figure D.95: Heave, wave steepness 1/60, squared inlet, Mass at ends

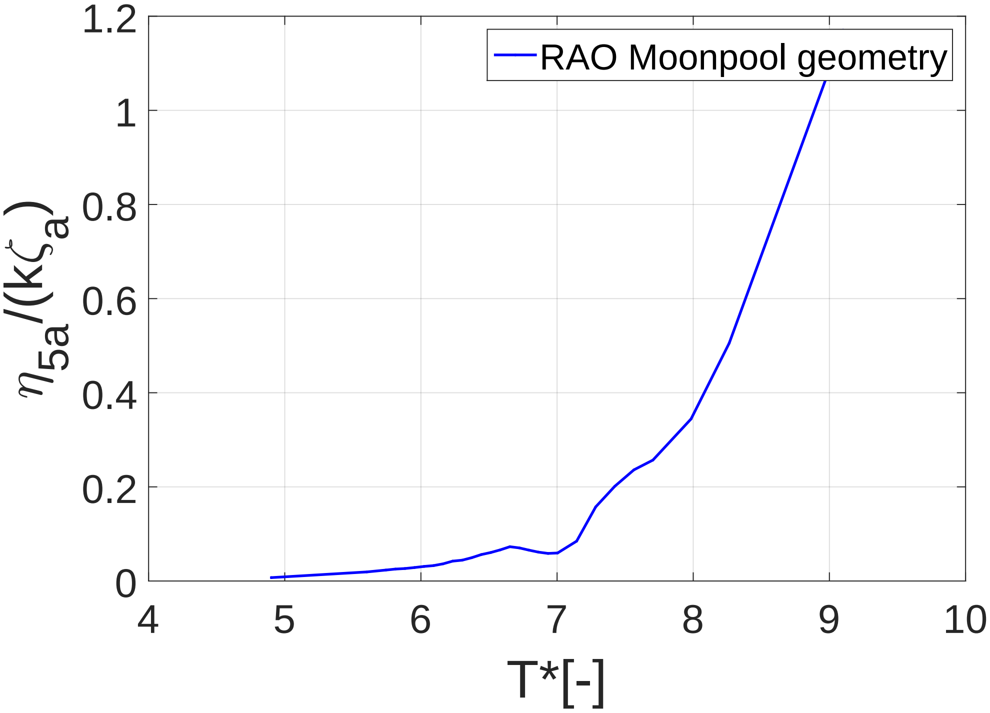

Figure D.96: Pitch, wave steepness 1/60, squared inlet, Mass at ends

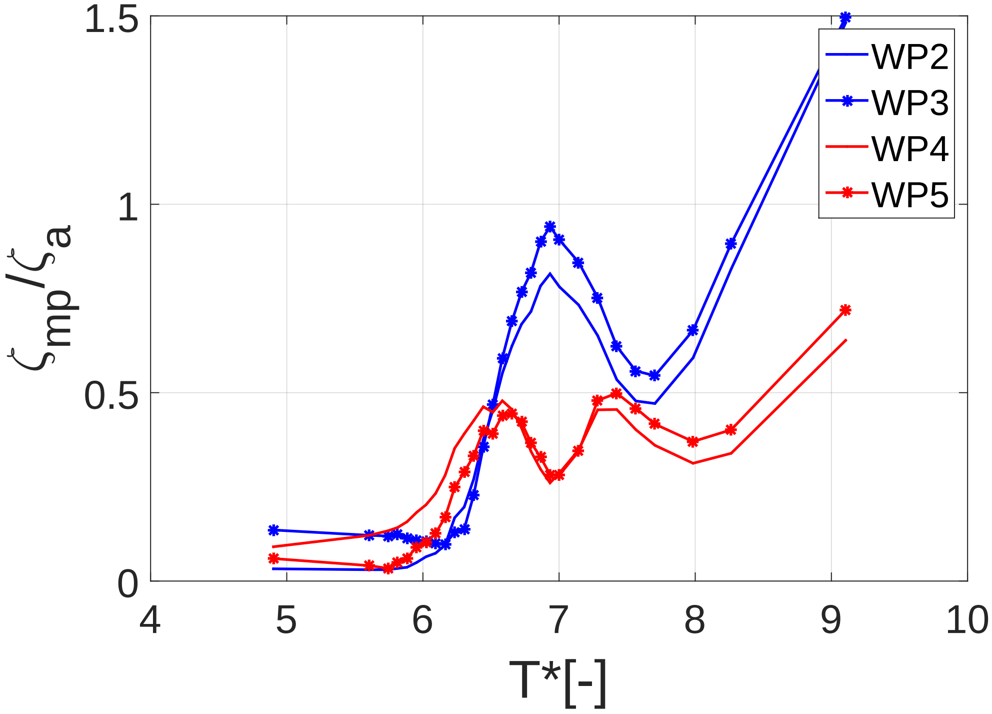

Figure D.97: Moonpools, wave steepness 1/60, squared inlet, Mass at ends

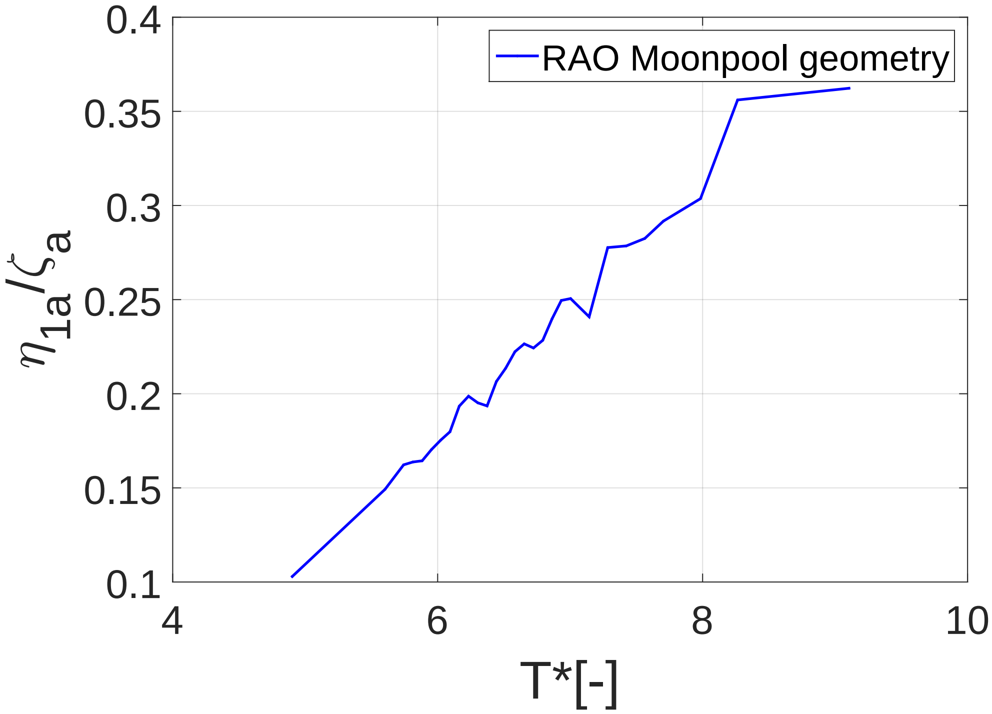

Figure D.98: Surge, wave steepness 1/45, squared inlet, Mass at ends

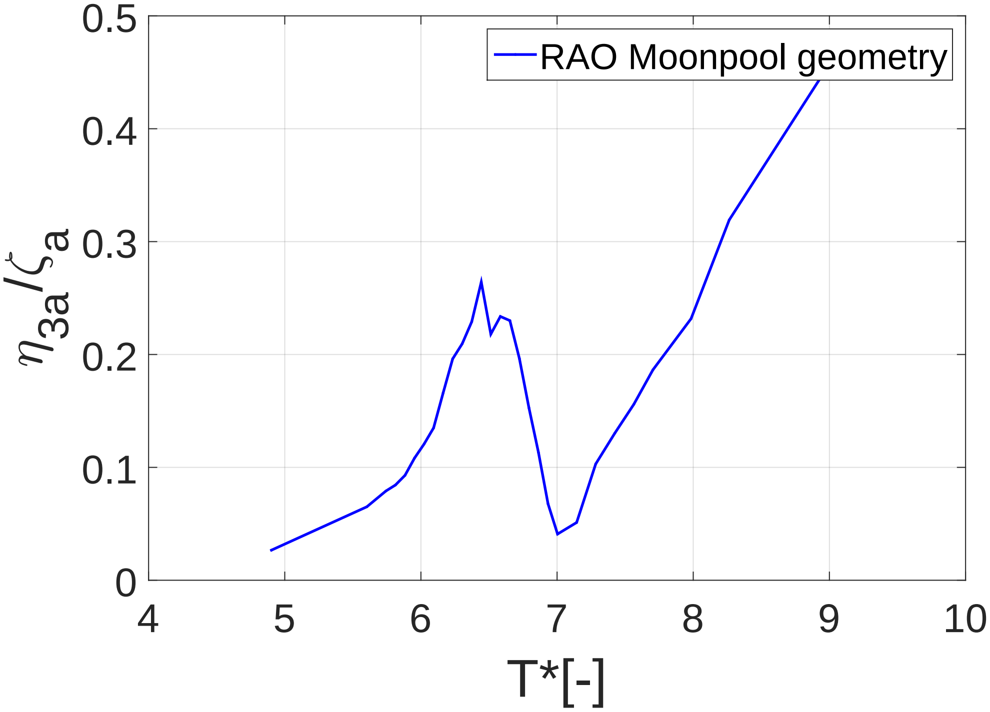

Figure D.99: Heave, wave steepness 1/45, squared inlet, Mass at ends

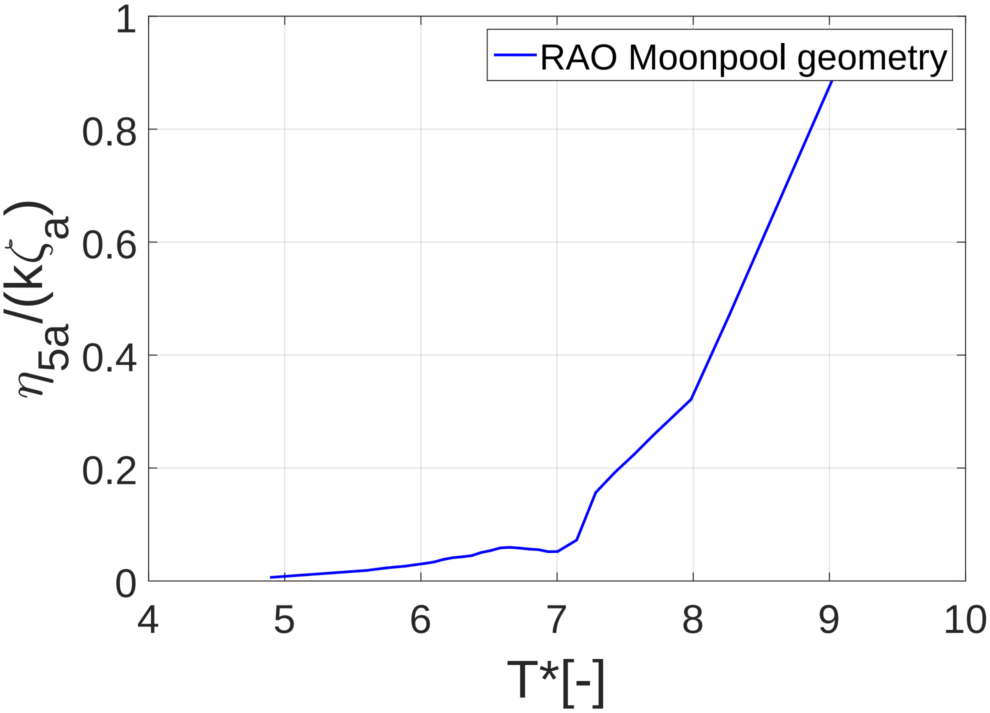

Figure D.100: Pitch, wave steepness 1/45, squared inlet, Mass at ends

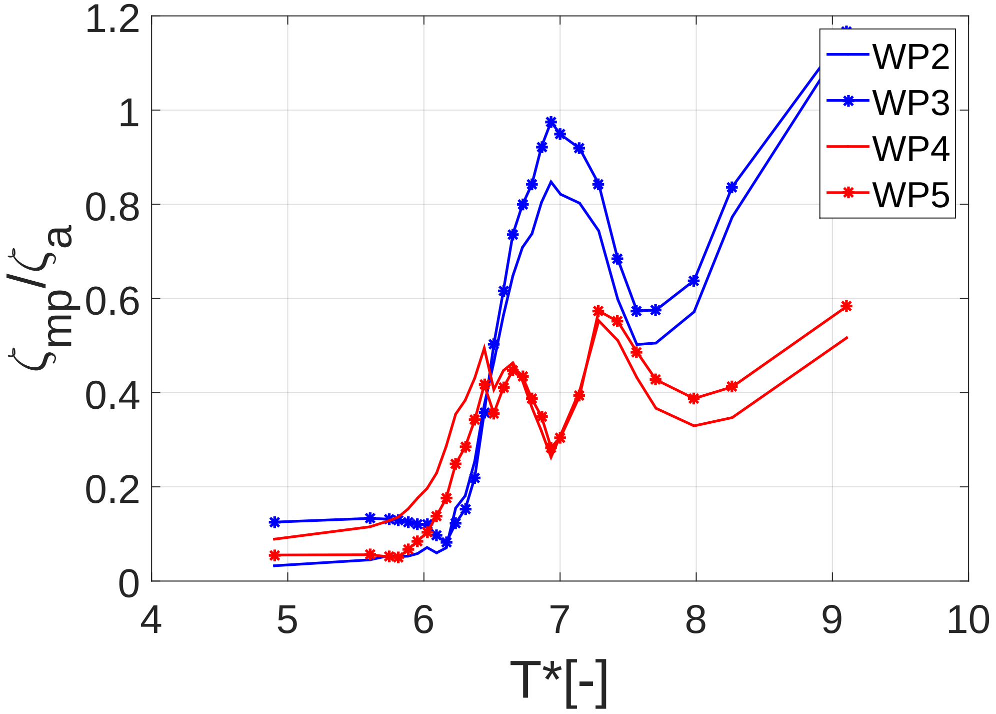

Figure D.101: Moonpools, wave steepness 1/45, squared inlet, Mass at ends

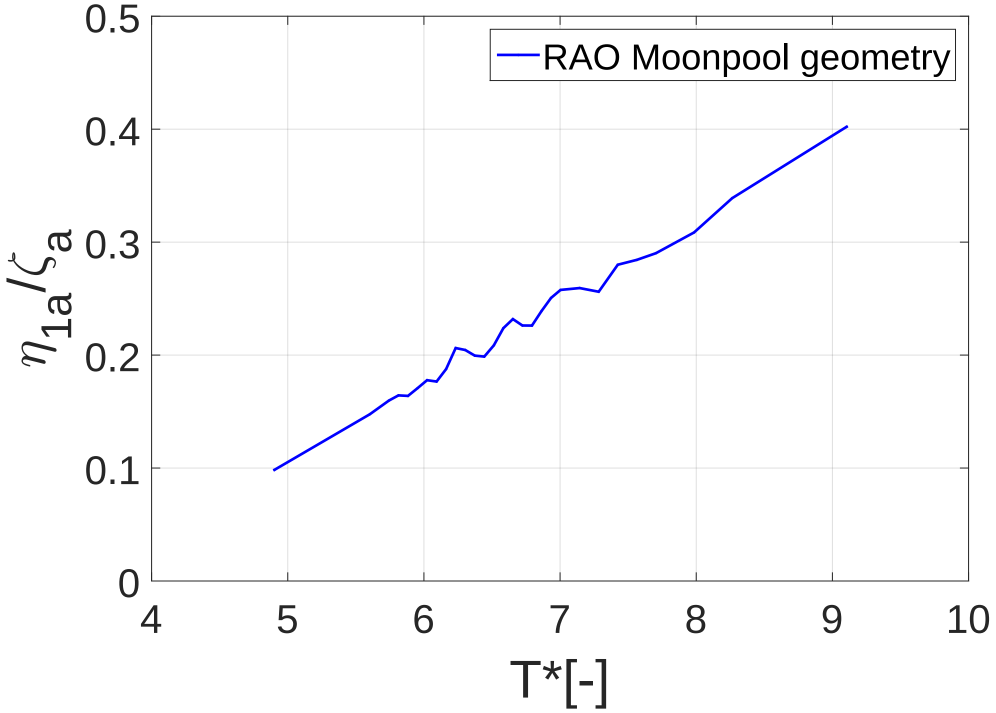

Figure D.102: Surge, wave steepness 1/30, squared inlet, Mass at ends

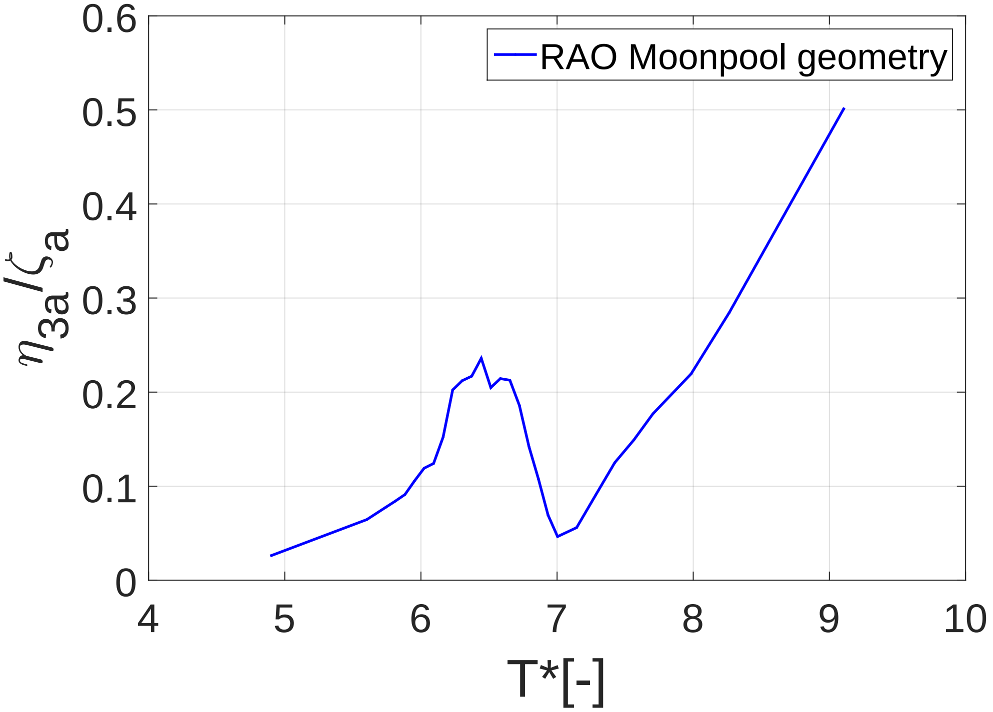

Figure D.103: Heave, wave steepness 1/30, squared inlet, Mass at ends

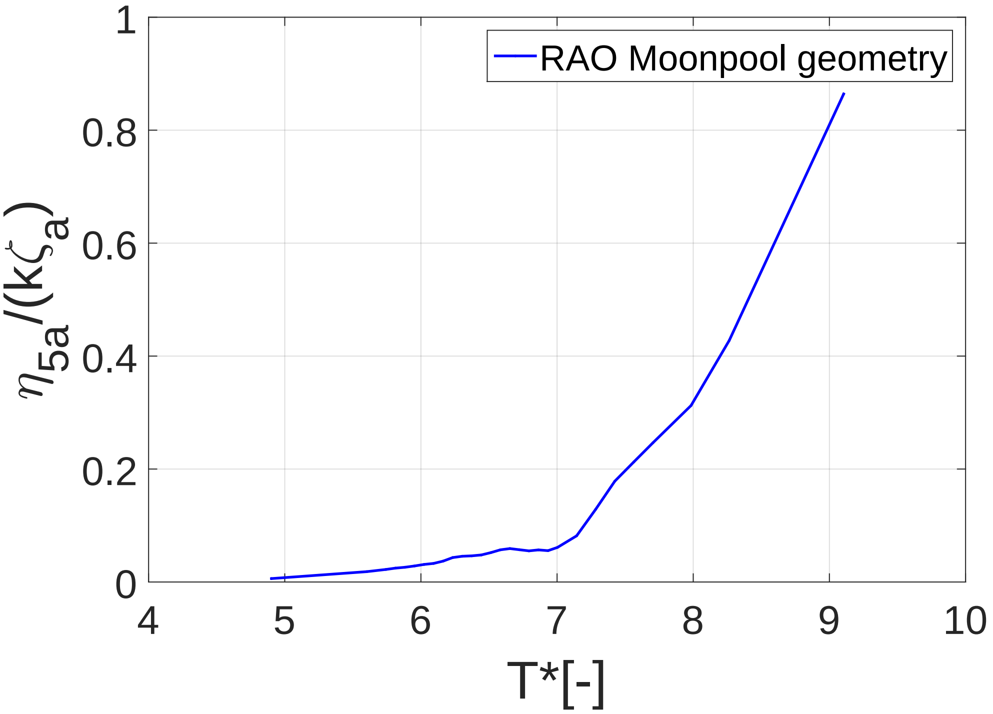

Figure D.104: Pitch, wave steepness 1/30, squared inlet, Mass at ends

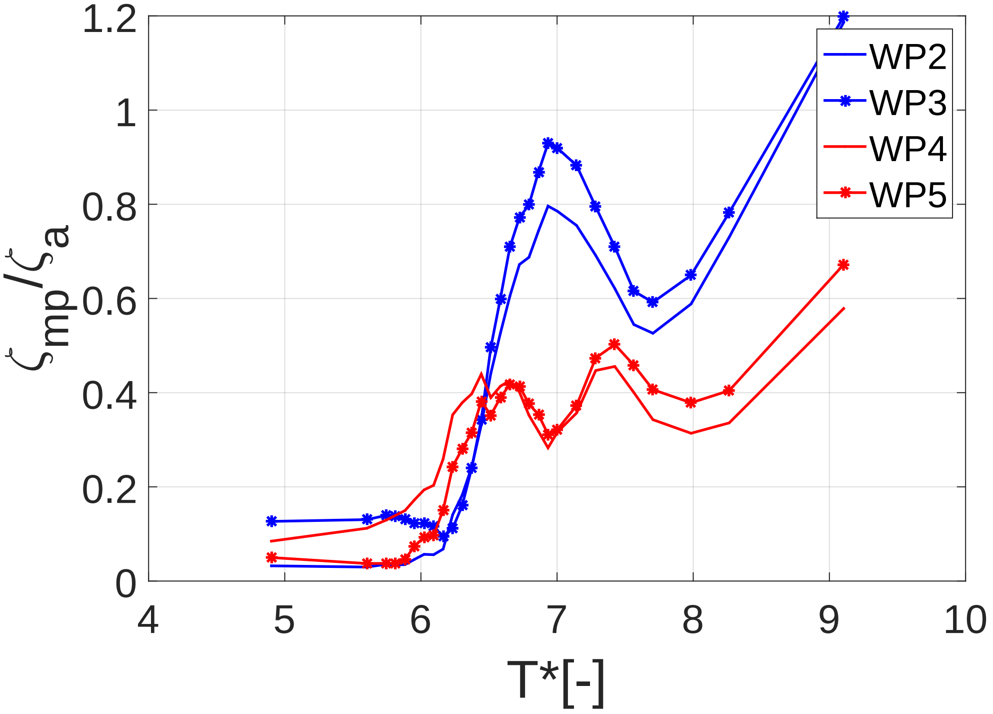

Figure D.105: Moonpools, wave steepness 1/30, squared inlet, Mass at ends

D.2.3 Appended Inlet Corners

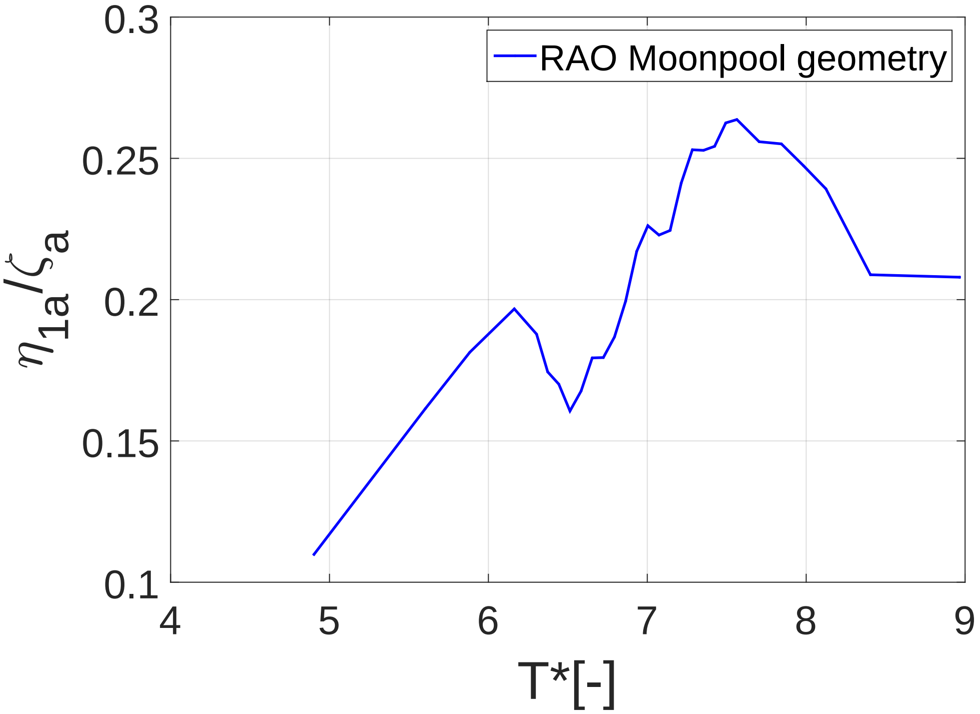

Figure D.106: Surge, wave steepness 1/60, App. 1 inlet, Mass in center

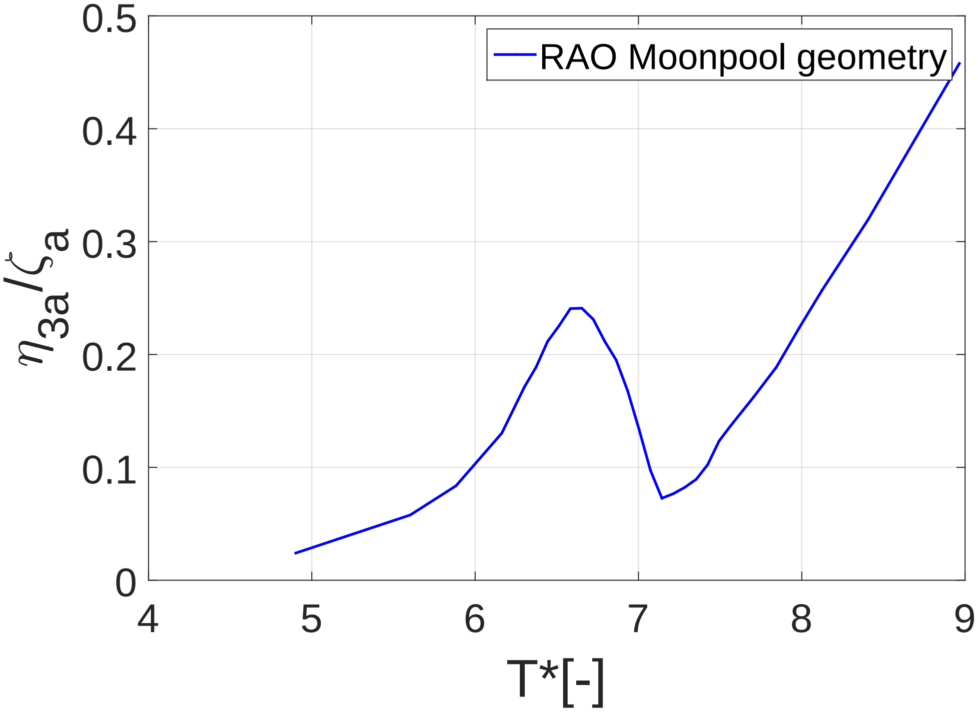

Figure D.107: Heave, wave steepness 1/60, App. 1 inlet, Mass in center

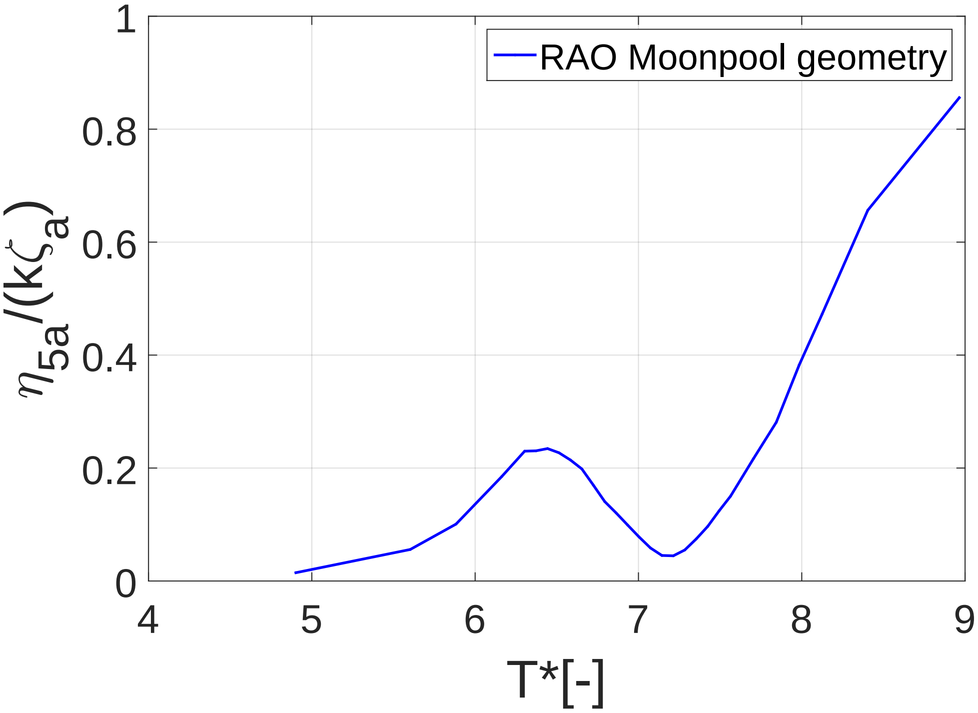

Figure D.108: Pitch, wave steepness 1/60, App. 1 inlet, Mass in center

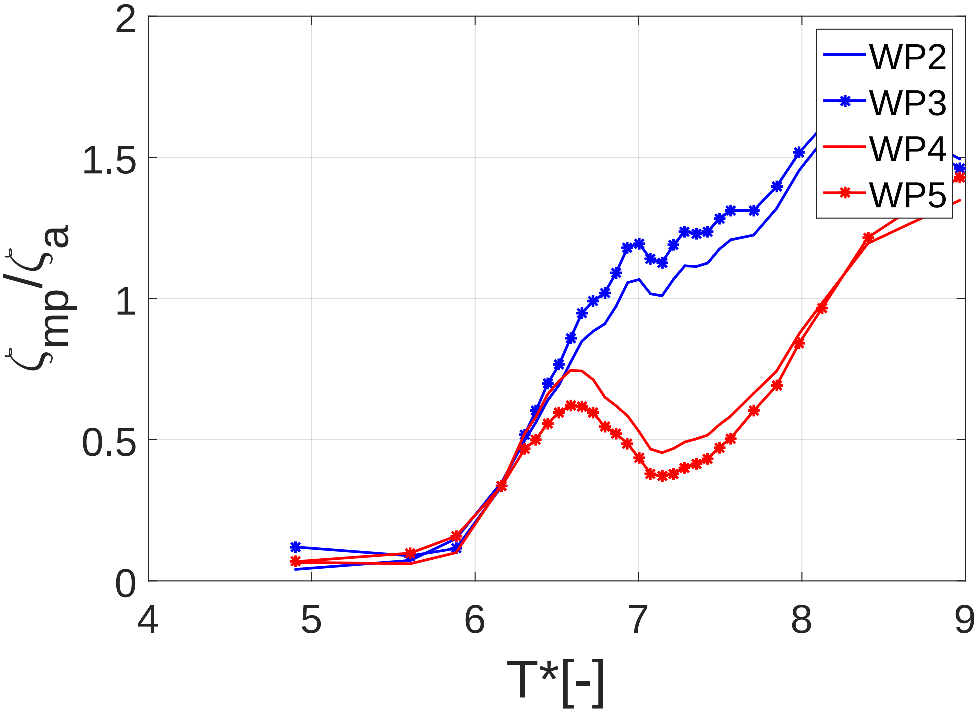

Figure D.109: Moonpools, wave steepness 1/60, App. 1 inlet, Mass in center

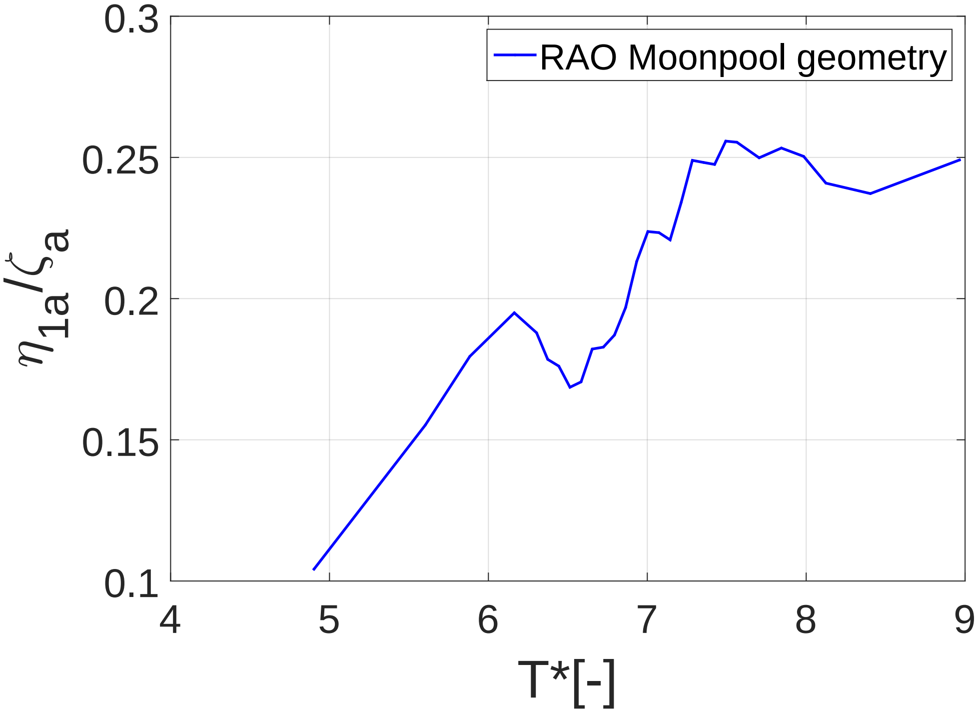

Figure D.110: Surge, wave steepness 1/45, App. 1 inlet, Mass in center

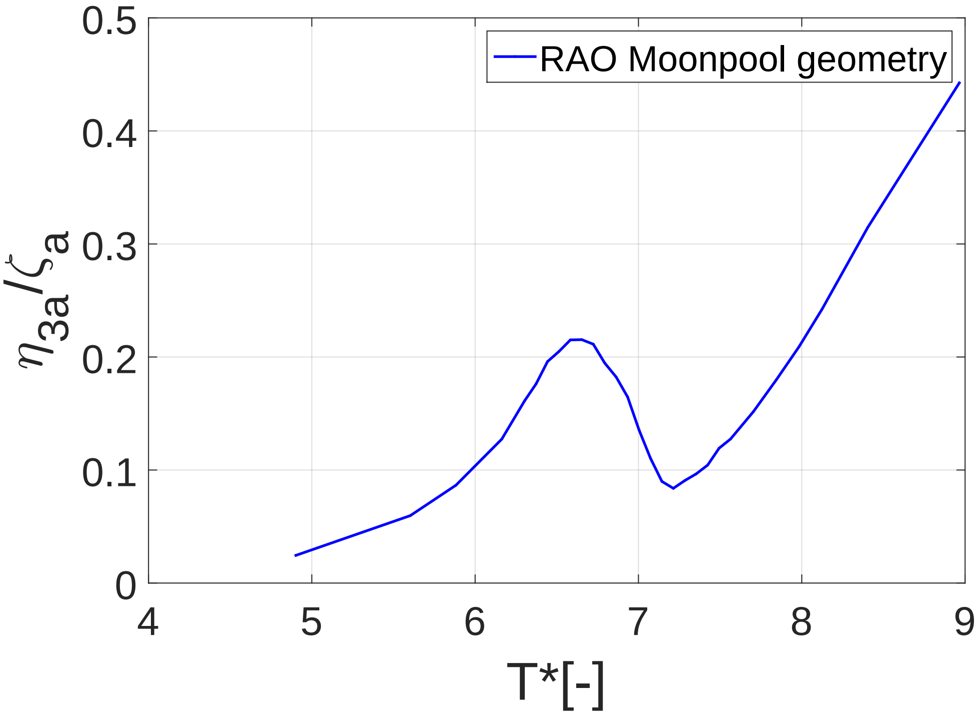

Figure D.111: Heave, wave steepness 1/45, App. 1 inlet, Mass in center

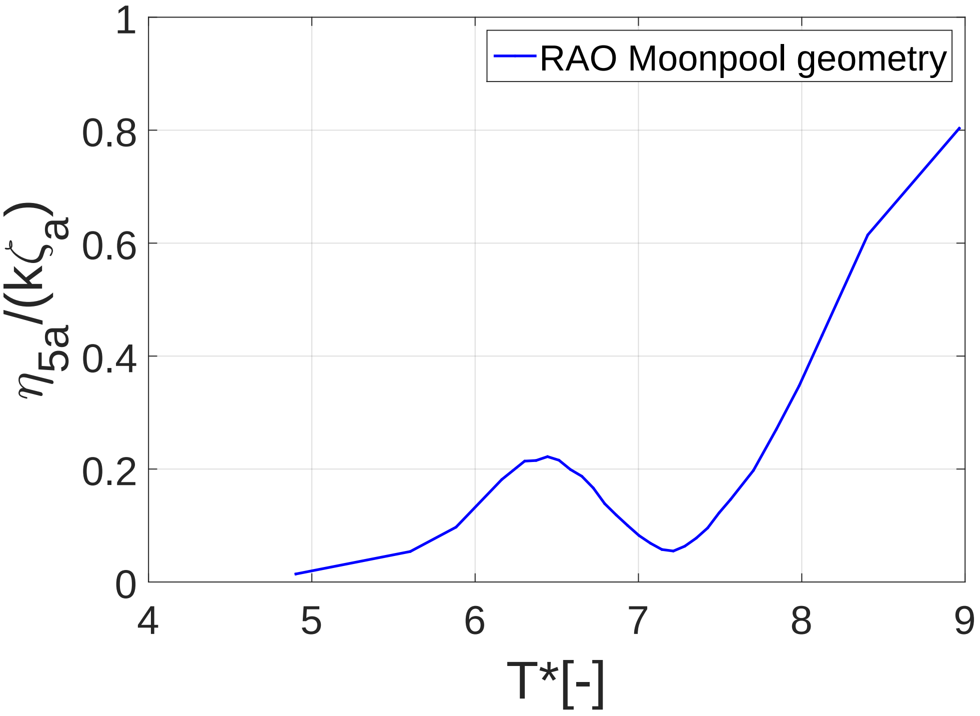

Figure D.112: Pitch, wave steepness 1/45, App. 1 inlet, Mass in center

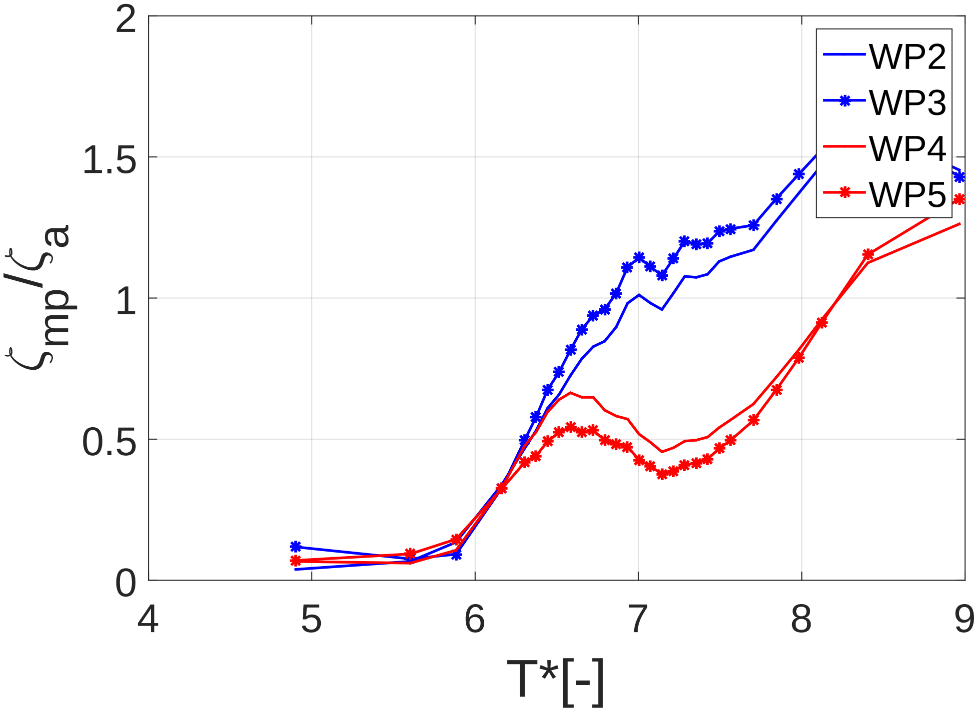

Figure D.113: Moonpools, wave steepness 1/45, App. 1 inlet, Mass in center

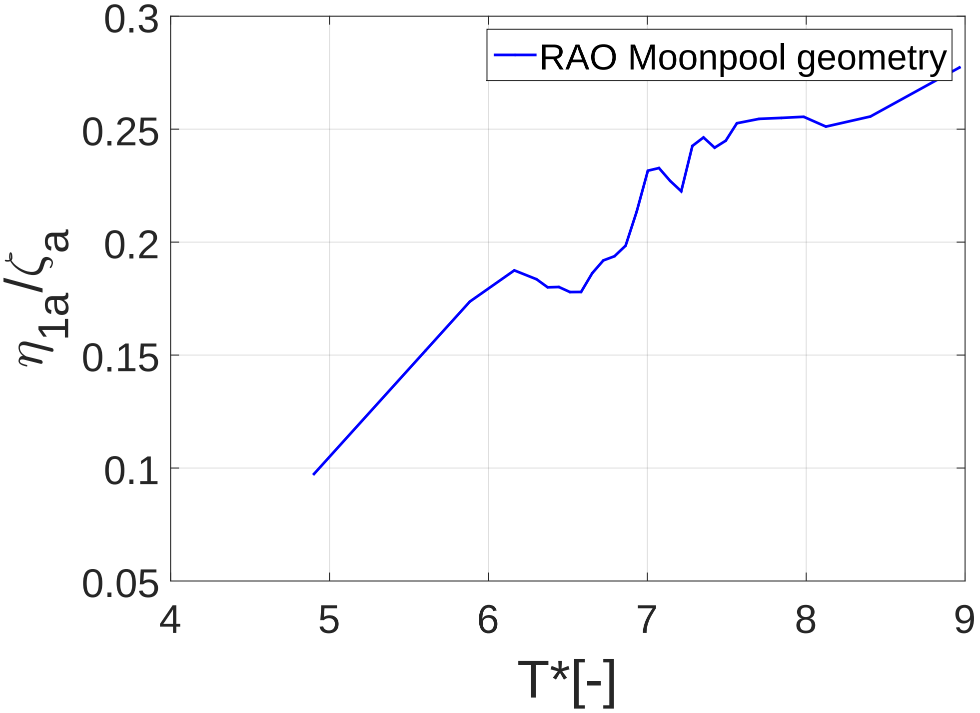

Figure D.114: Surge, wave steepness 1/30, App. 1 inlet, Mass in center

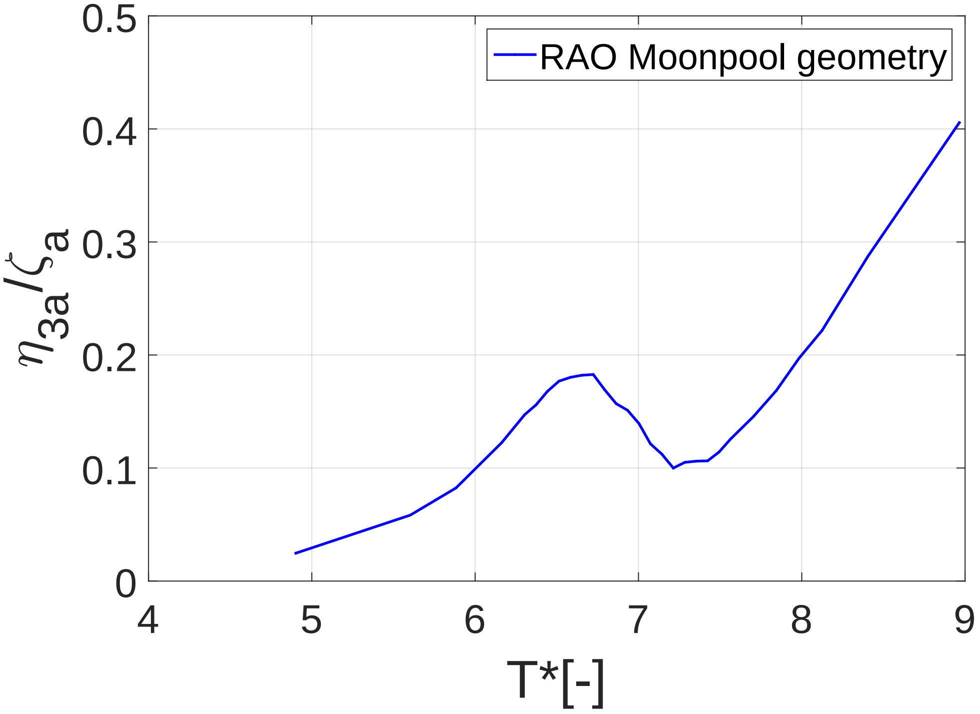

Figure D.115: Heave, wave steepness 1/30, App. 1 inlet, Mass in center

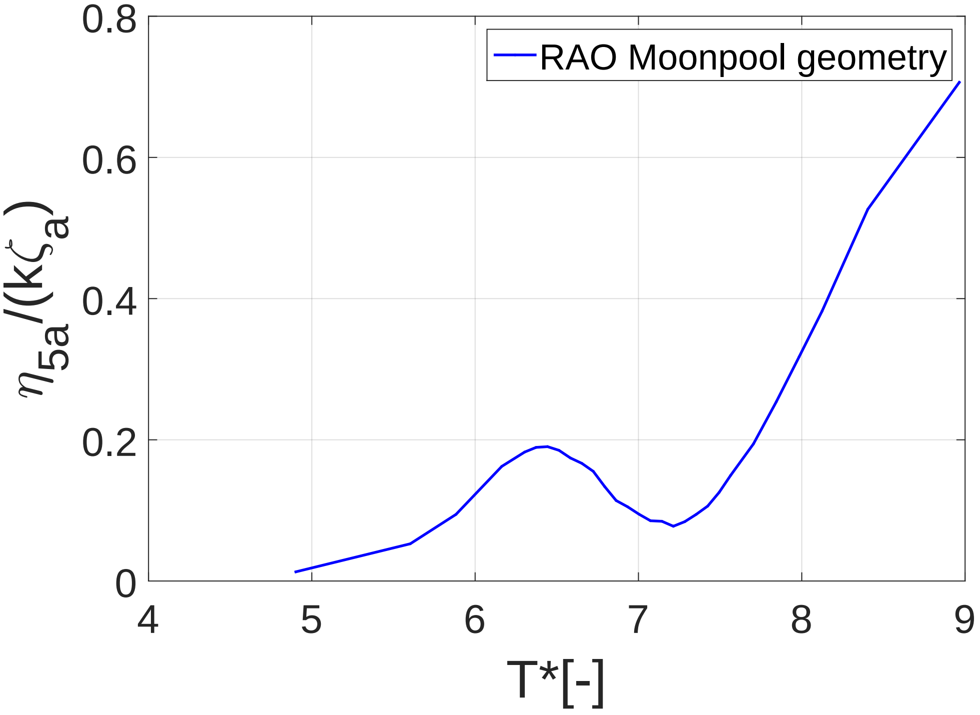

Figure D.116: Pitch, wave steepness 1/30, App. 1 inlet, Mass in center

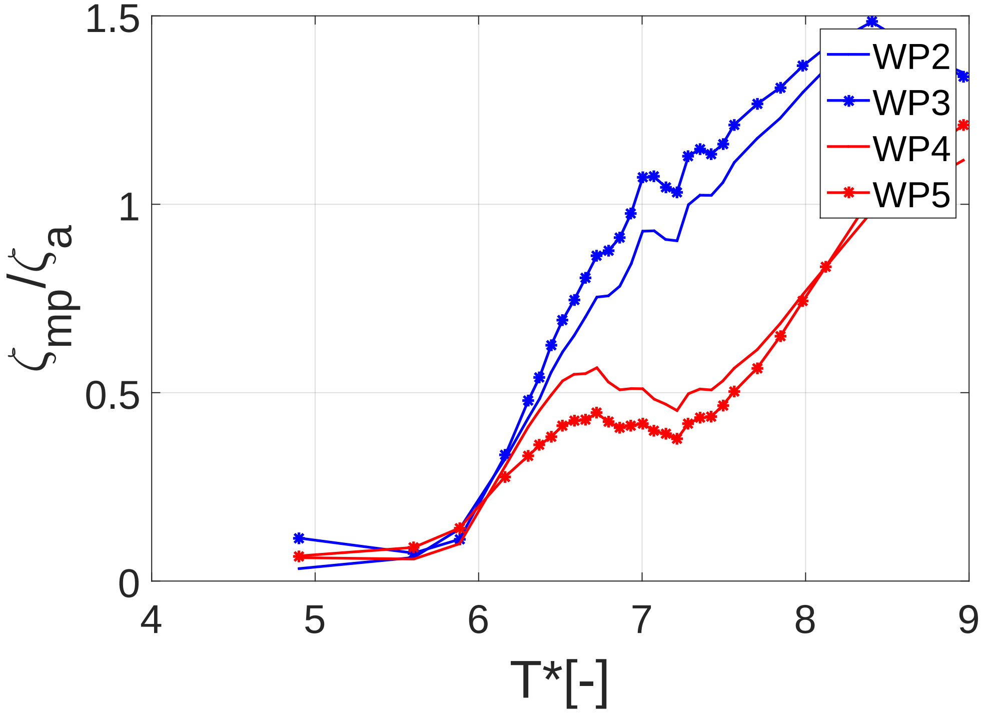

Figure D.117: Moonpools, wave steepness 1/30, App. 1 inlet, Mass in center

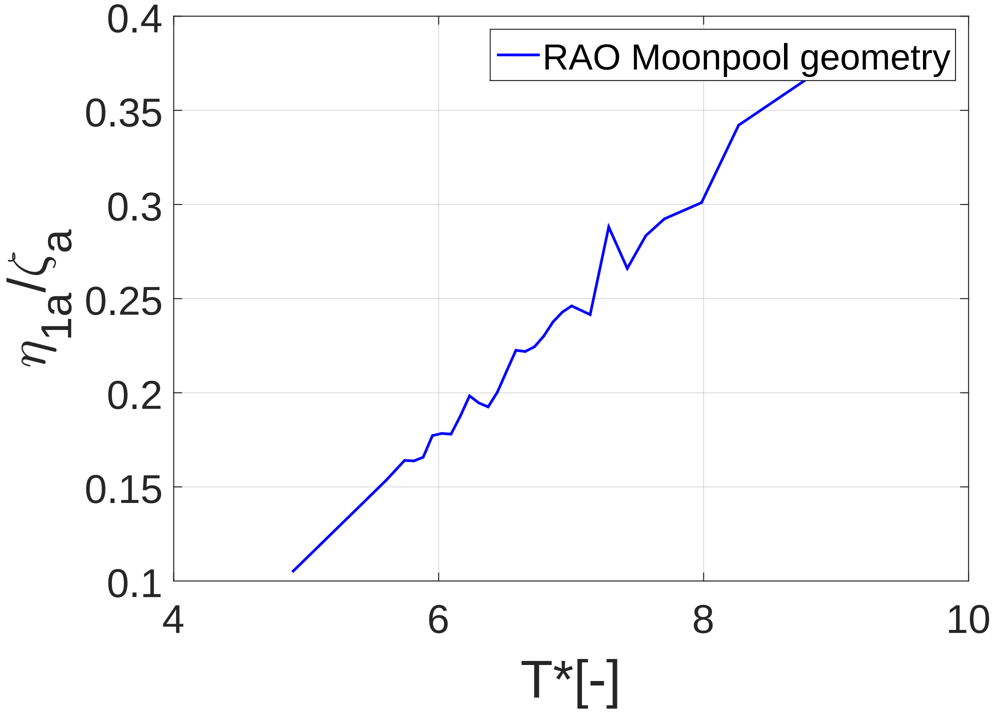

Figure D.118: Surge, wave steepness 1/60, App. 1 inlet, Mass at ends

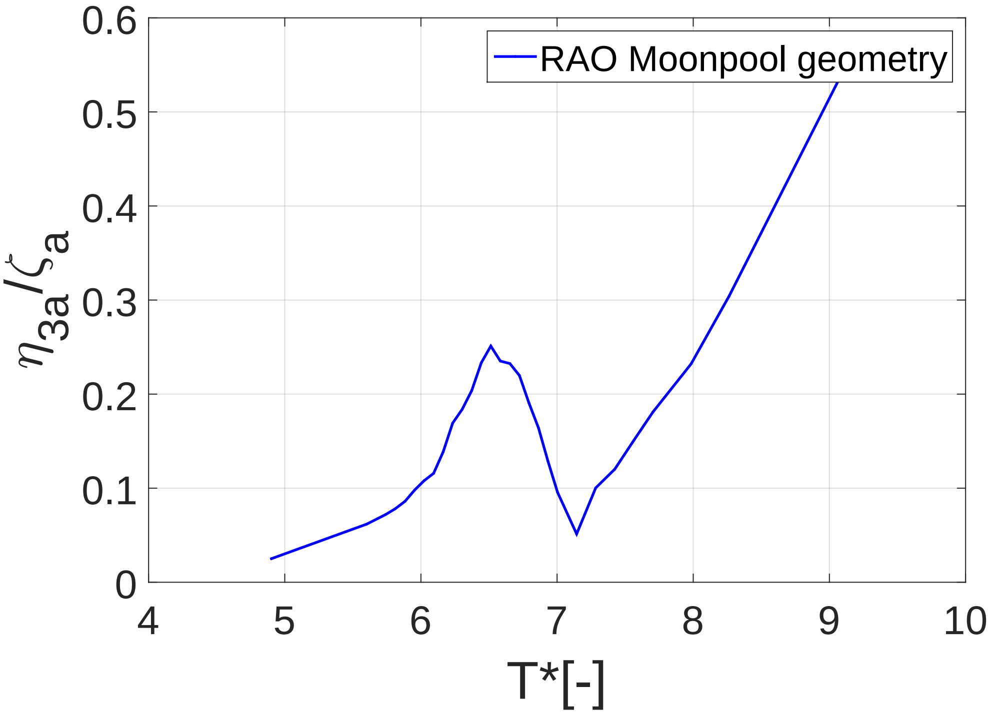

Figure D.119: Heave, wave steepness 1/60, App. 1 inlet, Mass at ends

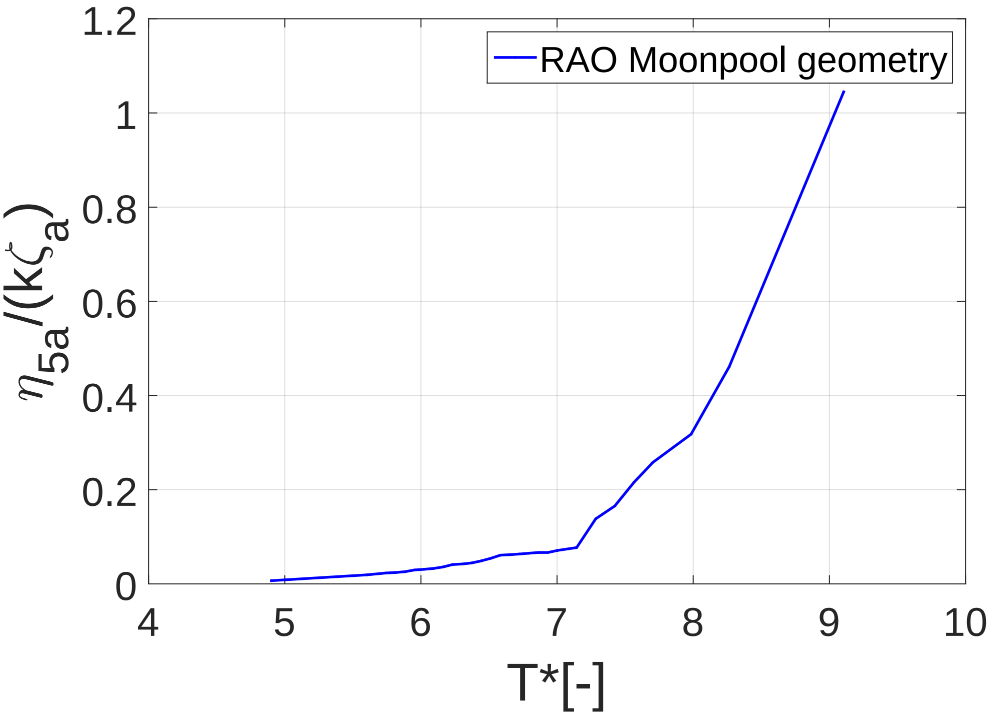

Figure D.120: Pitch, wave steepness 1/60, App. 1 inlet, Mass at ends

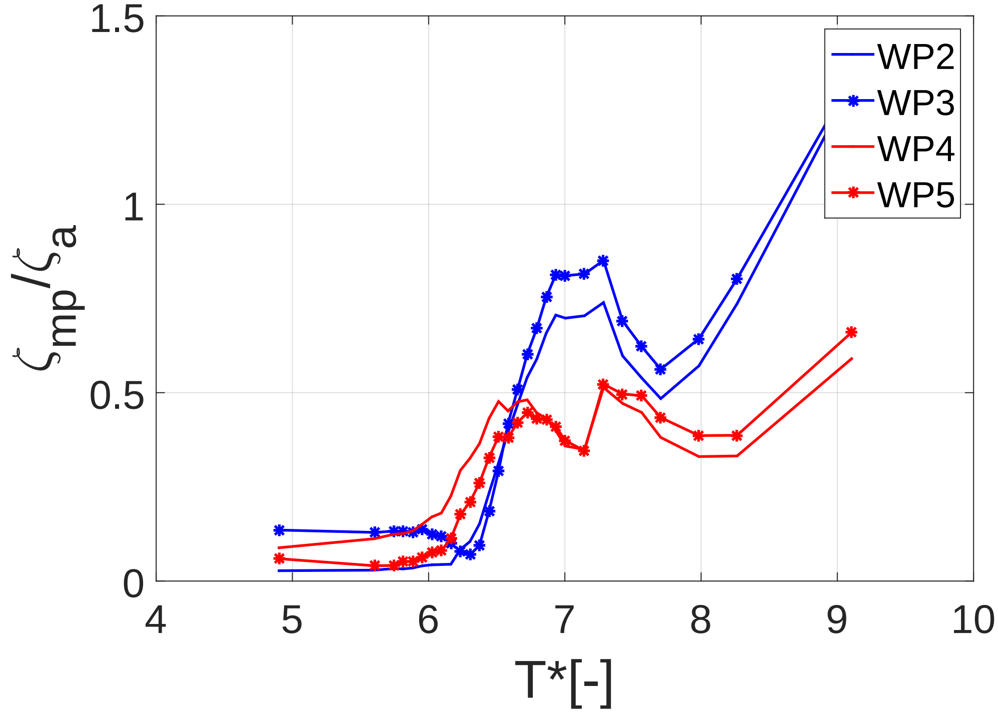

Figure D.121: Moonpools, wave steepness 1/60, App. 1 inlet, Mass at ends

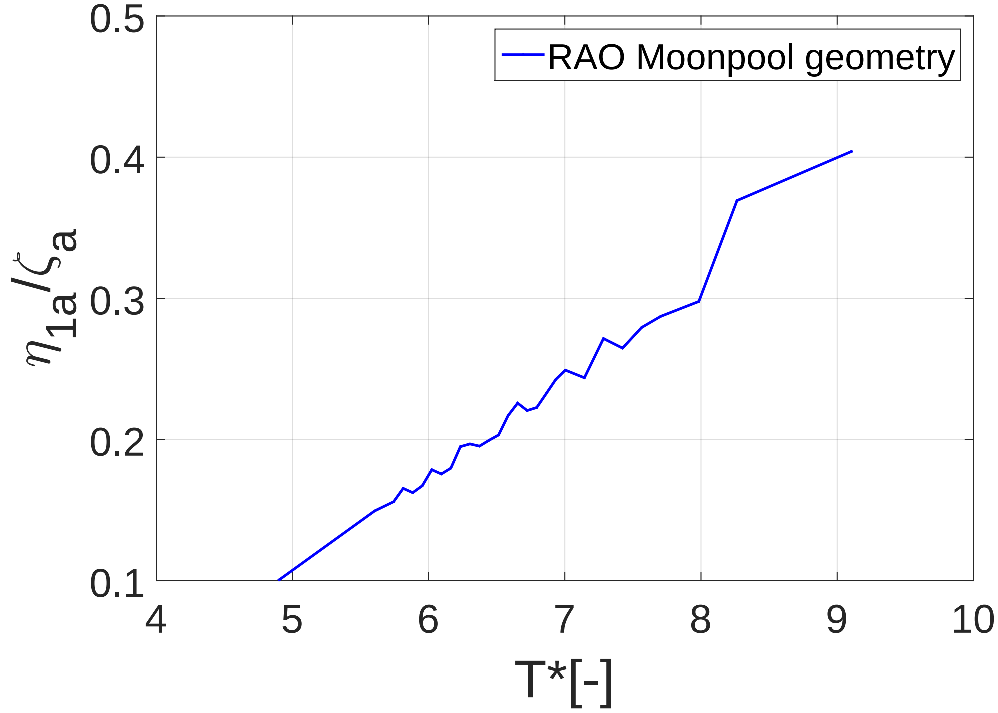

Figure D.122: Surge, wave steepness 1/45, App. 1 inlet, Mass at ends

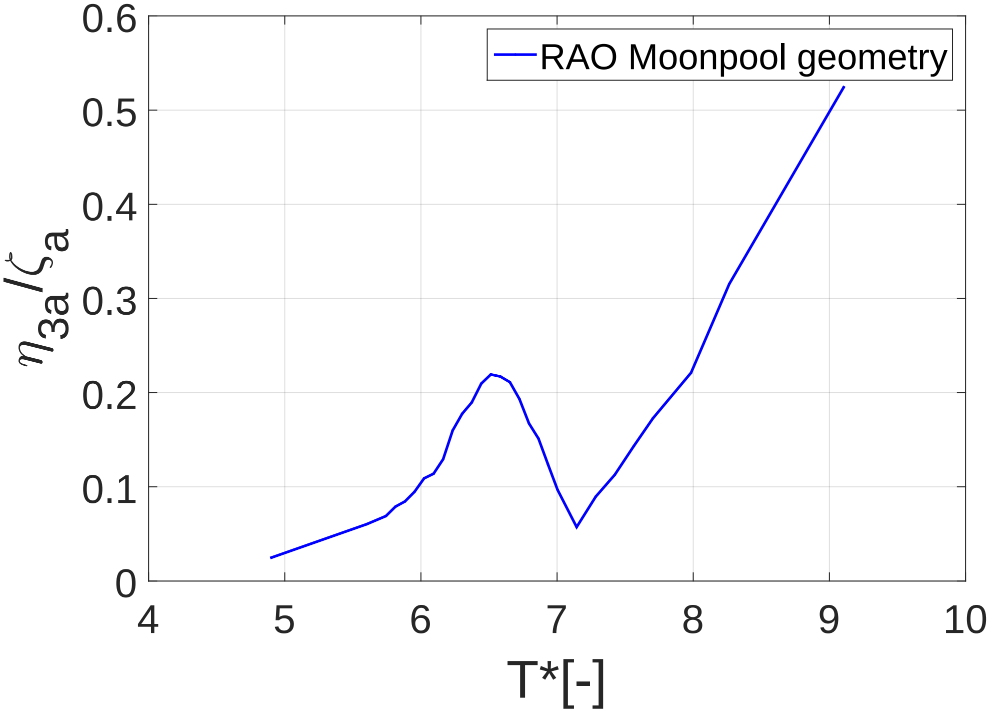

Figure D.123: Heave, wave steepness 1/45, App. 1 inlet, Mass at ends

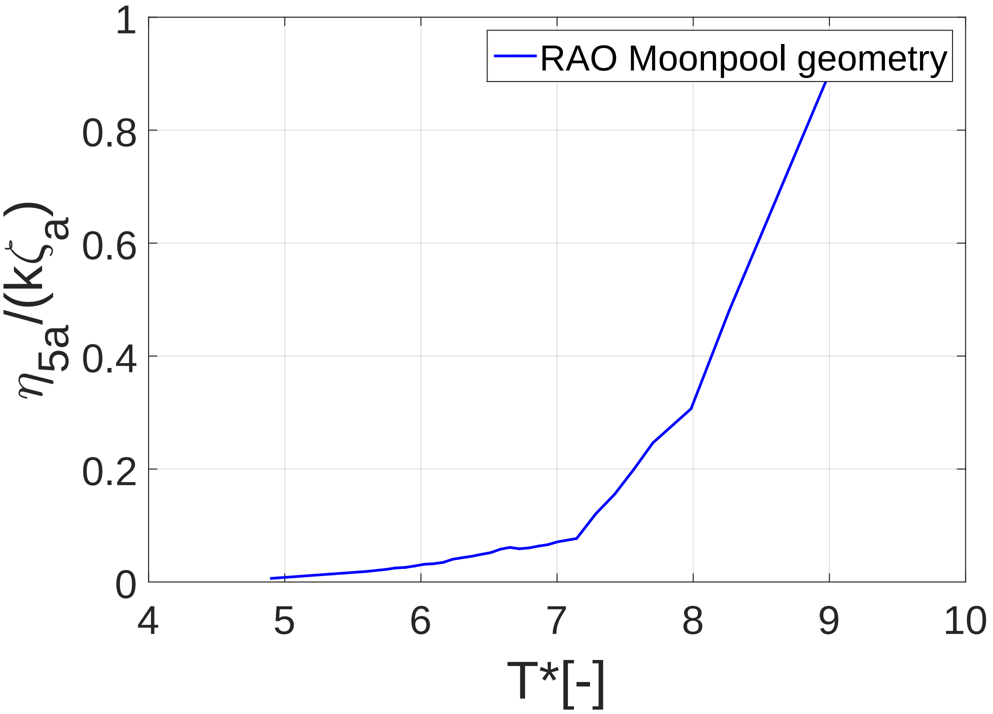

Figure D.124: Pitch, wave steepness 1/45, App. 1 inlet, Mass at ends

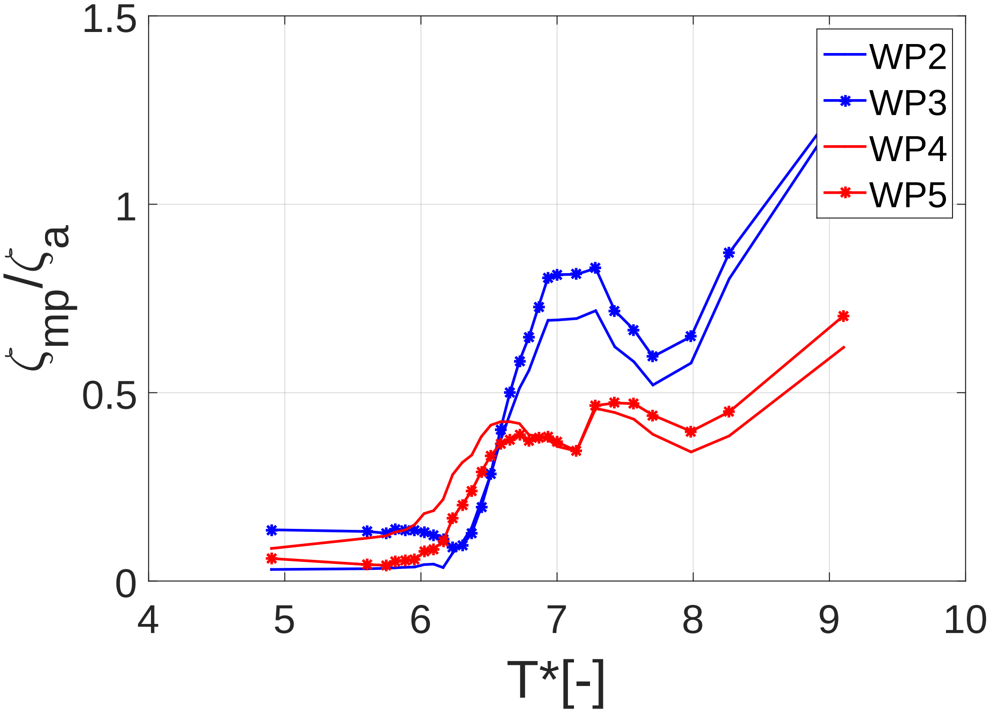

Figure D.125: Moonpools, wave steepness 1/45, App. 1 inlet, Mass at ends

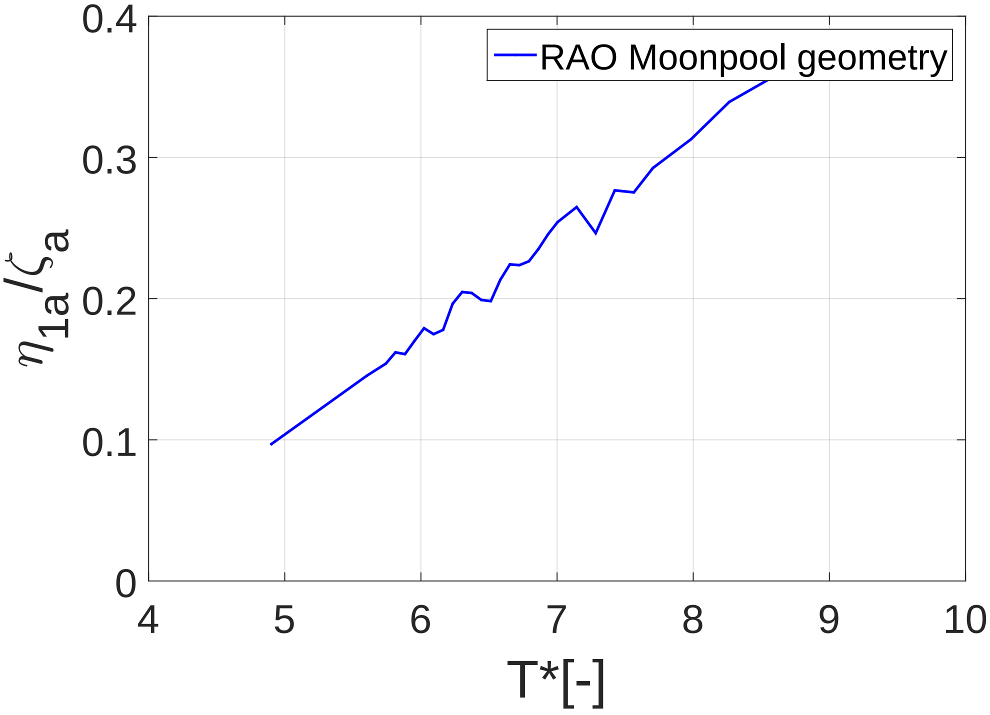

Figure D.126: Surge, wave steepness 1/30, App. 1 inlet, Mass at ends

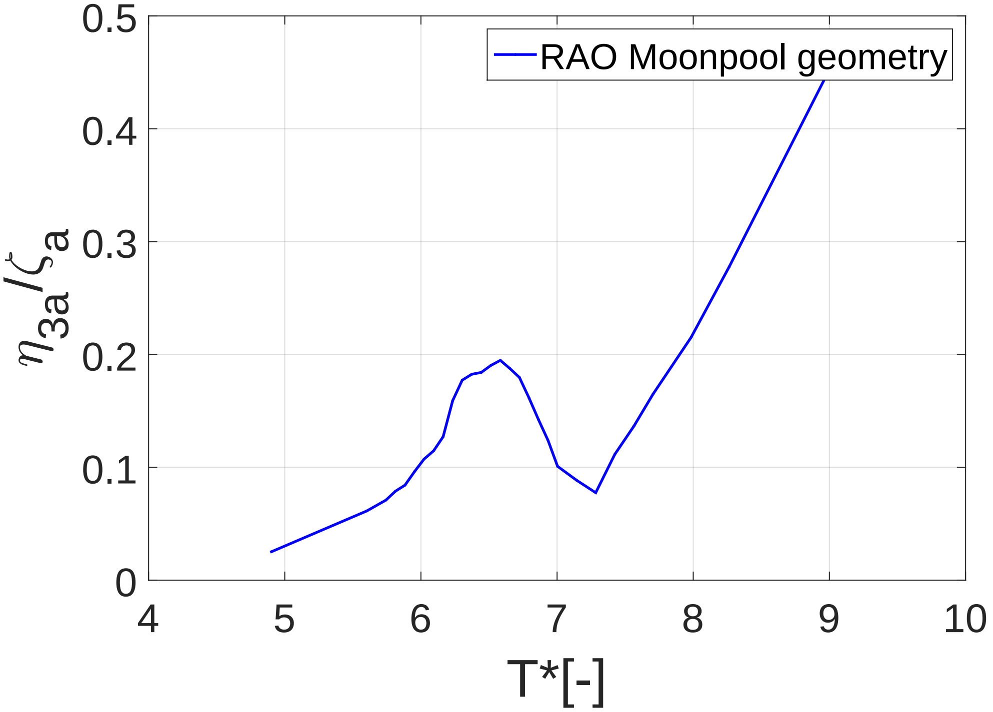

Figure D.127: Heave, wave steepness 1/30, App. 1 inlet, Mass at ends

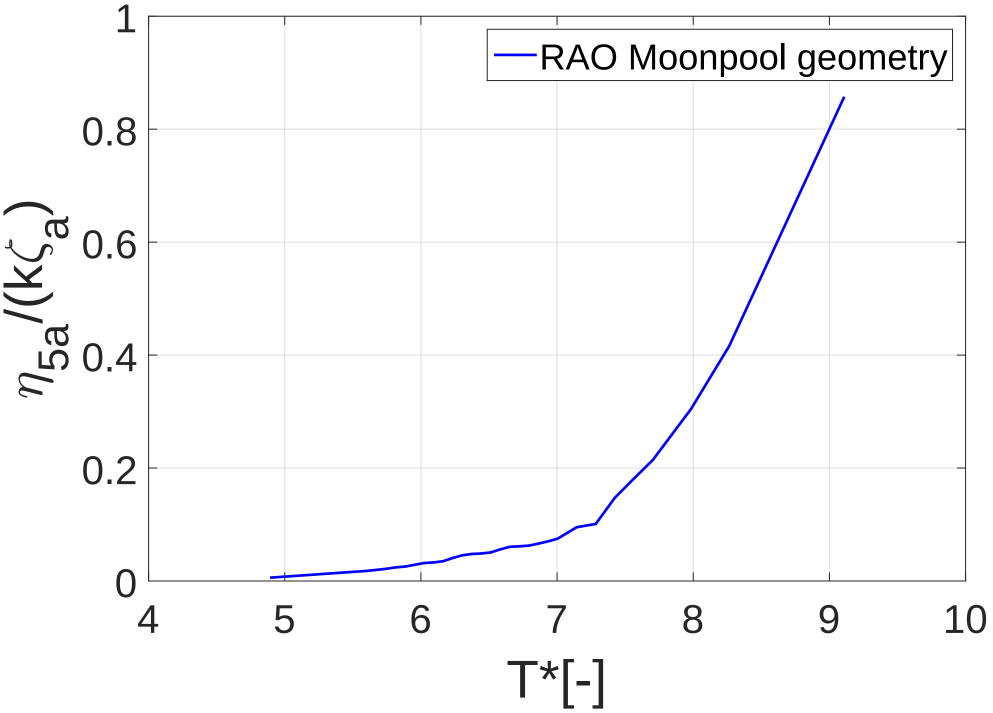

Figure D.128: Pitch, wave steepness 1/30, App. 1 inlet, Mass at ends

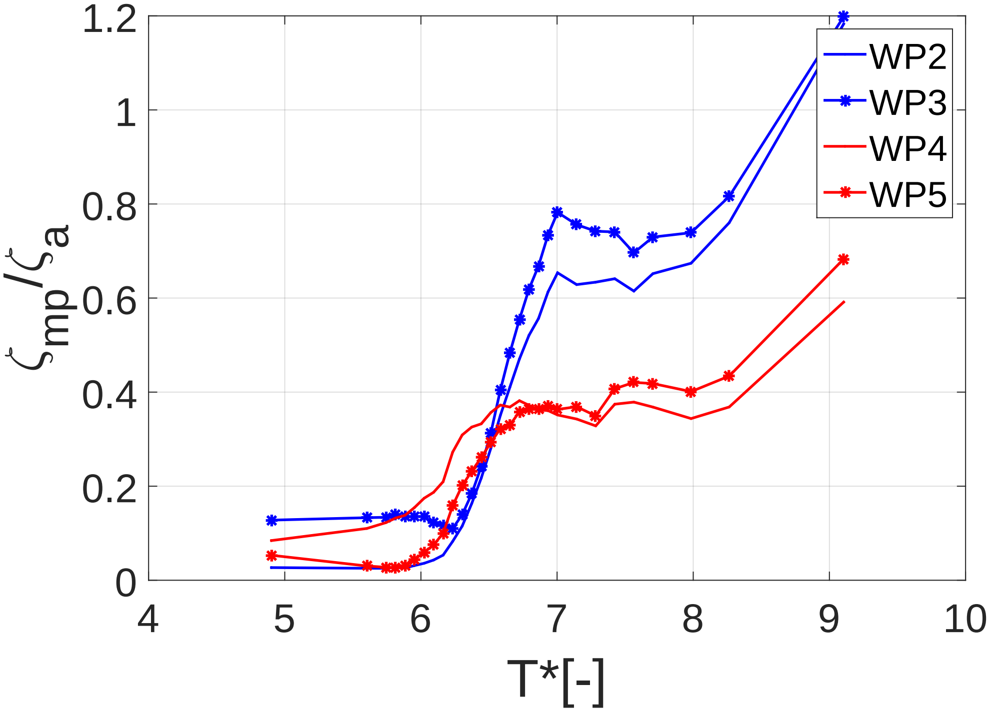

Figure D.129: Moonpools, wave steepness 1/30, App. 1 inlet, Mass at ends

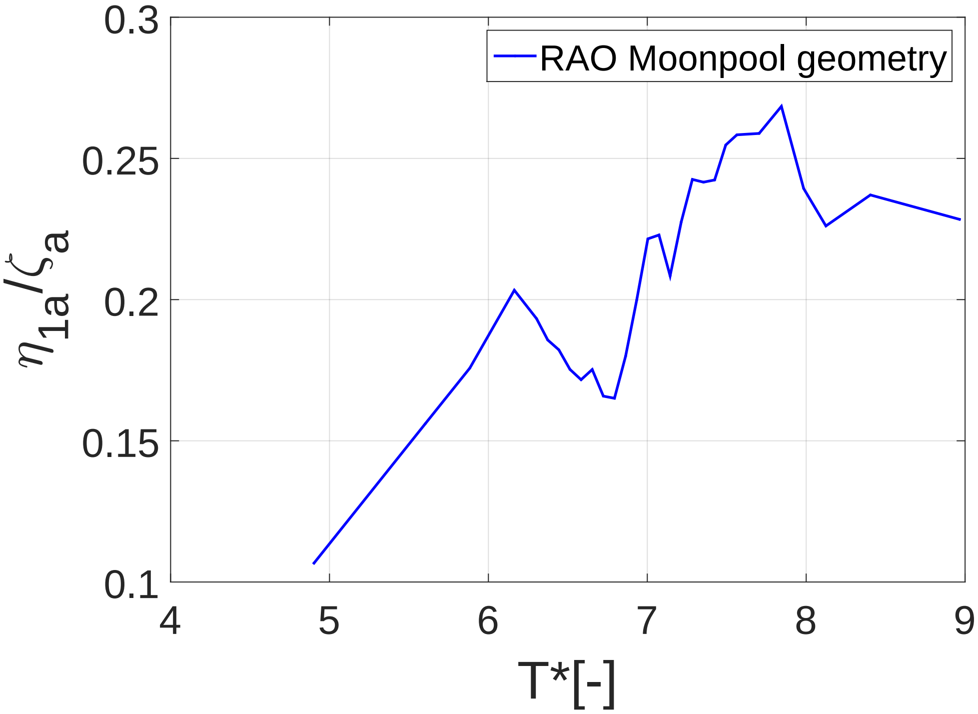

Figure D.130: Surge, wave steepness 1/60, App. 2 inlet, Mass in center

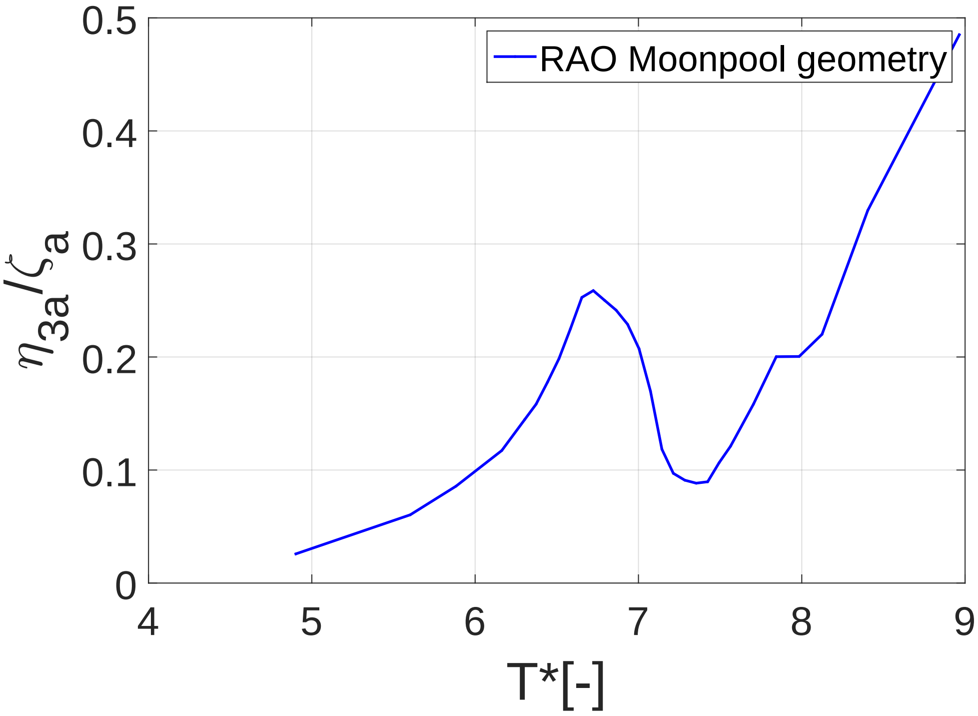

Figure D.131: Heave, wave steepness 1/60, App. 2 inlet, Mass in center

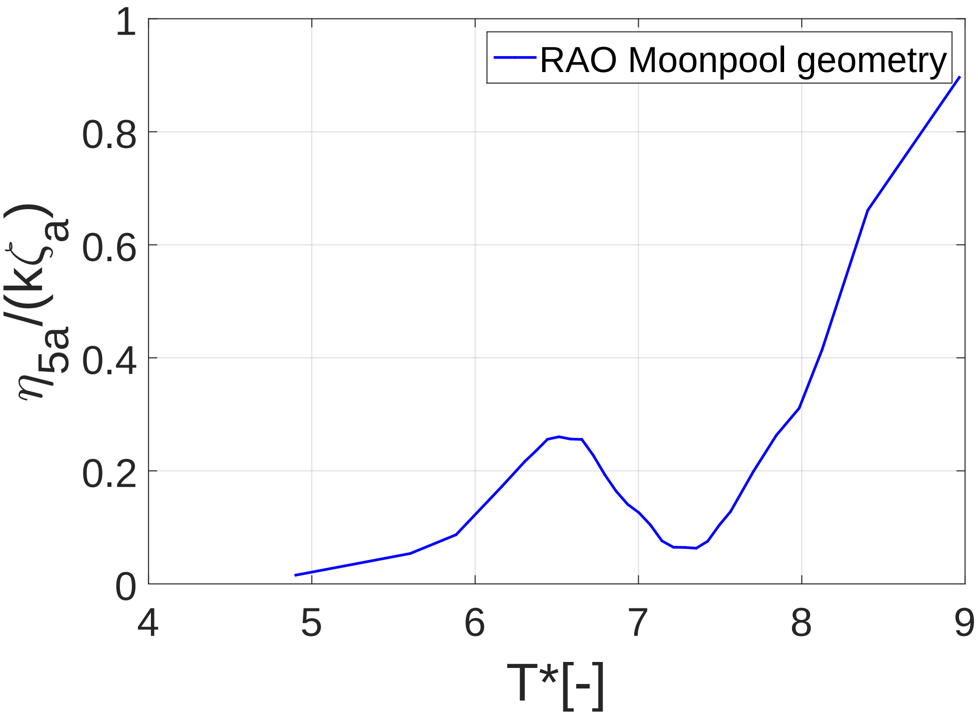

Figure D.132: Pitch, wave steepness 1/60, App. 2 inlet, Mass in center

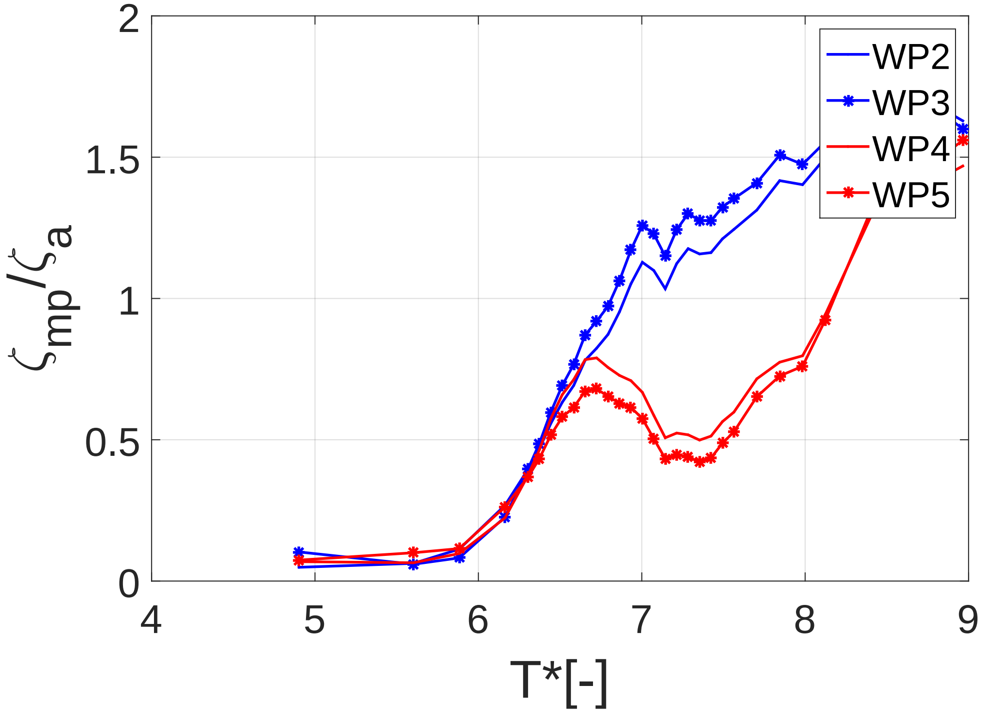

Figure D.133: Moonpools, wave steepness 1/60, App. 2 inlet, Mass in center

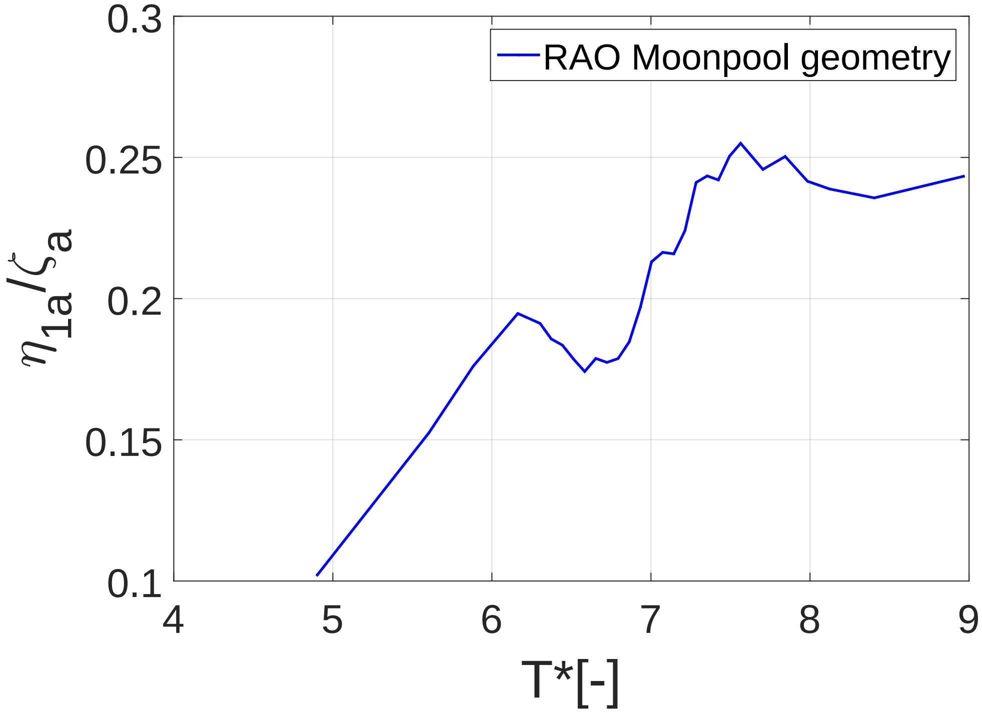

Figure D.134: Surge, wave steepness 1/45, App. 2 inlet, Mass in center

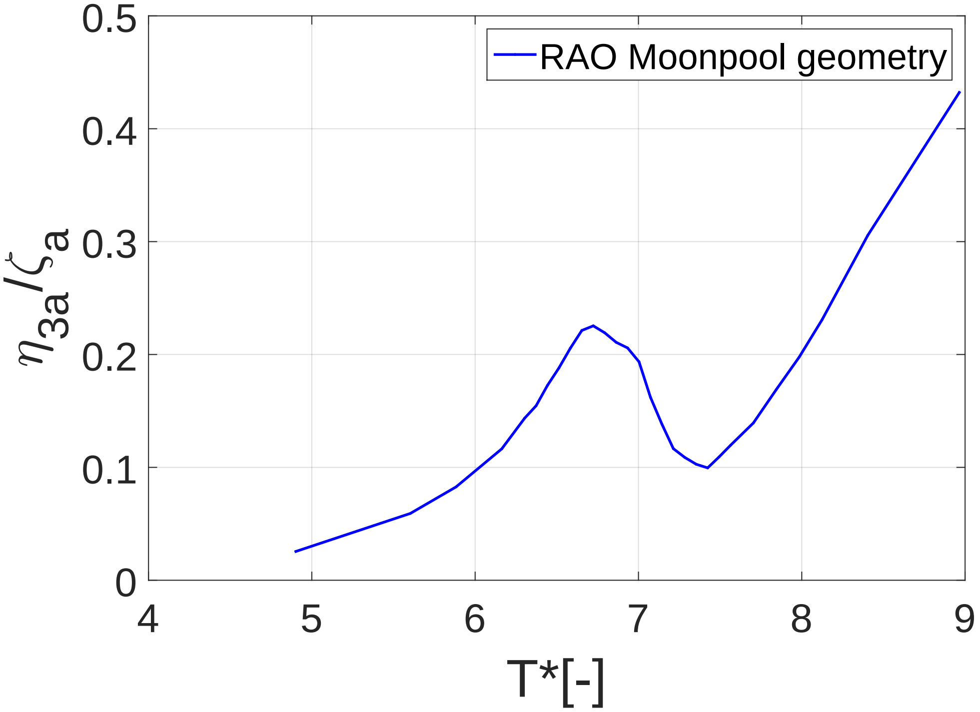

Figure D.135: Heave, wave steepness 1/45, App. 2 inlet, Mass in center

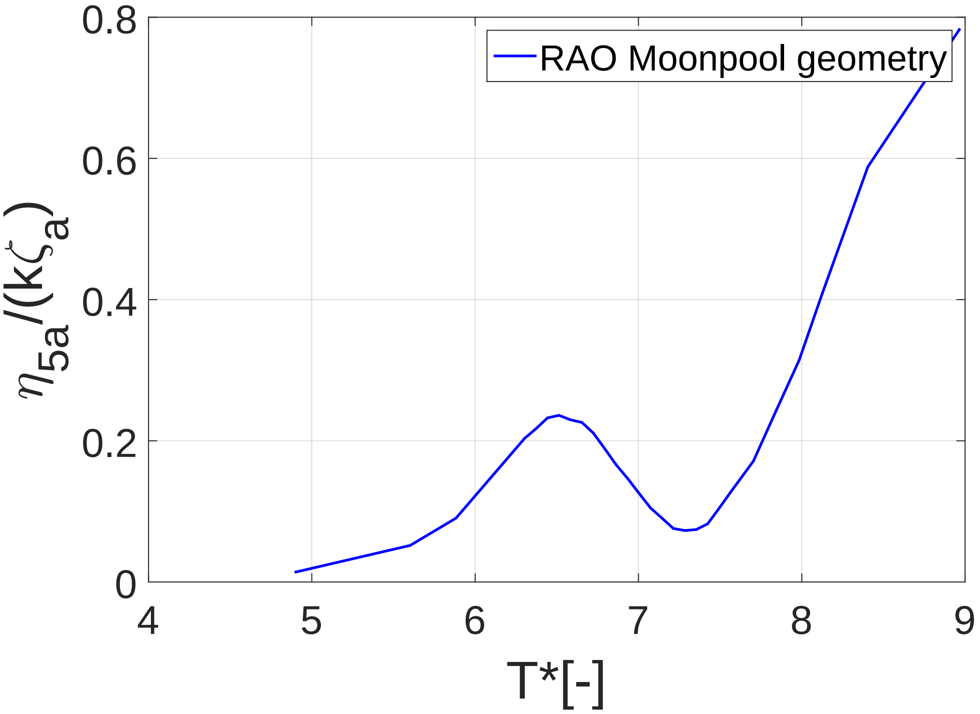

Figure D.136: Pitch, wave steepness 1/45, App. 2 inlet, Mass in center

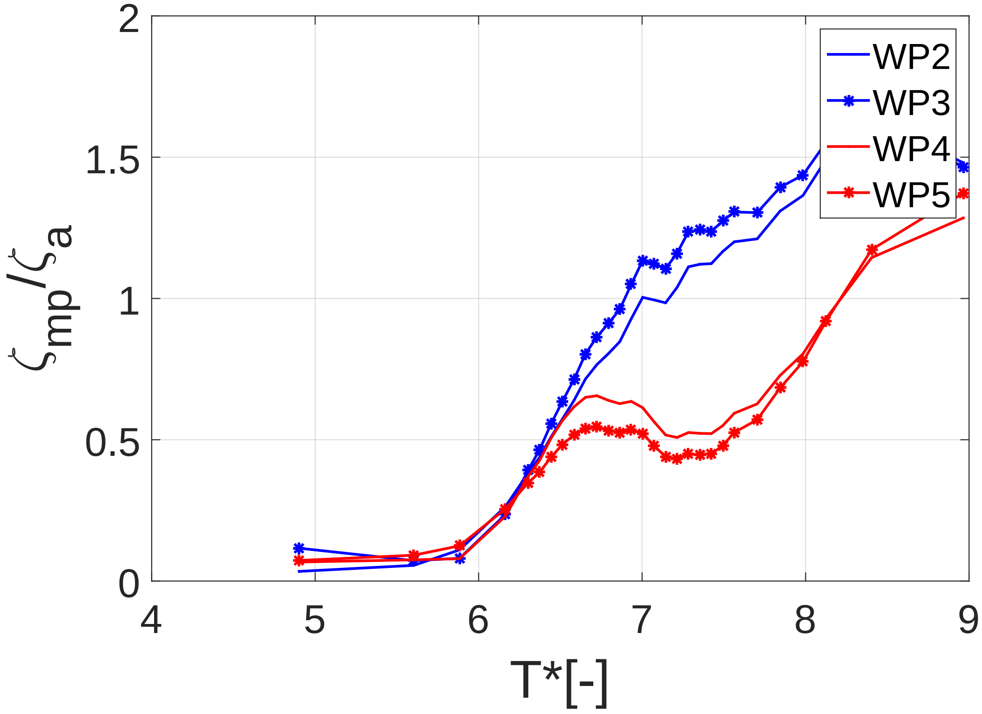

Figure D.137: Moonpools, wave steepness 1/45, App. 2 inlet, Mass in center

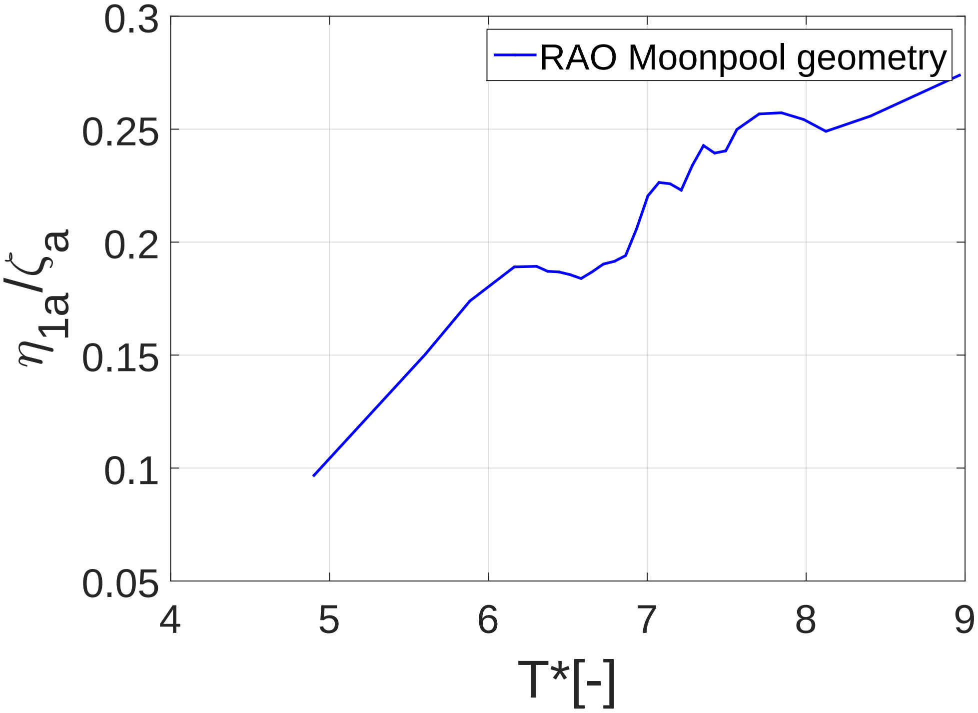

Figure D.138: Surge, wave steepness 1/30, App. 2 inlet, Mass in center

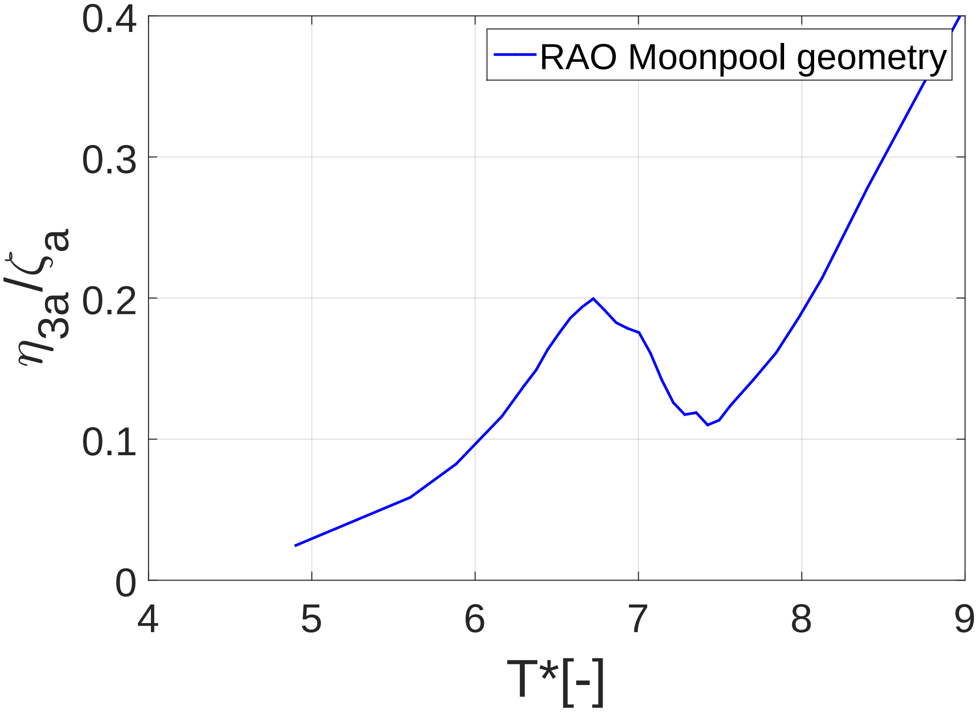

Figure D.139: Heave, wave steepness 1/30, App. 2 inlet, Mass in center

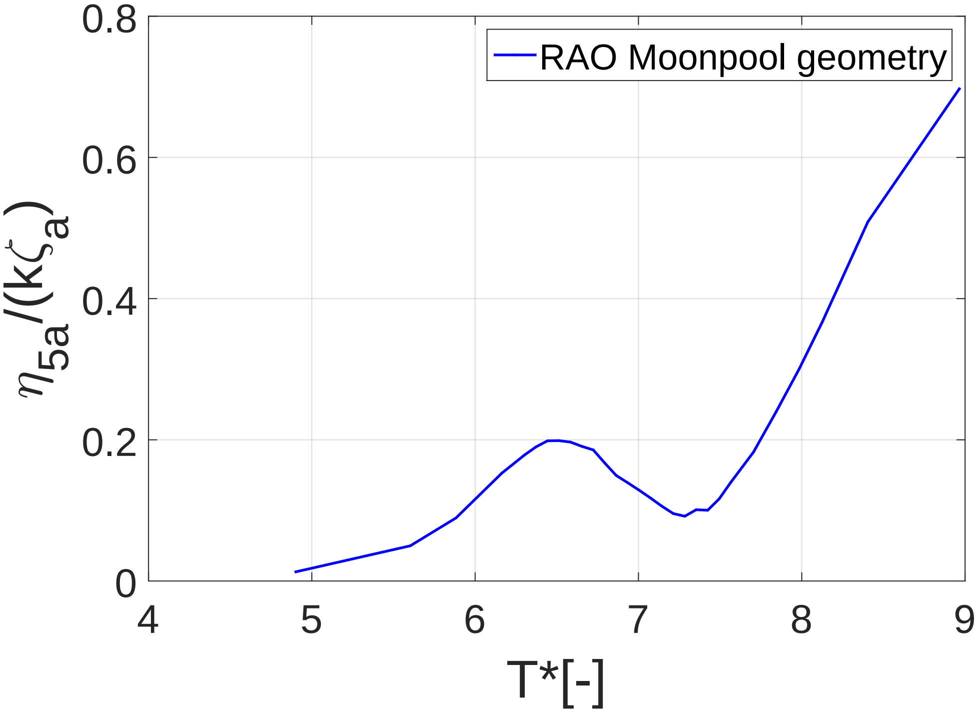

Figure D.140: Pitch, wave steepness 1/30, App. 2 inlet, Mass in center

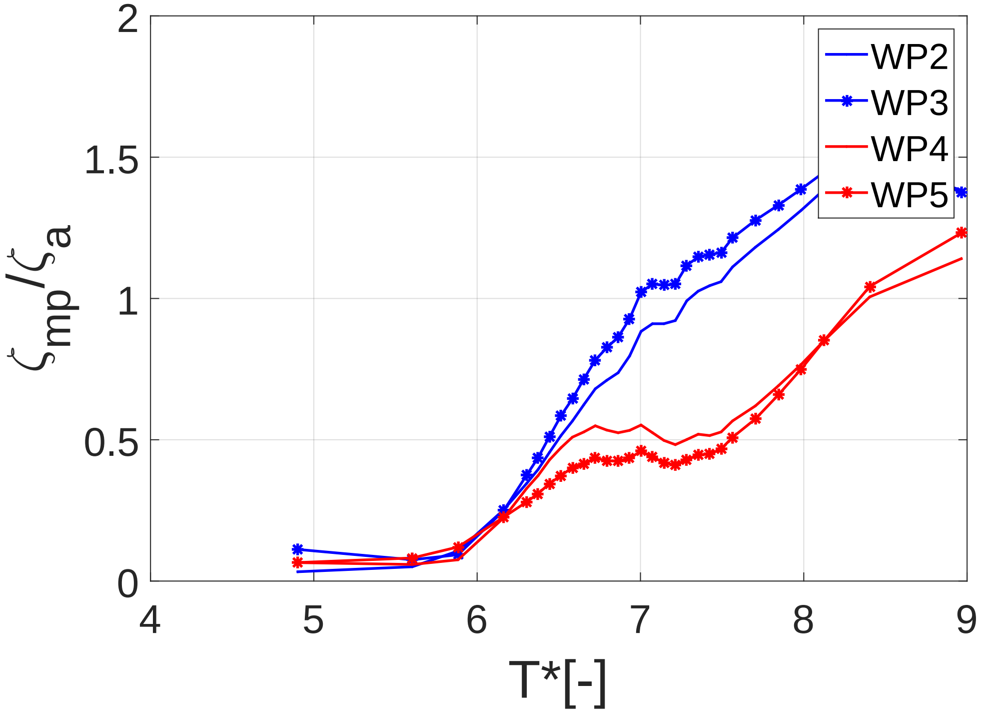

Figure D.141: Moonpools, wave steepness 1/30, App. 2 inlet, Mass in center

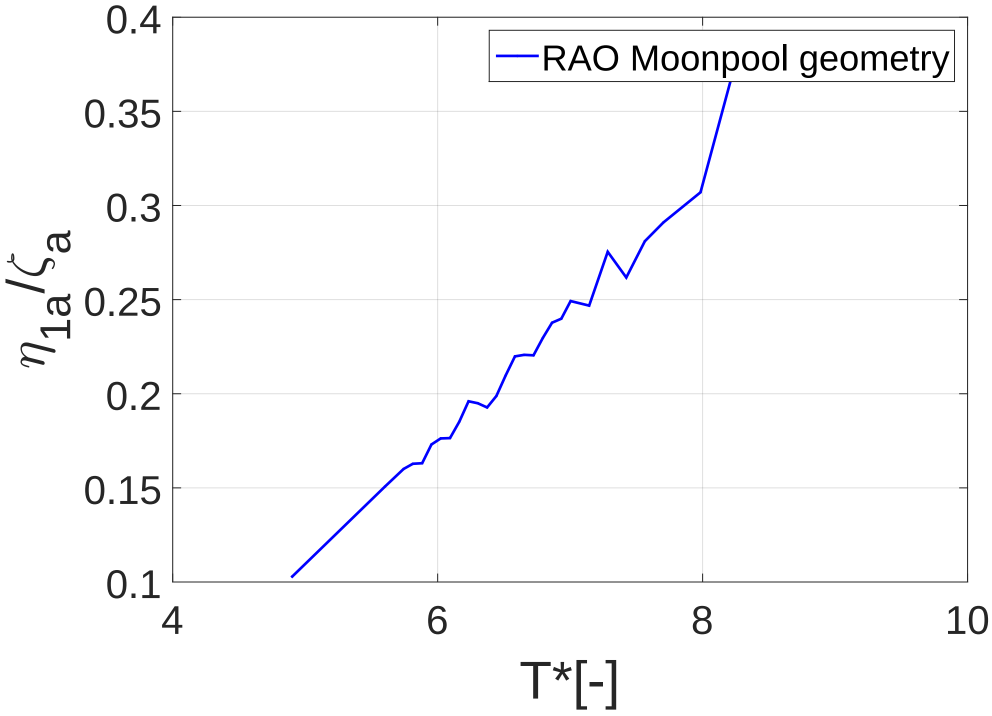

Figure D.142: Surge, wave steepness 1/60, App. 2 inlet, Mass at ends

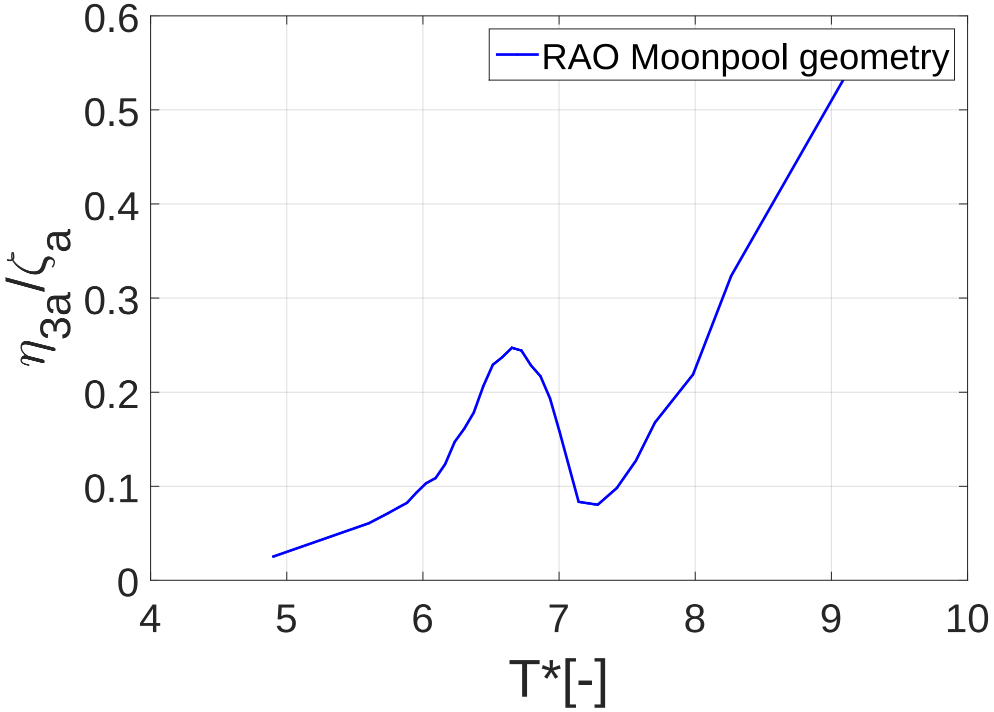

Figure D.143: Heave, wave steepness 1/60, App.2 inlet, Mass at ends

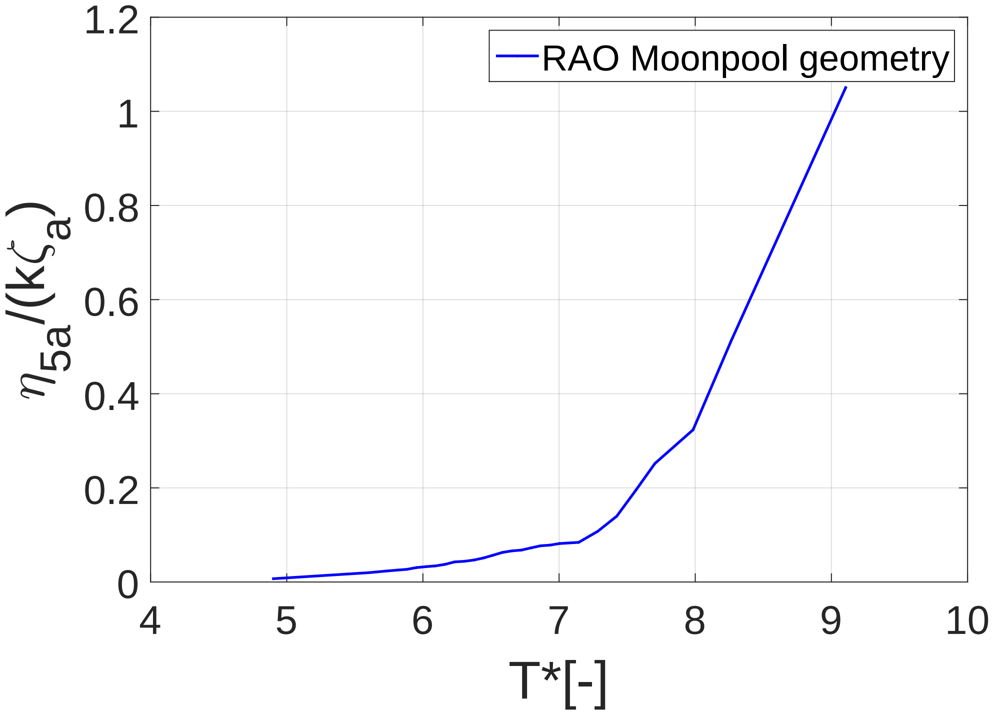

Figure D.144: Pitch, wave steepness 1/60, App. 2 inlet, Mass at ends

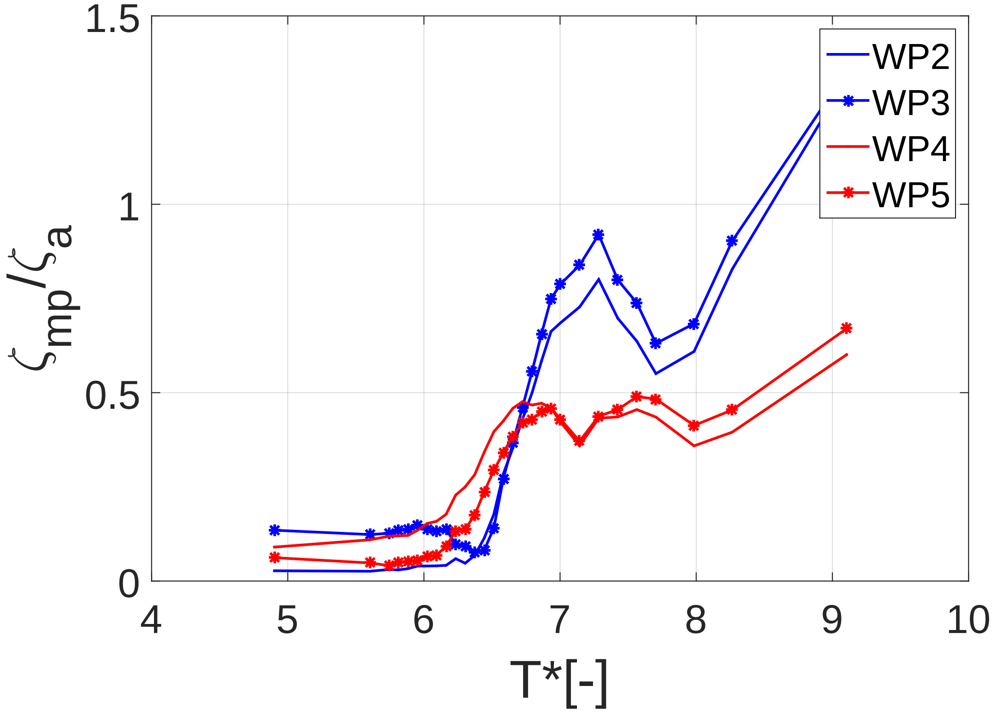

Figure D.145: Moonpools, wave steepness 1/60, App. 2 inlet, Mass at ends

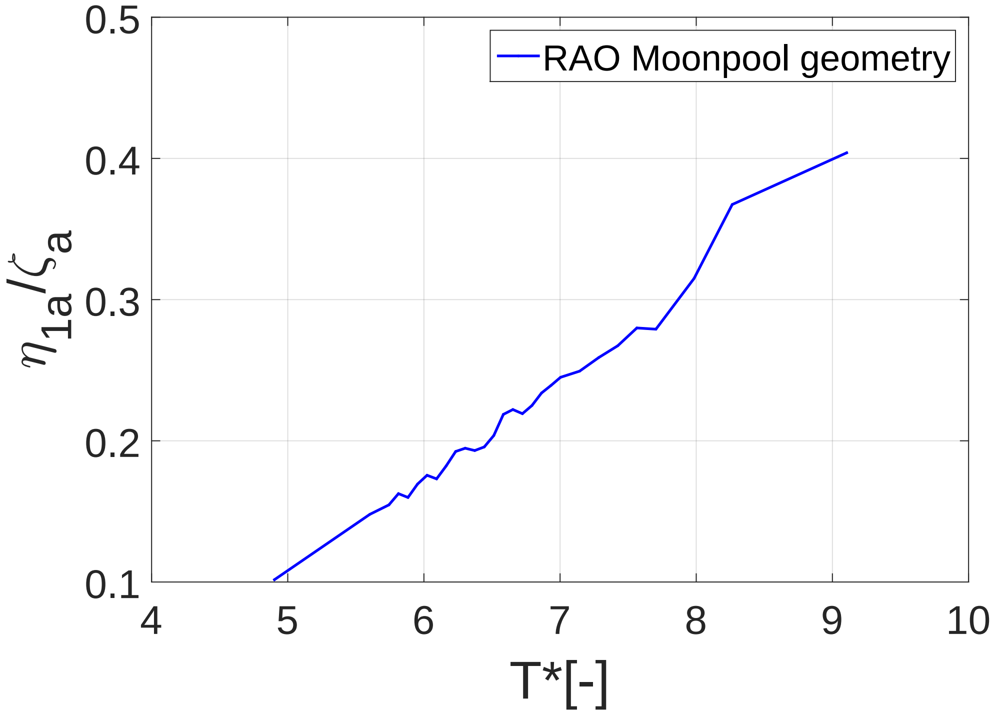

Figure D.146: Surge, wave steepness 1/45, App. 2 inlet, Mass at ends

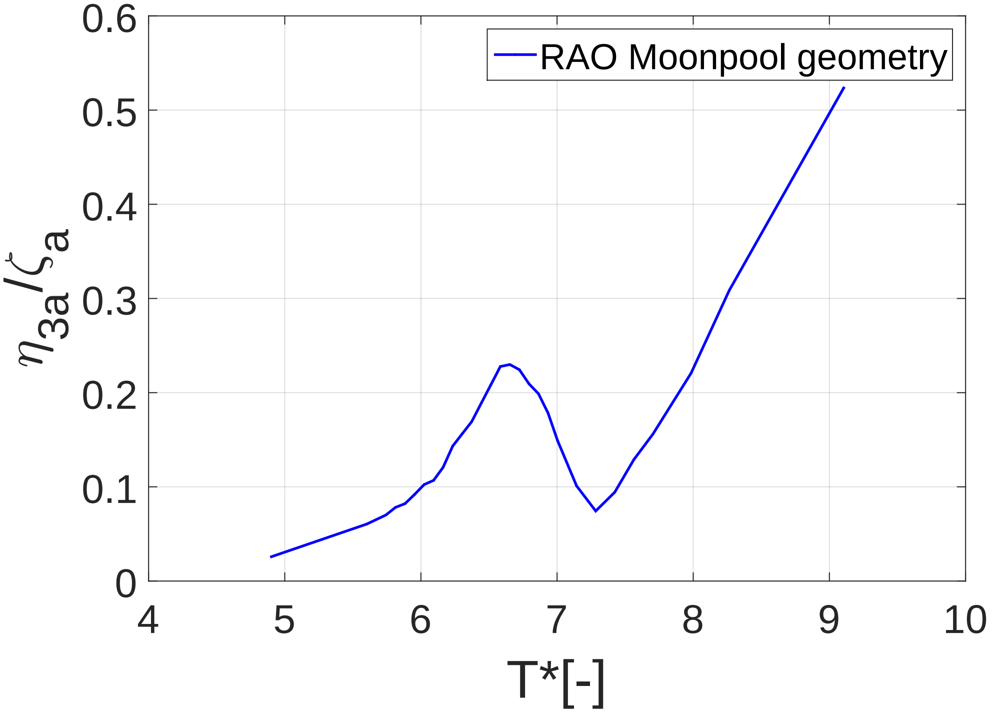

Figure D.147: Heave, wave steepness 1/45, App. 2 inlet, Mass at ends

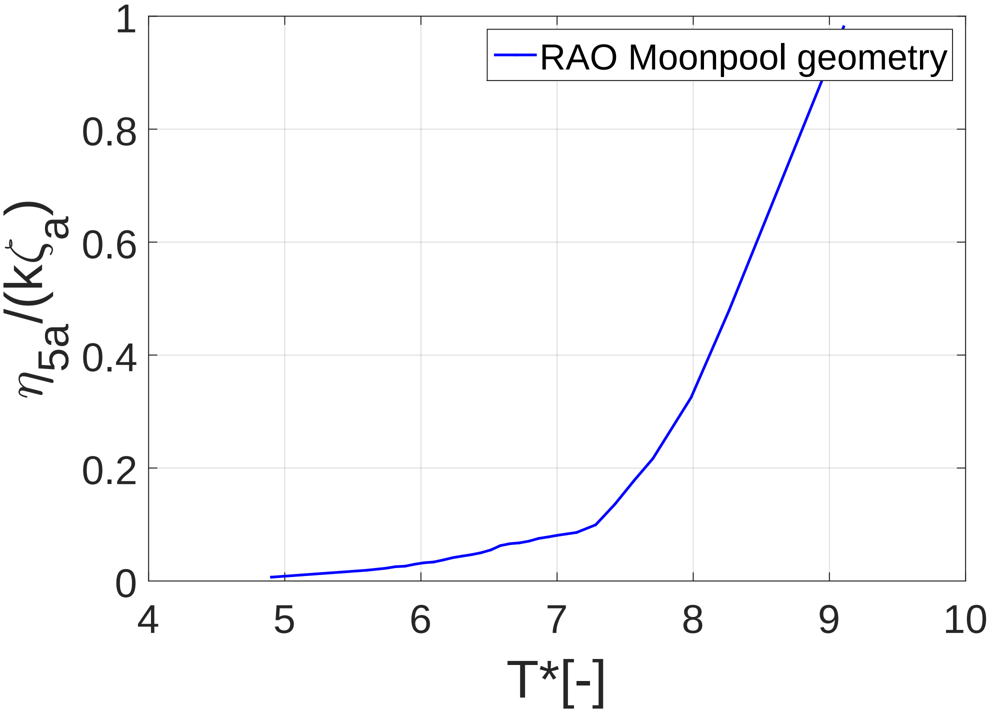

Figure D.148: Pitch, wave steepness 1/45, App.2 inlet, Mass at ends

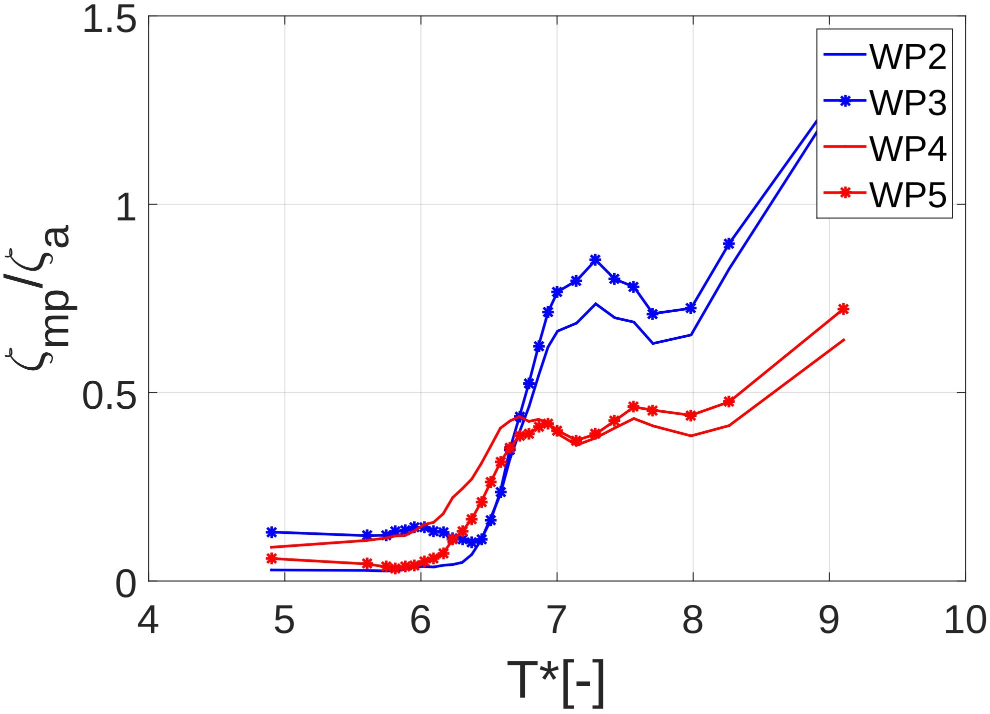

Figure D.149: Moonpools, wave steepness 1/45, App. 2 inlet, Mass at ends

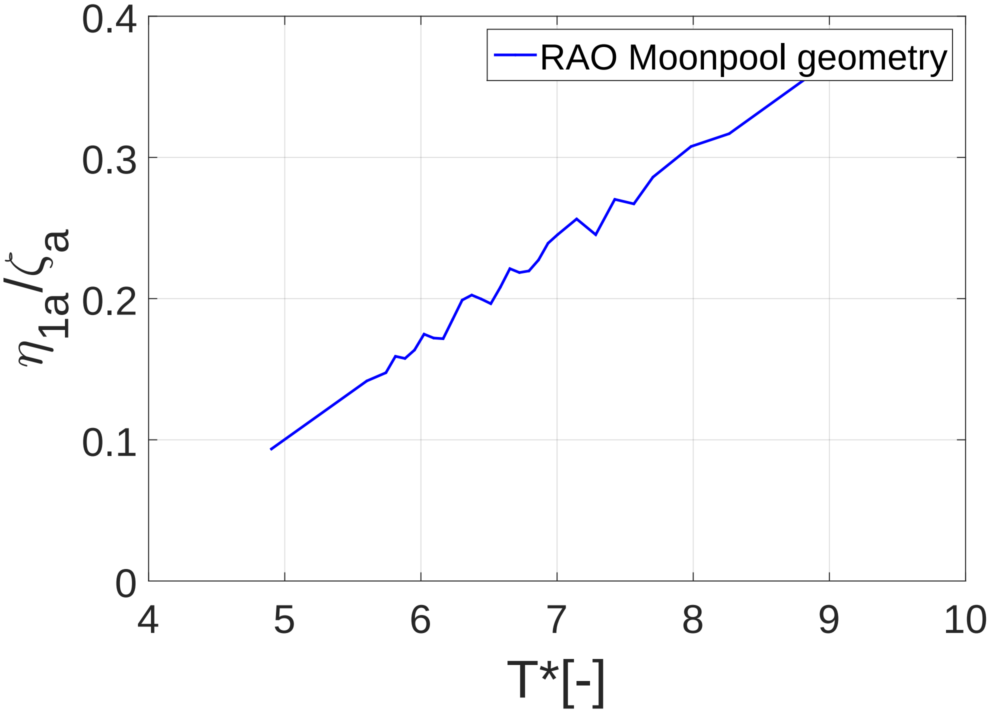

Figure D.150: Surge, wave steepness 1/30, App. 2 inlet, Mass at ends

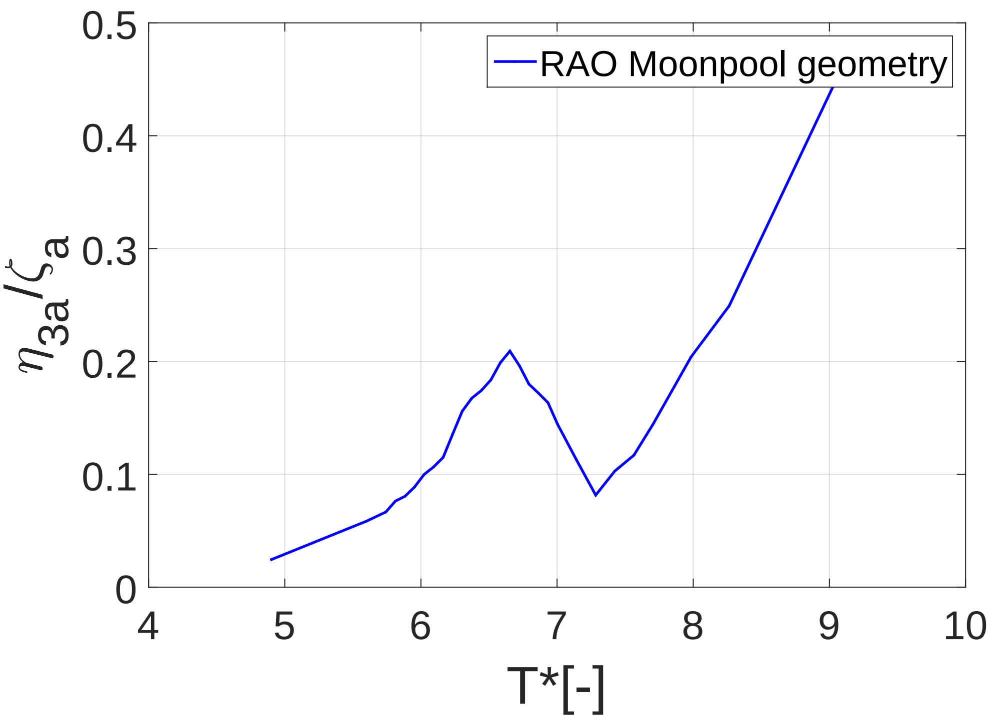

Figure D.151: Heave, wave steepness 1/30, App. 2 inlet, Mass at ends

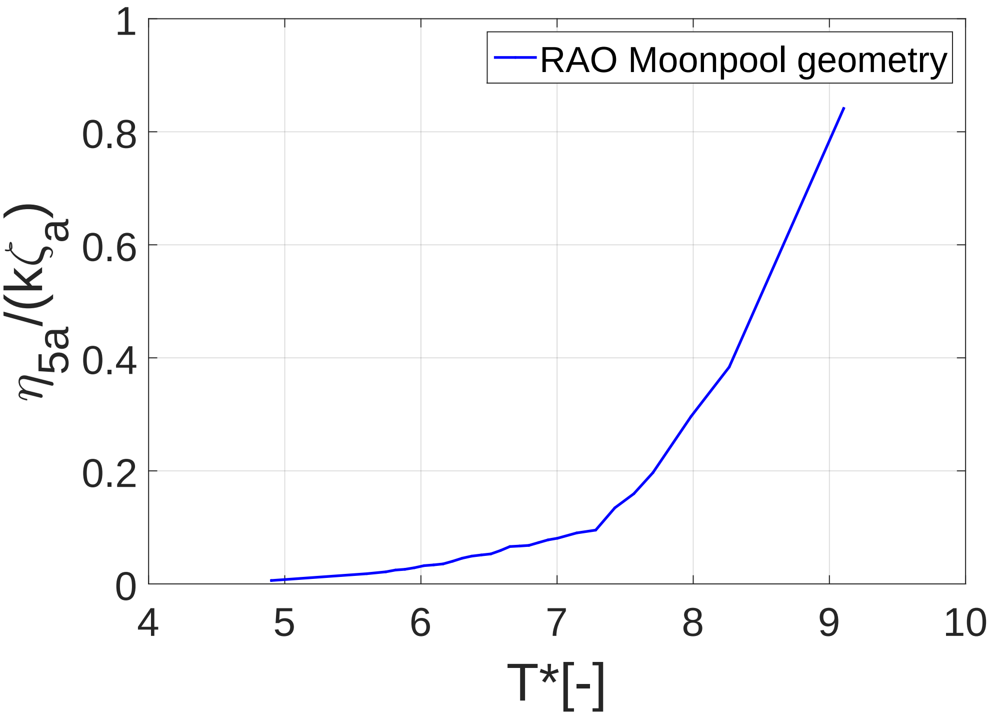

Figure D.152: Pitch, wave steepness 1/30, App. 2 inlet, Mass at ends

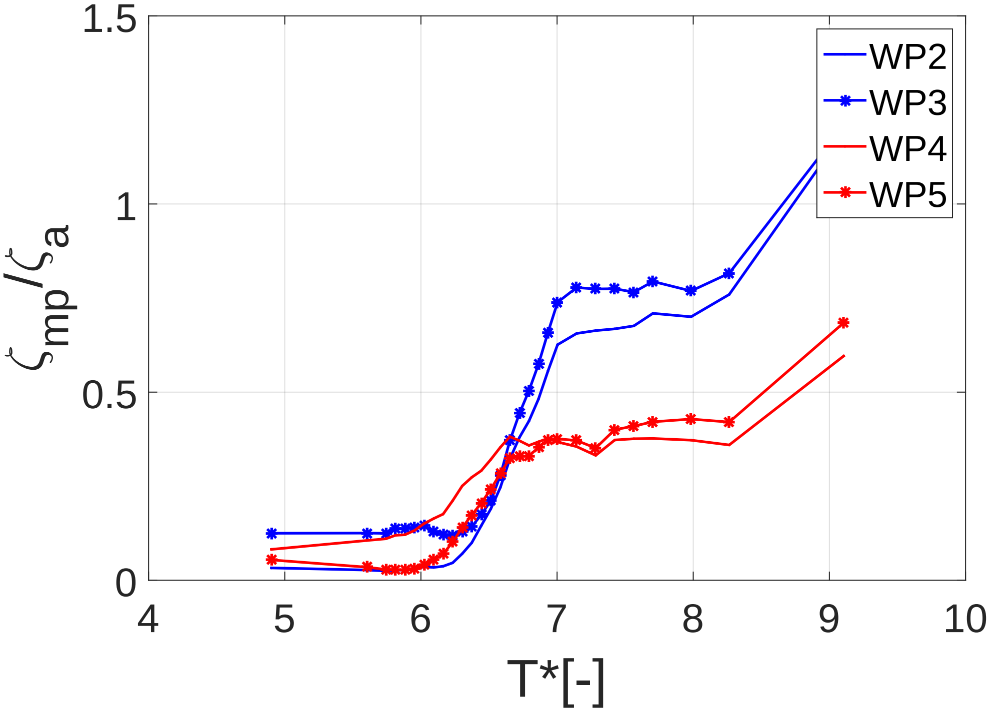

Figure D.153: Moonpools, wave steepness 1/30, App. 2 inlet, Mass at ends

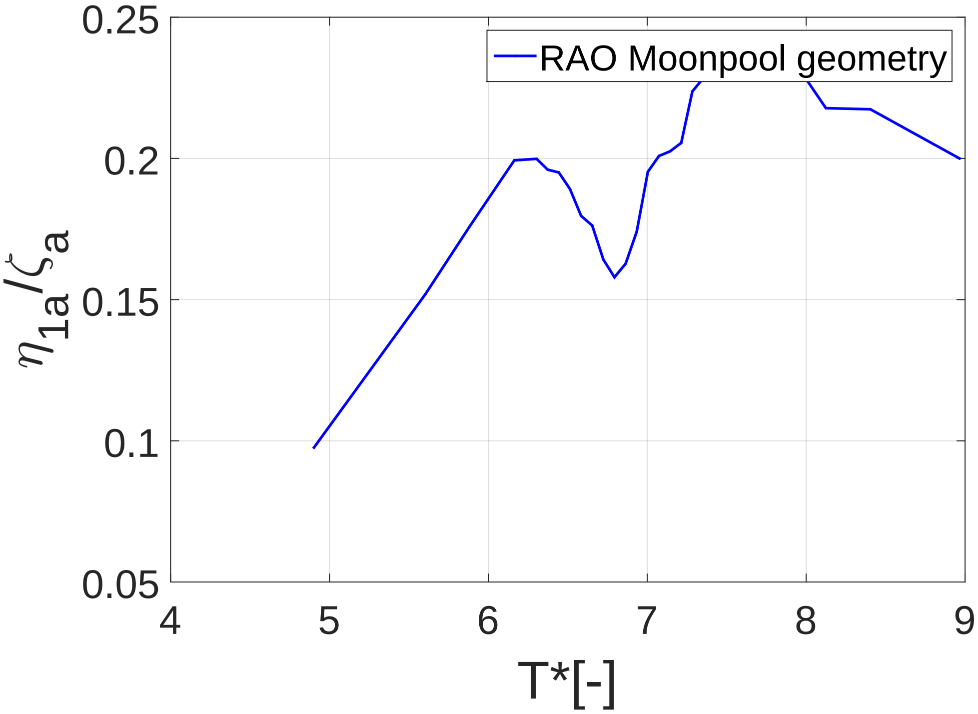

Figure D.154: Surge, wave steepness 1/60, App. 2 inlet, Mass in center

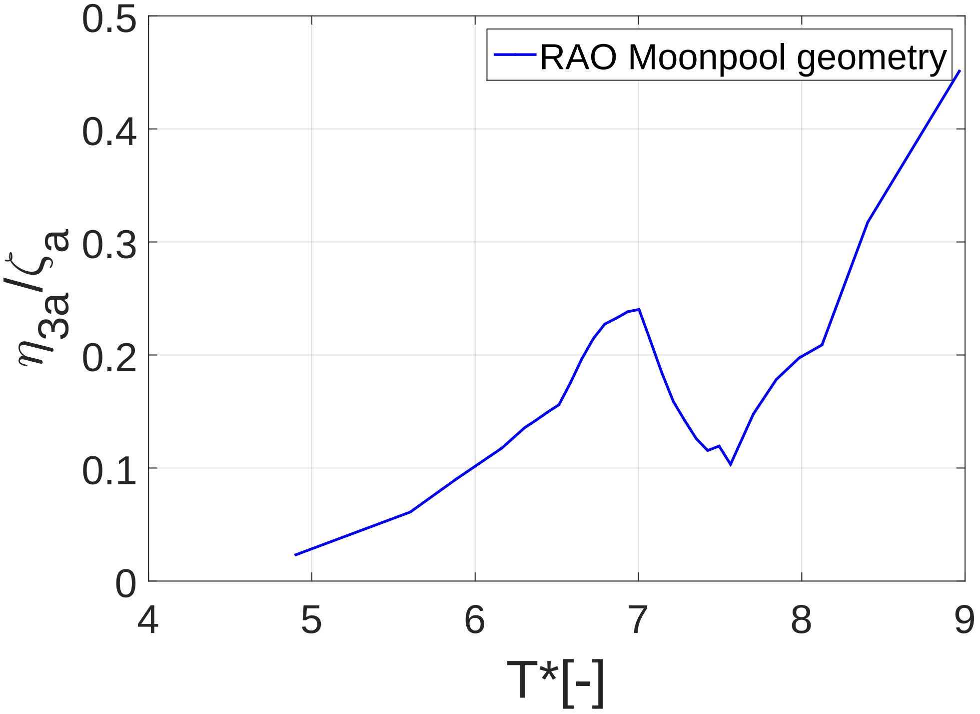

Figure D.155: Heave, wave steepness 1/60, App. 2 inlet, Mass in center

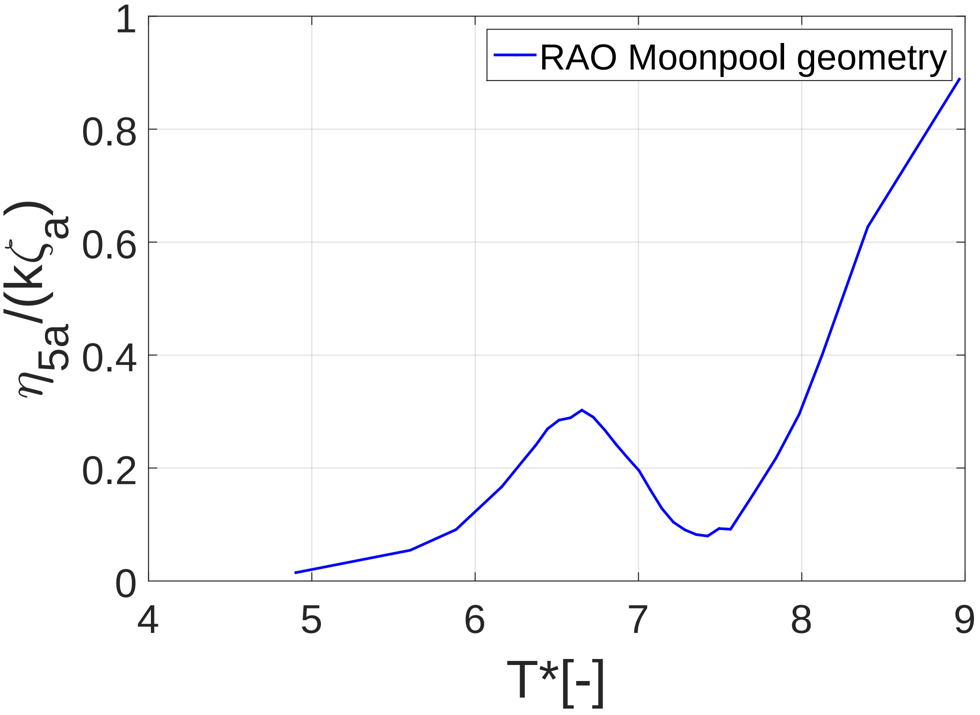

Figure D.156: Pitch, wave steepness 1/60, App. 2 inlet, Mass in center

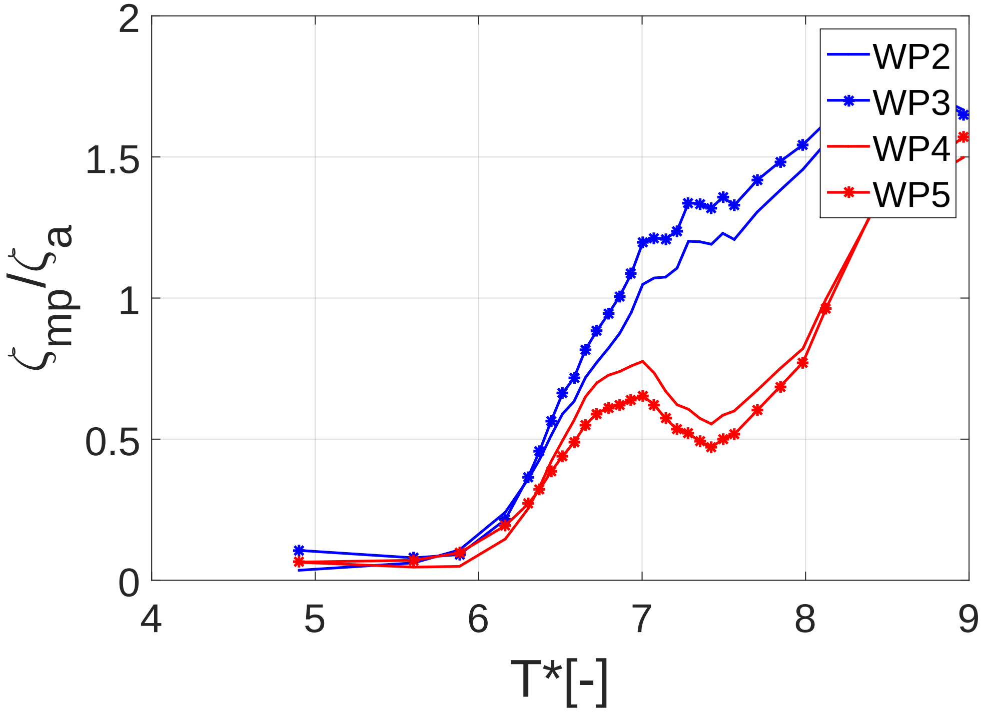

Figure D.157: Moonpools, wave steepness 1/60, App. 2 inlet, Mass in center

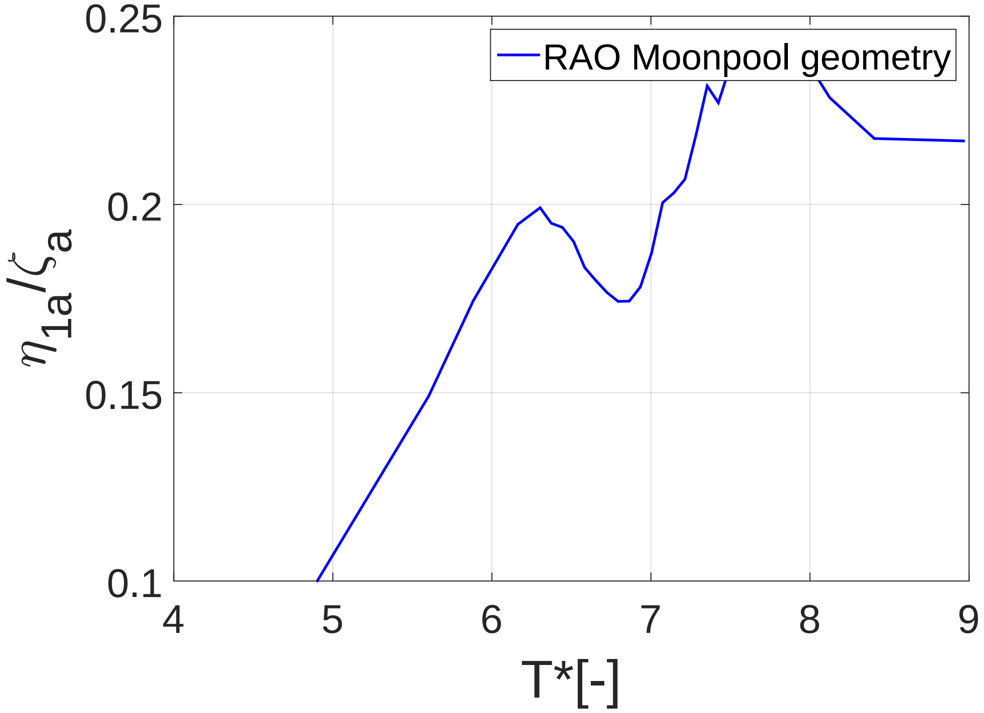

Figure D.158: Surge, wave steepness 1/45, App. 2 inlet, Mass in center

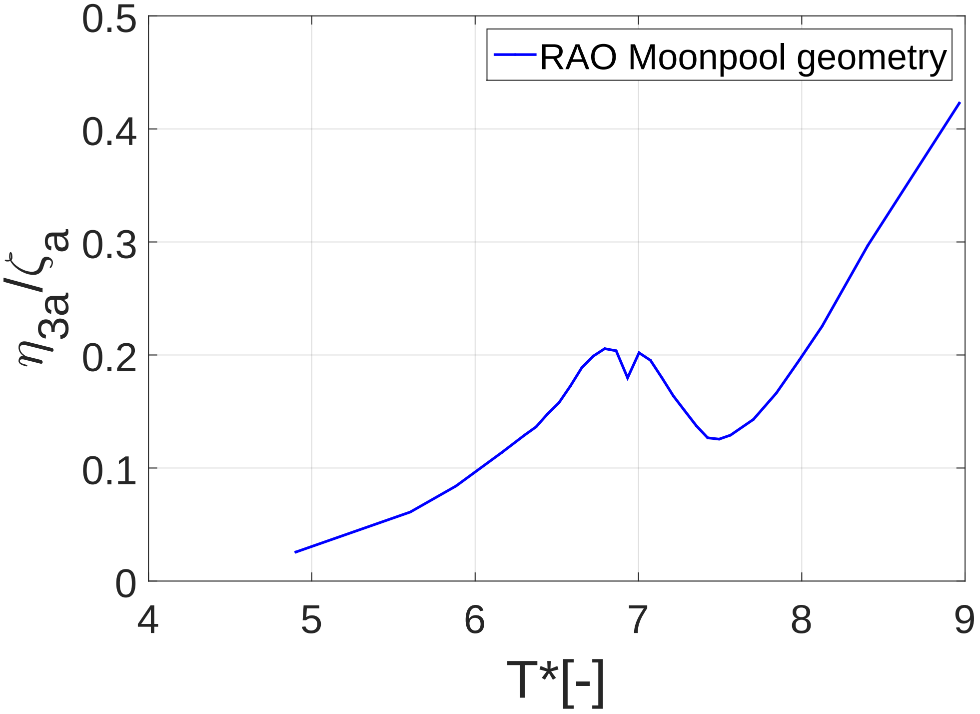

Figure D.159: Heave, wave steepness 1/45, App. 2 inlet, Mass in center

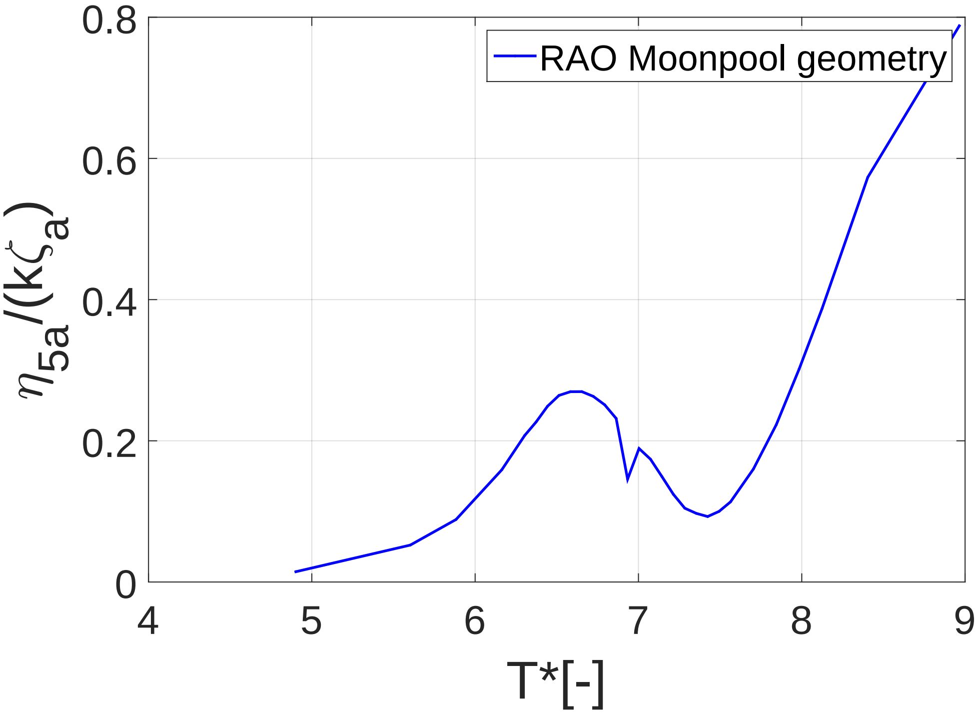

Figure D.160: Pitch, wave steepness 1/45, App. 2 inlet, Mass in center

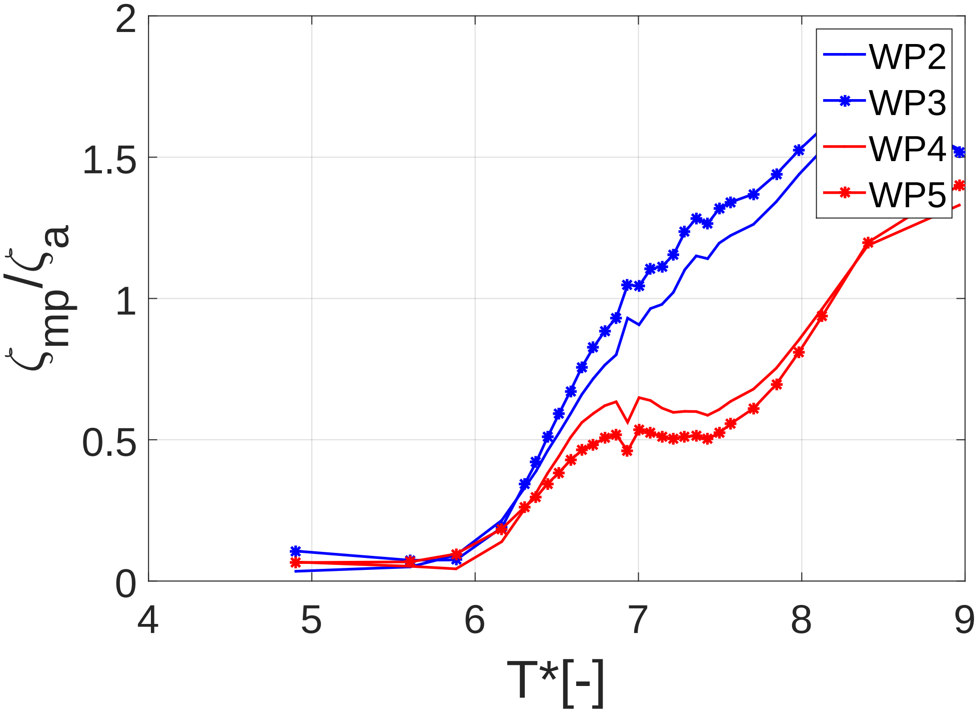

Figure D.161: Moonpools, wave steepness 1/45, App. 2 inlet, Mass in center

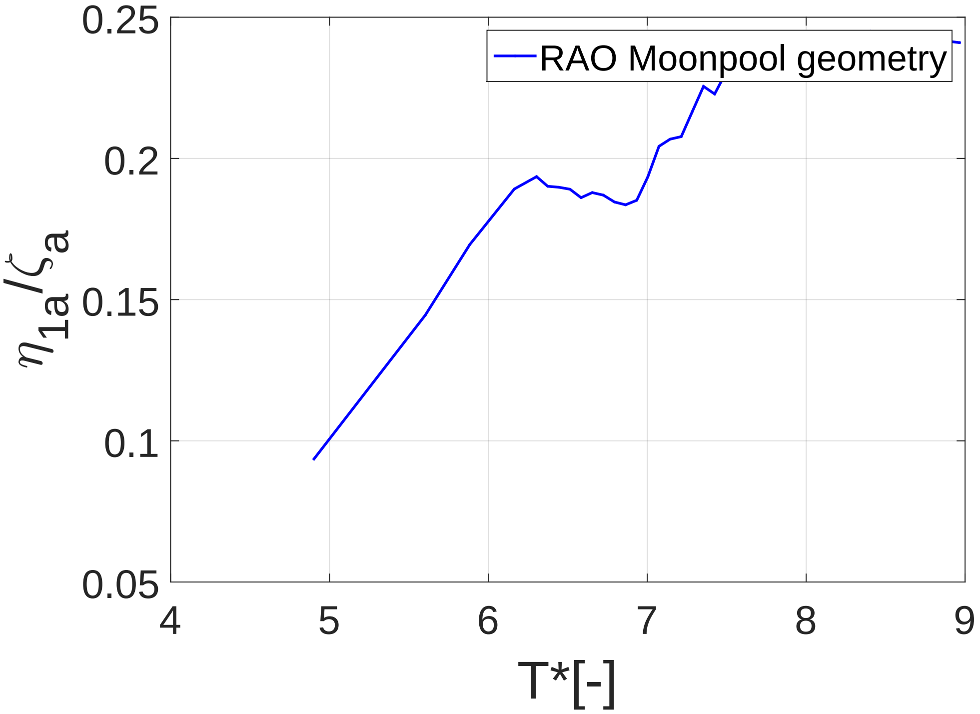

Figure D.162: Surge, wave steepness 1/30, App. 2 inlet, Mass in center

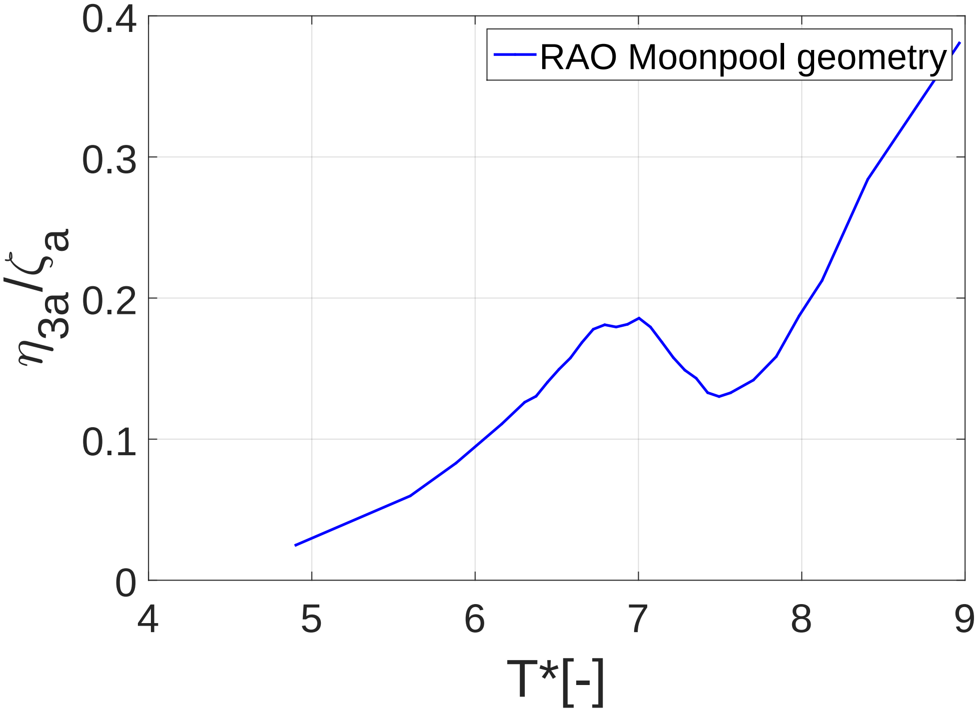

Figure D.163: Heave, wave steepness 1/30, App. 2 inlet, Mass in center

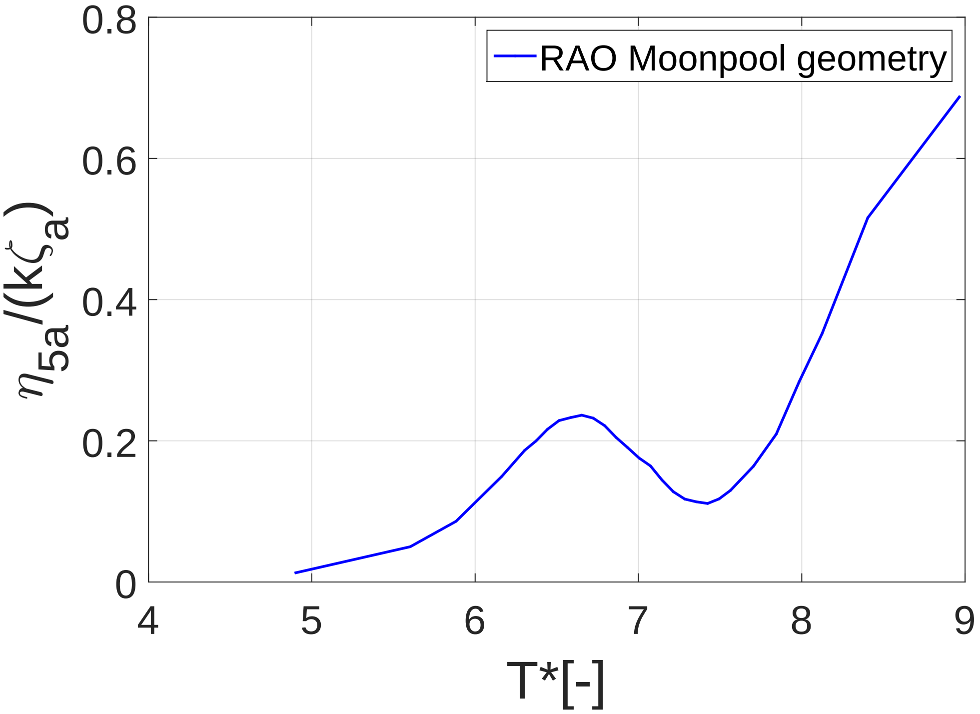

Figure D.164: Pitch, wave steepness 1/30, App. 2 inlet, Mass in center

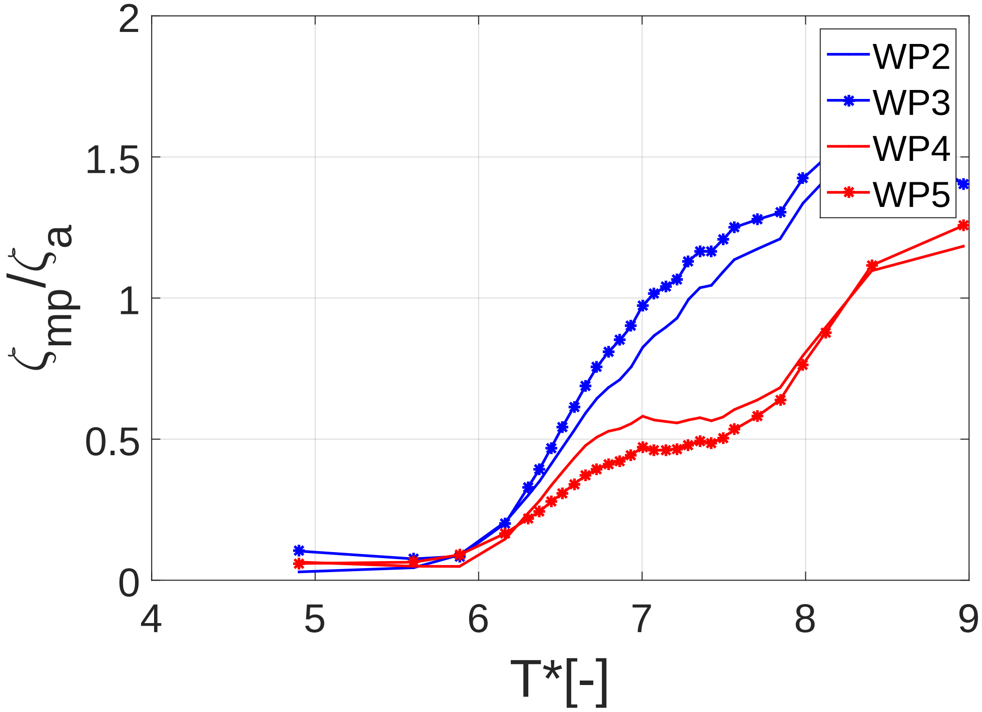

Figure D.165: Moonpools, wave steepness 1/30, App. 2 inlet, Mass in center

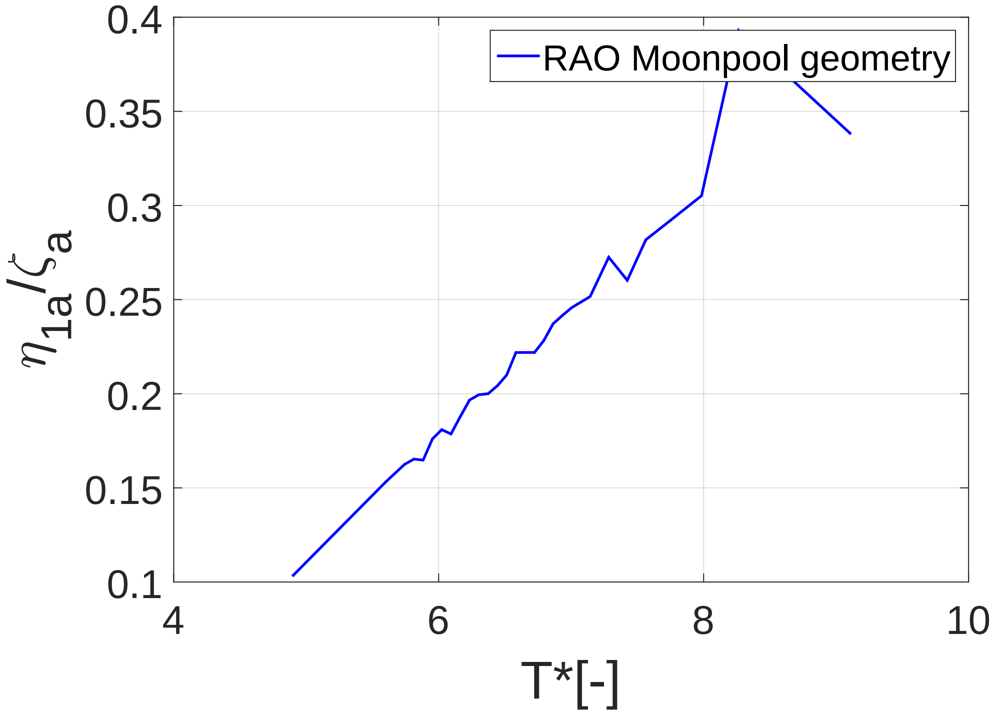

Figure D.166: Surge, wave steepness 1/60, App. 2 inlet, Mass at ends

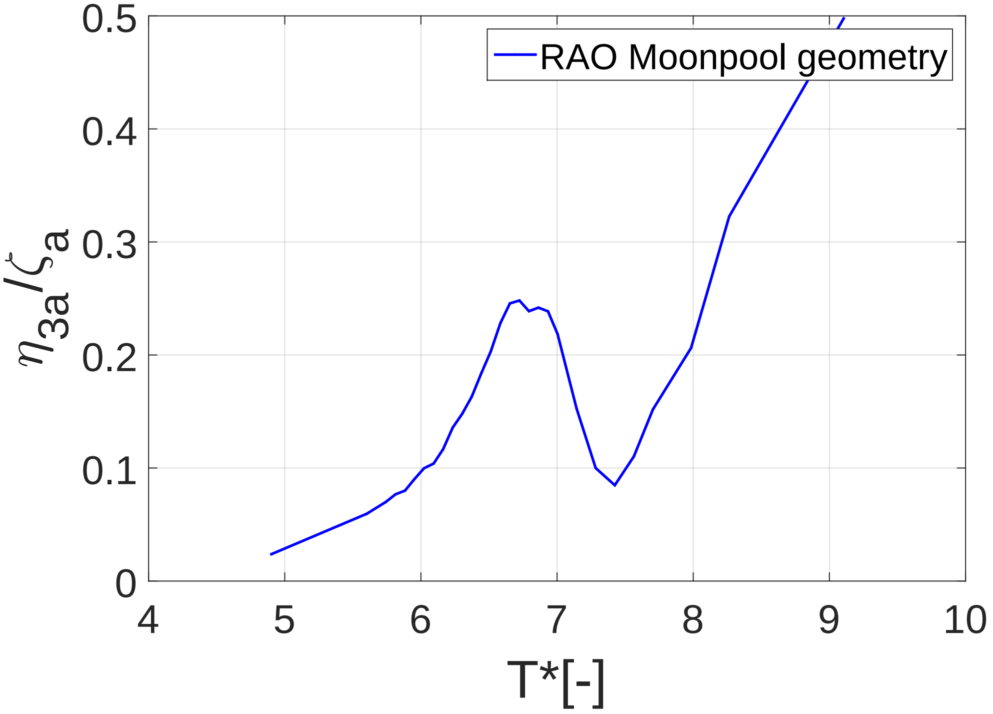

Figure D.167: Heave, wave steepness 1/60, App.2 inlet, Mass at ends

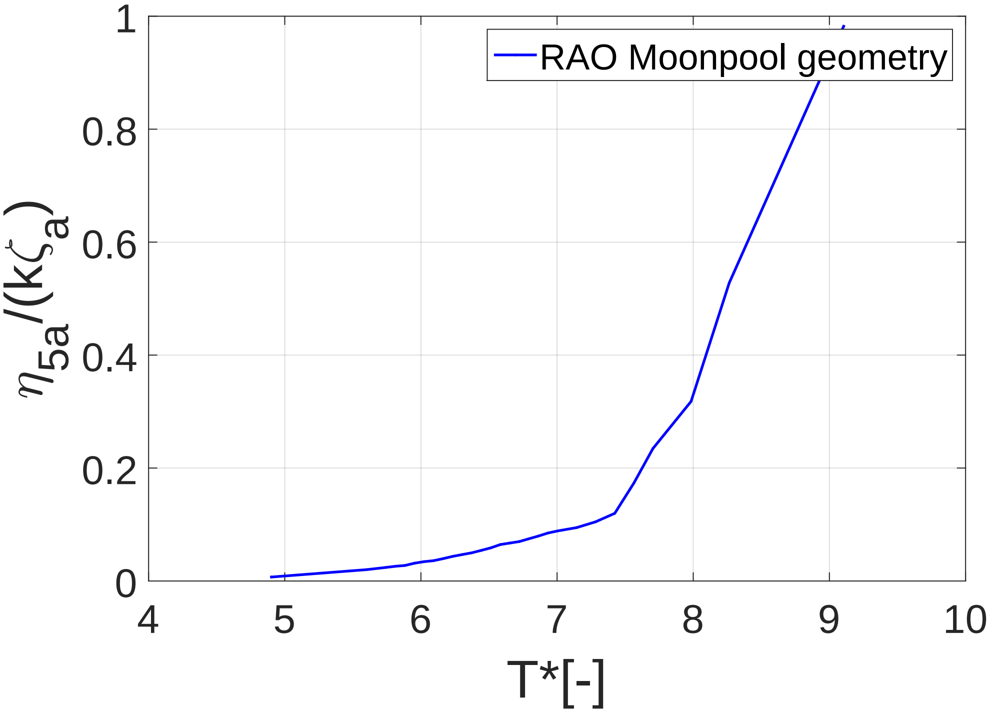

Figure D.168: Pitch, wave steepness 1/60, App. 2 inlet, Mass at ends

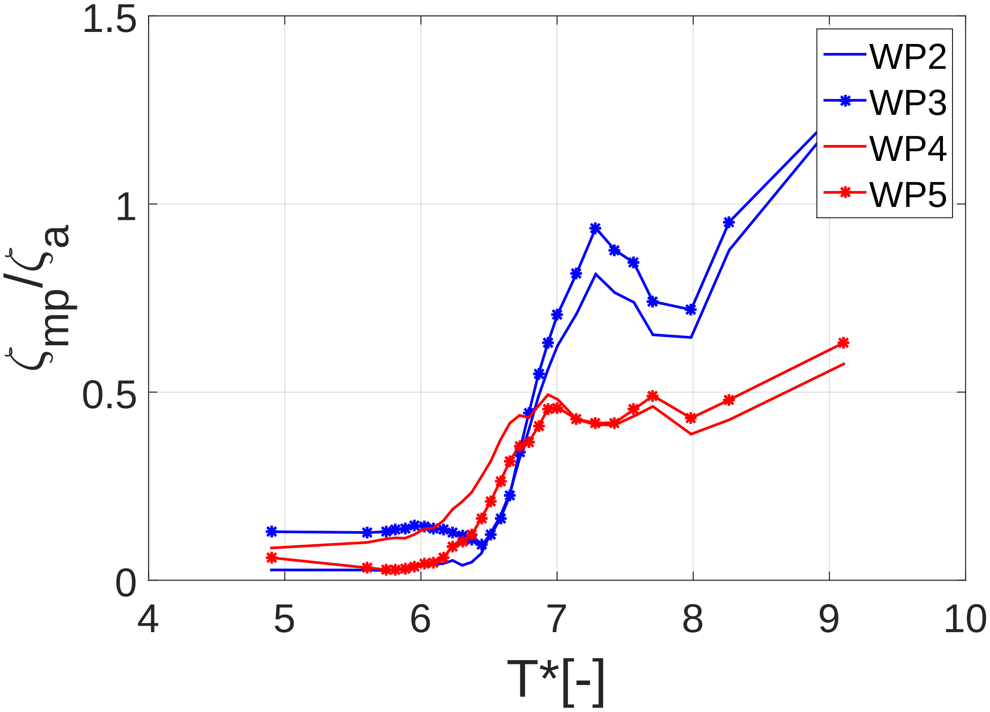

Figure D.169: Moonpools, wave steepness 1/60, App. 2 inlet, Mass at ends

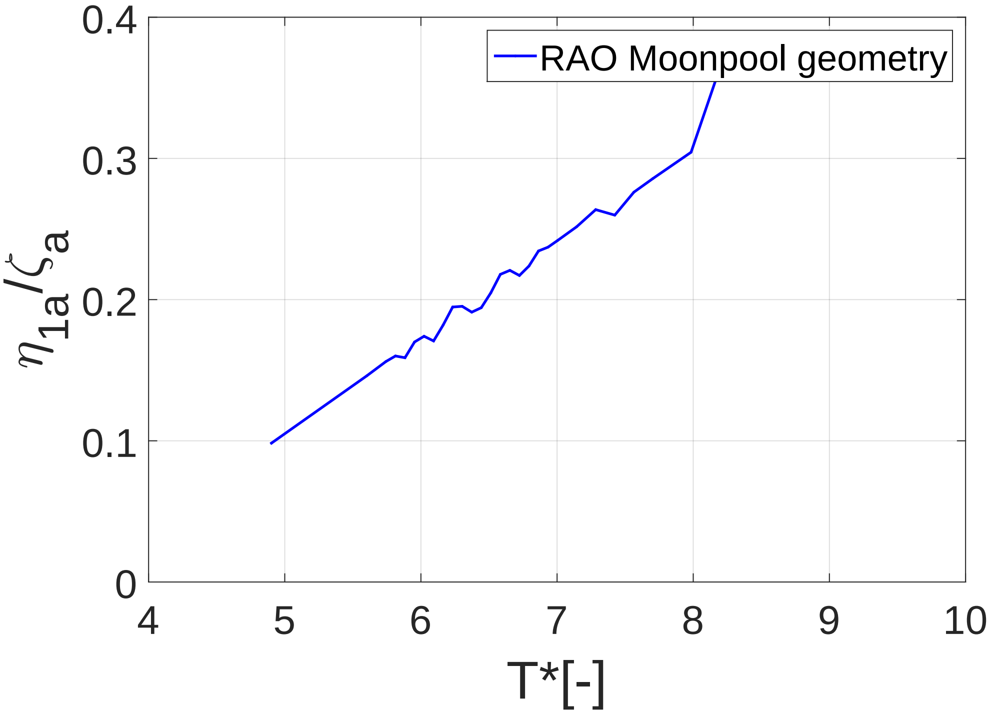

Figure D.170: Surge, wave steepness 1/45, App. 2 inlet, Mass at ends

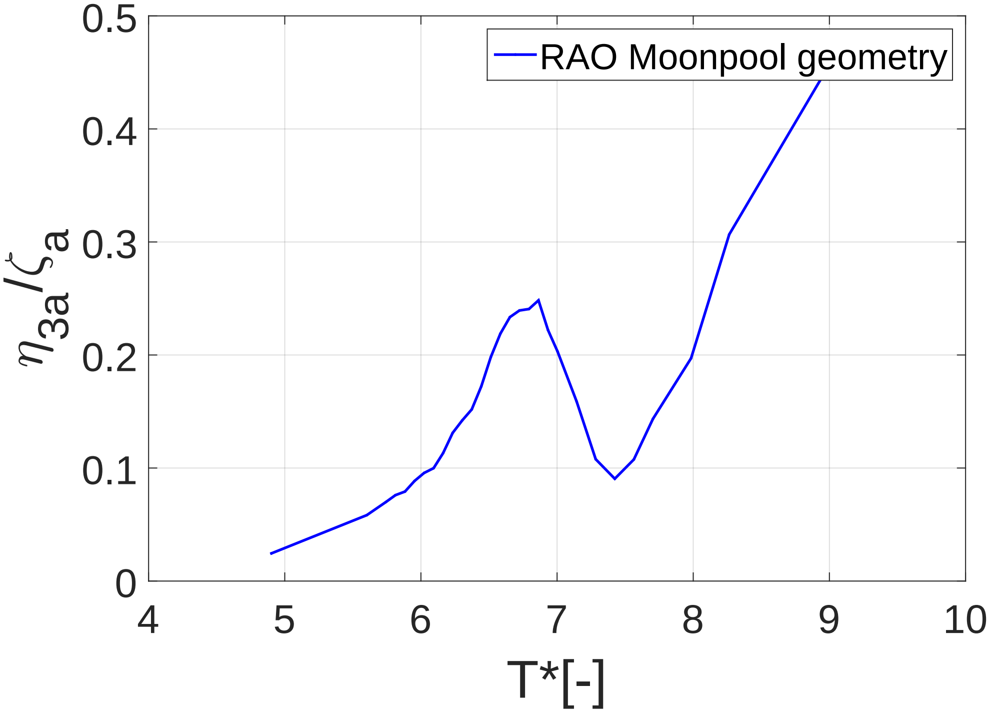

Figure D.171: Heave, wave steepness 1/45, App. 2 inlet, Mass at ends

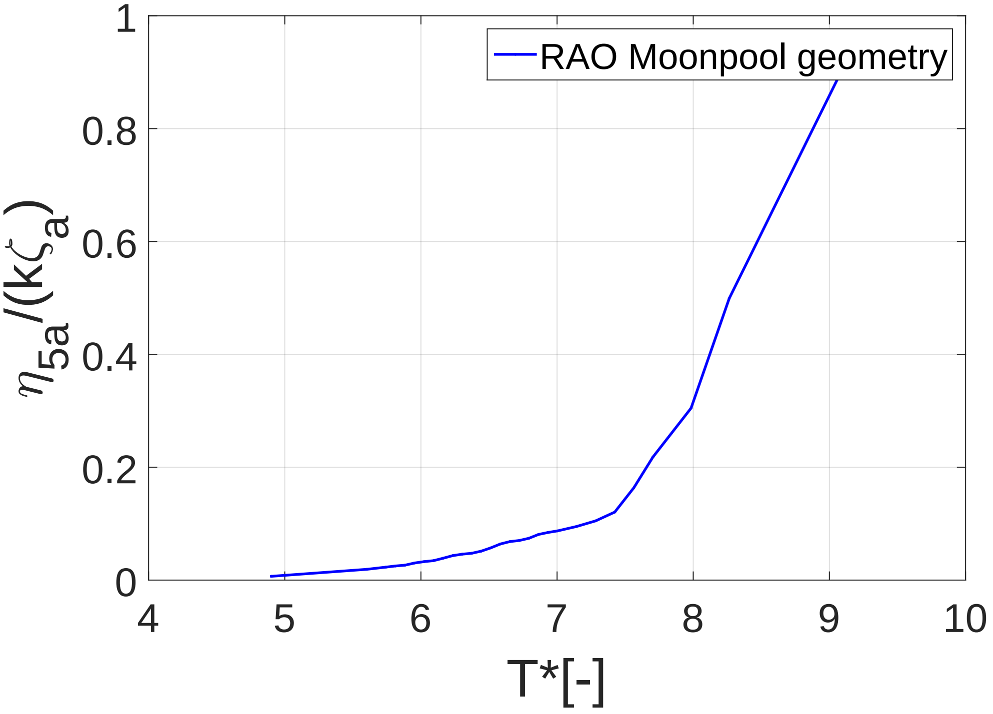

Figure D.172: Pitch, wave steepness 1/45, App.2 inlet, Mass at ends

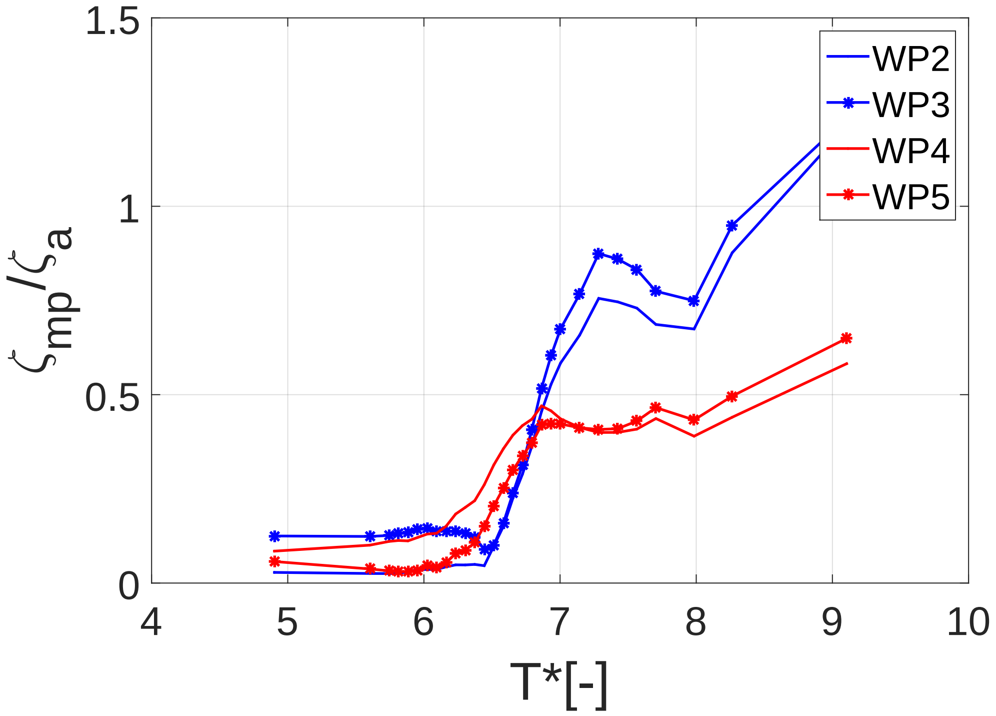

Figure D.173: Moonpools, wave steepness 1/45, App. 2 inlet, Mass at ends

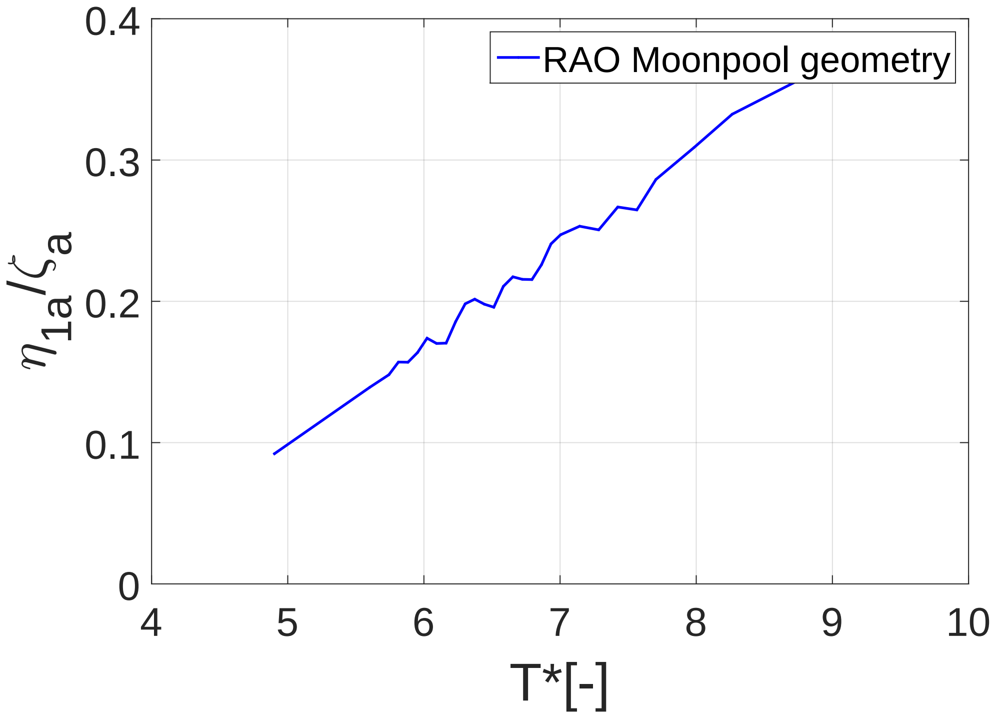

Figure D.174: Surge, wave steepness 1/30, App. 2 inlet, Mass at ends

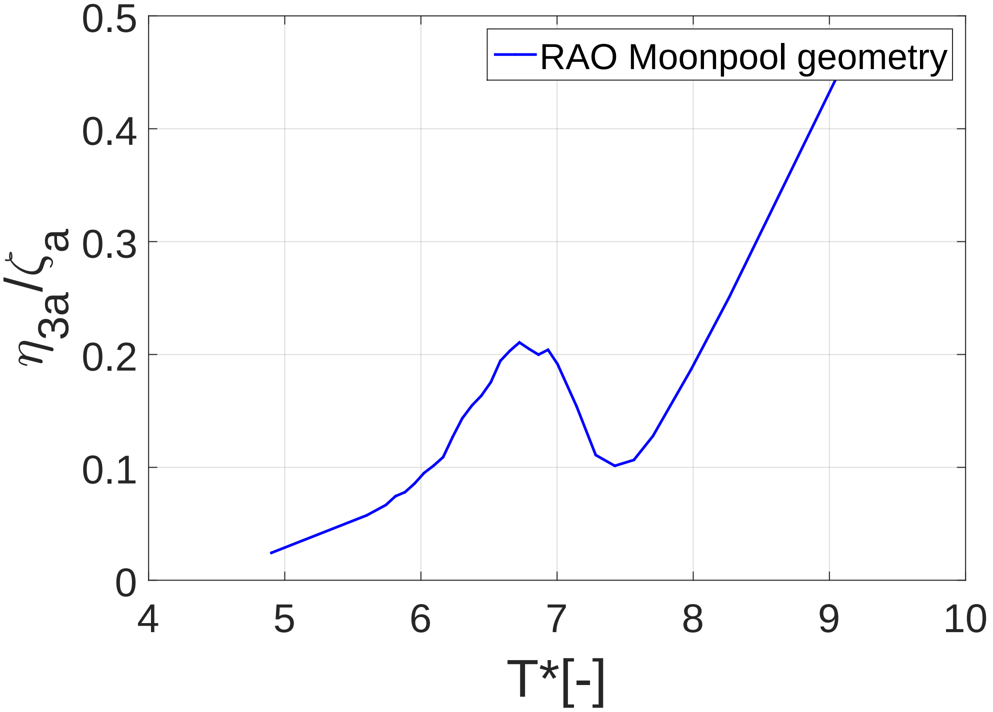

Figure D.175: Heave, wave steepness 1/30, App. 2 inlet, Mass at ends

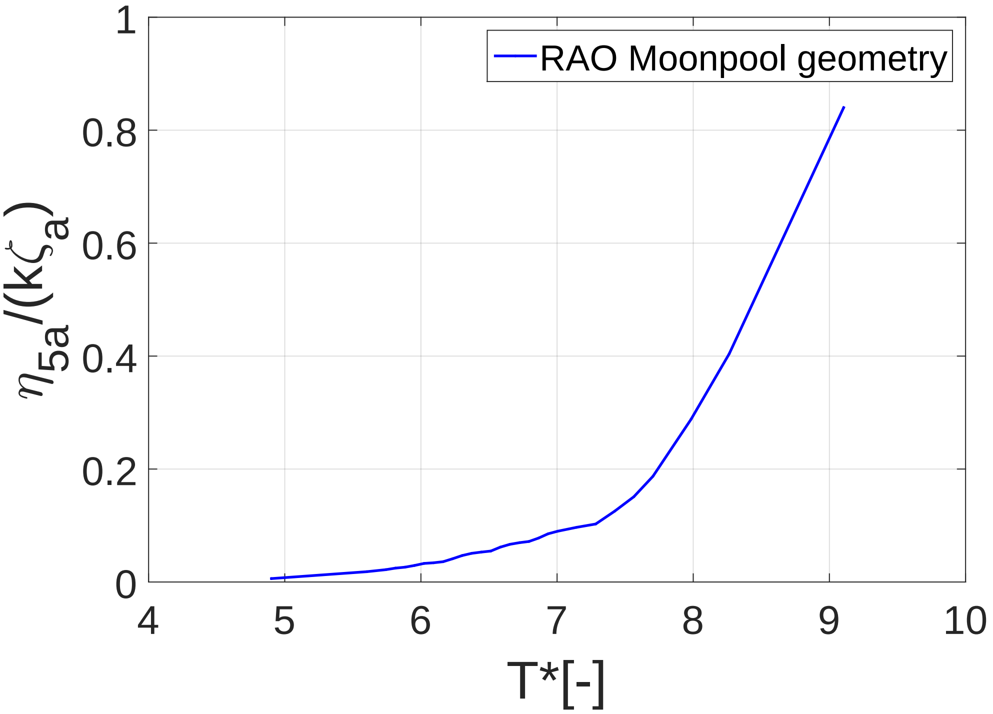

Figure D.176: Pitch, wave steepness 1/30, App. 2 inlet, Mass at ends

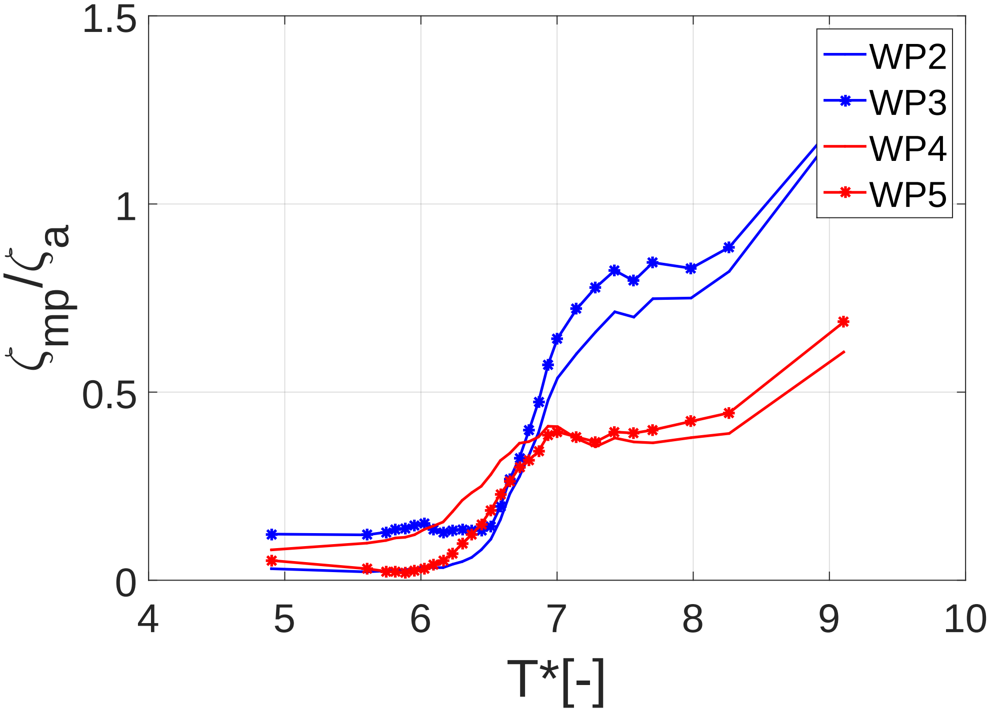

Figure D.177: Moonpools, wave steepness 1/30, App. 2 inlet, Mass at ends

Bibliography

Multiconsult floating bridge. `http://www.multiconsult.no/prosjekter/kryssing-av-sulafjorden-hengebru-pa-flytende-fundamenter/`, a. Accessed: 2016-05-25.

MetOcean. `http://www.multiconsult.no/prosjekter/kryssing-av-sulafjorden-metocean/`, b. Accessed: 2016-05-29.

OpenFOAM introduction page. `http://www.openfoam.com/documentation/user-guide/userch1.php`. Accessed: 2016-05-10.

OpenFOAM file structures. `http://www.openfoam.com/documentation/user-guide/case-file-structure.php`. Accessed: 2016-05-10.

OpenFOAM free surface flow. `http://openfoam.org/release/2-1-0/free-surface-flow/`. Accessed: 2016-05-11.

A. B. Aalbers. The water motions in a moonpool. *Ocean Engineering*, 11:557–597, 1984.

T. Bunnik, W. Pauw, and A. Voogt. Hydrodynamic analysis for side-by-side offloading. *ISOPE*, 2009.

Y. A. Çengel and J. M. Cimbala. *Fluid Mechanics Fundamentals and applications*. McGrawHill, 2010.

O. M. Faltinsen. *Sea Loads on Ships and Offshore Structures*. Cambridge Ocean University Press, 1990.

O. M. Faltinsen, O. F. Rognebakke, and A. N. Timokha. Two-dimensional resonant piston-like sloshing in a moonpool. *J. Fluid Mech.*, 575:359–397, 2007.

J. H. Ferziger and M. Perić. *Computational Methods for Fluid Dynamics*. Springer, third edition, 2002.

J. R. Fornier, M. Naciri, and Z. B. Chen. Hydrodynamics of two side-by-side vessels experiments and numerical simulations. *The International Society of Offshore and Polar Engineers*, 2006.

A. G. Fredriksen. *A numerical and experimental study of a two-dimensional body with moonpool in waves and current*. PhD thesis, Norwegian University of Science and Technology, 2015.

T. Kristiansen and O. M. Faltinsen. Application of a vortex tracking method to the piston-like behaviour in a semi-entrained vertical gap. *Applied Ocean Research*, 2008.

T. Kristiansen and O. M. Faltinsen. Gap resonance analyzed by a new domain-decomposition method combining potential and viscous flow. *Applied Ocean Research*, 2011.

C. M. Larsen. *Marin dynamikk*. Akademika forlag, NTNU, 2014.

L. Lu, L. Cheng, B. Teng, and M. Zhao. Numerical investigation of fluid resonance in two narrow gaps of three identical rectangular structures. *Applied Ocean Research*, 32:177–190, 2010.

P. McIver. Complex resonances in the water-wave problem for a floating structure. *J. Fluid Mech.*, 2005.

B. Molin. On the piston and sloshing modes in moonpools. *Cambridge University Press*, pages 27–50, 2001.

N. Moradi, T. Zhou, and L. Cheng. Geffect of inlet configuration on wave resonance in the narrow gap of two fixed bodies in close proximity. *Ocean Engineering*, 2015.

B. Pettersen. *TMR4247 MARIN TEKNIKK 3 HYDRODYNAMIKK*. Dept. of Marine technology, NTNU, Trondheim, 2007.

L. M. U. Reiersen. Investigation of moonpool resonance as vessel damping device, 2015.

S. Steen. *Experimental Methods in Marine Hydrodynamics*. Dept. of Marine technology, NTNU, Trondheim, 2014.

J. Tu, G.-H. Yeoh, and C. Liu. *Computational Fluid Dynamics, A Practical Approach*. Elsevier, second edition, 2013.

O. Zikanov. *Essential Computational Fluid Dynamics*. John Wiley Sons, INC., 2010.